Version 11.0
December 2011

Advanced Camera for Surveys Instrument Handbook for Cycle 20

(With Historical Information for the Inoperative HRC Channel)

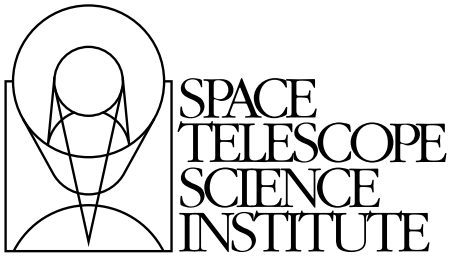

Space Telescope Science Institute
3700 San Martin Drive
Baltimore, Maryland 21218
help@stsci.edu

Operated by the Association of Universities for Research in Astronomy, Inc., for the National Aeronautics and Space Administration

User Support

For prompt answers to any question, please contact the STScI Help Desk.

- **E-mail:** help@stsci.edu
- **Phone:** (410) 338-1082
  (800) 544-8125 (U.S., toll free)

World Wide

Information and other resources are available on the ACS Web site:

- **URL:** http://www.stsci.edu/hst/acs

Revision History

Version	Date	Editors
11.0	December 2011	Ubeda, L., et al.
10.0	December 2010	Maybhate, A and Armstrong, A., et al.
9.0	January 2010	Maybhate, A., et al.
8.0	December 2007	Boffi, F.R., et al.
7.1	December 2006	Pavlovsky, C. et al.
7.0	October 2006	Pavlovsky, C., et al.
6.0	October 2005	Gonzaga, S., et al.
5.0	October 2004	Pavlovsky, C., et al.
4.0	October 2003	Pavlovsky, C., et al.
3.0	October 2002	Pavlovsky, C., et al.
2.1	July 2001	Pavlovsky, C., et al.
2.0	June 2001	Suchkov, A., et al.
1.0	June 2000	Jedrzejewski, R., et al.

Citation

In publications, refer to this document as:
Ubeda, L., et al. 2011, “ACS Instrument Handbook”, Version 11.0 (Baltimore: STScI).

Send comments or corrections to:
Space Telescope Science Institute
3700 San Martin Drive
Baltimore, Maryland 21218
E-mail: help@stsci.edu

Table of Contents

Acknowledgments

The technical and operational information contained in this Handbook is the summary of the experience gained by members of the STScI ACS/WFPC2 Team (AWT), the ACS group at the Space Telescope European Coordinating Facility (ST-ECF), and by the ACS Instrument Definition Team (IDT).

Members of the STScI ACS/WFPC2 Team are Linda Smith[1] (Lead), Amber Armstrong, Roberto Avila, Ralph Bohlin, Marco Chiaberge[1], Andrew Fruchter, David Golimowski, Shireen Gonzaga, Norman Grogin, Pey Lian Lim, Ray Lucas, Aparna Maybhate, Matt McMaster, Sara Ogaz, Anatoly Suchkov, and Leonardo Ubeda.

The ST-ECF ACS group is Martin Kuemmel, Harald Kuntschner, and Jeremy Walsh. The ST-ECF ceased operations on December 31, 2010.

The ACS IDT is Holland Ford (PI), Garth Illingworth (Deputy PI), George Hartig, Mark Rafal, Frank Bartko, Tom Broadhurst, Bob Brown, Chris Burrows, Ed Cheng, Mark Clampin, Jim Crocker, Paul Feldman, Marijn Franx, David Golimowski, Randy Kimble, John Krist, Tom La Jeunesse, Mike Lesser, Doug Leviton, George Miley, Marc Postman, Piero Rosati, Bill Sparks, Pam Sullivan, Zlatan Tsvetanov, Paul Volmer, Rick White, Bob Woodruff, Terence Allen, Kenneth Anderson, David Ardila, Narciso Benitez, John Blakeslee, Rychard Bouwens, Larry Bradley, Nicholas J.G. Cross, Ricardo Demarco, Tomotsugu Goto, Caryl Gronwall, Brad Holden, Nicole Homeier, Daniel Magee, André Martel, W. Jon McCann, Simona Mei, Felipe Menanteau, Gerhardt Meurer, Veronica Motta, Alessandro Rettura, Marco Sirianni, Hien Tran, and Andrew Zirm.

The contributions of Susan Rose (Sr. Technical Editor) are greatly appreciated.

1. European Space Agency (ESA)

CHAPTER 1:

Introduction

The Advanced Camera for Surveys (ACS), a third-generation instrument, was installed in the Hubble Space Telescope during Servicing Mission 3B, on March 7, 2002 (http://www.stsci.edu/hst/HST_overview/servicing_missions). Its primary purpose was to increase *HST* imaging discovery efficiency by about a factor of 10, with a combination of detector area and quantum efficiency that surpasses previous instruments.

ACS has three independent cameras that have provided wide-field, high resolution, and ultraviolet imaging capabilities respectively, using a broad assortment of filters designed to address a large range of scientific goals. In addition, coronagraphic, polarimetric, and grism capabilities have made the ACS a versatile and powerful instrument.

The *ACS Instrument Handbook*, which is maintained by the ACS-WFPC2 Team at STScI, describes the instrument properties, performance, operations, and calibration. It is the basic technical reference manual for the instrument, and should be used with other documents (listed in Table 1.1) for writing Phase I proposals, detailed Phase II programs, and for data analysis. (See Figure 1.1).

In May 2009, Servicing Mission 4 (SM4) successfully restored the ACS Wide Field Camera (WFC) to regular service after its failure in January 2007. Unfortunately, the ACS High Resolution Camera (HRC) was not restored to operation during SM4, so it cannot be proposed for new observations. Nevertheless, this handbook retains description of the HRC to support analysis of archived observations. The ACS Solar Blind Channel (SBC) was unaffected by the January 2007 failure of WFC and HRC. The SBC has remained in steady operation, and was not serviced during SM4. It remains available for new observations.

The documents in Table 1.1 can be downloaded from the ACS STScI Web site, http://www.stsci.edu/hst/acs. Paper copies can be requested by sending a message to help@stsci.edu or by calling 410-338-1082.

Table 1.1: Useful documents

Purpose	Document or Resource
General observatory information	*HST Primer* *http://www.stsci.edu/hst/proposing/proposing/documents/primer/primer_cover.html*
Phase I proposals	Proposing Overview http://www.stsci.edu/hst/proposing/docs/proposingOverview *Call for Proposals* http://www.stsci.edu/hst/hst/proposing/documents/cp/cp_cover.html
Phase II programs	*Phase II Proposal Instructions* http://www.stsci.edu/hst/programs/hst/proposing/docs/p2pi.html Astronomer's Proposal Tool (APT) for Phase II preparations http://apt.stsci.edu/ ACS Dither Pointing Patterns http://www.stsci.edu/hst/acs/proposing/dither
Data analysis	*ACS Data Handbook* http://www.stsci.edu/hst/acs/documents/handbooks/currentDHB/acs_cover.html *MultiDrizzle Handbook v3.0* http://www.stsci.edu/hst/HST_overview/documents/multidrizzle Space Telescope Analysis Newsletter http://www.stsci.edu/hst/acs/documents/isrs/hst/acs/documents/newsletters Instrument Science Reports http://www.stsci.edu/hst/acs/documents/isrs Post-observation Overview http://www.stsci.edu/hst/Post-observation ACS Data Calibration and Analysis http://www.stsci.edu/hst/acs/analysis
Instrument specific	ACS Web page http://www.stsci.edu/hst/acs

Figure 1.1: Handbook roadmap for proposal preparation.

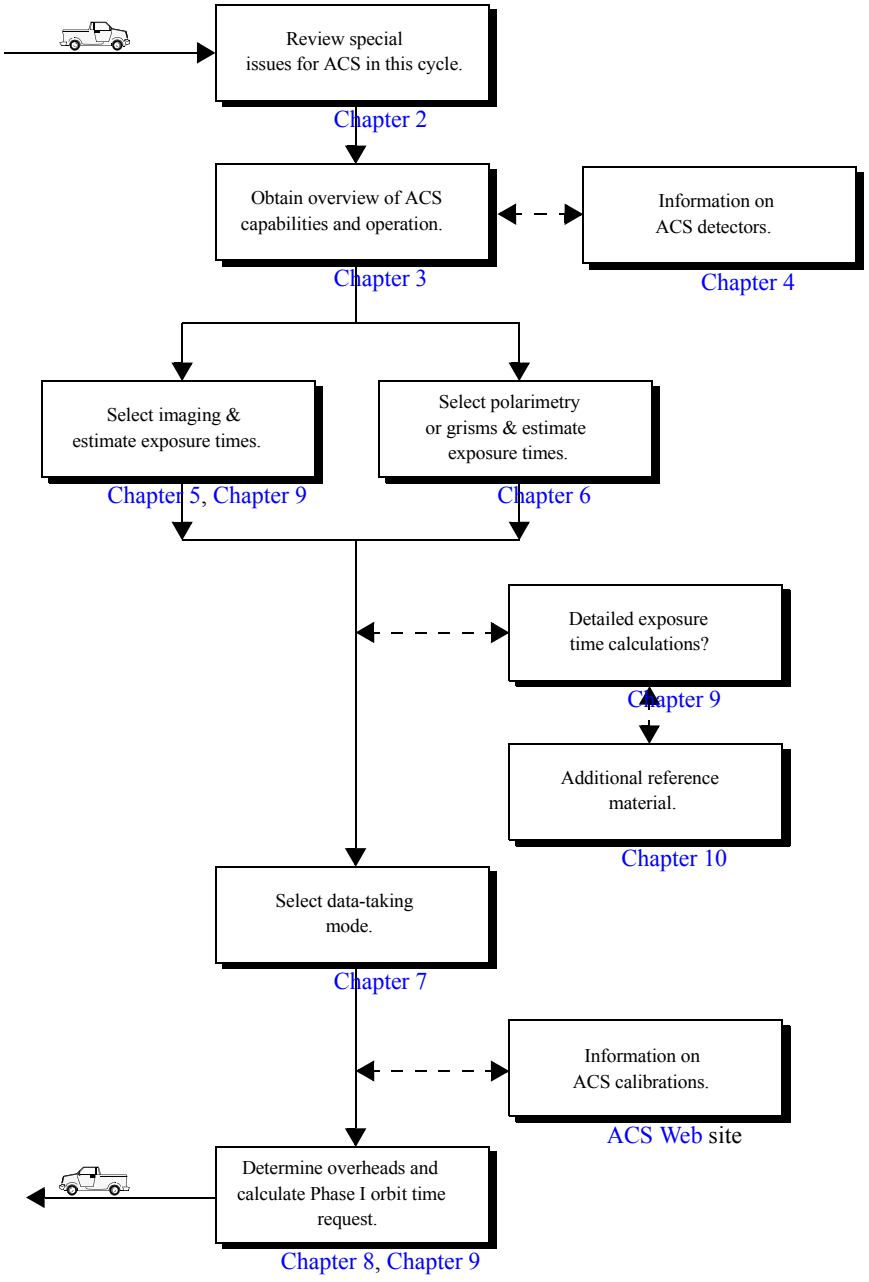

CHAPTER 2:

Changes After SM4 and Considerations for Cy20

In this chapter . . .

2.1 SM4 Repair of ACS

During the third EVA of SM4 on 16 May 2009, astronauts John Grunsfeld and Drew Feustel replaced the ACS CCD Electronics Box and Low Voltage Power Supply that incrementally failed in June 2006 and January 2007, causing the loss of the ACS Wide Field Channel and High Resolution Channel. The replacement components (CEB-R and LVPS-R) immediately restored the function of the WFC but not that of the HRC. Unfortunately, the damage in 2006 to the circuitry that controlled the HRC occurred upstream of the location repaired by the CEB-R. This situation was not unexpected, as the post-failure analysis of the nature and location of the short in the HRC circuitry was ambiguous. Consequently, only the WFC and the Solar Blind Channel (SBC) are available to observers in this cycle and beyond.

The CEB replacement (CEB-R) features new CCD controller and signal processing electronics based upon a programmable SIDECAR (system image, digitizing, enhancing, controlling, and retrieving) ASIC (Application-Specific Integrated Circuit) manufactured by Teledyne Scientific & Imaging. The dual-slope integrator within the

CEB-R delivers nearly 1 e^- lower read noise than was obtained with the old CEB. The CEB-R does, however, induce some low-level (1-2 DN) correlated noise and a spatially variable bias level in the WFC images. The bias level of each pixel also shifts by 0.02-0.3% of the signal. These artifacts are removable in post-image processing and should have little to no effect on most WFC science programs. Because the bias

gradient depends on the timing pattern of the CCD read out, fewer WFC subarray options are supported in this cycle than were supported in previously observing cycles.

Table 2.1 lists the basic characteristics of the WFC CCDs before the failure of ACS in January 2007 and after the installation of the CEB-R during SM4 in May 2009. The fourth column in the table lists the section in this Handbook where detailed information about each characteristic can be found. Further details on improvements can be found in ACS ISR 2011-04 (Golimowski et al., 2011).

Table 2.1: WFC Performance Summary

Characteristic	January 2007 (pre-SM4)	December 2011 (post-SM4)	Handbook Section
Read noise (e^-; gain = 2)	5.5	3.9-4.7	Section 4.3.3
Dark current (e^- /pix/hr)	10.7	20.3-23.4	Section 4.3.4
Hot pixels (%)	0.68	1.46	Section 4.3.5
Full well depth (e^-)	84,000	>80,000	Section 4.3.1
Non-linearity (%)	<0.1	<0.2	Section 4.3.1
CTE (1620 e^-; EPER)	<0.999949	0.99989	Section 4.3.7
Bias shift (%)	0.02	0.02-0.30[1]	Section 2.1

1. Before application of bias-shift correction algorithm.

2.2 Comparison of ACS/WFC and WFC3/UVIS

The UVIS channel of the Wide Field Camera 3 complements ACS/WFC over wavelengths ~ 3700 Å to 10,000 Å. Observers must determine which instrument is more appropriate for their science from the perspectives of field of view, pixel size, throughput, and filter availability. Table 2.2, Figure 2.1 and Figure 2.2 show these characteristics for each instrument. See Figures 5.8 (limiting magnitude for point sources) and Figure 5.9 (limiting magnitude for extended sources). ACS/WFC has a larger pixel scale (0.05 arcsec/pixel) than WFC3/UVIS (0.04 arcsec/pixel), so the field of view of ACS/WFC (202 x 202 $arcsec^2$) is considerably larger than that of WFC3/UVIS (162 x 162 $arcsec^2$). WFC3/UVIS is therefore preferred if angular resolution is more important than field of view. On the other hand, ACS/WFC is more sensitive than WFC3/UVIS at wavelengths longward of ~ 400 nm, so ACS/WFC should be used if greater sensitivity at red wavelengths is important. However, users must also consider ACS's inferior charge-transfer efficiency (CTE) compared to WFC3/UVIS, and its increased number of hot pixels caused by its lengthy exposure to *HST*'s trapped radiation environment. (See Section 4.3.7 for details.)

Table 2.2: Comparison of wavelength coverage, pixel scales, and fields of view of ACS and WFC3/UVIS. HRC is not longer available.

Instrument	Wavelength coverage (nm)	Average Pixel size (arcsec)	Field of View (arcsec^2)
WFC3 UVIS	200 - 1000	0.04	162 x162
ACS WFC	370 - 1100	0.05	202 x 202
ACS HRC	200 - 1100	0.028 x 0.025	29 x 25
ACS SBC	115 - 170	0.034 x 0.030	35 x 31

It is also possible to use both ACS/WFC and WFC3/UVIS in parallel. The separation of the two cameras is ~ 360" (see Figure 3.1).

2.3 Comparison of ACS/HRC and WFC3/UVIS

Because ACS/HRC is no longer available, WFC3/UVIS is the preferred camera for the 2000 Å to 3700 Å wavelength range. The Space Telescope Imaging Spectrograph (STIS) NUV-MAMA has imaging capabilities over some of this bandpass but it has a much smaller field of view and lower sensitivity. Table 2.2, Figure 2.1 and Figure 2.2 compare the imaging characteristics of ACS/HRC and WFC3/UVIS. The latter camera has twice the U-band throughput of ACS/HRC (Figure 2.2), a field of view that is 35 times larger than that of ACS/HRC, and a pixel scale that is 60% coarser than that of ACS/HRC. WFC3/UVIS is insensitive below 2000 Å. Far-UV imaging is provided by the ACS/SBC and the STIS/FUV-MAMA.

2.4 Dithering in Cycle 20

The ACS/WFPC2 Team recommends that observers dither (or offset) their observations to remove hot pixels, cosmetic defects, and cosmic rays in their combined images. Dithering allows optimal sampling of the point spread function and yields better images than are possible with the CR-SPLIT option, which does not remove hot pixels, permanent cosmetic defects (e.g., bad columns), or the gap between the WFC CCDs. Dithering is especially important in this cycle as the number of hot pixels has reached nearly 1.5% after many years in orbit.

Dithering can be performed in two ways:

1. explicit positional offsets between exposures via POS-TARG instructions; or
2. flexible predefined dither patterns which can be nested to implement different pixel subsampling strategies.

Both methods yield associations of images for data pipeline processing. Currently available predefined dither patterns and their recommended uses are described on the ACS Dither Web page,

http://www.stsci.edu/hst/acs/proposing/dither

The ACS/WFPC2 Team at STScI is available to help observers select dither patterns that best suit their science goals. Observers who choose not to dither their ACS/WFC exposures must justify not doing so in the Description of Observations section of their Phase I proposal.

Figure 2.1: *HST* total system throughputs as a function of wavelength.

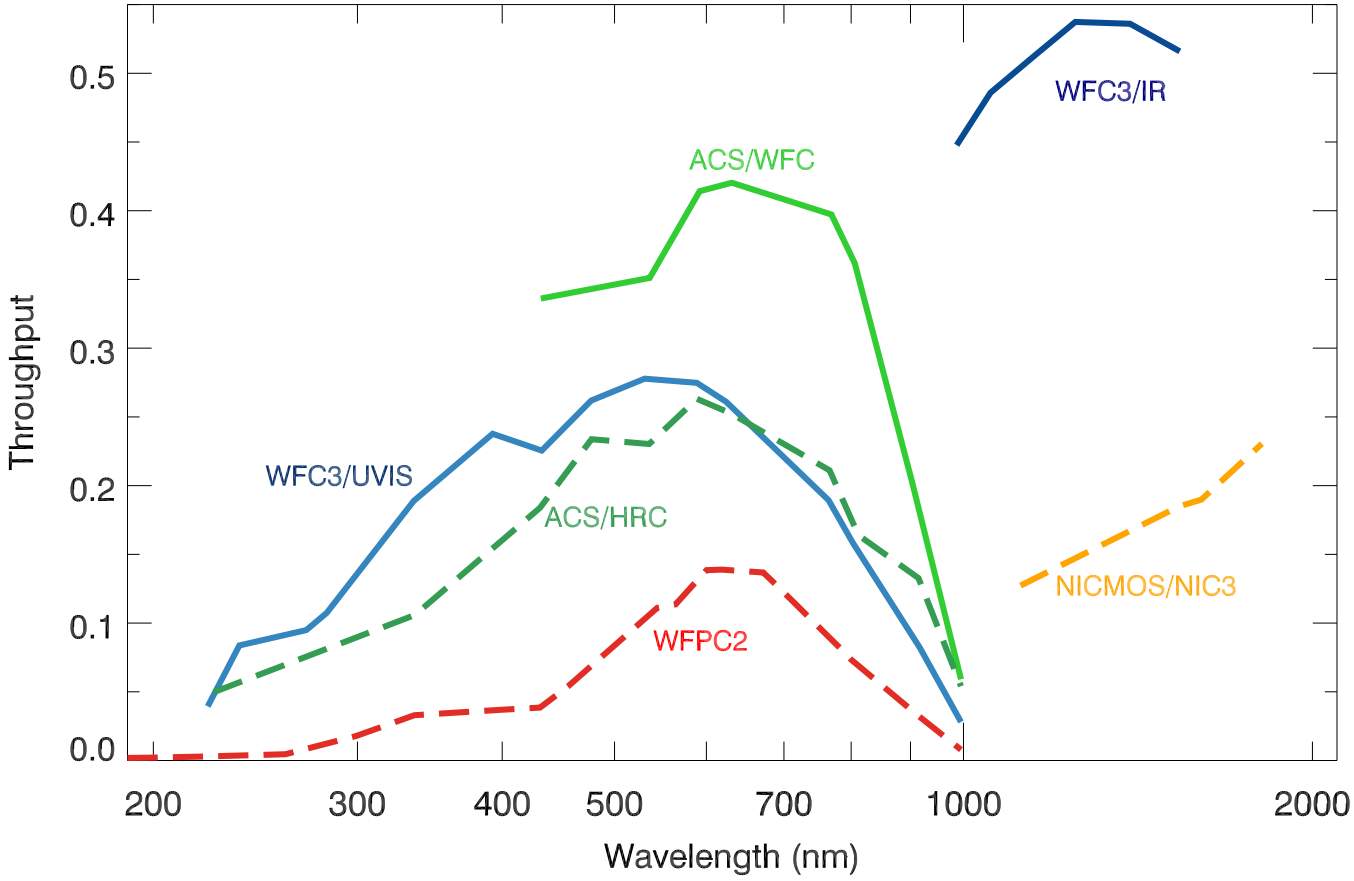

The plotted quantities are end-to-end throughputs, including filter transmissions calculated at the pivot wavelength of each broad-band filter. Full lines represent instruments currently active on board *HST*. Dashed lines represent instruments that are no longer offered (HRC, NICMOS) and a previously flown instrument (WFPC2).

Figure 2.2: *HST* survey discovery efficiencies.

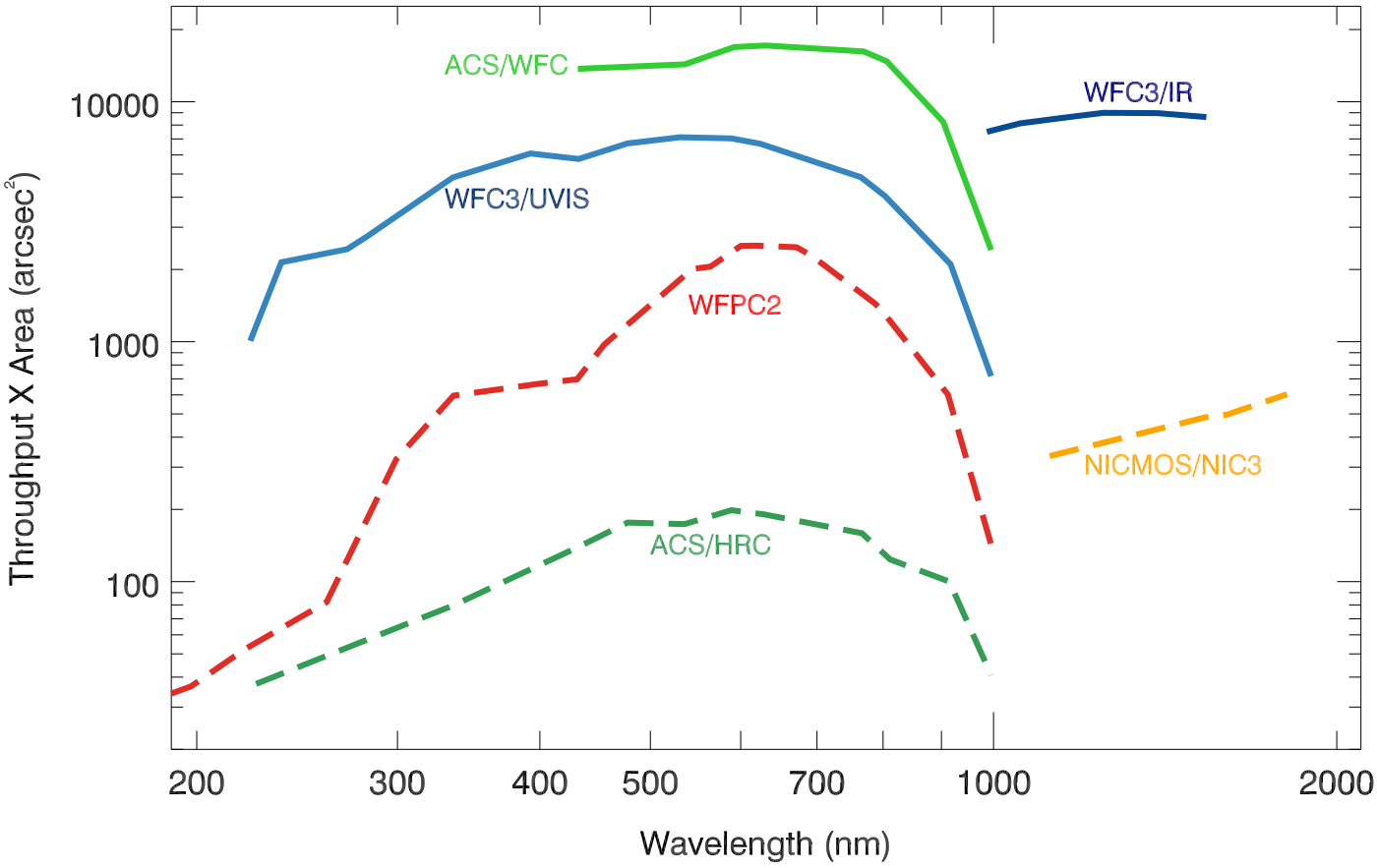

HST survey discovery efficiencies of the cameras, defined as the system throughput multiplied by the area of the field-of-view. Full lines represent instruments currently active on board *HST*. Dashed lines represent instruments that are no longer offered (HRC, NICMOS) and a previously flown instrument (WFPC2).

CHAPTER 3:

Introduction to ACS

In this chapter . . .

3.1 ACS Location in the *HST* Focal Plane

ACS is mounted in one of the axial instrument bays behind the *HST* primary mirror. The relative locations of the science instruments in the focal plane and their fields of view are shown schematically in Figure 3.1. When referring to the *HST* and its focal plane, we use a coordinate system that is fixed to the telescope and consists of three orthogonal axes: U1, U2 and U3. U1 lies along the optical axis, U2 is parallel to the solar-array rotation axis, and U3 is perpendicular to the solar-array axis. (Note: Some *HST* documentation uses the alternative V1, V2, V3 coordinate system for which V1=U1, V2= –U2 and V3= –U3.)

Figure 3.1: The *HST* field of view with the locations of the SI and the FGS apertures in the (U2,U3) focal plane. It shows the layout of the instrument entrance apertures in the telescope focal plane as projected onto the sky. The scale in arc seconds is indicated.

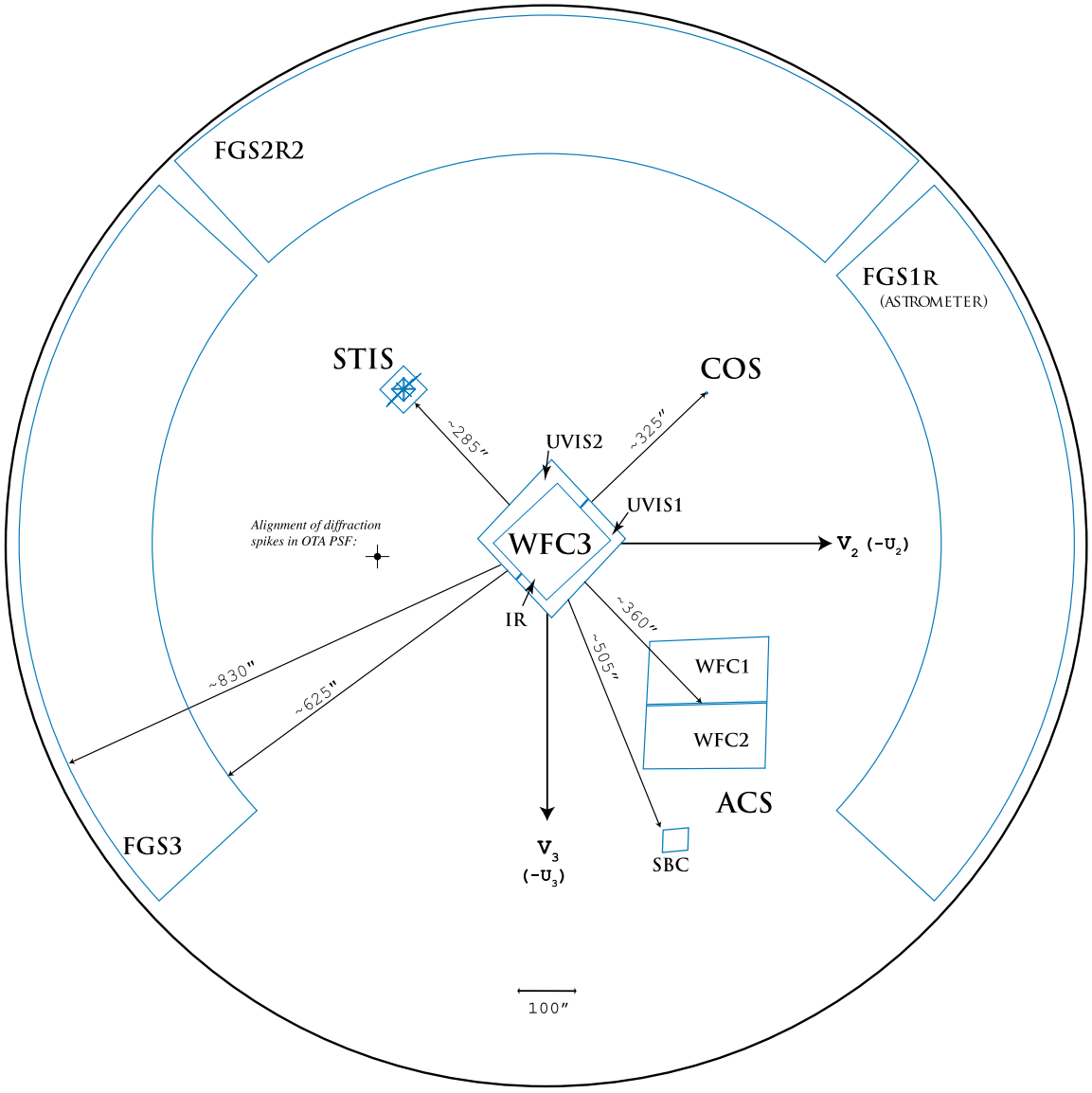

3.2 Instrument Capabilities

Online

Please check for updates on the ACS Web site.

ACS is a versatile instrument with a broad range of scientific capabilities:

- deep, wide-field imaging from visible to near-IR wavelengths (March 2002 to present).
- high spatial resolution imaging from near-UV to near-IR wavelengths (March 2002 to January 2007).
- solar blind UV imaging (March 2002 to present).

ACS was built with three channels, each optimized for a specific goal:

- Wide Field Channel (WFC): 202 x 202 arcsecond field of view from ~3500 Å to 11,000 Å, and peak efficiency of 48% (including the Optical Telescope Assembly (OTA)). The plate scale of ~0.05 arcseconds/pixel provides critical sampling at 11,600 Å.
- High Resolution Channel (HRC): 29 x 26 arcsecond field of view from ~1700 Å to 11,000 Å, and peak efficiency of 29%. The plate scale of ~0.027 arcseconds/pixel provided critical sampling at 6300 Å. HRC is no longer operational.
- Solar Blind Channel (SBC): 34.6 x 30.5 arcsecond field of view from 1150 Å to 1700 Å, plate scale of ~0.032 arcseconds/pixel, and peak efficiency of 7.5%.

In addition to its primary capabilities listed above, ACS has also provided:

- Grism spectroscopy: Low resolution (R ~100 @ 8000 Å) wide field spectroscopy from 5500 Å to 10,500 Å with WFC (and HRC before January 2007).
- Prism spectroscopy: low resolution (R ~100 @ 1500 Å) far-UV spectroscopy from 1250 Å to 1800 Å with SBC (and low resolution (R = 59 @ 2500 Å) near-UV spectroscopy from 1700 Å to 3900 Å with HRC before January 2007).
- Imaging Polarimetry: polarimetric imaging with WFC (and HRC before January 2007) with relative polarization angles of 0°, 60°, and 120°.
- Coronagraphy (before January 2007): aberrated beam coronagraphy with HRC from 2000 Å to 11,000 Å with 1.8 arcsecond and 3.0 arcsecond diameter occulting spots.

3.3 Instrument Design

3.3.1 Detectors

The ACS channels feature the following detectors:

- The WFC employs a mosaic of two 4096 x 2048 Scientific Imaging Technologies (SITe) CCDs. The 15 x 15 µm pixels provide ~0.05 arcseconds/pixel spatial resolution, with critical sampling at 11,600 Å, resulting in a nominal 202 x 202 arcsecond field of view (FOV). The spectral sensitivity of the WFC ranges from ~3500 Å to ~11,000 Å, with a peak efficiency of 48% at ~7000 Å (including OTA).
- The nonfunctioning HRC has a 1024 x 1024 SITe CCD, with 21 x 21 µm pixels that provided ~0.028 x 0.025 arcsecond/pixel spatial resolution with critical sampling at 6300 Å. This gave the HRC a nominal 29 x 26 arcsecond field of view. The spectral response of the HRC ranged from ~1700 Å to ~11,000 Å, and it has a peak efficiency of 29% at ~6500 Å (including OTA).
- The SBC detector is a solar-blind CsI microchannel plate (MCP) with Multi-Anode Microchannel Array (MAMA) readout. It has 1024 x 1024 pixels, each 25 x 25 µm in size. This provides a spatial resolution of ~0.034 x 0.030 arcseconds/pixels, producing a nominal FOV of 34.6 x 30.1 arcseconds. The SBC UV spectral response ranges from ~1150 Å to ~1700 Å with a peak efficiency of 7.5% at 1250 Å.

The WFC & HRC CCDs

The ACS CCDs are thinned, backside-illuminated full-frame devices cooled by thermo-electric cooler (TEC) stacks housed in sealed, evacuated dewars with fused silica windows. The spectral response of the WFC CCDs is optimized for imaging at visible to near-IR wavelengths, while the HRC CCD spectral response was optimized specifically for near-UV wavelengths. The WFC CCD camera produces a time-integrated image in the ACCUM data-taking mode as did the HRC CCD before January 2007. As with all CCD detectors, there is noise and overhead associated with reading out the detector following an exposure.

The minimum WFC exposure time is 0.5 seconds. The minimum time between successive identical full-frame WFC exposures is 135 seconds. The readout time can be reduced to as little as ~35 seconds for WFC subarrays. The dynamic range for a single exposure is ultimately limited by the depth of the CCD full well (~85,000 e^- for the WFC and 155,000 e^- for the HRC), which determines the total amount of charge that can accumulate in any one pixel during an exposure without saturation. Cosmic rays will affect all CCD exposures. CCD observations should be broken into multiple exposures whenever possible to allow removal of cosmic rays in post-observation data processing, see Section 4.3.6.

The SBC MAMA

The SBC MAMA is a photon-counting detector which provides a two-dimensional ultraviolet imaging and spectroscopic capability. It is operated only in ACCUM mode. To protect the MAMA against permanent damage from over-illumination, local and global brightness limits of 50 counts/second/pixel and 200,000 counts/second, respectively are imposed on all SBC targets. Note that the linearity of the MAMA deviates by 1% at a local (pixel) count rate of ~22 counts/second/pixel, which is half the bright object screening limit. The global count rate becomes similarly nonlinear at the screening limit of 200,000 counts/second. More information on the SBC's nonlinearity and bright object limits is given in Section 4.5, Section 4.6, and Section 7.2, and in ACS ISRs 98-03 and 99-07.

3.3.2 ACS Optical Design

The ACS design incorporates two main optical channels: one for the WFC, and one which is shared by the HRC and SBC. Each channel has independent corrective optics to compensate for spherical aberration in the *HST* primary mirror. The WFC has silver-coated optics to optimize instrument throughput in the visible and near-IR. The silver coatings cut off at wavelengths shortward of 3500 Å. The WFC has two filter wheels which it shared with the HRC, offering the possibility of internal WFC/HRC parallel observing for some filter combinations (Section 7.9). The optical design of the WFC is shown schematically in Figure 3.2. The HRC/SBC optical chain comprises three aluminized mirrors overcoated with MgF_2, shown schematically in Figure 3.3. The HRC or SBC channels are selected by means of a plane fold mirror (M3 in Figure 3.3). The HRC was selected by inserting the fold mirror into the optical chain so that the beam was imaged onto the HRC detector through the WFC/HRC filter wheels. The SBC channel is selected by moving the fold mirror out of the beam to yield a two mirror optical chain that focuses light through the SBC filter wheel onto the SBC detector. The aberrated beam coronagraph was accessed by inserting a mechanism into the HRC optical chain. This mechanism positioned a substrate with two occulting spots at the aberrated telescope focal plane and an apodizer at the re-imaged exit pupil. While there was no mechanical reason why the coronagraph could not be used with the SBC, for health and safety reasons, use of the coronagraph was forbidden with the SBC.

Figure 3.2: ACS optical design: Wide Field Channel (ACS/WFC).

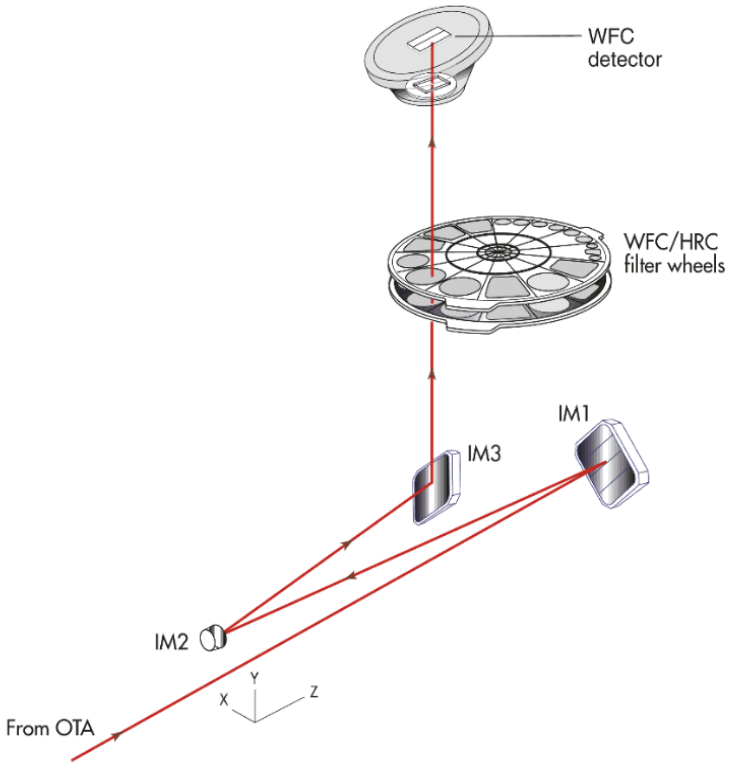

Figure 3.3: ACS optical design: High Resolution/Solar Blind Channels (ACS/HRC and ACS/SBC).

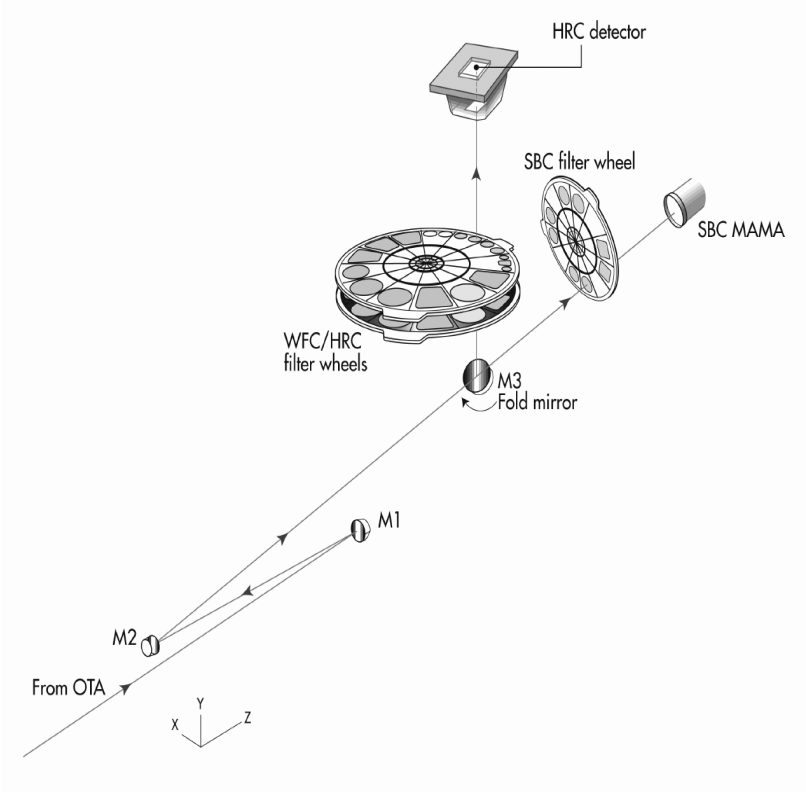

Filter Wheels

ACS has three filter wheels: two shared by the WFC and HRC, and a separate wheel dedicated to the SBC. The WFC/HRC filter wheels contain the major filter sets. Each wheel also contains one clear WFC aperture and one clear HRC aperture (see Chapter 5 for more on filters). Before January 2007, parallel WFC and HRC observations were possible for some filter combinations (auto-parallels). Because the filter wheels were shared, it was not possible to independently select the filter for WFC and HRC parallel observations.

Calibration-Lamp Systems

ACS has a calibration subsystem consisting of tungsten lamps and a deuterium lamp for internally flat fielding each of the optical channels. The calibration lamps illuminate a diffuser on the rear surface of the ACS aperture door, which must be closed for calibration exposures. Under normal circumstances, users are not allowed to use the internal calibration lamps.

3.4 Basic Instrument Operations

3.4.1 Target Acquisitions

For the majority of ACS observations, target acquisition is simply a matter of defining the appropriate aperture for the observation. Once the telescope acquires its guide stars, your target will be positioned within ~1 to 2 arcseconds of the specified aperture. For observations with the ramp filters, one must specify the desired central wavelength for the observation.

3.4.2 Typical ACS Observing Sequence

ACS is expected to be used primarily for deep, wide-field survey imaging. Important issues for observers to consider will be the "packaging" of their observations, how observations are CR-SPLIT to mitigate the impact of cosmic rays, how sub-stepping or "dithering" of images for removal of hot pixels is implemented, and how, if necessary, to construct a mosaic pattern to map the target. Narrowband observations with the WFC are more likely to be read noise limited, requiring consideration of optimum number of readouts. Observations with the MAMA detectors are not affected by cosmic rays or read noise, but long integration times will often be needed to obtain sufficient signal-to-noise.

A typical ACS observing sequence consists of a series of 10 to 20 minute dithered exposures for each desired filter. Observers will generally not take their own calibration exposures. See Chapter 7 for more details about observing strategies.

3.4.3 Data Storage and Transfer

At the conclusion of each exposure, the science data are read out from the detector and placed in ACS's internal buffer memory, where it is stored until it can be transferred to the *HST* solid state data recorder (and thereafter to the ground). The internal buffer memory is large enough to hold one WFC image, or sixteen SBC images, and so the buffer typically must be dumped before or during the following WFC exposure. If the following exposure is longer than ~339 seconds, then the buffer dump from the preceding exposure will be performed during integration (see Section 8.2 for a more complete discussion).

ACS's internal buffer stores the data in a 16 bit-per-pixel format. This structure imposes a maximum of 65,535 counts per pixel. For the MAMA detectors this maximum is equivalent to a limit on the total number of detected photons per pixel which can be accumulated in a single exposure. For the WFC, the 16 bit buffer format (and not the full well) limits the photons per pixel that can be accumulated without saturating in a single exposure when GAIN=0.5 or GAIN=1.0 are selected. This is not an issue when the default GAIN=2.0 is used. See Chapter 4 and Chapter 7 for a detailed description of ACS instrument operations.

3.5 ACS Quick Reference Guide

Please check for updates on the ACS Web site. Information regarding the HRC is provided for archival purposes only.

Table 3.1: Instrument characteristics.

	WFC	HRC (inoperable)	SBC
Field of View	202"× 202"	29"× 26"	34.6"× 30.8"
Plate Scale	~0.05"/pixel	~0.028 × 0.025"/pixel	~0.034 × 0.030"/pixel
Pixel Size	15 × 15 µm	21 × 21 µm	25 × 25 µm
Image Format	2 × 2048 × 4096 pixels	1024 × 1024 pixel	1024 × 1024 pixel
Spectral Response	~3500 Å to 11,000 Å	~1700 Å to 11,000 Å	~1150 Å to 1700 Å
Detector	SITe CCDs thinned backside illuminated, anti-reflection coated, multiphased pinned	SITe CCD thinned backside illuminated, anti-reflection coated, multiphased pinned	CsI MCP with MAMA readout
Detector Efficiency	~77% at 4000 Å ~83% at 6000 Å ~67% at 8000 Å	~33% at 2500 Å ~69% at 6000 Å ~53% at 8000 Å	~19.2% @ 1216 Å
Peak Efficiency[2]	48% at ~7000 Å	29% at ~6500 Å	7.5% at ~1250 Å
Read Noise	4.2 e^-	4.7 e^-	0 counts
Dark Current[2]	0.0062 e^-/s/pixel	0.0058 e^-/s/pixel	1.241 × 10^{-5} e^-/s/pixel
Full Well[2]	84,700 e^-	155,000 e^-	[1]Detector count rate linearity limit: 200,000 counts/sec Pixel count-rate linearity limit: ~22 counts/sec/pixel
Gain	0.5, 1.0, 1.4, and 2.0 e^-/DN (Max 65,535 DN)	1,2,4 and 8 e^-/DN (Max 65,535 DN)	n/a
Operating Temperature[2]	–81°C	–80°C	n/a

1. Loss of linearity occurs at count rates larger than these values. For more information, please see Section 4.5.6.
2. Average value for WFC1 and WFC2

Table 3.2: Calibration accuracies.

Attribute	WFC	HRC	SBC	Limiting factor
Distortion Solution Accuracy	0.1 pixel	0.1 pixel	0.25 pixel	Calibration & stability of geometric distortion[1]
Absolute Astrometry	0.2" to 0.5"	0.2" to 0.5"	0.2" to 0.5"	Guide Star Catalog uncertainties[2]
Absolute Photometry	2%	3%	5%	Absolute flux of standard stars
Relative Photometry within an Image	1%	1%	2%	Flat-field characterization or characterization of geometric distortion.
Repeated Photometry of Same Star	0.3%	0.3%	1%	Stability of flat field
Transformation to Standard Magnitude Systems	0.02 mag SDSS 0.025 mag WFPC2 0.03 mag BVRI	0.02 mag SDSS 0.025 mag WFPC2 0.03 mag BVRI	n/a	DQE curve determination Color terms
Polarimetry	1%	1%	n/a	
Wavelength Calibration	20 Å grism	12 Å grism	1 pixel prisms	Accuracy of dispersion solution
Spectrophotometry	6% (Grism)	10% (Grism)	20% (Prism)	

1. Anderson & King, ISR 04-15 (http://www.stsci.edu/hst/acs/documents/isrs/isr0415.pdf)
2. Koekemoer et al., ISR 05-06 (http://www.stsci.edu/hst/acs/documents/isrs/isr0506.pdf)

Table 3.3: ACS filters.

Filter type	Filter description	Camera
Broadband	Sloan Digital Sky Survey (SDSS): F475W, F625W, F775W, F850LP	WFC/HRC
	B, V, Medium V, Wide V, I: F435W, F555W, F550M, F606W, F814W	WFC/HRC
	Near-UV: F220W, F250W, F330W	HRC
	No Filter: CLEAR	WFC/HRC
Narrowband	Hα (2%), [OIII] (1%), [NII] (1%): F658N, F502N, F660N	WFC/HRC
	NeV (3440 Å): F344N	HRC
	Methane (8920 Å): F892N	HRC/[WFC[1]]
Ramp filters	2% bandpass (3700-10,700 Å): FR388N, FR505N, FR656N	WFC/HRC
	2% bandpass (3700-10,700 Å): FR423N, FR462N, FR716N, FR782N, FR853N, FR931N, FR1016N, FR551N, FR601N	WFC
	9% bandpass (3700-10,700 Å): FR459M, FR914M	WFC/HRC
	9% bandpass (3700-10,700 Å): FR647M	WFC
Spectroscopic	Grism: G800L	WFC/HRC
	Prism: PR200L	HRC
Polarizers	Visible (0°, 60°,120°): POL0V, POL60V, POL120V	HRC/[WFC[1]]
	Near-UV (0°, 60°, 120°): POL0UV, POL60UV, POL120UV	HRC/[WFC[1]]
Medium Band	Lyman-Alpha: F122M	SBC
Long Pass	MgF2, CaF2, BaF2, Quartz, Fused Silica: F115LP, F125LP, F140LP, F150LP, F165LP	SBC
Prisms	LiF, CaF2: PR110L, PR130L	SBC

1. Limited field of view (72" x 72") for these filters using WFC

Table 3.4: ACS polarizers.

Polarizer set	Filters	Filter comments
POL0UV, POL60UV, POL120UV	F220W	HRC NUV short
	F250W	HRC NUV long
	F330W	HRC U
	F435W	Johnson B
	F814W	Broad I
POL0V, POL60V, POL120V	F475W	SDSS g
	F606W	Johnson V
	F625W	SDSS r
	F658N	Hα
	F775W	SDSS i

Table 3.5: ACS dispersers.

Disperser	Channel	Wavelength range (Å)	Resolving power
G800L	WFC	1st order: 5500 to 10,500	100 @8000 Å
G800L	WFC	2nd order: 5000 to 8500	200 @8000 Å
G800L	HRC	1st order: 5500 to 10,500	140 @8000 Å
G800L	HRC	2nd order: 5500 to 8500	280 @8000 Å
PR200L	HRC	1700 to 3900	59 @2500 Å
PR110L	SBC	1150 to 1800	79 @1500 Å
PR130L	SBC	1250 to 1800	96 @1500 Å

Table 3.6: Useful tables and figures list.

Topics	Tables/Figures
Proposal Preparation Tips	Table 7.1: Science decision guide. . Table 7.2: Science feasibility guide. Table 9.1: Useful quantities for the ACS WFC, at -81C Table 9.2: Useful quantities for the ACS SBC.
Overheads	Table 8.1: Science exposure overheads: general. Table 8.2: ACS science exposure overhead times (minutes).
Aperture Parameters	Table 7.6: WFC aperture parameters. Table 7.7: Ramp filter apertures. Table 7.8: HRC aperture parameters. Table 7.9: SBC aperture parameters Table 7.10: Plate scales and axis angles for the 3 ACS channels. Figure 3.1: The HST field of view with the locations of the SI and the FGS apertures in the (U2,U3) focal plane. It shows the layout of the instrument entrance apertures in the telescope focal plane as projected onto the sky. The scale in arc seconds is indicated. Figure 7.8: Aperture and image feature orientation. Figure 7.9: ACS apertures in the V2/V3 reference frame.

Table 3.6: Useful tables and figures list.

Topics	Tables/Figures
Detector Characteristics	Table 3.1: Instrument characteristics. Table 4.1: WFC amplifier gain and read noise after installation of the CEB-R (valid after May 2009). Values apply to dual-slope integrator mode of pixel sampling. Table 4.7: SBC detector performance characteristics.
SBC Bright Object Protection Limits	Table 7.3: Absolute SBC count rate screening limits for nonvariable and variable objects. Table 7.4: Bright limit V-band magnitudes for observations with the SBC filters and prisms (no reddening). Table 7.5: Bright object protection policy for SBC observations.
Hot and Warm Pixels	Table 4.4: Creation rate of new hot pixels (pixel/day). Table 4.5: Annual permanent hot pixel growth (%). Figure 4.5: Hot Pixel Growth Rate for HRC and WFC
Charge Transfer Efficiency	Table 4.6: Charge transfer efficiency measurements for the ACS CCDs after installation in March 2002. (Based on an experiment performed with Fe55) Figure 4.10: Projected CTE losses in WFC (equivalently, the size of corrections)
Geometric Distortion	Figure 10.127: The geometric distortion map for the ACS/WFC, which shows only the non-linear component to the solution. Figure 10.129: The geometric distortion map for the HRC. Figure 10.131: The geometric distortion map for the ACS/SBC. Figure 10.132: The map of the effective pixel areas of the ACS/SBC. The areas are normalized to 0.025 arcsecond square pixels..
Encircled Energy	Table 5.4: Encircled energy measurements for the ACS channels. Table 9.3: Encircled energy comparison for WFC/F850LP. Figure 4.13: MAMA point spread function. Figure 5.11: Encircled energy for the CCD channels. Figure 5.12: Encircled energy for the SBC.
PSF	Figure 5.10: Kernels representing CCD pixel functions for HRC and WFC. Table 5.10: ACS Model PSFs in central 5x5 pixel region (SBC). Figure 5.11: Encircled energy for the CCD channels.
Plate Scale	Table 7.10: Plate scales and axis angles for the 3 ACS channels.
Filters	Table 3.3: ACS filters. Table 3.5: ACS dispersers. Table 5.1: ACS WFC/HRC filters in Filter Wheel #1. Table 5.2: ACS WFC/HRC filters in Filter Wheel #2. Table 5.3: ACS SBC filter complement. Table 5.6: In-band flux as a percentage of the total flux. Table 5.7: Visible-light rejection of the SBC F115LP imaging mode.
Polarizers:	Table 3.4: ACS polarizers. Table 6.1: Filters that can be used in conjunction with the ACS polarizers. Table 6.2: Examples of polarizer and non-polarizer exposures in a Phase II proposal.

Table 3.6: Useful tables and figures list.

Topics	Tables/Figures
Photometry	Table 5.5: V detection limits for ACS, HRC, and SBC direct imaging. Table 9.1: Useful quantities for the ACS WFC, at -81C Table 9.2: Useful quantities for the ACS SBC. Table 10.1: Color corrections AB_n to go from Johnson V magnitude to AB magnitude for the WFC. Table 10.2: Color corrections AB_n to go from Johnson V magnitude to AB magnitude for the HRC. Table 10.3: Color corrections AB_n to go from Johnson V magnitude to AB magnitude for the SBC.
Limiting Magnitudes for Direct Imaging	Table 5.5: V detection limits for ACS, HRC, and SBC direct imaging. Figure 5.8: HST Limiting Magnitude for point sources in 10 hours, as a function of wavelength. Point source limiting magnitude achieved with a signal to noise of 5 in a 10 hour long exposure with optimal extraction. Figure 5.9: HST Limiting Magnitude for extended sources in 10 hours, as a function of wavelength.
Spectroscopy	Table 6.3: Optical parameters of ACS dispersers. Table 6.4: V detection limits for the ACS grism/prism modes. Figure 6.15: Sensitivity versus wavelength for WFC G800L. Figure 6.16: Sensitivity versus pixel position for WFC G800L. Figure 6.18: Sensitivity versus wavelength for HRC G800L. Figure 6.19: Sensitivity versus pixel position for HRC G800L. Figure 6.21: Sensitivity versus wavelength for HRC/PR200L. The numbers indicate the resolving power (R) and the offset from the direct image in pixels (Dx) as functions of wavelength. Figure 6.22: Sensitivity versus wavelength for SBC PR110L. The numbers indicate the resolving power (R) and the offset from the direct image in pixels (Dx) as functions of wavelength. Figure 6.24: Sensitivity versus wavelength for SBC/PR130L. The numbers indicate the resolving power (R) and the offset from the direct image in pixels (Dx) as functions of wavelength.
Sky Backgrounds	Table 9.4: Approximate zodiacal sky background as a function of ecliptic latitude and ecliptic longitude. (In V magnitudes per square arcseconds.) Table 9.5: Geocoronal emission lines. Table 9.6: High sky backgrounds. Figure 9.1: High sky background intensity as a function of wavelength. Figure 9.2: Background contributions in V magnitude per $arcseconds^2$ Figure 9.3: Extinction versus wavelength.
Calibration Accuracies	Table 3.2: Calibration accuracies. Figure 4.5: Hot Pixel Growth Rate for HRC and WFC Figure 4.6: WFC Dark Current Histogram for Chip 1

CHAPTER 4:

Detector Performance

In this chapter. . .

4.1 Overview

ACS employs two fundamentally different types of detectors: CCDs for use from the near-UV to the near-IR, and a Multi-Anode Microchannel Array (MAMA) detector for use in the far-UV. The CCD and the MAMA detectors impose unique limitations on the feasibility of observations. This chapter covers the properties of the ACS detectors and descriptions of how to optimize scientific programs and ensure the feasibility of observations.

4.2 The CCDs

Information regarding the HRC is provided for archival purposes only. Please check for updates regarding WFC on the ACS Web site.

4.2.1 Detector Properties

WFC Properties

The WFC/CCD consists of two 4096 x 2048 charge-coupled devices that are sensitive from the violet to the near-IR. These CCDs are thinned, backside-illuminated devices manufactured by Scientific Imaging Technologies (SITe) and are butted together along their long dimension to create an effective 4096×4096 array with a gap corresponding to approximately 50 pixels between the chips. The CCD camera design incorporates a warm dewar window, designed to prevent buildup of contaminants on the window that cause a loss of UV throughput. A summary of the ACS CCD performance is given in Table 3.1.

HRC

The HRC CCD is a flight-spare STIS 1024×1024 CCD and is a thinned, backside-illuminated device, manufactured at SITe. The coating uses a process developed by SITe to provide good quantum efficiency in the near-ultraviolet. The performance characteristics and specifications are given in Table 3.1

4.2.2 CCD Spectral Response

The responsive quantum efficiency (RQE) of the WFC and HRC CCDs is shown in Figure 4.1; the RQE includes corrections needed to reproduce the instrument sensitivity measured on orbit (ACS ISR 2007-06). The total spectral response of the camera (see Figure 5.7) is given by the product of the RQEs shown here and the throughput of optical elements of the camera. For example, the WFC silver coated mirrors enhance the reflectivity in the near-IR but impose a violet cutoff below 370nm.

Figure 4.1: Responsive quantum efficiency of the HRC CCD (solid line) and WFC CCDs (dashed line).

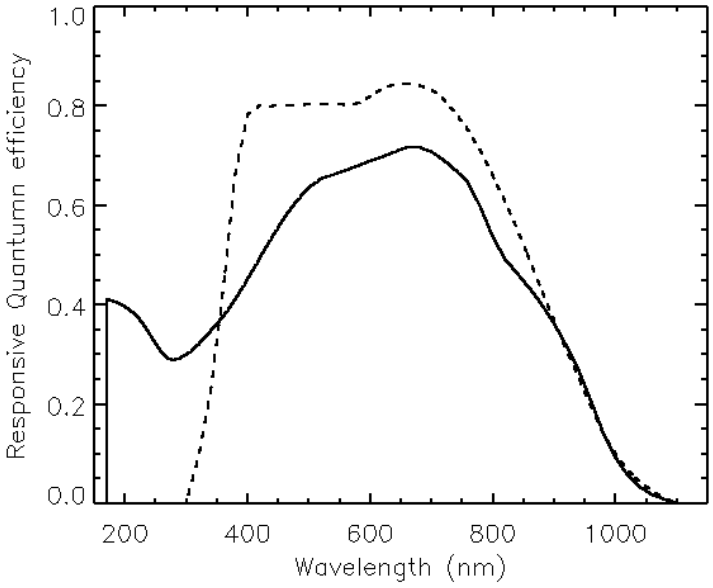

4.2.3 Quantum Efficiency Hysteresis

Based on current data, the ACS CCDs do not suffer from quantum efficiency hysteresis (QEH). The CCDs respond in the same way to light levels over their whole dynamic range, irrespective of the previous illumination level.

4.2.4 CCD Long-Wavelength Fringing

Like most thinned CCDs, the ACS CCDs exhibit fringing longward of ~7500 Å. The fringing is caused by interference of incident light reflected between the front and back surfaces of the CCD. The amplitude of the fringes is a strong function of wavelength and spectral bandpass. Only the F892N filter shows a fringe pattern for white light illumination. The fringe pattern is stable and is removed to first order by the F892N flat field for continuum sources.

4.2.5 Readout Format

WFC

Each CCD is read out as a 4144×2068 array, including physical and virtual overscans. Two amplifiers are used to read out each CCD. The final images consist of 24 columns of physical overscan, 4096 columns of pixel data, and another 24 columns of physical overscan. Each column consists of 2048 rows of pixel data followed by 20 rows of virtual overscan. The orientation of the CCD is such that for the grism spectra, the dispersed images have wavelength increasing from left to right in the positive x-direction.

HRC

The HRC CCD was read out as a 1062 × 1044 array, including physical and virtual overscans. There are 19 columns of physical overscan, followed by 1024 columns of pixel data, and then 19 more columns of physical overscan. Each column consists of 1024 rows of pixel data followed by 20 rows of virtual overscan. As with the WFC, the orientation of the HRC CCD was chosen so that grism images have wavelength increasing from left to right.

4.2.6 Analog-To-Digital Conversion

Electrons that accumulate in the CCD pixels are read out and converted to data numbers (DN) by the analog-to-digital converter (ADC). The ADC output is a 16 bit number, producing a maximum of 65,535 DN in one pixel.

Before the failure of ACS in January 2007, the WFC and HRC CCDs could be operated at ADC gains of 1, 2, 4 or 8 electrons/DN. The current CCD Electronics Box (CEB-R) installed during SM4 changed the WFC's ADC operational gains to 0.5, 1.0, 1.4, and 2.0 electrons/DN. **All four new gains are available to the observer but only the GAIN=2.0 option is fully supported by the ACS Team.** Although lower ADC gains can in principle increase the dynamic range of faint source observations by reducing quantization noise, the improvement is not significant for the WFC.

Table 4.1 shows the gain and read noise values of the four WFC amplifiers measured during the orbital verification period after SM4 for each commanded gain available with the dual-slope integrator pixel sampling mode of the CEB-R. The read noise values apply to the imaging (light-sensitive) regions of the CCD quadrants and are about 0.1 electrons higher than the measured values in the corresponding overscan regions.

For archival purposes, Table 4.2 and Table 4.3 show the gain and read noise values of the four WFC amplifiers and the default HRC amplifier C when operated with Side 1 (March 2002 to June 2006) and Side 2 (June 2006 to January 2007) of the original CEB. The readnoise values in Tables 4.1, 4.2, and 4.3 apply to the image areas.

Table 4.1: WFC amplifier gain and read noise after installation of the CEB-R (valid after May 2009). Values apply to dual-slope integrator mode of pixel sampling.

CCD	Amp	Gain (e^-/DN)				Read Noise (e^-)			
		0.5	1.0	1.4	2.0[1]	0.5	1.0	1.4	2.0[1]
WFC1	A	0.53	1.03	1.45	2.020	3.92	4.05	4.28	4.57
WFC1	B	0.50	0.96	1.36	1.886	3.24	3.36	3.61	3.91
WFC2	C	0.53	1.03	1.45	2.017	3.54	3.69	3.95	4.25
WFC2	D	0.53	1.02	1.45	2.011	3.31	3.43	3.71	4.04

1. Default Gain.

Table 4.2: CCD gain and read noise operated under Side 1 of original CEB (March 2002 to June 2006).

CCD	Amp	Gain (e^-/DN)			Read noise (e^-)		
		1	2[1]	4	1	2[1]	4
WFC1	A	1.000	2.002	4.01	5.57	5.84	--
WFC1	B	0.972	1.945	3.90	4.70	4.98	--
WFC2	C	1.011	2.028	4.07	5.18	5.35	--
WFC2	D	1.018	1.994	4.00	4.80	5.27	--
HRC	C	1.163	2.216	4.235	4.46	4.80	5.86

1. Default Gain.

Table 4.3: CCD gain and read noise operated under Side 2 of original CEB (June 2006 to January 2007).

CCD	Amp	Gain (e^-/DN)			Read noise (e^-)		
		1	2[1]	4	1	2[1]	4
WFC1	A	1.000	2.002	4.01	5.29	5.62	--
WFC1	B	0.972	1.945	3.90	4.45	4.74	--
WFC2	C	1.011	2.028	4.07	5.03	5.34	--
WFC2	D	1.018	1.994	4.00	4.55	4.89	--
HRC	C	1.163	2.216	4.235	4.36	4.82	5.44

1. Default Gain.

4.2.7 Flat Fields

WFC

The WFC flat field reference images are constructed from both ground-based and on-orbit data. Ground-based flats with signal-to-noise ratios of ~300 per pixel were obtained for all filters. Low-frequency refinements of these pixel flats were made using in-flight dithered observations of a rich star field (see ACS ISRs 2002-08 and 2003-10).

These low-frequency flats (L-flats) initially showed a corner-to-corner sensitivity gradient across the CCDs of 10-18%, depending on wavelength.

The L-flats were updated in July 2006 after the operating temperature of the WFC was lowered to -81 °C (see ACS ISR 2006-06). The resulting flat fields are accurate to 1% over the WFC field of view for most broad-band filters and to 2% for F850LP and the narrow-band filters. Observations of a rich star field were obtained shortly after the ACS repair in May 2009 and have been used to verify that the L-flats remain stable.

Internal observations made during SMOV SM4 show that the P-flats (high frequency pixel-to-pixel flats) are also stable.

Figure 4.2 shows the corrected WFC ground flats for several broadband filters. The 50 pixel gap between the top and bottom CCDs is not shown. Because the two CCDs were cut from the same silicon wafer and underwent similar processing, their sensitivities are continuous across the gap. The central doughnut-like structure is wavelength dependent. The pixels in the central region are less sensitive than surrounding pixels in the blue F435W flat, but they are more sensitive in the red F850LP flat. See ACS ISRs 2001-11, 2002-04, 2003-10, 2003-11, 2005-02, and 2005-09 for more information.

HRC

The HRC ground flats were refined using in-flight dithered observations of a rich star field designed to track low-frequency sensitivity variations. These L-flats revealed a corner-to-corner sensitivity gradient across the CCD of 6-12%, depending on wavelength. NUV flats were constructed from in-flight images of the bright Earth (see ACS ISR 2003-02) and include both the pixel-to-pixel and low-frequency structure of the detector response.

The HRC flat fields have a signal-to-noise of ~300 per pixel and support photometry to ~1% over the full HRC field of view. Figure 4.3 shows the corrected HRC ground flats derived for 6 broadband optical filters. The doughnut-like structure in the WFC flats is not seen in the HRC flats. For further discussion of HRC flat fields, see ACS ISRs 2001-11 and 2002-04.

Figure 4.2: WFC flat field.

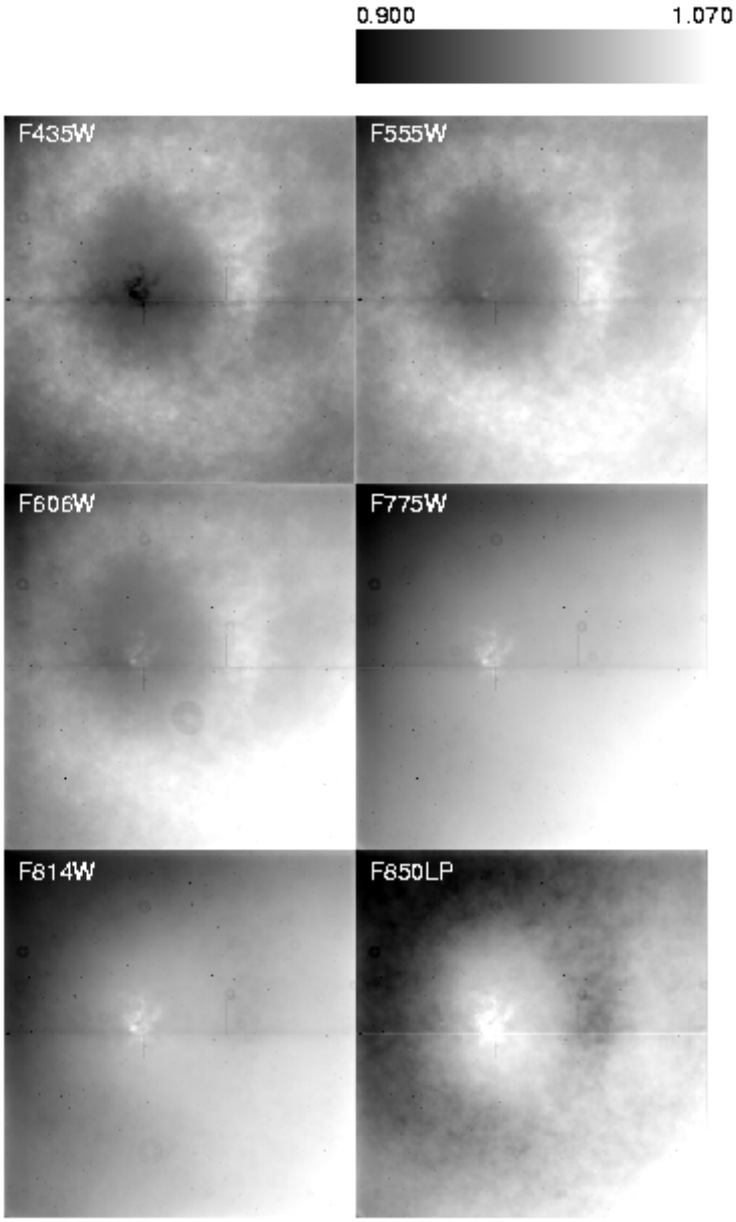

Figure 4.3: HRC flat field.

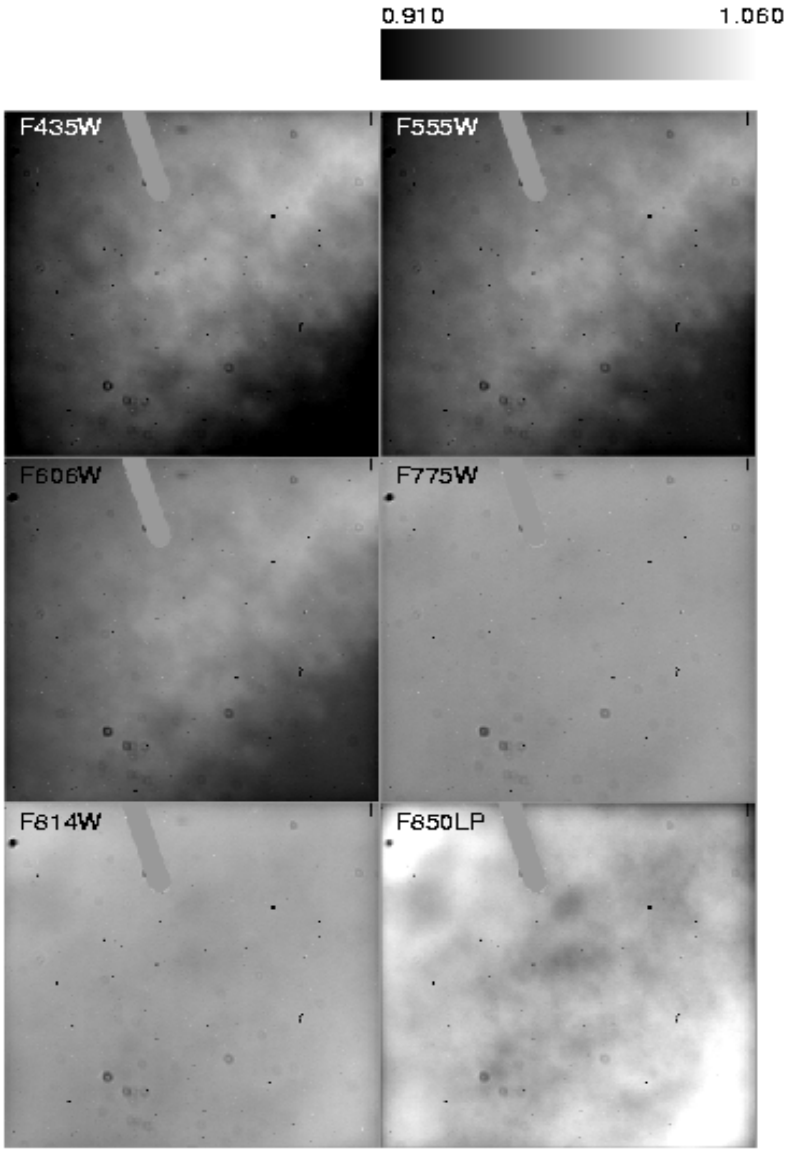

4.3 CCD Operations and Limitations

4.3.1 CCD Saturation: The CCD Full Well

Information regarding the HRC is provided for archival purposes only. Please check for updates regarding WFC on the ACS Web site.

The average full well depths for the ACS CCDs are given in Table 3.1 as 84,700 e^- for the WFC and 155,000 e^- for the HRC, but the pixel-to-pixel values vary by ~10% and ~18% across the fields of view of the WFC and the HRC, respectively. When the CCD is over-exposed, pixels will saturate and excess charge will flow into adjacent pixels along the column. This condition is known as "blooming" or "bleeding." Extreme overexposure does not cause any long-term damage to the CCDs, so there are no bright object limits for the ACS CCDs. When using ADC gains of 2 for the WFC and 4 for the HRC, the linearity of the detectors deviates by less than 1% up to the full well depths. On-orbit tests using aperture photometry show that this linearity is maintained when summing over pixels that surround an area affected by charge bleeding, even when the central pixel is saturated by 10 times its full well depth (see ACS ISR 2004-01 for details).

4.3.2 CCD Shutter Effects on Exposure Times

The ACS camera has a very fast shutter; even the shortest exposure times are not significantly affected by the finite travel time of the shutter blades. On-orbit testing reported in ACS ISR 2003-03 verified that shutter shading corrections are not necessary to support 1% relative photometry for either the HRC or WFC.

Four exposure times are known to have errors of up to 4.1%; e.g., the nominal 0.1 seconds HRC exposure was really 0.1041 seconds. These errant exposure times are accommodated by updates to the reference files used in image pipeline processing. No significant differences exist between exposure times controlled by the two shutters (A and B), with the possible exception of non-repeatability up to ~1% for WFC exposures in the 0.7 to 2.0 second range. The HRC provided excellent shutter time repeatability.

4.3.3 Read Noise

WFC

Please check for updates on the ACS Web site.

The read noise levels in the physical overscan and imaging regions of the four WFC amplifiers were measured for all gain settings during the orbital verification period following the installation of the CEB-R in SM4. The average WFC read noise is about 25% lower than before SM4. This reduction is due to the use in the CEB-R of a dual-slope integrator (DSI) in the pixel signal processing chain instead of the clamp-and-sample method of pixel sampling used in the original CEB. The DSI method offers lower signal processing noise at the expense of a spatially variable, but temporally stable, bias level.

Prior to failure of the original CEB, the WFC read noise had been generally constant with time. After a transit through the South Atlantic Anomaly (SAA) on 29 June 2003, the read noise of amplifier A changed from ~4.9 to ~5.9 e^- rms. Although the telemetry did not show any anomaly in any WFC components, it is likely that the sudden increase was caused by radiation damage. Amplifier A was the only amplifier that showed this anomaly. The amplitude of the variation (~1 e^-) was the same for ADC gains 1 and 2. After the following anneal (see Section 4.3.5), the read noise dropped to ~5.5 e^- and remained constant for 27 days. After the following two anneal cycles, the read noise stabilized at ~5.6 e^-. Figure 4.4 shows the read noise in the image area for amplifier A during the instability period. The read noise of the other amplifiers was very stable between the installation of ACS in March 2002 and the failure of ACS in January 2007.

Although amplifier A has higher read noise than the other amplifiers, most WFC broadband science observations are sky limited. Narrowband observations are primarily read noise limited.

HRC

Prior to January 2007, the read noise of the HRC was monitored using only the default amplifier C and the default gain of 2 e^-/DN. No variations were observed with time. The read noise measured in the physical overscan and image areas were consistent with the pre-flight values of 4.74 e^- (see Table 4.2 and Table 4.3).

Figure 4.4: Read noise jump in WFC Amp A (occurred on June 29, 2003).

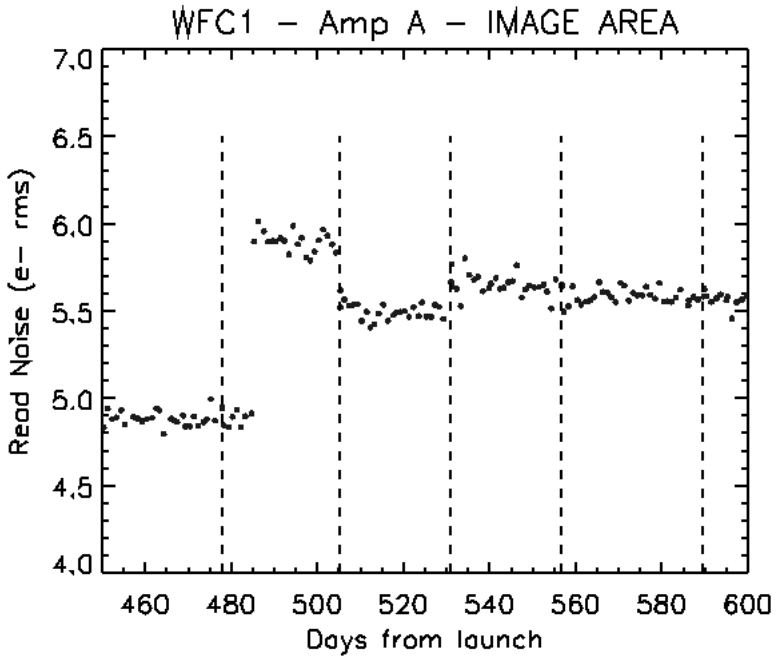

Increase in read noise of WFC Amp A after SAA passage on 29 June 2003. The vertical dashed lines indicate annealing dates. See Table 4.1, Table 4.2, and Table 4.3 for a history of CCD gain and readout noise values.

4.3.4 Dark Current

Online

Please check for updates on the ACS Web site.

All ACS CCDs are buried channel devices which have a shallow n-type layer implanted below the surface to store and transfer the collected signal charge away from the traps associated with the Si-SiO_2 interface. Moreover, ACS CCDs are operated in Multi-pinned Phases (MPP) mode so that the silicon surface is inverted and the surface dark current is suppressed. ACS CCDs therefore have very low dark current. The WFC CCDs are operated in MPP mode only during integration, so the total dark current figure for WFC includes a small component of surface dark current accumulated during the readout time.

Like all CCDs operated in a Low Earth Orbit (LEO) radiation environment, the ACS CCDs are subject to radiation damage by energetic particles trapped in the radiation belts. Ionization damage and displacement damage are two types of damage caused by protons in silicon. The MPP mode is very effective in mitigating the damage due to ionization such as the generation of surface dark current due to the creation of trapping states in the Si-SiO_2 interface. Although only a minor fraction of

the total energy is lost by a proton via non-ionizing energy loss, the displacement damage can cause significant performance degradation in CCDs by decreasing the charge transfer efficiency (CTE), increasing the average dark current, and introducing pixels with very high dark current (hot pixels). Displacement damage to the silicon lattice occurs mostly due to the interaction between low energy protons and silicon atoms. The generation of phosphorous-vacancy centers introduces an extra level of energy between the conduction band and the valence band of the silicon. New energetic levels in the silicon bandgap have the direct effect of increasing the dark current as a result of carrier generation in the bulk depletion region of the pixel. As a consequence, the dark current of CCDs operated in a radiative environment is predicted to increase with time.

Ground testing of the WFC CCDs, radiated with a cumulative fluence equivalent to 2.5 and 5 years of on-orbit exposure, predicted a linear growth of ~1.5 e^-/pixel/hour/year.

The dark current in ACS CCDs is monitored three days per week with the acquisition of four 1000 seconds dark frames (totaling 12 images per week). Dark frames are used to create reference files for the calibration of scientific images, and to track and catalog hot pixels as they evolve. The three daily frames are combined together to remove cosmic rays and to extract hot pixel information for any specific day. The dark reference files are generated by combining two weeks of daily darks in order to reduce the statistical noise. The hot pixel information for a specific day is then added to the combined bi-weekly dark. In order to study the evolution of the dark current with time, the modal dark current value in the cosmic-ray free daily darks is calculated. As expected, the dark current increases with time. The observed linear growth rates of dark current are 2.1 and 1.6 e^-/pixel/hour/year for WFC1 and WFC2 respectively, and 2.1 e^-/pixel/hour/year for the HRC CCD. These rates are in general agreement with the ground test predictions.

At the beginning of the side-2 operation in July 2006 the temperature set point of the WFC was lowered from -77 °C to -81 °C (documented in ACS TIR 2006-02[1]). Following SM4, we measure a dark current of 20 - 25 e^-/pixel/hour among the four amplifiers. We have reverted to 12-hour anneals.

The dark current growth with time post-SM4 is measured to be 2.2 and 1.3 e-/pixel/hour/year for the periods 2009-10 and 2010-11 for both CCDs. Dark current and hot pixels depend strongly on the operating temperature. The reduction of the operating temperature of the WFC CCDs reduced the number of hot pixels by almost 50% (See Figure 4.5). The dark rate shows a clear drop on July 4, 2006, when the temperature was changed. Figure 4.6 illustrates the before-and-after effect directly. The new operating temperature brought the dark current of the WFC CCDs back to the level eighteen months after the launch.

1. TIRs (Technical Instrument Reports) are available upon request. Please contact help@stsci.edu for a copy.)

Figure 4.5: Hot Pixel Growth Rate for HRC and WFC

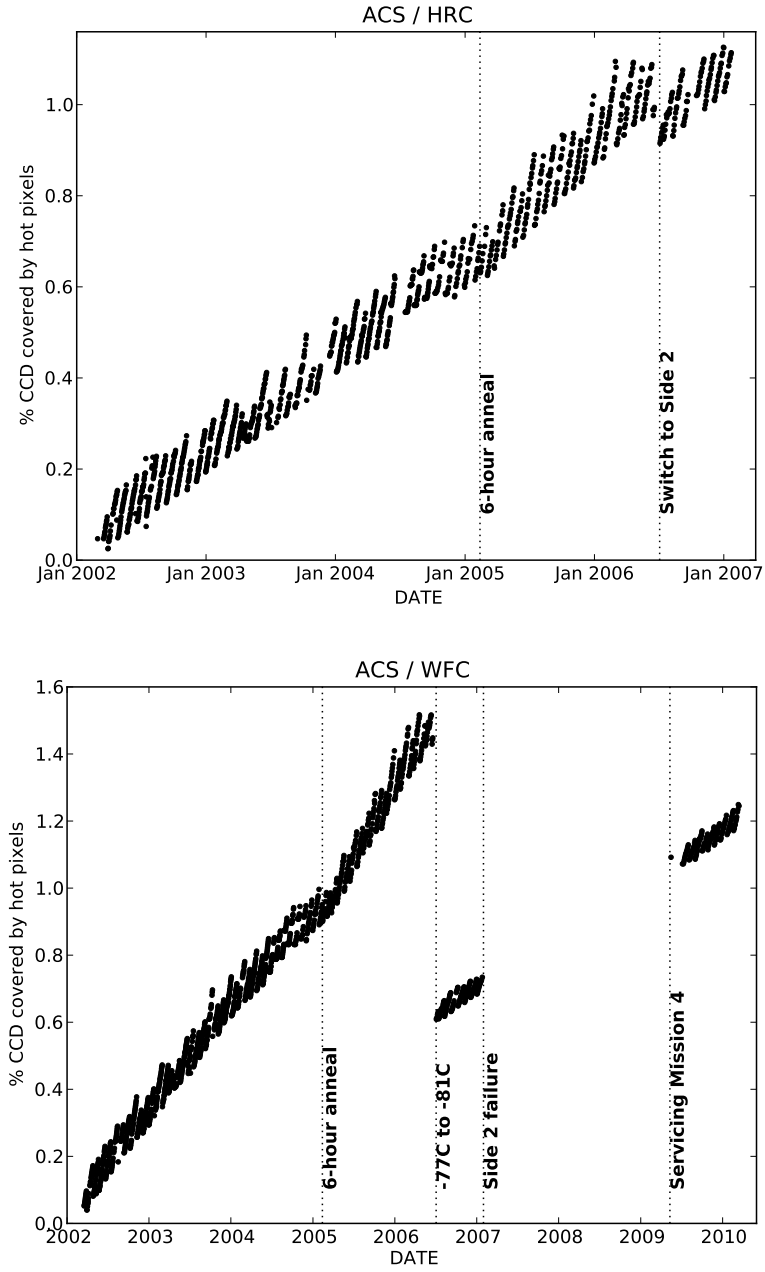

The figures above show hot pixel (DQ flag 16) growth rates in the WFC, and in the HRC during most of its entire mission. The sawtooth patterns correspond to ACS anneal cycles. In the HRC, the growth rate increased slightly when the anneal duration was switched from 12 hours to 6 hours. The slight drop in hot pixels coincided with the switch to Side 2 electronics. In the lower figure for WFC, the sawtooth patterns also correspond to ACS anneal cycles. The growth rate slightly increased when the anneal duration was switched from 12 hours to 6 hours. Post-SM4 anneals are once again 12 hours long. The temperature change from -77 C to -81 C resulted in a significant drop in hot pixels.

Figure 4.6: WFC Dark Current Histogram for Chip 1

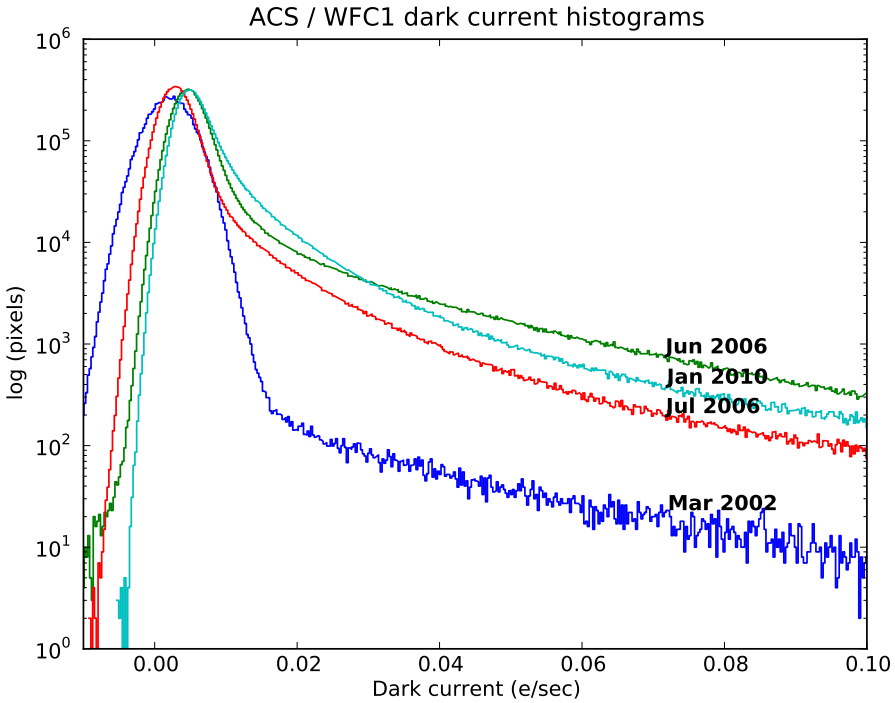

The lines illustrate the growth of hot pixels over time. Decrease in dark current and in the number of hot pixels, were seen when the WFC temperature was changed from -77 C to -81 C on July 4, 2006 (note differences shown for June and July 2006). For post-SM4, dark current in January 2010 (-81 C) was almost identical to June 2006 (-77 C), but the former still had less hot pixels. Statistics for chip 2 are nearly identical.

4.3.5 Warm and hot pixels

Online

Please check for updates on the ACS Web site.

In the presence of a high electric field, the dark current of a single pixel can be greatly enhanced. Such pixels are called hot pixels. Although the increase in the mean dark current with proton irradiation is important, of greater consequence is the large increase in dark current nonuniformity.

We have chosen to classify the field-enhanced pixels into two categories: warm and hot pixels. The definition of "warm" and "hot" pixel is somewhat arbitrary. We have chosen a limit of 0.08 e^-/pixel/seconds as a threshold above which we consider a pixel to be "hot". We identify "warm" pixels as those which exceed by about 5 σ (was 0.02 e^-/pixel/second but after SM4 it is 0.04 e^-/pixel/second) the normal distribution of the pixels in a dark frame up to the threshold of the hot pixels (See Figure 4.6) for a typical dark rate pixel distribution.

Warm and hot pixels accumulate as a function of time on orbit. Defects responsible for elevated dark rate are created continuously as a result of the ongoing displacement damage on orbit. The number of new pixels with a dark current higher than the mean

dark date increases every day by few to several hundreds depending on the threshold. The reduction of the operating temperature of the WFC CCDs has dramatically reduced the dark current of the hot pixels and therefore many pixels previously classified as hot are now warm or normal pixels.

Table 4.4: Creation rate of new hot pixels (pixel/day).

Threshold (e^-/pixel/second)	WFC(-77 °C)	WFC (-81 °C)	HRC(-80 °C)
>0.02	815 ± 56	N.A.	125 ± 12
>0.04	616 ± 22	427 ± 34	96 ± 2
>0.06	480 ± 13	292 ± 8	66 ± 1
>0.08	390 ± 9	188 ± 5	48 ± 1
>0.10	328 ± 8	143 ± 12	35 ± 1
>1.00	16 ± 1	10 ± 1	1 ± 0.5

Table 4.5: Annual permanent hot pixel growth (%).

Threshold (e^-/pixel/second)	WFC(-77 °C)	WFC (-81 °C)	HRC(-80 °C)
>0.02	1.60	N.A.	1.54
>0.04	0.78	0.32	0.52
>0.06	0.46	0.18	0.29
>0.08	0.30	0.16	0.21
>0.10	0.23	0.13	0.17
>1.0	0.03	0.02	0.02

Most of these new hot pixels are transient. Like others CCDs on *HST*, the ACS devices undergo a monthly annealing process. (The CCDs and the thermal electric coolers are turned off and the heaters are turned on to warm the CCDs to ~19 °C.) Although the annealing mechanism at such low temperatures is not yet understood, after this "thermal cycle" the population of hot pixels is greatly reduced (see Figure 4.5). The anneal rate depends on the dark current rate; very hot pixels are annealed more easily than warmer pixels. For pixels classified as "hot" (those with dark rate > 0.08 e^-/pix/sec) the anneal rate is ~82% for WFC and ~86% for HRC.

Annealing has no effect on the normal pixels that are responsible for the increase in the mean dark current rate. Such behavior was also seen with STIS and WFC3 CCDs during ground radiation testing. Since the anneals cycle do not repair 100% of the hot pixels, there is a growing population of permanent hot pixels (see Figure 4.7 and Figure 4.6).

Figure 4.7: A subsection of WFC1 dark frames taken at different epochs showing the increasing population of hot pixels. From left to right: before launch, and 1, 2, 3, and 4 years on orbit.

In principle, warm and hot pixels could be eliminated by the superdark subtraction. However, some pixels show a dark current that is not stable with time but switches between well defined levels. These fluctuations may have timescales of a few minutes and have the characteristics of random telegraph signal (RTS) noise. The dark current in field-enhanced hot pixels can be dependent on the signal level, so the noise is much higher than the normal shot noise. As a consequence, since the locations of warm and hot pixels are known from dark frames, they are flagged in the data quality array. The hot pixels can be discarded during image combination if multiple exposures have been dithered.

The standard CR-SPLIT approach allows rejection of cosmic rays, but hot pixels cannot be eliminated in post-observation processing without dithering between exposures.

Observers who previously used CR-SPLIT for their exposures are advised to use a dither pattern instead. Dithering by at least a few pixels allows the removal of cosmic ray hits and hot pixels in post-observation processing.

For example, a simple `ACS-WFC-DITHER-LINE` pattern has been developed that shifts the image by 2 pixels in X and 2 pixels in Y along the direction that minimizes the effects of scale variation across the detector. The specific parameter values for this pattern are given on the ACS dithering Web page at:

`http://www.stsci.edu/hst/acs/proposing/dither.`

Additional information can be found in the *Phase II Proposal Instructions*.

Given the transient nature of hot pixels, users are reminded that a few hot pixels may not be properly flagged in the data quality array (because they spontaneously "healed" or because their status changed in the period spanning the reference file and science frame acquisition), and therefore could create false positive detections in some science programs.

4.3.6 Cosmic Rays

Studies have been made of the characteristics of cosmic ray impacts on the HRC and WFC. The fraction of pixels affected by cosmic rays varies from 1.5% to 3% during a 1000 second exposure for both cameras, similar to what was seen on WFPC2 and STIS. This number provides the basis for assessing the risk that the target(s) in any set of exposures will be compromised. The affected fraction is the same for the WFC and HRC despite their factor of two difference in pixel areas because the census of affected pixels is dominated by charge diffusion, not direct impacts. Observers seeking rare or serendipitous objects, as well as transients, may require that every single WFC pixel in at least one exposure among a set of exposures is free from cosmic ray impacts. For the cosmic ray fractions of 1.5% to 3% in 1000 seconds, a single ~2400 second orbit must be broken into 4 exposures of 500 to 600 seconds each to reduce the number of uncleanable pixels to 1 or less. Users seeking higher S/N (lower read noise) may prefer the trade-off of doing 3 exposures of ~800 seconds, where CR-rejection should still be very good for most purposes. But we do NOT recommend 2 long exposures (i.e. 1200 seconds), where residual CR contamination would be unacceptably high in most cases. We recommend that users dither these exposures to remove hot pixels as well as cosmic rays (see Section 7.4).

The flux deposited on the CCD from an individual cosmic ray does not depend on the energy of the cosmic ray but rather the distance it travels in the silicon substrate. The electron deposition due to individual cosmic rays has a well defined cut-off below 500 e^- and a median of ~1000 e^- (see Figure 4.8 and Figure 4.9).

Figure 4.8: Electron deposition by cosmic rays on WFC.

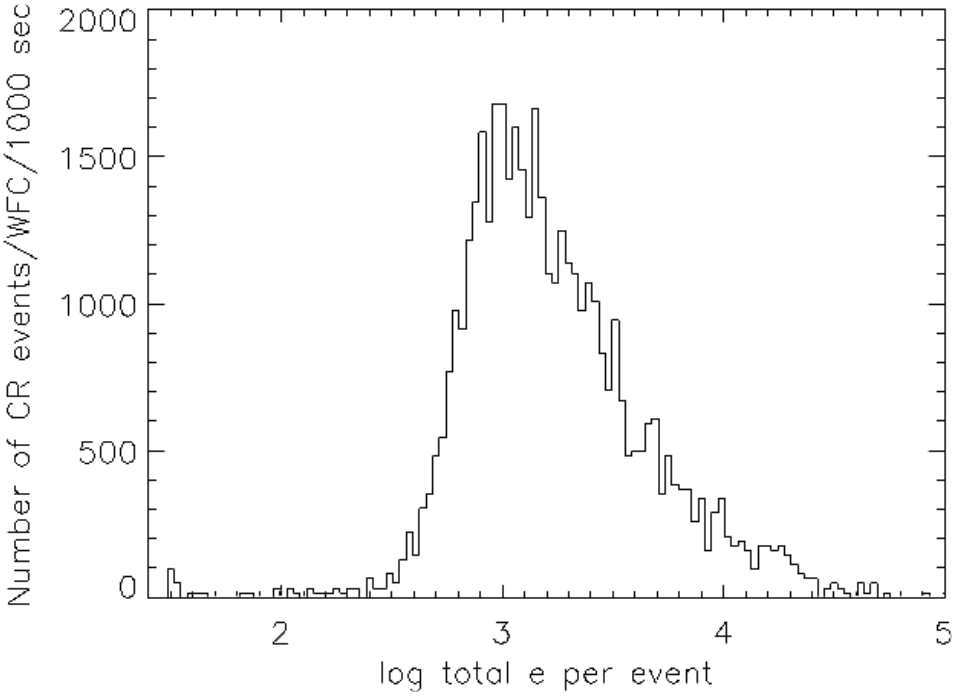

Figure 4.9: Electron deposition of cosmic rays on HRC.

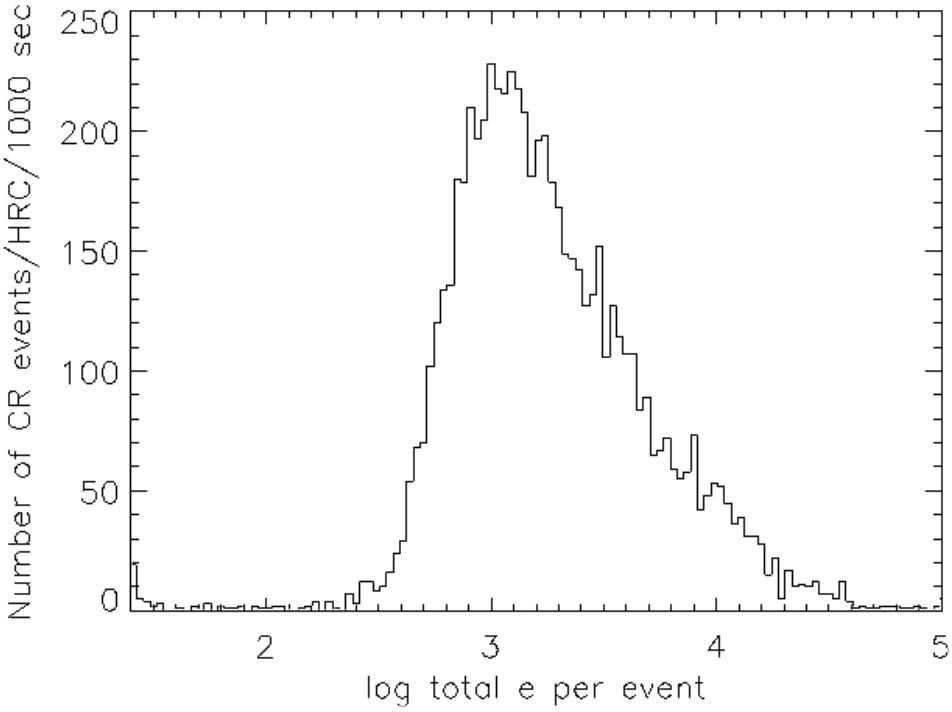

The distribution of the number of pixels affected by a single cosmic ray is strongly peaked at 4 to 5 pixels. Although a few events are seen which encompass only one pixel, examination of these events indicate that at least some, and maybe all of these sources are actually transient hot pixels or unstable pixels which can appear hot in one exposure (with no charge diffusion) and normal in the next. Such pixels are very rare but do exist. There is a long tail in the direction towards increasing numbers of attached pixels.

Distributions of sizes and anisotropies can be useful for distinguishing cosmic rays from astrophysical sources in a single image. The size distribution for both chips peaks near 0.4 pixels as a standard deviation (or 0.9 pixels as a FWHM). This is much narrower than for a PSF and is thus a useful discriminant between unresolved sources and cosmic rays.

4.3.7 Charge Transfer Efficiency

Online

Please check for updates on the ACS Web site.

Charge transfer efficiency (CTE) is a measure of how effectively the CCD moves charge between adjacent pixels during read out. A perfect CCD would be able to transfer 100% of the charge as the charge is shunted across the CCD and out through

the serial register and its CTE would be unity. In practice, small traps in the silicon lattice compromise this process by holding on to electrons, releasing them at a later time. Depending on the trap type, the release time ranges from a few microseconds to several seconds. For large charge packets (several thousands of electrons), losing a few electrons along the way is not a serious problem, but for smaller (~100e^- or less) signals, it can have a substantial effect.

The CTE numbers for the ACS CCDs at the time of installation are given in Table 4.6. While the numbers look impressive, remember that reading out the WFC CCD requires 2048 parallel and 2048 serial transfers, so that almost 2% of the charge from a pixel in the corner opposite the readout amplifier was lost.

Table 4.6: Charge transfer efficiency measurements for the ACS CCDs after installation in March 2002. (Based on an experiment performed with Fe55)

CCD	Parallel	Serial
WFC1	0.999995	0.999999
WFC2	0.999995	0.999999
HRC	0.999983	0.999994

Like other CCD cameras aboard *HST*, ACS has suffered degraded CTE due to radiation damage since its installation in 2002. Since 2003, specific calibration programs aimed at characterizing the effects of the CTE on stellar photometry were performed (Riess, ACS ISR 2003-09). First characterizations of the effects of a decreasing CTE for WFC were made by Riess & Mack (ACS ISR 2004-06). Meanwhile, results from the internal CTE calibration programs showed that CTE appears to decline linearly with time, and that CTE losses are stronger for lower signal levels (Mutchler & Sirianni, ACS ISR 2005-03). However, in order to derive an accurate correction formula for photometry, a number of observations at different epochs and for different levels of sky background and stellar fluxes have to be accumulated. The results of the observations taken through March 2006 are described by Chiaberge et al. (ACS ISR 2009-01) and are summarized here. For WFC, significant photometric losses are apparent for stars undergoing numerous parallel transfers (y-direction). Extrapolated to 2011, the losses should be 5-10% for typical observing parameters, rising to ~50% in worst cases (faint stars, low background). The size of the photometric loss appears to have a strong power-law dependence on the stellar flux, as seen for other CCDs flown on *HST*.

The dependence on background is significant, but for faint targets there is little advantage to increasing the background intentionally (e.g., by post-flashing) due to the added shot noise. However, in some specific cases, it may instead be useful to choose the filter in order to obtain a higher background (e.g. F606W). CTE degradation also has an impact on astrometry (see ACS ISR 2007-04). Therefore, for astrometric programs of relatively bright objects, the use of post-flash may be considered. No losses are apparent for WFC due to serial transfers (x-direction). Correction formulae are presented in ACS ISR 2009-01 to correct photometric losses as a function of a source's position, flux, background, and time. Using data obtained both as part of SM4-SMOV and Cycle 17 External CTE Calibration Program (Sept. 2009), we have

verified that the predictions of the photometric correction formula are still accurate within the errors. Users are encouraged to check the ACS Web page for updates. Further details on CTE corrections can be found in the ACS ISR 2011-01 (Bohlin & Anderson, 2011).

Figure 4.10 shows the predicted photometric losses for the WFC due to imperfect parallel CTE as a function of time. These curves are based on the formulae published in ACS ISR 2009-01. We consider three "typical" science applications:

1. A "worst case scenario" of a star of magnitude 20 in the VEGAMAG system observed with the F502N narrow band filter for a short exposure time (30s), thus giving rise to a very low sky background level.
2. A Type Ia supernova at z~1.5 close to its peak brightness (~ 26.5 mag in VEGAMAG), observed with F775W and 600s exposure time.
3. A PSF with a flux of 1 e^-/s observed for 1000s with a filter that gives rise to a sky background level of 80 e^-.

Figure 4.10: Projected CTE losses in WFC (equivalently, the size of corrections)

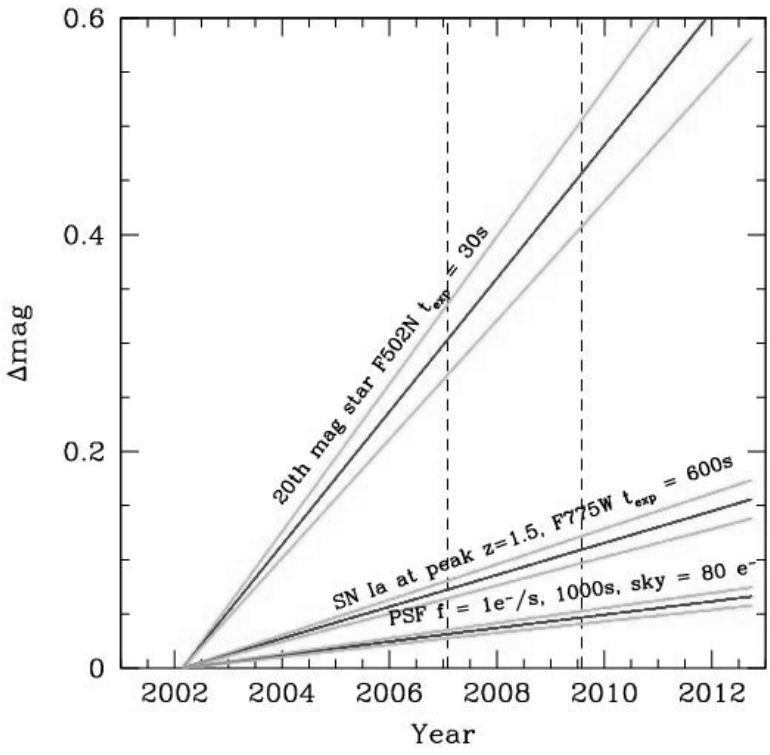

Predicted impact of CTE on science images for WFC (the three scenarios described above). The magnitude loss is estimated for a star located at the chip middle point along Y=1024 and refers to counts measured in a 3-pixel aperture. The light gray lines indicate 1-sigma error on the value obtained with the correction formula. The two vertical dashed lines refer to the epoch of the ACS failure in January 2007 and to a time shortly after the SM4 repair in May 2009.

Anderson & Bedin (2010 PASP 122, 1035) have developed an empirical approach based on the profiles of warm pixels to characterize the effects of CTE losses for the ACS Wide Field Camera.

Their algorithm first develops a model that reproduces the observed trails and then inverts the model to convert the observed pixel values in an image into an estimate of the original pixel values.

The ACS Team is currently testing a new version of CALACS containing two significant improvements: automatic removal of bias stripes using the pre-scan region (see Section 5.2.6); and the pixel-based CTE correction based on the paper by Anderson & Bedin.

In addition to the standard data products (CRJ, FLT and DRZ files) there will be three new files (CRC, FLC and DRC) which will contain the CTE-corrected data products. Users will be able to choose whether to use the standard or CTE-corrected products. Both sets of data will be corrected for bias striping. This new version of CALACS applies the CTE correction to the raw images and requires CTE-corrected dark reference files. The ACS Team is currently making the dark reference frames for the entire ACS archive.

The latest version of the algorithm works very well for intermediate to high flux levels (> 200 electrons) and it has been greatly improved in order to become more effective at low flux levels (< 100 electrons).

It also employs a more accurate time and temperature dependence for CTE over the ACS lifetime.

The results of the Anderson & Bedin correction on stellar fields are found to be in agreement with the photometric correction formula of Chiaberge et al. (ACS ISR 2009-01).

The new version of CALACS will be available in early 2012. Please refer to the ACS Web site for the latest information.

4.3.8 UV Light and the HRC CCD

In the optical, each photon generates a single electron. However, in the near-UV, shortward of ~3200 Å there is a finite probability of creating more than one electron per UV photon (see Christensen, O., *J. App. Phys*. **47**,689, 1976). At room temperature the theoretical quantum yield (i.e., the number of electrons generated for a photon of energy $E > 3.5eV$ ($\lambda \sim 3500$ Å)), is $Ne = E(eV)/3.65$. The HRC CCDs quantum efficiency curve has not been corrected for this effect. The interested reader may wish to see the *STIS Instrument Handbook* for details on the signal-to-noise treatment for the STIS CCDs.

4.4 The SBC MAMA

4.4.1 MAMA Properties

The ACS MAMA detector is the STIS flight spare STF7. It provides coverage from 1150 Å to 1700 Å. The MAMA detector is a photon-counting device which processes events serially. The ACS MAMA only operates in the accumulate (ACCUM) mode, in which a time-integrated image is produced. Unlike the STIS MAMAs, the ACS does not offer the high-resolution (2048 × 2048) mode or time-tagged data acquisition. The primary benefits afforded by the STIS and ACS MAMAs, in comparison with previous *HST* UV spectroscopic detectors such as those in the GHRS and FOS, are high spatial resolution, two-dimensional imaging over a relatively large field of view, and narrow slits that lower contamination by the sky.

Figure 4.11 illustrates the design of the MAMA, which has an opaque CsI photocathode deposited directly on the face of the curved microchannel plate (MCP). Target photons strike the photocathode, liberating single photoelectrons which pass into the MCP, where a pulse of ~4×10^5 e^- is generated. The pulse is recorded by an anode array behind the photocathode and detected by the MAMA electronics which rejects false pulses and determines the position of the photon event on the detector.

The field electrode, or *repeller wire*, repels electrons emitted from the microchannel plate back into the channels. This provides an increase in quantum efficiency of the detector at the price of an increase in the detector point spread function halo. The repeller wire voltage is always on for SBC observations.

Figure 4.11: Design of the SBC MAMA.

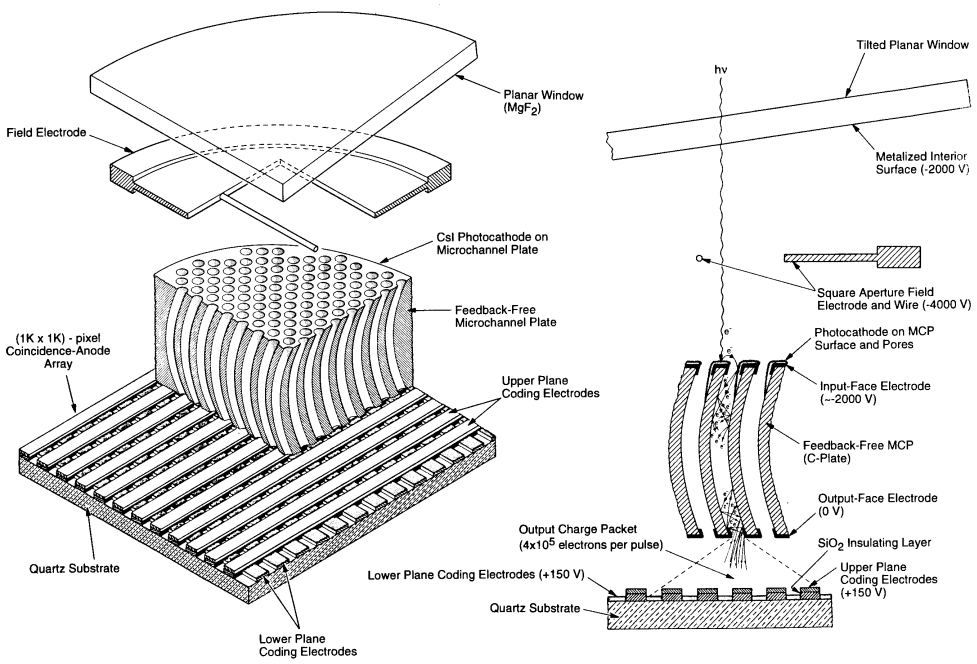

Table 4.7: SBC detector performance characteristics.

Characteristic	SBC MAMA performance
Photocathode	CsI
Wavelength range	~1150 to1700 Å
Pixel format	1024 × 1024 pixel
Pixel size	25 × 25 µm
Plate scale	~0.034 × 0.030 ″/pixel
Field of view	34.6″ x 30.8″
Quantum efficiency	19.2% @ 1216 Å
Dark count[1]	~5×10^{-5} e^-/second/pixel
Global count-rate linearity limit[2]	200,000 counts/second
Local count-rate linearity limit[2]	~22 counts/second/pixel
Visible light DQE	< 1.2×10^{-9} above 400 nm

1. The dark count increases with the length of time the SBC is turned on, beginning at about 10^{-5} electrons/pixel/second and increasing by about a factor of five over two hours.
2. Rate at which counting shows 1% deviation from linearity.

4.4.2 SBC Spectral Response

The total transmission curve for the SBC with the PR110L prism is shown in Figure 4.12. The peak photocathode response occurs at Lyman-α. Its spectral response is defined by the cutoff of the MgF_2 window at 1150 Å at short wavelengths, and by the relatively steep decline of the CsI photocathode at long wavelengths.

Observations of flux calibration stars and a G-type star using the SBC PR110L prism have revealed that the sensitivity of the MAMA detector to optical and near-UV light is apparently much larger than previously thought (Boffi et al., TIR 2008-02[2]).

Estimates of the real SBC throughput indicates that the detector efficiency is factors of approximately 50 and 1000 higher at wavelengths of 3000 Å and 4000 Å respectively compared to ground testing. For a solar type spectrum, this can mean that one-half or more of the counts detected are due to optical and near-UV photons, rather than from the expected FUV photons. The updated sensitivity curve has been incorporated both in the Exposure Time Calculator (ETC) and in Synphot[3] since November 2007. There is also some evidence that this red leak changes as the SBC detector warms up, increasing by as much as 30% over the course of 5 orbits. It is not yet clear if this red leak has also been increasing secularly over time. STIS FUV MAMA data seem to show a similar, although perhaps somewhat smaller effect.

For dispersed PR110L and PR130L observations, it is straightforward to identify this extra red light; however, it clearly also affects SBC imaging observations done with the long pass filters. Until this effect is better understood and calibrated, extreme caution should be used when interpreting FUV imaging observations of red targets. Observers who need to measure FUV fluxes of red targets may wish to consider interleaving observations with two different SBC long pass filters (e.g., F140LP and F165LP), so that the difference in the count rates can be used to isolate the true FUV flux.

2. TIRs (Technical Instrument Reports) are available upon request. Please contact help@stsci.edu for a copy.)

3. Synphot will soon be replaced by the pysynphot package, a significantly improved re-implementation of Synphot written in Python. Please visit the pysynphot Web page at: http://stsdas.stsci.edu/pysynphot.

Figure 4.12: Total transmission curve for ACS SBC plus the PR110L prism.

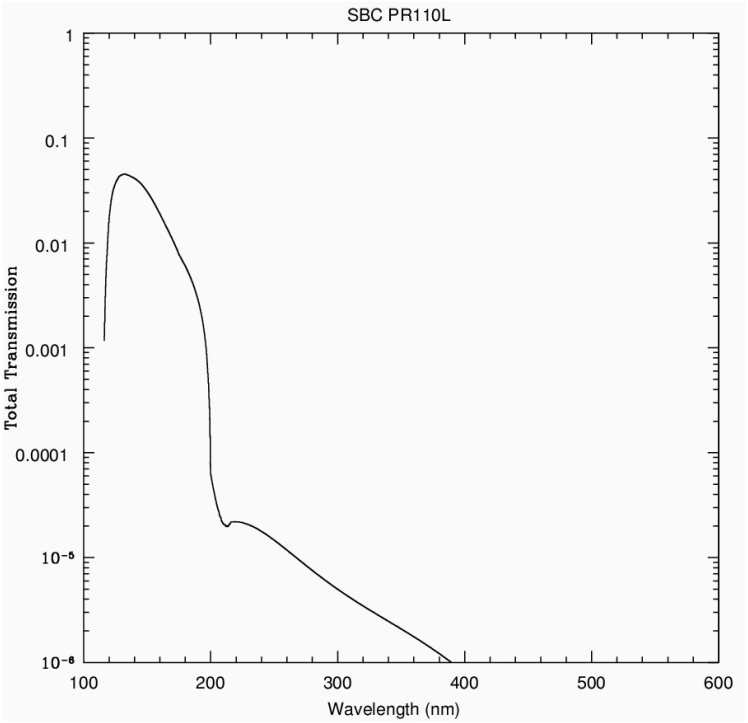

4.4.3 Optical Performance

The SBC exhibits low-level extended wings in the detector point-spread function (PSF). Sample MAMA detector PSF profiles are shown in Figure 4.13.

Figure 4.13: MAMA point spread function.

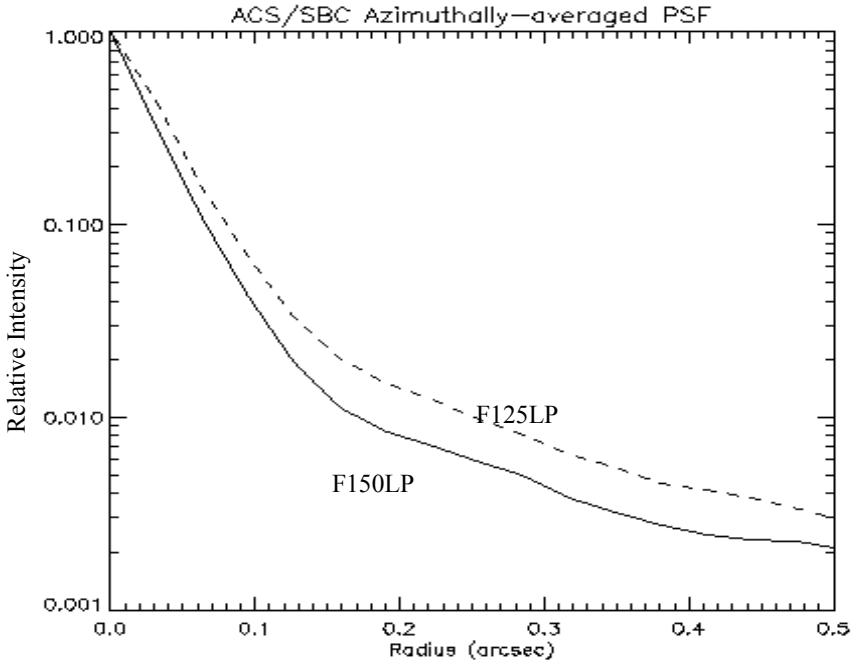

4.5 SBC Operations and Limitations

4.5.1 SBC Scheduling Policies

The STIS MAMA control electronics are subject to resets due to cosmic-ray upsets. Therefore, STIS MAMAs are operated only during the contiguous orbits of each day that are free of the South Atlantic Anomaly (SAA). Even though the design of the ACS MAMA control electronics in the SBC was modified so that they would not be susceptible to cosmic-ray hits, the background count rate still exceeds the bright object limits for the SBC during SAA passage. Consequently, the SBC will in general only be scheduled for use during SAA-free orbits.

4.5.2 MAMA Overflow of the 16 Bit Buffer

The MAMA is a photon-counting detector: as each event is recorded, the buffer memory for the corresponding pixel is incremented by one integer. The buffer memory stores values as 16 bit integers; hence the maximum number it can accommodate is 65,535 counts per pixel in a given ACCUM mode observation. When accumulated counts per pixel exceed this number, the values will wrap, i.e., the memory resets to 0. As an example, if you are counting at 25 counts/second/pixel, you will reach the MAMA "accumulation" limit in ~44 minutes.

One can keep accumulated counts per pixel below this value by breaking individual exposures into multiple identical exposures, each of which is short enough that fewer than 65,535 counts are accumulated per pixel. There is no read noise for MAMA observations, so no penalty is paid in lost signal-to-noise ratio when exposures are split. There is only a small overhead for each MAMA exposure (see Section 8.2).

Keep the accumulated counts per SBC pixel below 65,535 by breaking single exposures into multiple exposures, as needed.

4.5.3 MAMA Darks

MAMA detectors have intrinsically low dark currents. An example of the dark current variation across the detector can be seen in Figure 4.14. Ground test measurements of the ACS MAMA showed count rates in the range of 10^{-5} to 10^{-4} counts per pixel per second as the temperature varied from 28 °C to 35 °C. The count rate increased by about 30% for one degree increase in temperature. In-flight measurements, taken weekly throughout June and July 2002, show count rates between $8x10^{-6}$ and 10^{-5}. These measurements were taken as soon as the MAMA was turned on and were therefore at the lower end of the temperature range. A 10 hour observation in SMOV (SM3B), long enough for nominal temperatures to be reached, yielded a dark current of 1.2×10^{-5} counts per second per pixel. Monthly monitoring shows the in-flight dark current to be about $9x10^{-6}$ counts per second per pixel.

A comparison of the dark rate as a function of temperature is shown in Figure 4.15. As a function of temperature the behavior of the dark current was essentially unchanged. No long-term increase in the dark rate was found. Due to the insignificant dark current, dark corrections are no longer performed in the ACS pipeline.

The ACS MAMA has a broken anode which disables rows 600 to 605. There are three dark spots smaller than 50 microns at positions (334,977), (578,964), and (960,851), as well as two bright spots at (55,281) and (645,102) with fluctuating rates that are always less than 3 counts per second. The reference pixel has been moved to (512,400) to avoid these areas (see Table 7.9)

Figure 4.14: MAMA dark image.

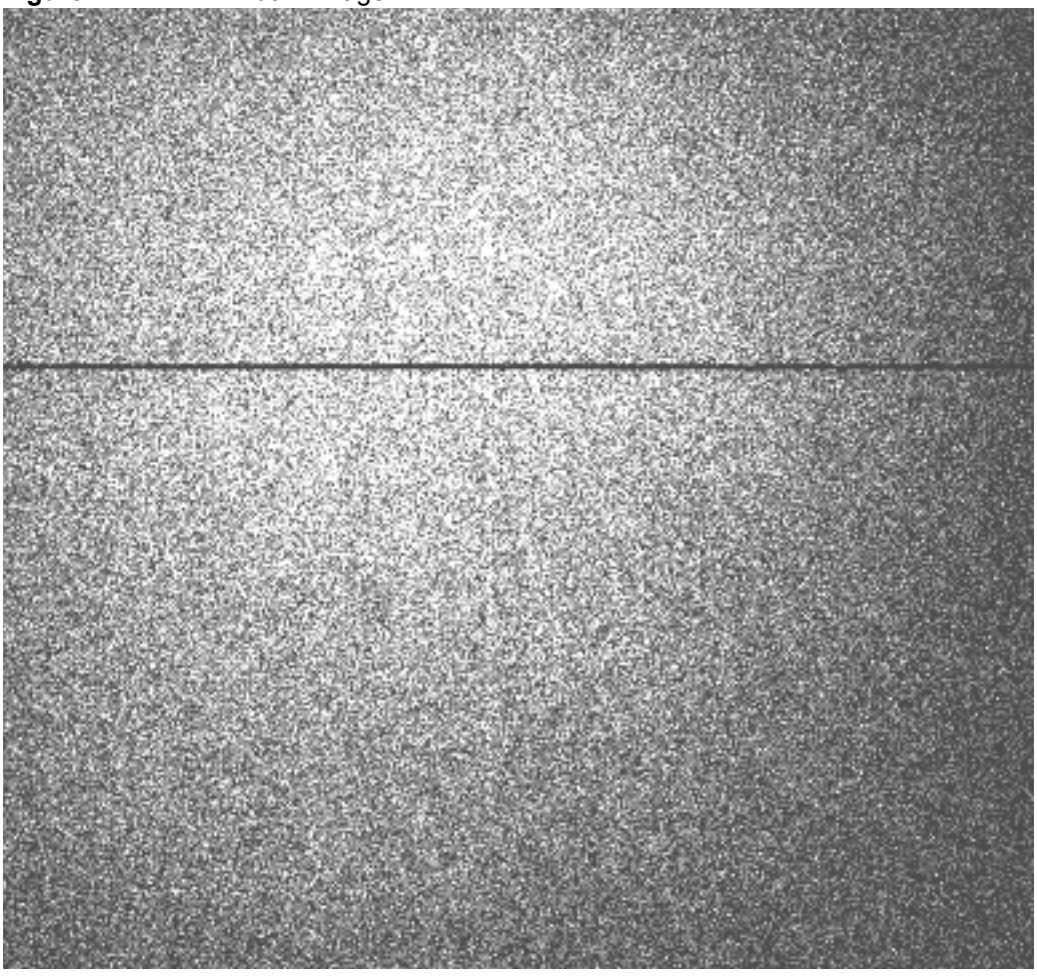

Full frame MAMA dark image. The average dark rate in this image is 5 x 10^{-5} counts per second per pixel.

Figure 4.15: SBC Dark Rate and Operating Temperature

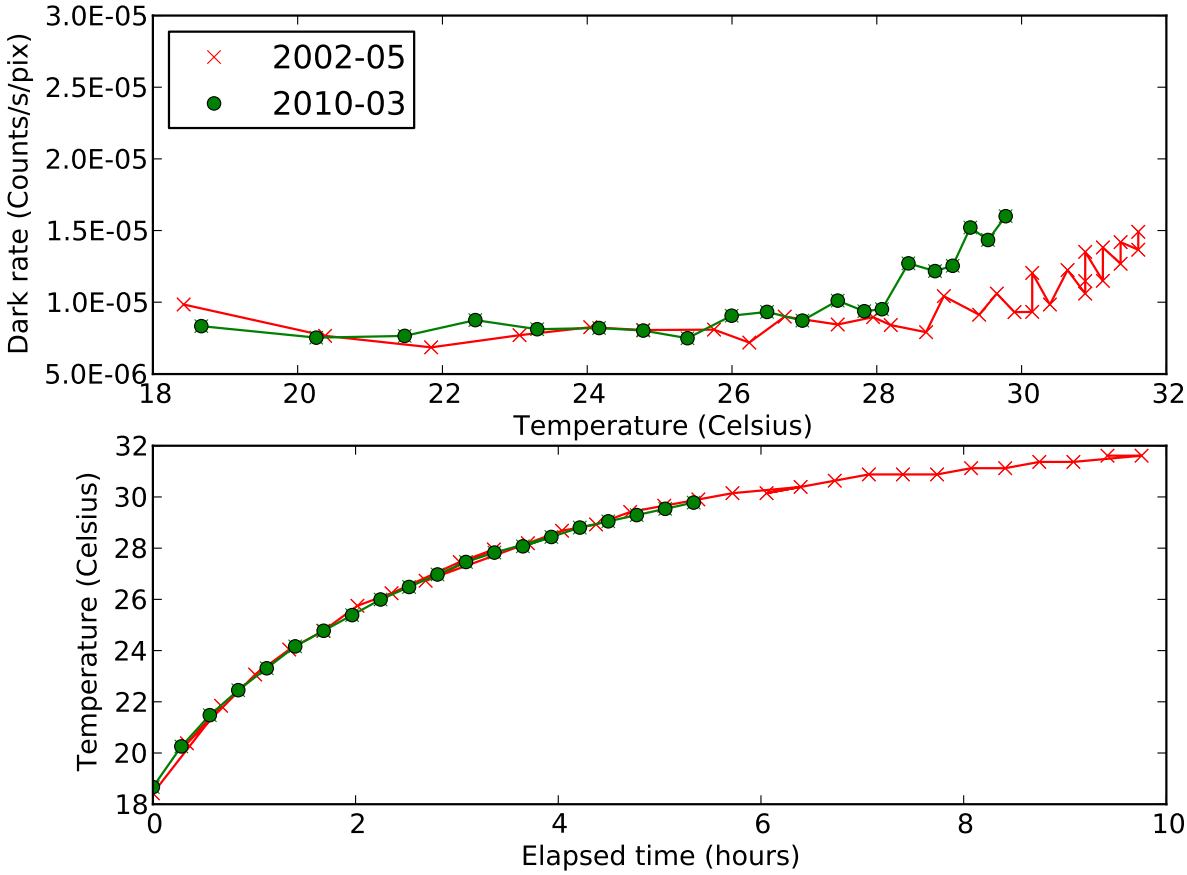

Upper panel: SBC Dark Rate (counts s^{-1} pix^{-1}) as a function of the operating temperature in Celsius. Lower panel: The operating temperatures vs. time elapsed since SBC was switched on. Red crosses and green circles are data from May 2002 and March 2010, respectively. Dark rates have remained stable since ACS activation in 2002 and are unaffected by SM4. For both epochs, dark rates are stable for operating temperatures below 28 Celsius (for about 4 hours after being switched on).

4.5.4 SBC Signal-To-Noise Ratio Limitations

MAMA detectors are capable of delivering signal-to-noise ratios of order 100:1 per resolution element (2×2 pixels) or even higher. Tests in orbit have demonstrated that such high S/N is possible with STIS (Kaiser et al., 1998, (PASP, 110, 978); Gilliland, STIS ISR 1998-16). For targets observed at a fixed position on the detector, the signal-to-noise ratio is limited by systematic uncertainties in the small-scale spatial and spectral response of the detector. The MAMA flats show a fixed pattern that is a combination of several effects including beating between the MCP array and the anode pixel array, variations in the charge-cloud structure at the anode, and low-level capacitive cross-coupling between the fine anode elements. Intrinsic pixel-to-pixel variations are of order 6% but are stable to $< 1\%$. Photometric accuracy can be improved by averaging over flat field errors by dithering the observation (see Section 7.4).

4.5.5 SBC Flatfield

Figure 4.16: MAMA Flat Field.

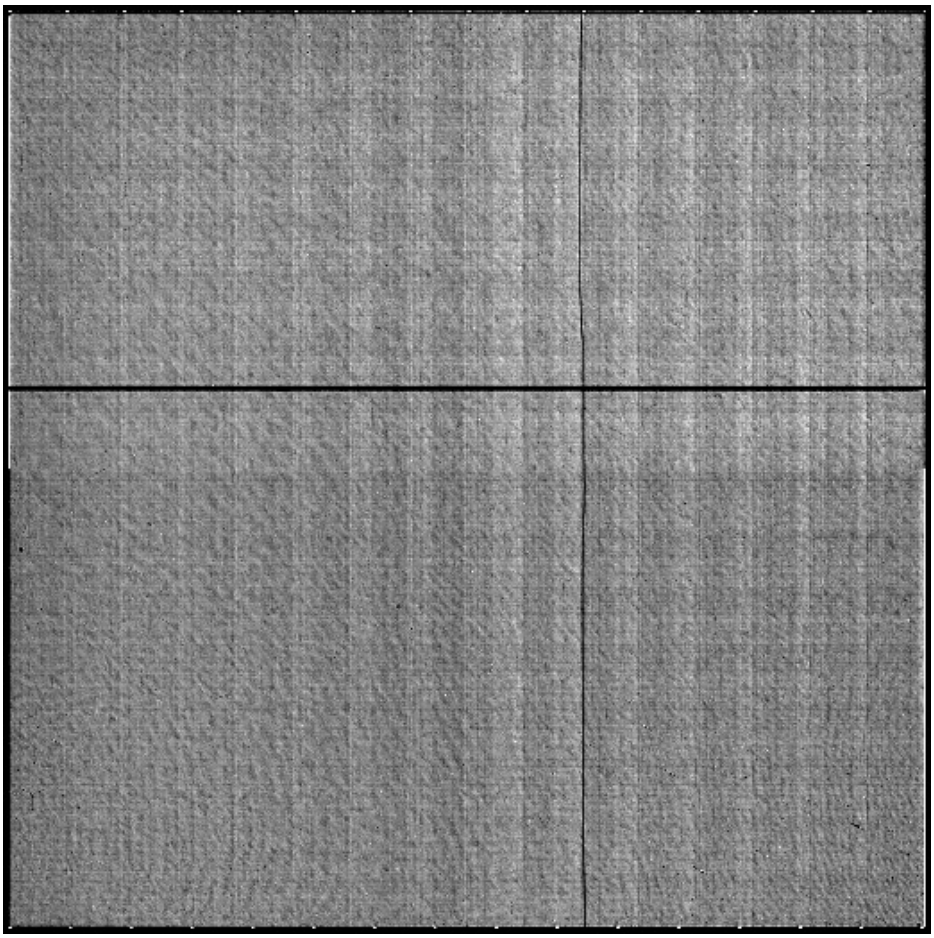

Wavelength independent P-Flat for the SBC MAMA (full frame shown).

The SBC requires two types of flat fields: the "pixel-to-pixel flats" (or P-flats), which take care of the high-frequency structures in the detector sensitivity, and the "low-order flats" (or L-flats), which handle the low-frequency components. Current P-flats were derived by Bohlin & Mack (ACS ISR 2005-04) using the on-board deuterium lamp and were found to be independent of wavelength. The P-flat in Figure 4.16 shows the effect of the disabled broken anode for rows 600 to 605 and of the shadow of the repeller wire around column 577.

Low-frequency flatfield corrections for the SBC imaging modes have been derived using multiple exposures of the globular cluster NGC6681 (Mack, et al., ACS ISR 2005-13). Variations of ±6% (full range) were found for the F115LP and F125LP filters, ±8% for the F140LP and F150LP filters, and ±14% for the F165LP filter. The F122M filter was not included in this analysis due to lack of sufficient data. The L-flat shows a similar general pattern in all filters, with the required correction increasing with wavelength. Analysis of this stellar data showed a decline in the average UV sensitivity with time at a level of 2 to 4% per year over the first 1.6 years of operation.

The sensitivity appears to have leveled off after this time. A slight sensitivity loss as a function of temperature (~0.1%/degree) was also discovered. These effects were also detected for the STIS FUV-MAMA detector (see STIS ISRs 2003-01 and 2004-04).

Following the repair of the ACS WFC in May 2009, no significant changes in the average SBC sensitivity have been found.

4.5.6 SBC Nonlinearity

Global

The MAMA detector becomes nonlinear (i.e., photon impact rate not equal to photon count rate) at globally integrated count rates exceeding 200,000 counts/second. The MAMA detector and processing software are also unable to count reliably at rates exceeding 285,000 counts/second. For these reasons, and to protect the detectors from over-illumination, observations yielding global count rates above 200,000 counts/second are not allowed (see Section 4.6).

Local

The MAMA pixels are linear to better than 1% up to ~22 counts/second/pixel. Nonlinearity at higher count rates is image-dependent such that the nonlinearity of one pixel depends on the photon rate affecting neighboring pixels. Consequently, it is impossible to correct reliably for the local nonlinearity in post-observation data processing. MAMA detectors are also subject to damage at high local count rates, so observations yielding local count rates above 50 counts/second/pixel are not allowed (see Section 4.6).

4.6 SBC Bright-Object Limits

STScI is responsible for ensuring that the MAMA detectors are not damaged by over-illumination. Consequently, procedures and rules have been developed to protect the MAMA. We ask all users to share this responsibility by reading and taking note of the information in this section, and designing observing programs that operate in the safe regime for these detectors. The safety of all proposed SBC targets and fields must be discussed in the Phase I proposal, so that their feasibility can be assessed by the TAC and STScI.

4.6.1 Overview

The SBC detector is subject to catastrophic damage at high global and local count rates, and cannot be used to observe sources that exceed the defined safety limits. The potential detector damage mechanisms include over-extraction of charge from the microchannel plates causing permanent reduction of response, ion feedback from the microchannel plates causing damage to the photocathode, and release of gas which can overpressure the tube. For more information, see ACS ISR 98-03.

To safeguard the detector, checks of the global (over the whole detector) and local (per pixel) illumination rates are automatically performed in flight for all SBC exposures. The *global illumination rate* is monitored continuously; if the global rate approaches the level where the detector can be damaged, the high voltage on the detector is automatically turned off. This event can result in the loss of all observations scheduled to be taken with that detector for the remainder of the calendar (~1 week). The *peak local illumination rate* is measured over the SBC field at the start of each new exposure. If the local rate approaches the damage level, the SBC filter wheel will be used to block the light, since there is no "shutter". Also, all subsequent SBC exposures in the observation set will be lost until a new filter is requested.

Sources that would over-illuminate the SBC detector cannot be observed. It is the responsibility of the observer to avoid specifying observations that exceed the limits described below. Please refer to Section 7.2 for more information and address this issue in your Phase I proposal.

4.6.2 Observational Limits

To ensure the safety of the SBC detector and the robustness of the observing timeline, we have established observational limits on the incident count rates. Observations which exceed the allowed limits will not be scheduled. The allowed limits are given in Table 7.3, which includes separate limits for nonvariable and irregularly-variable sources. The limits for irregular variable sources are a factor 2.5 more conservative than for sources with predictable fluxes. Predictable variables are treated as nonvariable for this purpose. Examples of sources whose variability is predictable are Cepheids or eclipsing binaries. Irregularly variable sources are, for instance, cataclysmic variables or AGN.

SBC observations of targets subject to large, unpredictable outbursts must be preceded by ground-based monitoring within the previous 24 hours, or by a WFC3/UVIS observation a couple of orbits in advance. In the latter case, the observation must be included in the Phase I orbit request. For further information about checking for SBC bright object limits while planning your observations, please refer to Section 7.2.

CHAPTER 5:

Imaging

In this chapter . . .

5.1 Imaging Overview

HRC has been unavailable since January 2007. Information regarding HRC is provided for archival purposes.

ACS has been used to obtain images through a variety of optical and ultraviolet filters. For WFC and HRC imaging, the desired filter in one filter wheel is rotated into position and a CLEAR aperture in the other filter wheel is automatically selected. (Users need not specify CLEAR in their *HST* proposals.) For SBC imaging, the single filter wheel is rotated to the desired position. Every third slot (#1, 4, 7, 10) in the SBC filter wheel is opaque, so the wheel must only be rotated to an adjacent slot to block the beam if a bright object limit violation occurs.Table 5.1,Table 5.2, and Table 5.3 summarize the filters available for imaging with each channel. Figures 5.1 through 5.6 show the filter transmission curves, and Figure 5.7 shows the integrated system throughputs.

The CCD filter wheels contain filters of two different sizes. Some filters (F435W, F475W, F502N, F550M, F555W, F606W, F625W, F658N, F660N, F775W, F814W, F850LP, and, G800L) are full-sized filters that can be used with both WFC and HRC. Others (F220W, F250W, F330W, F344N, F892N, POL0UV, POL60UV, POL120UV,

POL0V, POL60V, POL120V, and PR200L) are smaller, giving a full unvignetted field of view when used with the HRC, but a vignetted field of view of only 72×72 arcseconds^2 when used with the WFC. Use of the small UV filters with WFC is not supported due to the unpredictable behavior of the silver coating shortward of 4000 Å.

The ACS ramp filters are designed to allow narrow or medium band imaging centered at an arbitrary wavelength. Each ramp filter is divided into three segments, of which only the middle segment was used with the HRC. More information is available in Section 7.3.1.

Filterless WFC or HRC is available, but unsupported, by specifying CLEAR as the filter name. Rough wavelengths and bandwidths for CLEAR imaging are listed in Table 5.1. CLEAR imaging yields significantly degraded WFC PSFs, but only slightly degraded HRC PSFs. See ACS ISR 2003-03 for more details about CLEAR imaging.

Table 5.1: ACS WFC/HRC filters in Filter Wheel #1.
(HRC information is provided for archival purposes only.)

Filter name	Central wavelength (Å)	Width (Å)	Description	Camera
CLEAR	6200	5200	Clear aperture	WFC/HRC
F555W	5346	1193	Johnson V	WFC/HRC
F775W	7764	1528	SDSS i	WFC/HRC
F625W	6318	1442	SDSS r	WFC/HRC
F550M	5580	547	Narrow V	WFC/HRC
F850LP	9445	1229	SDSS z	WFC/HRC
POL0UV	2000 to 6000	-	0° UV polarizer	HRC[/WFC][1]
POL60UV	2000 to 6000	-	60° UV polarizer	HRC[/WFC][1]
POL120UV	2000 to 6000	-	120° UV polarizer	HRC[/WFC][1]
F892N	8917	154	Methane (2%)	HRC[/WFC][1]
F606W	5907	2342	Broad V	WFC/HRC
F502N	5022	57	[OIII] (1%)	WFC/HRC
G800L	5800 to 11,000	-	Grism (R~100)	WFC/HRC
F658N	6584	78	Hα (1%)	WFC/HRC
F475W	4760	1458	SDSS g	WFC/HRC

1. [/WFC] indicates that polarizer filters, designed for the HRC field of view, induces vignetting when used with the WFC, producing a 72 by 72 arcsecond^2 field of view.

Table 5.2: ACS WFC/HRC filters in Filter Wheel #2.
(Information regarding the HRC is provided for archival purposes only.).

Filter name	Central wavelength (Å)	Width (Å)	Description	Camera
CLEAR	6000	5200	Clear aperture	WFC/HRC
F660N	6602	40	[NII] (1%)	WFC/HRC
F814W	8333	2511	Broad I	WFC/HRC
FR388N	3710 to 4050	2%	[OII] Ramp—middle segment	WFC/HRC
FR423N	4050 to 4420	2%	[OII] Ramp—inner segment	WFC
FR462N	4420 to 4820	2%	[OII] Ramp—outer segment	WFC
F435W	4297	1038	Johnson B	WFC/HRC
FR656N	6270 to 6850	2%	Hα Ramp—middle segment	WFC/HRC
FR716N	6850 to 7470	2%	Hα Ramp—inner segment	WFC
FR782N	7470 to 8160	2%	Hα Ramp—outer segment	WFC
POL0V	4000 to 8000	-	0° Visible Polarizer	HRC[/WFC][1]
F330W	3354	588	HRC U	HRC
POL60V	4000 to 8000	-	60° Visible Polarizer	HRC[/WFC][1]
F250W	2696	549	Near-UV broadband	HRC
POL120V	4000 to 8000	-	120° Visible Polarizer	HRC[/WFC][1]
PR200L	2000 to 4000	-	NUV Prism (R~100 @ 200 nm)	HRC
F344N	3434	60	Ne V (2%)	HRC
F220W	2228	485	Near-UV broadband	HRC
FR914M	7570 to 10,710	9%	Broad Ramp—middle segment	WFC/HRC
FR853N	8160 to 8910	2%	IR Ramp—inner segment	WFC
FR931N	8910 to 9720	2%	IR Ramp—outer segment	WFC
FR459M	3810 to 5370	9%	Broad Ramp—middle segment	WFC/HRC
FR647M	5370 to 7570	9%	Broad Ramp—inner segment	WFC
FR1016N	9720 to 10,610	2%	IR Ramp—outer segment	WFC
FR505N	4820 to 5270	2%	[OIII] Ramp—middle segment	WFC/HRC
FR551N	5270 to 5750	2%	[OIII] Ramp—inner segment	WFC
FR601N	5750 to 6270	2%	[OIII] Ramp—outer segment	WFC

1. [/WFC] indicates that polarizer filters, designed for the HRC field of view, induces vignetting when used with the WFC, producing a 72 by 72 arcsecond^2 field of view.

Table 5.3: ACS SBC filter complement.

Filter name	Description
F115LP	MgF_2 (1150 Å longpass)
F125LP	CaF_2 (1250 Å longpass)
F140LP	BaF_2 (1400 Å longpass)
F150LP	Crystal quartz (1500 Å longpass)
F165LP	Fused Silica (1650 Å longpass)
F122M	Ly-α (λ = 1200 Å, Δλ = 60 Å)
PR110L	LiF Prism (R~100)
PR130L	CaF_2 Prism (R~100)

Figure 5.1: ACS broad-band filters.

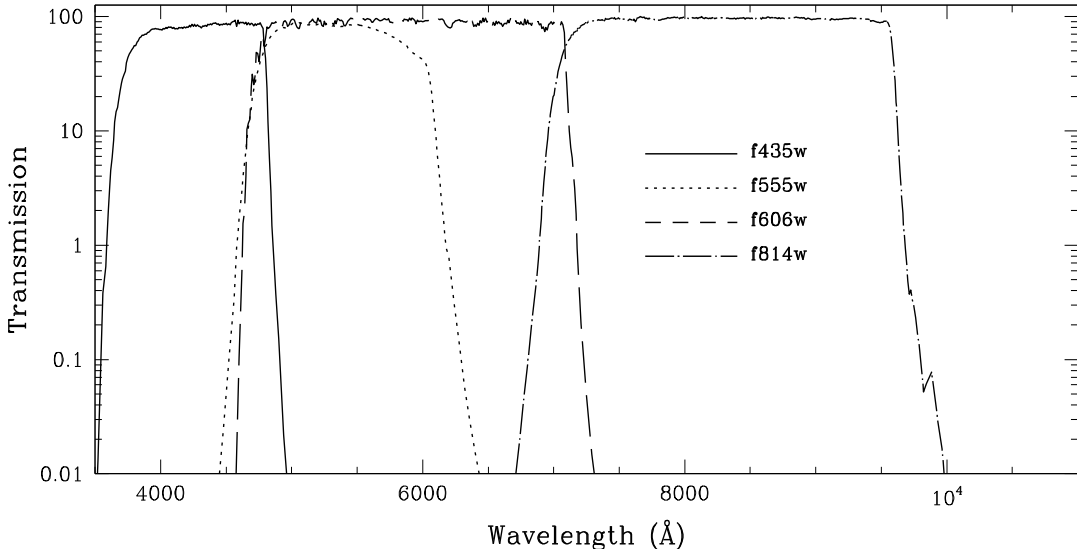

Figure 5.2: ACS SDSS filters.

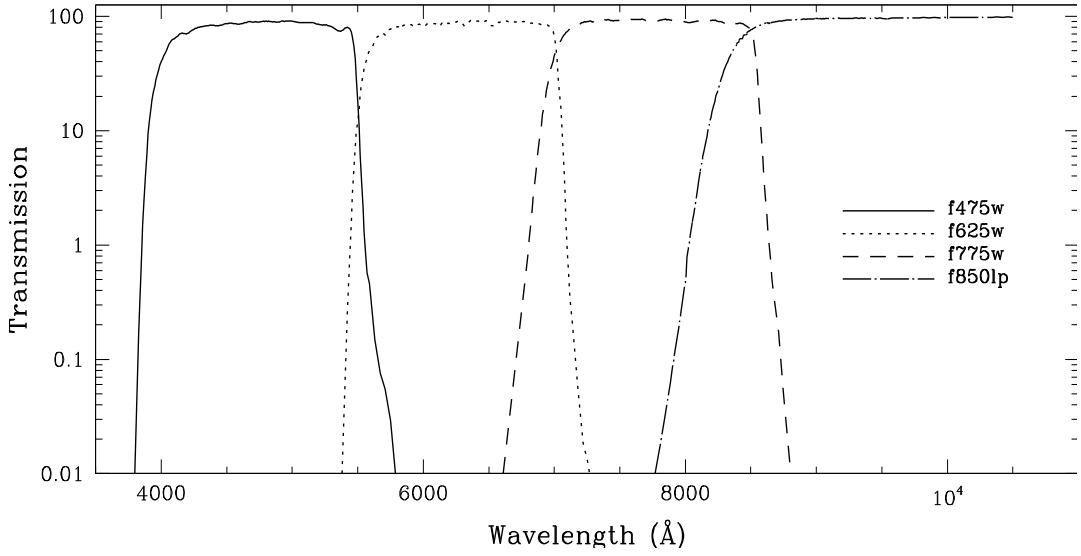

Figure 5.3: ACS UV and medium-band filters.

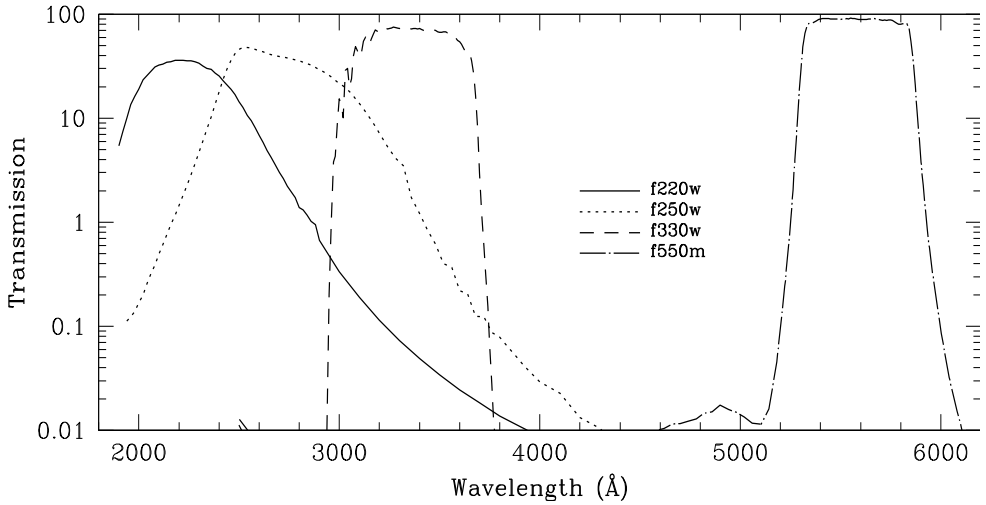

Figure 5.4: ACS narrow band filters.

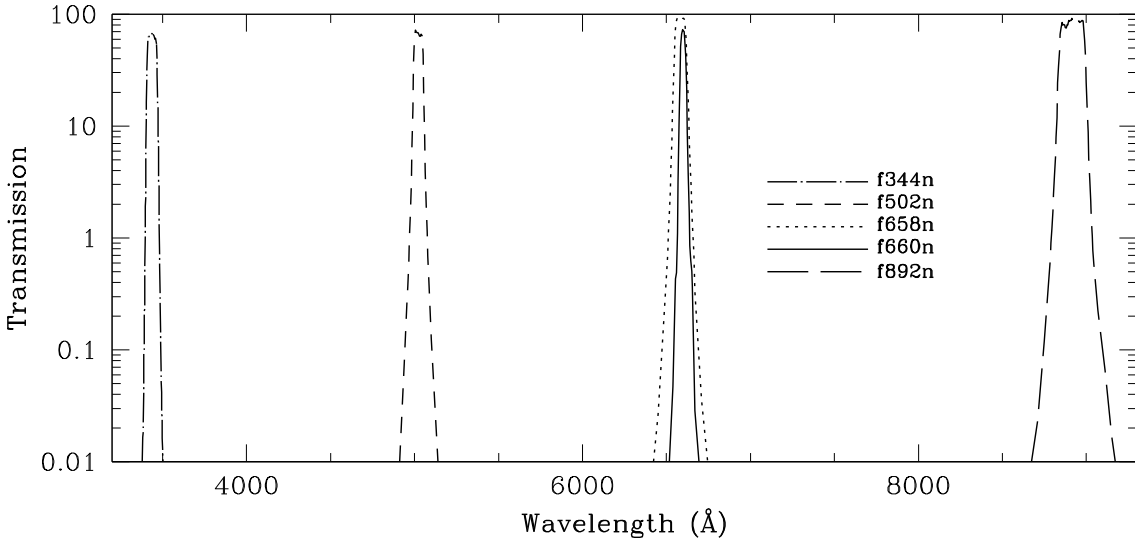

Figure 5.5: ACS SBC filters.

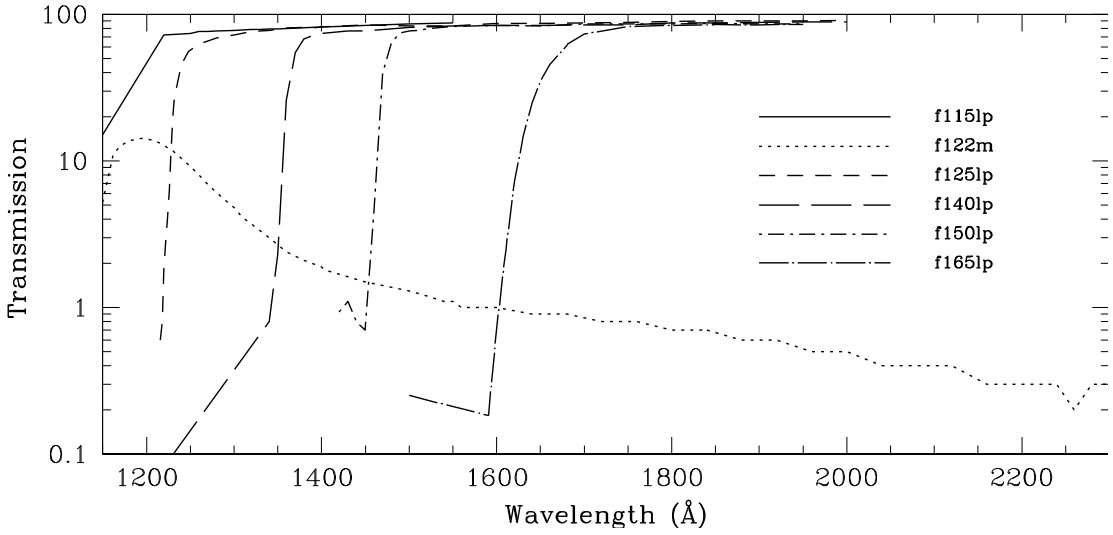

Figure 5.6: Comparison between the ACS and WFPC2 ramp filters.

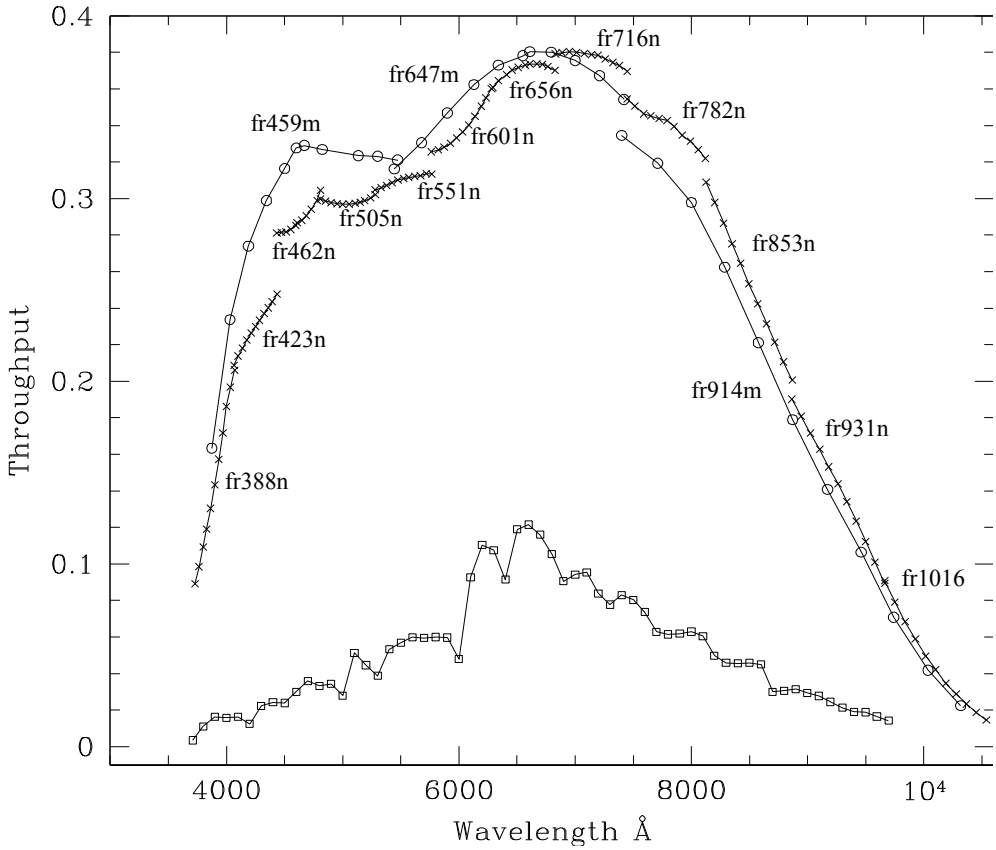

The crosses and open circles are for the ACS narrow and medium band ramps. The open squares are for the 4 WFPC2 ramps. For each of the ACS ramps the peak throughput that was calculated for eleven central wavelength values is plotted. For the WFPC2 ramps, the peak throughput calculated every 100 Å within the field of view of any of the 4 chips, and a 0° filter rotation angle (as mapped in Figures 3.4 and 3.5 of the *WFPC2 Instrument Handbook*), are plotted.

5.2 Important Considerations for ACS Imaging

The following characteristics of ACS should be considered when planning ACS observations or archival research:

- The WFC and HRC shared two filter wheels. Consequently, when the cameras were used simultaneously, only the filter for the primary camera was selectable.
- The ACS cameras are intended to be used with a single filter. Unfiltered or two-filter imaging yields significantly degraded PSFs (particularly for the WFC), so these modes are typically used only for polarization observations or HRC coronagraphic acquisitions. The polarizers have zero optical thickness, so they can and should be used with another filter.

- The geometric distortion of the WFC is significant and causes the projected pixel area to vary by ±9% over the field of view. This distortion affects both the photometric accuracy and the astrometric precision, and must be accounted for when the required accuracy is better than 10%.
- The ratios of in- and out-of-band transmission for ACS CCD UV filters are similar to those of WFPC2, after accounting for differences in the camera's QE. The ACS F220W, F250W, and F330W filter have small red leaks, which are documented in ACS ISR 2007-03.
- The cosmic ray fluxes of HRC and WFC are comparable to those of STIS and WFPC2, respectively. Typical observations should be split or dithered for cosmic ray rejection. See Section 4.3.5 for more information about dithering strategies for removing cosmic rays and hot pixels.
- The large number of parallel and serial shifts required to read out the WFC makes WFC photometry and astrometry more vulnerable to degrading charge transfer efficiency than other *HST* CCD cameras. Section 4.3.7 details the current expectations for CTE performance.
- The default gain setting for WFC observations is GAIN=2. Users may also select gains 0.5, 1.0, and 1.4, but only GAIN=2 is supported by STScI. (see Section 7.6).
- At wavelengths longer than ~ 8000 Å, internal scattering in the HRC CCD produced an extended PSF halo. Only a small number of observations were affected because WFC was mostly used at these wavelengths. The WFC CCDs were treated with a front-side metallization that eliminates the large angle, long wavelength halo problem for wavelengths less than 9000 Å. For observations of red targets with the F850LP refer to Section 9.3.2.
- The ACS filter set is not as large as WFC3. In particular, WFC3/UVIS has an extensive set of narrow band filters and Strömgren filters that are not available with ACS. On the other hand, ACS has polarizers and ramp filters unlike WFC3.

5.2.1 Optical Performance

Following the fine-alignment and focus activities of the SM3B Orbital Verification period, the optical qualities of all three ACS channels were judged to have met their design specifications. The encircled energy values for the WFC, HRC, and SBC obtained during this time are given in Table 5.4.

Table 5.4: Encircled energy measurements for the ACS channels.

Channel	Encircled energy	
	Center of field	Edge of field
WFC at 632.8 nm in 0.25 arcseconds diameter	80.0%	79.4%
HRC at 632.8 nm in 0.25 arcseconds diameter	81.8%	81.6%
SBC at 121.6 nm in 0.10 arcseconds diameter	28%	---

5.2.2 CCD Throughput Comparison

Figure 5.7 compares the wavelength-dependent throughputs of the ACS WFC and HRC with those of WFC3/UVIS, WFC3/IR, NICMOS/NIC3, and WFPC2.

5.2.3 Limiting Magnitudes

Table 5.5 contains the detection limits in Johnson-Cousins V magnitudes for unreddened O5 V, A0 V, and G2 V stars, generated using the ETC. WFC and HRC values used the parameters CR-SPLIT=2, GAIN=2, and a 0.2 arcsecond circular aperture. For the SBC, a 0.5 arcsecond circular aperture was used. An average sky background was used in these examples. However, limiting magnitudes are sensitive to the background levels; for instance, the magnitude of an A0 V in the WFC using the F606W filter changes by ±0.4 magnitudes at the background extremes. Figure 5.8 shows a comparison of the limiting magnitude for point-sources achieved by the different cameras with a signal to noise of 5 in a 10 hour exposure. Figure 5.9 shows a comparison of the time needed for extended sources to attain ABMAG=26.

Figure 5.7: *HST* total system throughputs as a function of wavelength. The plotted quantities are end-to-end throughputs, including filter transmissions calculated at the pivot wavelength of each broad-band filter.

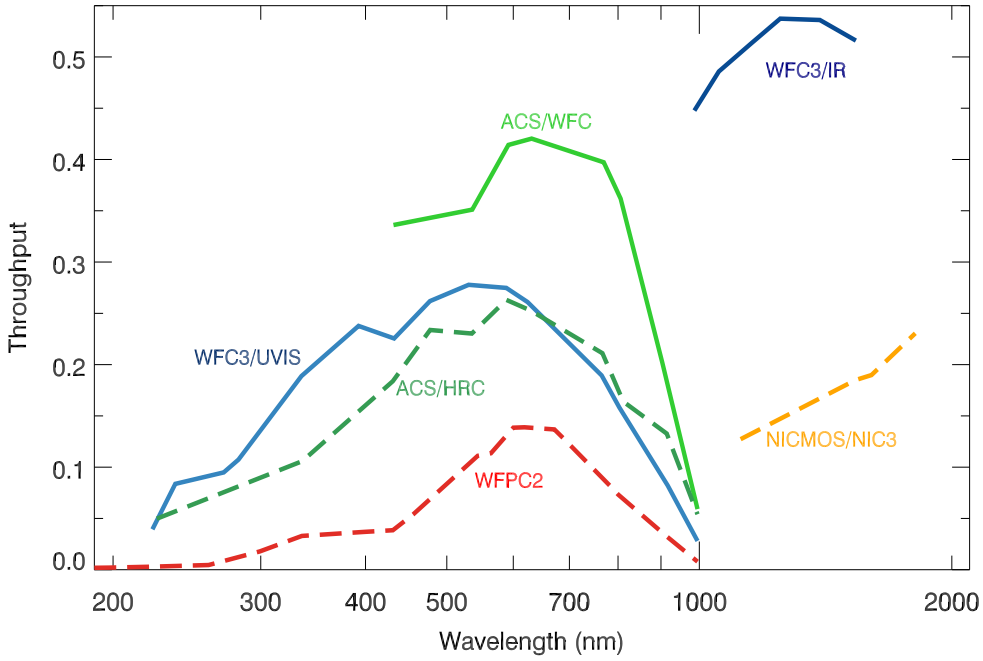

Figure 5.8: *HST* Limiting Magnitude for point sources in 10 hours, as a function of wavelength. Point source limiting magnitude achieved with a signal to noise of 5 in a 10 hour long exposure with optimal extraction.

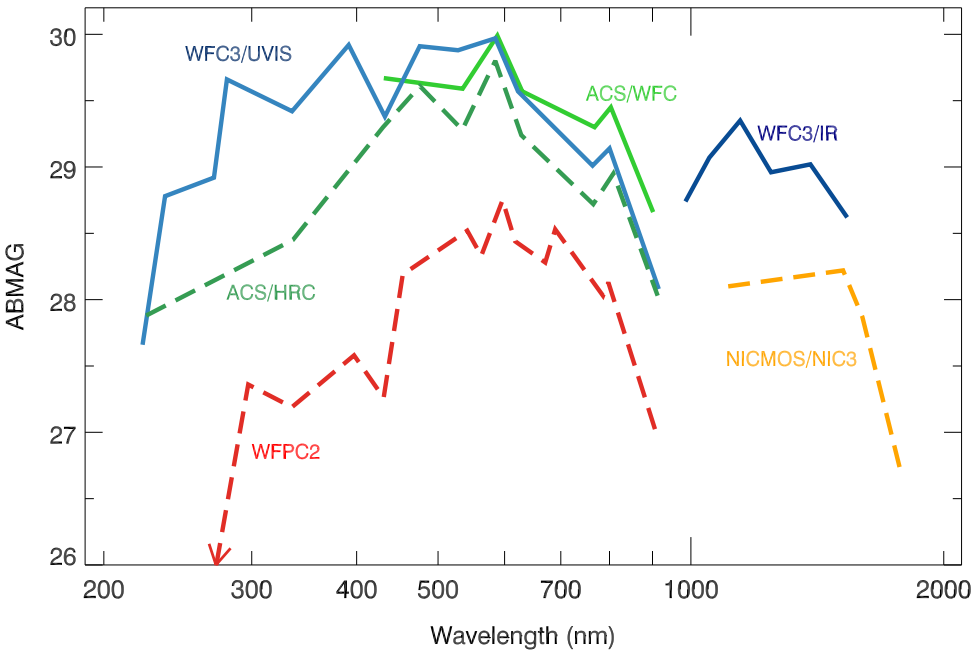

Figure 5.9: *HST* Limiting Magnitude for extended sources in 10 hours, as a function of wavelength.

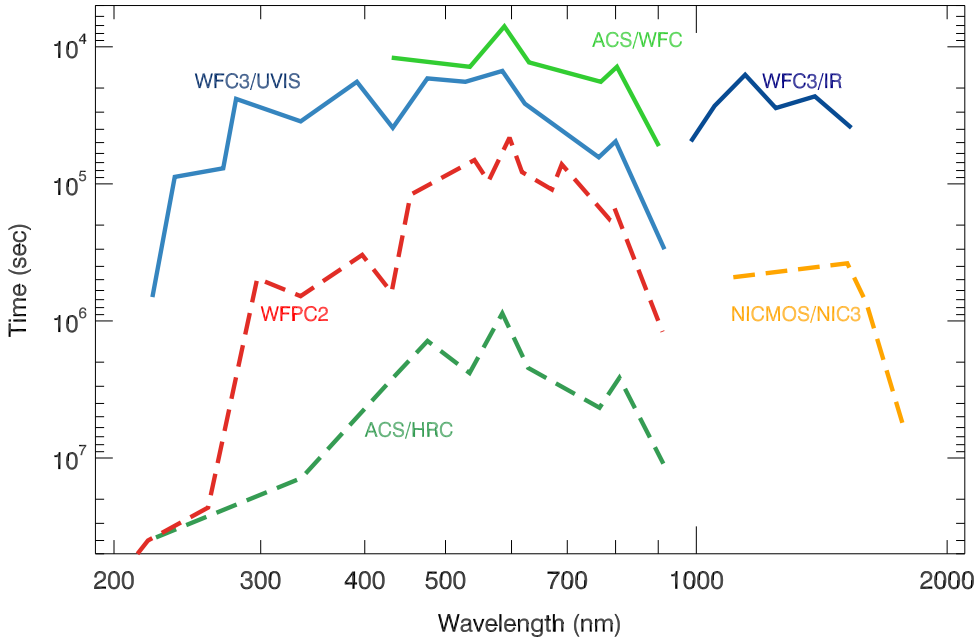

Table 5.5: V detection limits for ACS, HRC, and SBC direct imaging.

Camera	Filter	V limit (S/N = 5, exposure time = 1 hour)		
		O5 V (Kurucz model)	A0 V (Vega)	G2 V (Sun)
WFC	F606W	27.8	27.8	28.0
WFC	F814W	26.7	27.0	27.7
HRC	F330W	26.8	24.8	24.1
HRC	F606W	27.3	27.3	27.5
SBC	F125LP	27.8	23.2	13.5

5.2.4 Signal-To-Noise Ratios

Chapter 10 contains plots of exposure time versus magnitude for a desired signal-to-noise ratio. These plots are useful for determining the exposure times needed for your scientific objectives. More accurate estimates require the use of the ACS ETC (http://etc.stsci.edu/etc).

5.2.5 Saturation

Both CCD and SBC imaging observations are subject to saturation at high total accumulated counts per pixel. For the CCDs, this is due either to the depth of the full well or to the 16 bit data format. For the SBC, this is due to the 16 bit format of the buffer memory (see Section 4.3.1 and Section 4.5.2).

5.2.6 Faint Horizontal Striping in WFC CCDs

Subsequent to the replacement of the ACS CCD Electronics Box during SM4, all WFC images show horizontal striping noise that is roughly constant across each row of read-out in all four WFC amplifiers. This striping is the result of a 1/f noise on the bias reference voltage, and has an approximately Gaussian amplitude distribution with standard deviation of 0.9 electrons. The contribution of the stripes to the global read noise statistics is small, but the correlated nature of the noise may affect photometric precision for very faint sources and very low surface brightnesses.

During Cycle 17, STScI developed and tested an algorithm for removing the stripes from WFC science images. The algorithm is effective when the science image is not excessively crowded such that a row-by-row background level becomes difficult to estimate. Because the stripe removal code is not universally effective, it is not currently applied as part of the ACS calibration pipeline. Instead, STScI has released the stripe removal algorithm to the community as a stand-alone task that can be run on ACS data retrieved from the HST archive. This task, **acs_destripe**, has been written in Python as part of the **acstools** package in the public release of STScI_Python. As a Python task, it can be run from PyRAF, any Python interpreter or even the operating system command-line, to correct post-SM4 pipeline-calibrated images (_flt.fits). Please see the ACS Web site for details on running this code.Further details regarding the WFC striping and its mitigation are provided in the ACS ISR 2011-05 (Grogin et al. 2011).

Because the WFC bias striping noise is so consistent among the four read-out amplifiers, and because it also manifests within the WFC pre-scan regions, STScI is working to incorporate a pre-scan based de-striping algorithm into the ACS calibration pipeline CALACS, which will be available by early 2012. This permits consistent striping-noise mitigation for all post-SM4 WFC full-frame images, including calibration images as well as arbitrary science images, given the trade-off of slightly less precise striping-noise reduction for “low-complexity” science images. This pre-scan based de-striping algorithm, as well as its implementation in CALACS, will be described in an upcoming ACS Instrument Science Report (Anderson & Grogin, in prep.).

5.3 Wide Field Optical CCD Imaging

The Wide Field Channel of ACS was designed primarily for high throughput observations at visible wavelengths. The use of protected silver mirror coatings, the small number of reflections, and the use of a red sensitive CCD have provided the high throughput required for this camera at the expense of a 3700 Å blue cutoff. The WFC detectors are two butted 2K by 4K thinned, backside-illuminated, SITe CCDs with a red optimized coating and long-λ halo fix. The plate scale is 0.050 arcseconds per pixel, which provides a good compromise between adequately sampling the PSF and a wide field of view. The WFC PSF is critically sampled at 11,600 Å and undersampled by a factor 3 at the blue end of the WFC sensitivity range (3700 Å). It is possible to achieve a final reconstructed FWHM of 0.100 to 0.140 arcseconds for well-dithered observations. Because the WFC PSF FWHM is largely dependent on the blurring

caused by CCD charge diffusion, dithering will not be able to recover the full resolution of the optical system. See Section 7.4 for more discussion of how to use dithered observations to optimally sample the PSF.

The optical design of the camera introduces a two-component geometric distortion. The detectors themselves are at an angle with respect to the optical axis. This produces an 8% stretching of one pixel diagonal compared to the other. As a result, WFC pixels project on the sky as rhombuses rather than squares. These effects are purely geometrical and are routinely corrected in the ACS data reduction pipeline. The second component of geometric distortion is more complex. This distortion causes up to ±9% variation in effective pixel area and needs to be taken into account when doing accurate photometry or astrometry as the effective area of the detector pixels varies nonlinearly with field position. See Section 10.3 for a detailed discussion of the distortion in ACS.

5.3.1 Filter Set

WFPC2 and Johnson-Cousins filters

All of the most commonly used WFPC2 filters are included in the ACS filter set. In addition to a medium and a broad V band filter (F550M and F606W), there is a complete Johnson-Cousins *BVI* set (F435W, F555W, F814W).

Sloan Digital Sky Survey filters

The Sloan Digital Sky Survey (SDSS) *griz* filter set (F475W, F625W, F775W, F850LP) is designed to provide high throughput for the wavelengths of interest and excellent rejection of out-of-band wavelengths. The filters were designed to provide wide, non-overlapping filter bands that cover the entire range of CCD sensitivity from blue to near-IR wavelengths.

Narrow Band filters

The Hα (F658N), [OIII] (F502N), and [NII] (F660N) narrow band filters are full-size, and can be used with both the WFC and HRC.

Ramp filters

ACS includes a complete set of ramp filters that provide full coverage of the WFC wavelength range at 2% and 9% bandwidth. Each ramp filter consists of three segments. The inner and outer filter segments can be used with the WFC only, while the middle segments could be used by both WFC and HRC. Unlike the WFPC2, where the desired wavelength is achieved by offsetting the telescope, the wavelength of ACS ramps is selected by rotating the filter while the target is positioned in one of the pre-defined apertures. The monochromatic field of view of the ramp filters is approximately 40 by 80 arcseconds. Details of how to use the ramp filters are given in Section 7.3.

Polarizer filters

The WFC/HRC filter wheels contain polarizers with pass directions spaced by 60°, optimized for both the UV (POL0UV, POL60UV, and POL120UV) and the visible (POL0V, POL60V, and POL120V). All the polarizer filters are sized for the HRC field of view. They induce vignetting when used with the WFC, for which the FOV will be

about 72 x 72 arcseconds^2. More information on the use of the polarizers is given in Chapter 6.

Grism and Prism

The CCD channels also have a grism (G800L) for use with both WFC and HRC from 5500 Å to 11,000 Å, and a prism (PR200L) for use with the HRC from 1600 Å to 3500 Å. These are described in more detail in Chapter 6.

5.4 High-Resolution Optical and UV Imaging

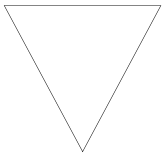

Information regarding the HRC is provided for archival purposes only.

Before its failure in January 2007, the High Resolution Channel of ACS was the primary camera for near-UV imaging. HRC provided high throughput at blue wavelengths and better PSF sampling than either the WFC or other CCD cameras on *HST*. HRC's pixel size critically sampled the PSF at 6300 Å and undersampled the PSF at the blue end of its sensitivity range (2000 Å) by a factor of 3.0. Well-dithered observations with the HRC led to a reconstructed PSF FWHM of 0.03 arcsec at ~4000 Å, increasing towards longer wavelengths. For these reasons, HRC was used mostly for UV and blue imaging. It was also used for red imaging when PSF sampling was important. The photometric accuracy of the HRC was generally higher than that of the WFC. HRC also included a coronagraph that is discussed in Section 6.2. HRC's CCD scattered red light into a wide-angle halo (as does STIS's CCD). Production constraints prevented the remediation of this halo by front-side metallization, which was done for WFC's CCD. Although most of the HRC imaging occurred in the UV, users are cautioned to take into account the effect of the long wavelength halo when the HRC was used in combination with near-IR filters (see Section 5.6.5).

5.4.1 Filter Set

The HRC-specific filters were mostly UV and blue. The set included UV and visible polarizers (discussed in Section 6.1), a prism (PR200L, discussed in Section 6.3), three medium-broad UV filters (F330W, F250W, and F220W) and two narrow band filters (F344N and F892N). Use of the UV filters with the WFC is not supported because of the uncertainty of the WFC silver coating transmission below 4000 Å. All broad, medium and narrow band WFC filters could be used with the HRC whenever better PSF sampling was required. Generally, the throughput of WFC was higher than that of HRC where their sensitivities overlapped. Only some of the WFC ramp segments -- the FR459M and FR914M broad ramps, and the FR505N [OIII], FR388N [OII], and FR656N (H) narrow ramps -- could be used with the HRC because only the middle segment overlapped with the HRC FOV.

5.4.2 Multiple Electron Events

Unlike the WFPC2 CCD, the HRC CCD was directly sensitive to UV photons and was much more effective in detecting them. When a detector has non-negligible sensitivity over more than a factor of two in wavelength, however, it is possible for a UV photon to generate more than one electron and thus be counted more than once. This effect was noted during ground testing of the HRC CCD and also has been noted for the STIS CCD. The effect is only important shortward of 3200 Å, reaching approximately 1.7 e-/photon at 2000 Å. Multiple counting of photons must be accounted for when estimating QE and the noise level of a UV observation because multiple photons distort the Poisson noise distribution of the electrons.

5.4.3 Red Leaks

When designing a UV filter, high suppression of out-of-band transmission, particularly at red wavelengths, must be balanced with overall in-band transmission. HRC's very high blue quantum efficiency made it possible to obtain red-leak suppression comparable to that of WFPC2 while using much higher transmission filters. Red leak calibration data was obtained in Cycle 14 and are described in ACS ISR 2007-03. Table 5.6 shows the ratio of in-band versus total flux for a few UV and blue filters in the now-defunct HRC, where the boundary between in-band and out-of-band flux is defined as the 1% transmission point. The same ratio is also listed for the equivalent WFPC2 filters. Correction factors for different stellar spectral types and non-stellar spectra are found in ACS ISR 2007-03. Red leaks were not a problem for F330W, F435W, and F475W. Red leaks were more important for F250W and F220W. In particular, accurate UV photometry of M stars requires correction for the F250W red leak and is essentially impossible in F220W. For F220W, red-leak correction is also necessary for G and K stars.

Table 5.6: In-band flux as a percentage of the total flux.

Stellar type	WFPC2 F218W	HRC F220W	WFPC2 F255W	HRC F250W	WFPC2 F300W	HRC F330W	WFPC2 F439W	HRC F435W	WFPC2 F450W	HRC F475W
O5 V	99.8	99.6	99.7	99.7	99.9	99.9	99.9	99.9	99.9	99.9
B1 V	99.7	99.6	99.6	99.7	99.9	99.9	99.9	99.9	99.9	99.9
A1 V	99.5	98.8	99.5	99.0	99.9	99.9	99.9	99.9	99.9	99.9
F0 V	98.7	97.0	98.5	98.3	99.4	99.9	99.9	99.9	99.9	99.9
G2 V	91.5	88.7	96.3	97.1	98.8	99.9	99.9	99.9	99.8	99.9
K0 V	91.4	60.6	96.2	95.2	98.7	99.9	99.9	99.9	99.8	99.9
M2 V	47.0	1.5	84.6	62.4	75.2	99.9	99.9	99.9	99.6	99.9

5.5 Ultraviolet Imaging with the SBC

The Solar Blind Channel is the ACS camera optimized for UV imaging. The SBC uses the same optical train as the HRC and is comparable in performance to the FUV MAMA of STIS. The use of the repeller wire increases the quantum efficiency of the detector by ~30%, but adds a halo to the PSF. Bright object limits are discussed in detail in Section 7.2.

5.5.1 Filter Set

Several filters are available for use with the SBC, including a Lyman α narrow band filter (F122M), a long pass quartz filter (F150LP), MgF_2 filter (F115LP), and a CaF_2 filter (F125LP). The SBC also includes two additional long pass filters (F140LP and F165LP) as well as prisms (discussed in Section 6.3). A list of filters is given in Table 5.3

5.5.2 Red Leaks

The visible light rejection of the SBC is excellent, but users should be aware that stars of solar type or later will have a significant fraction of the detected flux coming from outside the nominal wavelength range of the detector. This is discussed in greater detail in Section 4.4.2, and more information is available in Table 5.7.

Table 5.7: Visible-light rejection of the SBC F115LP imaging mode.

Stellar type	Percentage of all detected photons which have λ < 1800 Å	Percentage of all detected photons which have λ < 3000 Å
O5V	97.7	100
B1 V	98.7	100
A0 V	95.6	99.7
G0 V	29.0	40.5
K0 V	0.	5.4

The star spectra are from the Pickles catalog (Pickles A.J., 1998, PASP 110, 863).

5.5.3 SBC Imaging Filter Shifts

The SBC focal surface, like that of the HRC, is tilted significantly with respect to the chief ray. Because the MAMA detector is a STIS spare, its window is approximately parallel to the MCP surface and the whole detector must tilt to achieve good focus over the field. Because the window is therefore tilted, “lateral color” is introduced, which would result in dispersion-induced degradation of the PSF, so the filters are canted in the opposite direction to that of the window to ameliorate the color. The filter thickness is matched to the mean index of refraction over its bandpass

to maintain focus. These result in unavoidable image location offsets between filters. In contrast, the WFC and HRC filters and windows are normal to the chief ray and the detector surfaces are tilted within their housings to match the focal surface tilt. In Table 5.8, we list the shifts for each SBC imaging filter with respect to the F115LP filter. No pointing compensations are made for these offsets.

Table 5.8: Shifts between SBC imaging filters.

Spectral Element	Offset (pixels) in the x direction	Offset (pixels) in the y direction
F115LP	0	0
F122M	0	0
F125LP	-5	15
F140LP	-7	21
F150LP	-3	11
F165LP	-4	12

5.6 ACS Point Spread Functions

The ACS point spread function has been studied in ground test measurements, and by using on-orbit data and models generated by the **Tiny TIM** software (http://www.stsci.edu/software/tinytim/) developed by J. Krist and R. Hook. As with other *HST* instruments, the ACS point spread function is affected by both optical aberrations and geometric distortions. Point sources imaged with WFC and HRC experience blurring due to charge diffusion into adjacent pixels because of CCD subpixel variations, which reduces the limiting magnitudes that can be reached by WFC/HRC. The SBC PSF and the long-wavelength HRC PSF are also affected by a halo produced by the detectors themselves.

5.6.1 CCD Pixel Response Function

The sharpness of the CCD PSF is somewhat degraded by charge diffusion into adjacent pixels. The effect is usually described in terms of the pixel response function (PRF), which gives the distribution of flux from within the pixel into adjacent pixels. Charge diffusion results in ~0.5 magnitude loss in the WFC limiting magnitude at short wavelengths (the worst case). At longer wavelengths and at all wavelengths for the HRC the reduction in the limiting magnitude is ~0.2 magnitudes or less. Due to variations in the CCD thickness, charge diffusion is not constant over the field of view.

At different wavelengths, the CCD pixel response functions can be represented by the following kernels (for the center of the field):

Figure 5.10: Kernels representing CCD pixel functions for HRC and WFC.

$$K_{HRC} = \begin{bmatrix} 0.02 & 0.07 & 0.02 \\ 0.07 & 0.64 & 0.07 \\ 0.02 & 0.07 & 0.02 \end{bmatrix}, \quad K_{WFC} = \begin{bmatrix} 0.04 & 0.11 & 0.04 \\ 0.11 & 0.40 & 0.11 \\ 0.04 & 0.11 & 0.04 \end{bmatrix}$$

at $\lambda = 4000$ Å,

$$K_{HRC} = \begin{bmatrix} 0.02 & 0.06 & 0.02 \\ 0.06 & 0.68 & 0.06 \\ 0.02 & 0.06 & 0.02 \end{bmatrix}, \quad K_{WFC} = \begin{bmatrix} 0.03 & 0.10 & 0.03 \\ 0.10 & 0.48 & 0.10 \\ 0.03 & 0.10 & 0.03 \end{bmatrix}$$

at $\lambda = 5500$ Å, and

$$K_{HRC} = \begin{bmatrix} 0.02 & 0.04 & 0.02 \\ 0.04 & 0.76 & 0.04 \\ 0.02 & 0.04 & 0.02 \end{bmatrix}, \quad K_{WFC} = \begin{bmatrix} 0.02 & 0.07 & 0.02 \\ 0.07 & 0.64 & 0.07 \\ 0.02 & 0.07 & 0.02 \end{bmatrix}$$

at $\lambda = 8000$ Å.

More details on ACS CCD charge diffusion are given in ACS ISR 2006-01. For details on CTE-induced photometric losses for ACS/WFC and techniques to correct for them, see ACS ISR 2006-01.

5.6.2 Model PSFs

Table 5.9 and Table 5.10 give ACS model PSFs in the central 5×5 pixel region in two filters. Numbers listed are the fraction of the total energy received in each pixel. The models have been generated using Tiny TIM, taking into account the *HST* optical aberrations and obscurations as well as the CCD pixel response function. Field dependent geometrical distortions are included. The real PSF will also differ from the model because of the jitter in the *HST* pointing, *HST* focus variation (focus breathing), and other instrumental effects, some of which are briefly discussed below. For further details on the PSF variations and an effective procedure to model them, see ACS ISR 2006-01.

Table 5.9: ACS Model PSFs in the central 5x5 pixel region (CCD).

WFC model PSF, filter F435W					WFC model PSF, filter F814W				
0.00	0.01	0.01	0.01	0.00	0.01	0.01	0.02	0.01	0.01
0.01	0.04	0.07	0.05	0.02	0.01	0.03	0.07	0.03	0.02
0.02	0.08	0.17	0.08	0.02	0.02	0.07	0.18	0.07	0.02
0.01	0.04	0.08	0.04	0.01	0.01	0.03	0.07	0.03	0.01
0.00	0.01	0.02	0.01	0.00	0.01	0.02	0.02	0.01	0.00
HRC model PSF, filter F435W					**HRC model PSF, filter F814W**				
0.01	0.01	0.01	0.01	0.01	0.00	0.01	0.02	0.01	0.00
0.02	0.03	0.06	0.03	0.01	0.01	0.04	0.05	0.04	0.01
0.01	0.06	0.16	0.06	0.01	0.02	0.05	0.08	0.05	0.02
0.01	0.03	0.07	0.03	0.01	0.01	0.04	0.05	0.04	0.01
0.01	0.02	0.01	0.01	0.01	0.00	0.01	0.02	0.01	0.00

Table 5.10: ACS Model PSFs in central 5x5 pixel region (SBC).

SBC PSF at 120 nm					SBC PSF at 160 nm				
<0.01	0.01	0.01	0.01	<0.01	<0.01	<0.01	<0.01	<0.01	<0.01
0.01	0.02	0.03	0.02	0.01	<0.01	0.02	0.04	0.02	<0.01
0.01	0.03	0.15	0.03	0.01	<0.01	0.04	0.20	0.04	<0.01
0.01	0.02	0.03	0.02	0.01	<0.01	0.02	0.04	0.02	<0.01
<0.01	0.01	0.01	0.01	<0.01	<0.01	<0.01	<0.01	<0.01	<0.01

5.6.3 Encircled Energy

In general, the ACS channels encircled energy distribution has been found to be within the original instrument specifications. Figure 5.11 and Figure 5.12 show the ACS encircled energy curves derived from on-orbit images. Tabulated values of the encircled energy for most filters are available in Sirianni et al. 2005 (PASP 117, 1049).

Due to telescope breathing over short time scales and focus drifts over long time scales, users are encouraged to measure the encircled energy directly from their science images, rather than depending on the tabulated values, where deviations at small radii may be significant.

Further details on the encircled energy calibration can be found in the ACS ISR 2011-02, Bohlin, R. (2011).

5.6.4 Geometric Distortions

Geometric distortions produce a significant impact on the shape of the PSF in all three of the ACS channels, as can readily be seen in Figure 5.13 and Figure 5.14, which display WFC and HRC PSF images. The log stretch enhances the spider diffraction patterns, which the distortion renders non-perpendicular, and the outer Airy rings, which appear elliptical. The distortion owes primarily to the tilt of the focal surface to the chief ray at the large OTA field angles of the ACS apertures. The linear, field-independent approximation for the WFC produces a difference in plate scale of about 8% between the two diagonals of the field and, in the HRC and SBC, about a 16.5% difference in scale between orthogonal directions rotated about 20° from the aperture edges. Field-dependent distortions, measured as actual vs. predicted distances from field center, amount to about 2% peak in the WFC and about 1% in the HRC and SBC. The distortion solutions are stable following the WFC repair.

The distortions render the pixels, as projected on the sky, trapezoidal in shape and their area varies over the field by about 19% and 3.5% in the WFC and HRC/SBC, respectively. These variations have significant ramifications concerning appropriate techniques for flat-fielding and photometric calibration, especially when complicated by resampling in order to combine dithered image sets. Related issues are the manner in which the halation effects of the HRC and SBC detectors are removed and the treatment of spectra from the prisms and grism, which are not subject to the same distortion effects.

More details concerning geometric distortions in ACS can be found in ACS ISR 2002-02, ACS ISR 2004-15, ACS ISR 2007-08 and ACS ISR 2008-02. An introduction to ***calacs***, is available in the *ACS Data Handbook* which is posted on the STScI ACS Web page. Information about ***multidrizzle***, which applies corrections for geometric distortion, is available on-line at:

`http://stsdas.stsci.edu/multidrizzle/`

MultiDrizzle will soon be replaced, first in the pipeline and later in user software, by a new program called AstroDrizzle (for “astrometric drizzle”). This new software will make image combination simpler and less error prone, and allow for better handling of astrometry.

Figure 5.11: Encircled energy for the CCD channels.

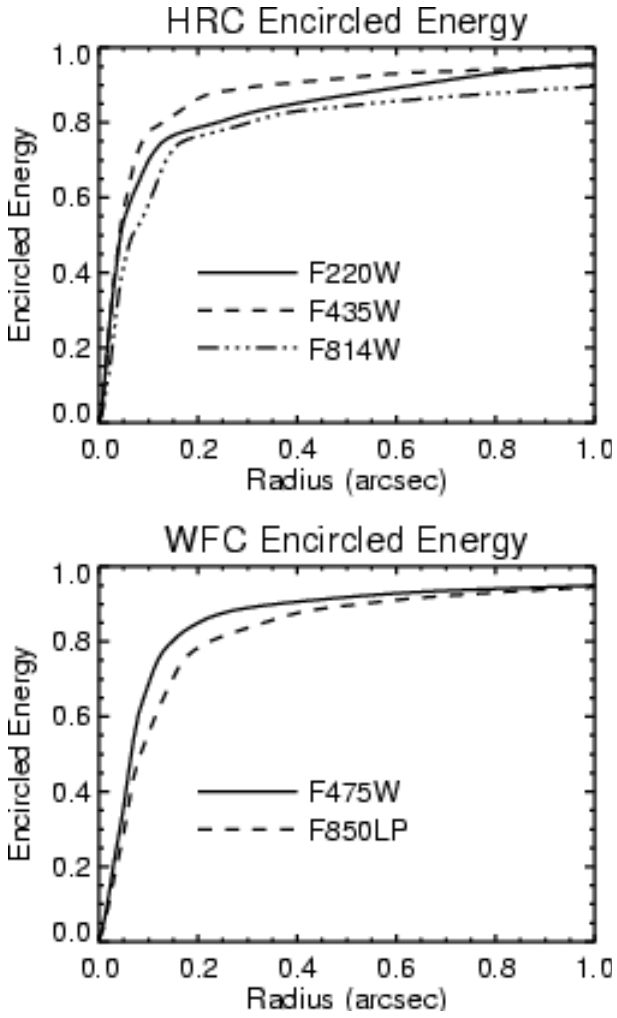

Figure 5.12: Encircled energy for the SBC.

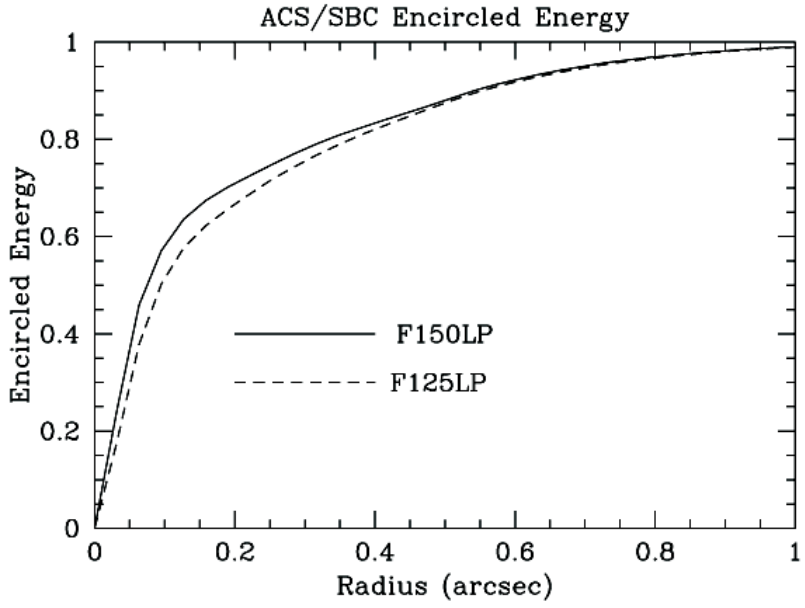

Figure 5.13: ACS WFC PSF - F625W.

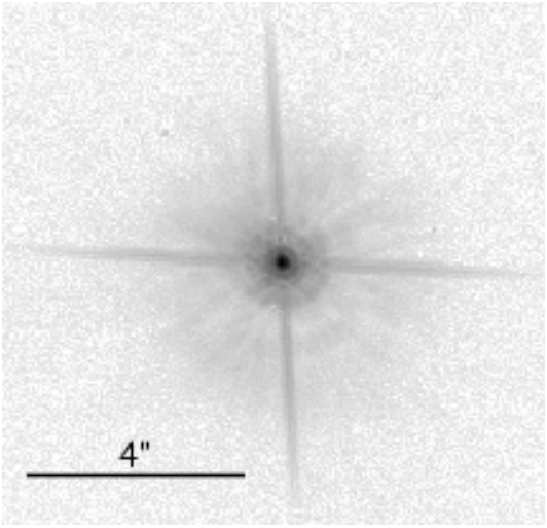

Figure 5.14: ACS HRC PSF - F625W.

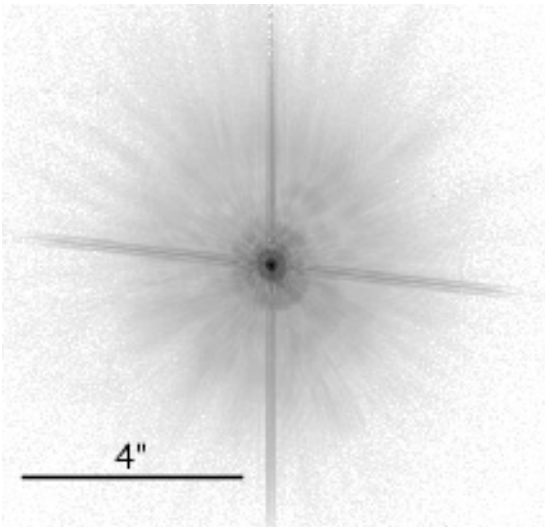

5.6.5 PSFs at Red Wavelengths and the UV

The CCDs used in the HRC and WFC suffer from a halo that is caused by very red photons passing through the device and being scattered back into the detector by the mounting substrate. This creates a large halo in HRC images beyond 7000 Å and WFC images past 9000 Å. At 8000 Å in the HRC, the halo contains about 10% of the light. At 10,000 Å, it contains about 30% and increases the surface brightness of the PSF wings by over an order of magnitude, overwhelming the PSF diffraction rings and spikes. A discussion of this may be found in Gilliland & Riess 2002 (*HST Calibration Workshop)* at:

http://www.stsci.edu/largefiles/hst/HST_overview/documents/calworkshop/workshop2002/CW2002_Papers/gilliland.pdf

In the F850LP filter, in particular, extremely red stars show a progressive loss of flux in small to moderate sized apertures as a function of color. Additional information can

be found in Sirianni et al. 2005, PASP, 117, 1049 and ACS ISR 2007-06. These papers provide a detailed recipe to correct for this effect. This halo effect is only partially treated by the ETC. Observers can use ***synphot*** (see Section 9.3.2) to accurately calculate the photometry of red sources in the SDSS z-filter.

Long wavelength photons that pass through the CCD can also be scattered by the electrode structure on the back side of the device and will create two spikes that extend roughly parallel to the x-axis. These spikes are seen at wavelengths longer than 9500 Å in both the HRC and WFC (see Figure 5.15 and Figure 5.16).

Figure 5.15: ACS WFC PSFs (10" x 10"). FR914M images are saturated.

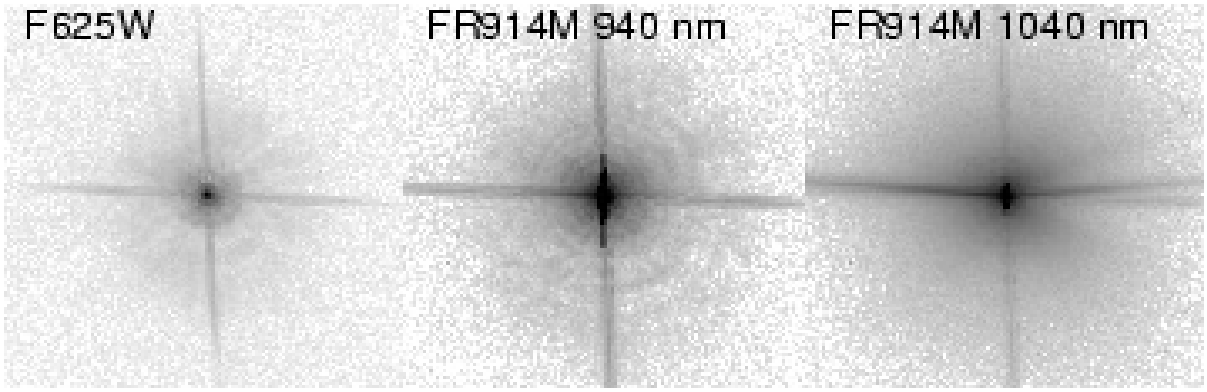

Figure 5.16: ACS HRC PSFs (3.25" x 3.25").

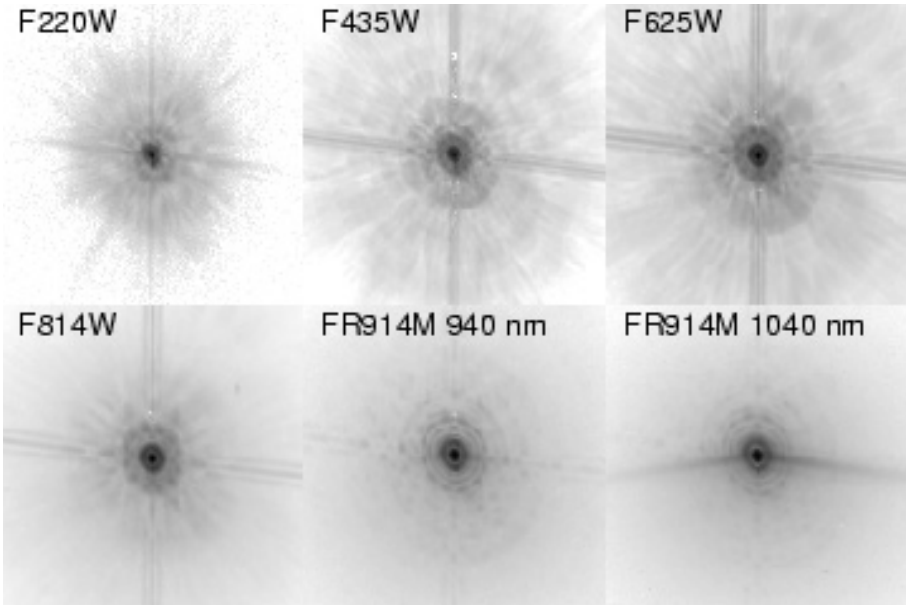

In the UV the core of the PSF becomes rather asymmetrical due to mid-frequency optical surface errors. In the SBC, a halo is created by charge migration at the

microchannel plate surface. This effect, seen previously in STIS MAMA images, broadens the PSF core and redistributes a small portion of flux into a broad halo that can be approximated by a Gaussian with FWHM ~20 pixels. The peak flux for a point source centered on a pixel is reduced by 30 to 40% depending on wavelength.

The encircled energy curves presented in this handbook and incorporated into the ETC include all of the scattering effects discussed here.

5.6.6 Residual Aberrations

Residual aberration levels at the center of the field in each camera are 1/30 wave (HRC) and 1/20 wave (WFC) rms at 5500 Å (excluding defocus). Coma and astigmatism are minimized at the field center of each camera. The ACS PSF varies far less over the field of view than those of WFPC2 and STIS. WFPC2 especially suffered from a variable obscuration pattern that significantly altered the PSF structure depending on field position. Lacking the additional obscurations present in WFPC2, ACS PSF variations are instead due to changes in aberrations and charge diffusion.

At the extreme corners of the WFC field, increased astigmatism slightly elongates the PSF core. The axis of elongation rotates by 90° if the system passes through focus due to breathing. This may affect ellipticity measurements of small galaxies with bright cores at the field edges. Focus variations in the WFC, which alter the amount of light in the peak, are largely due to detector surface height irregularities and amount to the equivalent of 5 microns of breathing (1/18 wave rms). The largest focus offset is along the gap between the two CCDs. Variations in the width of the PSF core are dominated by changes in CCD charge diffusion, which is dependent on the thickness of the detector (12 to 17 microns for the WFC). The PSF FWHM in F550M, for example, can vary by 20% (0.10 to 0.13 arcseconds) over the field. More information about the dependence of the WFC PSF on OTA temperature and breathing is provided in ACS ISR 2007-12 and ACS ISR 2008-03.

The PSFs in the HRC and SBC are reasonably constant over their fields. The HRC FWHM is 0.060 to 0.073 arcseconds in F550M. More details on ACS PSF field variations are provided in ACS ISR 2003-06. The Tiny Tim PSF simulator includes field dependent aberrations and charge diffusion and may be used to estimate the impact of these variations. Information about the dependence of the WFC PSF on OTA temperature and breathing is provided in ACS ISR 2007-12 and ACS ISR 2008-03.

CHAPTER 6:

Polarimetry, Coronagraphy and Prism/Grism Spectroscopy

In this chapter. . .

6.1 Polarimetry

HRC has been unavailable since January 2007. Information about the HRC is provided for archival purposes.

6.1.1 Introduction

ACS offers two sets of polarizers, one optimized for near-UV/blue wavelengths (POLUV) and one optimized for visible/red wavelengths (POLV). These polarizers can be combined with most of the ACS filters (Table 6.1), allowing polarimetry in both continuum and line emission. Rudimentary spectropolarimetry is possible by using the polarizers in conjunction with the dispersing elements. The large number of

possible spectropolarimetric modes prevents automatic calibration of these modes by STScI, so observers must request additional orbits for their own spectropolarimetric calibrations. For normal polarimetric imaging, the location of the target remains fixed on the detector as successive images are obtained using a suitable filter and each of the constituent polarizers of the desired set. The varying intensities of the source in the successive images provide the basic polarimetric data for the source.

Table 6.1: Filters that can be used in conjunction with the ACS polarizers.

Polarizer set	Filters	Filter comments
POL0UV	F220W	HRC NUV short
POL60UV	F250W	HRC NUV long
POL120UV	F330W	HRC U
	F435W	Johnson B
	F814W	Broad I
POL0V	F475W	SDSS g
POL60V	F606W	Johnson V
POL120V	F625W	SDSS r
	F658N	Hα
	F775W	SDSS i

6.1.2 Performance of ACS Polarizers

At least three polarized images are required to determine the degree and position angle of polarization as well as the total intensity of the source. Each set of ACS polarizers comprise three polarizing filters with relative position angles 0°, 60°, and 120°. The polarizers are aplanatic optical elements coated with Polacoat 105UV (POLUV set) and HN32 polaroid (POLV set). The POLUV set is effective throughout the visible region; its useful range is approximately 2000 Å to 8500 Å. The POLV set is optimized for the visible region of the spectrum and is fully effective from 4500 Å to about 7500 Å.

The relative performance of the POLUV and POLV polarizers are shown in Figure 6.1. The POLV set provides superior perpendicular rejection in the 4500 Å to 7500 Å bandpass, while the POLUV set delivers lower overall rejection across a wider range from 2000 Å to 7500 Å. Performance degrades at wavelengths longer than about 7500 Å, but useful observations may still be obtained up to approximately 8500 Å. In such cases, imperfect rejection of orthogonally polarized light must be considered during data analysis.

Figure 6.1: Throughput and rejection of the ACS polarizers.

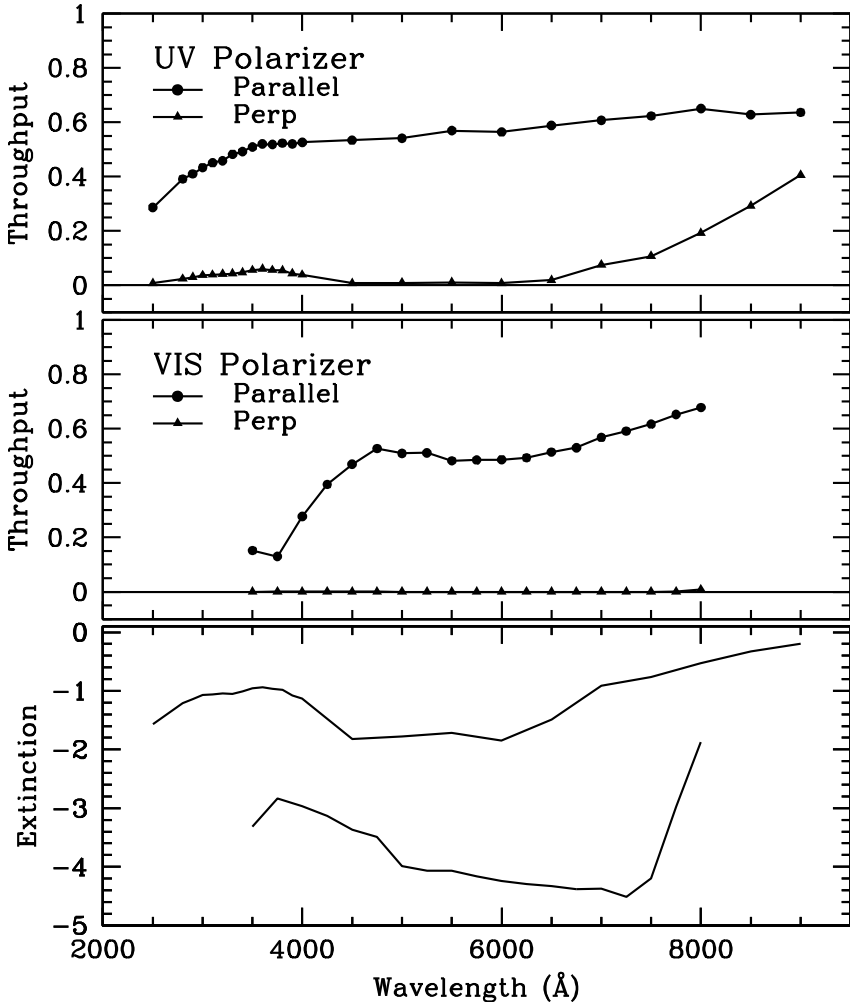

In the top two boxes, the upper curve is the parallel transmission, while the lower curve is the perpendicular transmission. The bottom panel shows the logarithm of the ratio of perpendicular to parallel transmission.

The ACS polarizers are effectively perfect. Consequently, the Stokes parameters (I, Q, U) can be computed using simple arithmetic. Using im1, im2, and im3 to represent the images taken through the polarizers POL0, POL60, and POL120 respectively, the Stokes parameters are:

$$Q = \frac{2}{3}(2im1 - im2 - im3)$$

$$U = \frac{2}{\sqrt{3}}(im3 - im2)$$

$$I = \frac{2}{3}(im1 + im2 + im3)$$

These parameters can be converted to the degree of polarization (P) and the polarization angle (θ) measured counterclockwise from the x axis as follows:

$$P = \frac{\sqrt{Q^2 + U^2}}{I}$$

$$\theta = \frac{1}{2}\tan^{-1}(U/Q)$$

A more detailed analysis, including allowances for imperfections in the polarizers, is given by Sparks & Axon (1999, *PASP*, 111, 1298), who found that the important parameter in experiment design is the product of expected degree of polarization and signal-to-noise. For three perfect polarizers oriented at 60° relative position angles (as in ACS), the uncertainty in the degree of polarization P (which ranges from 0 for unpolarized light to 1 for fully polarized light) is approximately the inverse of the signal-to-noise per image. Specifically, Sparks & Axon found

$$\log\left(\frac{\sigma_P}{P}\right) = -0.102 - 0.9898\log(P\langle \mathrm{S/N}\rangle_i)$$

where $\langle \mathrm{S/N}\rangle_i$ is the signal-to-noise of the ith image; and

$$\log\sigma_\theta = 1.514 - 1.068\log(P\langle \mathrm{S/N}\rangle_i)$$

This analysis pertains to ideal polarizers with no instrumental polarization. However, the ACS polarizers (especially the POLUV polarizers) allow significant leakage of cross-polarized light and the instrumental polarization of the WFC is ~2% (see ACS ISR 2004-09). The instrumental polarization of the HRC ranged from a minimum of 4% in the red to 14% in the far-UV. Other effects, such as phase retardance in the mirrors, may be significant as well. Please consult the STScI Web pages for more detailed information, especially the *ACS Data Handbook*:

http://www.stsci.edu/hst/acs/documents/handbooks/currentDHB/acs_cover.html

and ISRs at:

http://www.stsci.edu/hst/acs/documents/isrs.

6.1.3 Implementation of ACS Polarizers

The ACS polarizers are easy to use. The observer selects the camera (either HRC or WFC) and the spectral filter, then takes successive images with the three polarizers of the VIS set (POL0V, POL60V, POL120V) or the UV set (POL0UV, POL60UV, POL120UV). Once the camera and polarizer set are specified, the scheduling system automatically generates the slews that place the target in the optimal region of the field of view.

Because the POLUV and POLV sets are housed on separate filter wheels, the number of spectral filters available to each set is restricted. The available filters were

determined according to the relative performance of the polarizers and the near-UV limitations of the WFC caused by its silver mirror coatings.

The POLUV polarizers are mounted on Filter Wheel 1 and may be crossed with the near-UV filters mounted on Filter Wheel 2. The POLV polarizers are mounted on Filter Wheel 2 and may be crossed with filters on Filter Wheel 1, namely the primary broadband filters, and discrete narrowband filters Hα, [OII], and their continuum filters. Because supported calibration time is limited, STScI does not support the use of ramp filters with either polarizer set. GOs must plan their own calibration observations if they use the ramp filters with the polarizers.

The polarizer sets were designed primarily for use with the HRC, where they offer a full unvignetted field of view (29×26 arcseconds) with any allowed imaging, spectroscopic, and coronagraphic combinations. When used with the WFC, the polarizers provide an unvignetted circular field of view with a diameter 70 arcseconds. Although this field of view is significantly smaller than the normal WFC field of view, it is approximately five times larger than that obtained with the HRC. To avoid the gap between the WFC CCDs and to optimize readout noise and CTE effects, the scheduling system will automatically slew the target to pixel (3096,1024) on the WFC1 CCD whenever the WFC aperture and polarizer sets are selected. To reduce camera overhead times, a 2048 x 2048 subimage centered on the target will be readout from WFC1 (Table 6.2).

Occasionally observers desire non-polarized images of targets at the same location on the detector as their polarized images. Doing so was straightforward with the HRC; one merely had to take an exposure without the polarizer in place. However, WFC polarimetry automatically invokes a large slew from the non-polarimetric imaging position. To obtain a non-polarized image at the same physical detector location as the polarized images, one must specify the WFC1-2K aperture instead of the WFC aperture (Table 6.2).

Table 6.2: Examples of polarizer and non-polarizer exposures in a Phase II proposal.

Aperture	Filters	Comment
HRC	F606W, POL0V	1024 x 1024 image centered at usual `HRC` aperture.
HRC	F606W, POL60V	Same but with `POL60V`.
HRC	F606W, POL120V	Same but with `POL120V`.
HRC	F606W	Non-polarizer image centered at same detector location as polarizer exposure.
WFC	F606W, POL0V	Target automatically placed at WFC1 pixel (3096,1024); 2048 x 2048 image.
WFC	F606W, POL60V	Same but with `POL60V`.
WFC	F606W, POL120V	Same but with `POL120V`.
WFC1-2K	F606W	Non-polarizer image at same detector location. Target at WFC1 pixel (3096,1024); 2048 x 2048 image.

Table 6.1 lists the filters for which imaging polarimetry is available. STScI provides polarimetric calibration for the most popular of these filters. Filters not listed will not be calibrated, so users desiring imaging polarimetry in those bandpasses must include the necessary calibrations in their proposals.

6.1.4 Challenges and Limitations of ACS Polarimetry

The most accurate ACS polarimetry was obtained in the visible bands (i.e., F606W) with the HRC and POLV polarizers. This mode had the advantage of very high rejection of perpendicular polarization and known mirror coatings with readily modeled properties. Because the WFC mirror coatings are proprietary, models of their polarization properties (e.g., the phase retardance of the IM3 mirror) are unavailable. Consequently, calibrating WFC polarized images is much more difficult than calibrating the HRC images.

UV polarimetry with ACS is challenging because the POLUV polarizers have relatively poor orthogonal rejection and the instrumental polarization of the HRC, which was 4% to 7% in the visible, rose to 8% to 9% in the UV and reached 14% at 2200 Å (see ACS ISR 2004-09). Far-UV polarimetry is especially challenging because the POLUV properties are not well-characterized shortwards of 2800 Å, and they appear to change rapidly with wavelength. Moreover, the low UV transmission of the POLUV polarizers and the poor rejection in the far-red exacerbate the red leaks seen in the far-UV spectral filters.

The polarizers contribute a weak geometric distortion that rises to about 0.3 pixels near the edges of the HRC field-of-view. This distortion is caused by a weak positive lens in the polarizers that is needed to maintain proper focus when multiple filters are in the beam. The POLV polarizers also have a weak ripple structure intrinsic to their polaroid coatings. These ripples contribute an additional ±0.3 pixel distortion with a very complex structure (see ACS ISR 2004-10 and ACS ISR 2004-11). All these geometric effects are correctable with the drizzle software. However, astrometry will be less accurate with the polarizers because of residual errors and imperfect corrections.

Finally, the POL0V and POL60V filters contain bubbles which impact the PSF and flat fields. These bubbles are far out of focus and appear as large concentric bright and dark rings (400 pixels diameter in WFC, 370 pixels in HRC) and streaks in the flat fields. The worst case appeared in HRC POL60V images, where the amplitude of the artifacts reaches ±4% in the flats and the affected region was roughly centered at pixel (835,430). Polarimetric combinations involving POL0V or the WFC are relatively minor, with typical amplitudes of ±1%. Observers requiring precision polarimetry should avoid these regions of the field of view. Although the polarizer flats attempt to correct these features (see ACS ISR 2005-10), the corrections are imperfect and dependent on the brightness and angular size of the target. The locations of these features and their effects can be discerned more accurately by examining the P-flats for the respective spectral filter crossed with the visual polarizers.

6.2 Coronagraphy

Coronagraphy with ACS is unavailable because the HRC has been unavailable since January 2007. The information related to the HRC is provided for archival purposes only.

The ACS High Resolution Camera has a user-selectable coronagraphic mode for imaging faint objects (circumstellar disks, substellar companions) near bright point sources (stars or luminous quasar nuclei). The coronagraph suppresses the diffraction spikes and rings of the occulted source below the level of the scattered light, most of which is caused by surface errors in the *HST* optics. The coronagraph was added after ACS construction began, at which point it was impossible to insert it into the aberration-corrected beam. Instead, the system is deployed into the aberrated beam, which is subsequently corrected by the ACS optics. Although it is not as efficient as a corrected-beam coronagraph (especially for imaging close to the occulted source) the HRC coronagraph significantly improves the high-contrast imaging capabilities of *HST*. Care must be taken, however, to design an observation plan that properly optimizes the coronagraph's capabilities and accounts for its limitations.

6.2.1 Coronagraph Design

A schematic layout of the ACS coronagraph is shown in Figure 6.2. The aberrated beam from the telescope first encounters one of two occulting spots. The beam continues to the M1 mirror, which forms an image of the *HST* entrance pupil on the M2 mirror, which corrects for the spherical aberration in the *HST* primary mirror. The coronagraph's Lyot stop is placed in front of M2. A fold mirror directs the beam onto the CCD detector. The field is 29 x 26 arcseconds with a mean scale of 0.026 arcseconds/pixel. Geometric distortion results in effectively non-square pixels. The coronagraph can be used over the entire HRC wavelength range of λ = 2000 Å to 10,000 Å using a variety of broad-to-narrowband filters.

The occulting spots are placed in the plane of the circle of least confusion of the converging aberrated beam. The balance of defocus and spherical aberration at this location allows maximal occulted flux and minimal spot radius. The angular extent of the PSF in this plane necessitates larger spots than would be used in an unaberrated beam Figure 6.3.

Figure 6.2: Schematic layout of the ACS HRC coronagraph. The upper left inset shows a schematic of the coronagraph mechanism that can be flipped in-and-out of the HRC optical path.

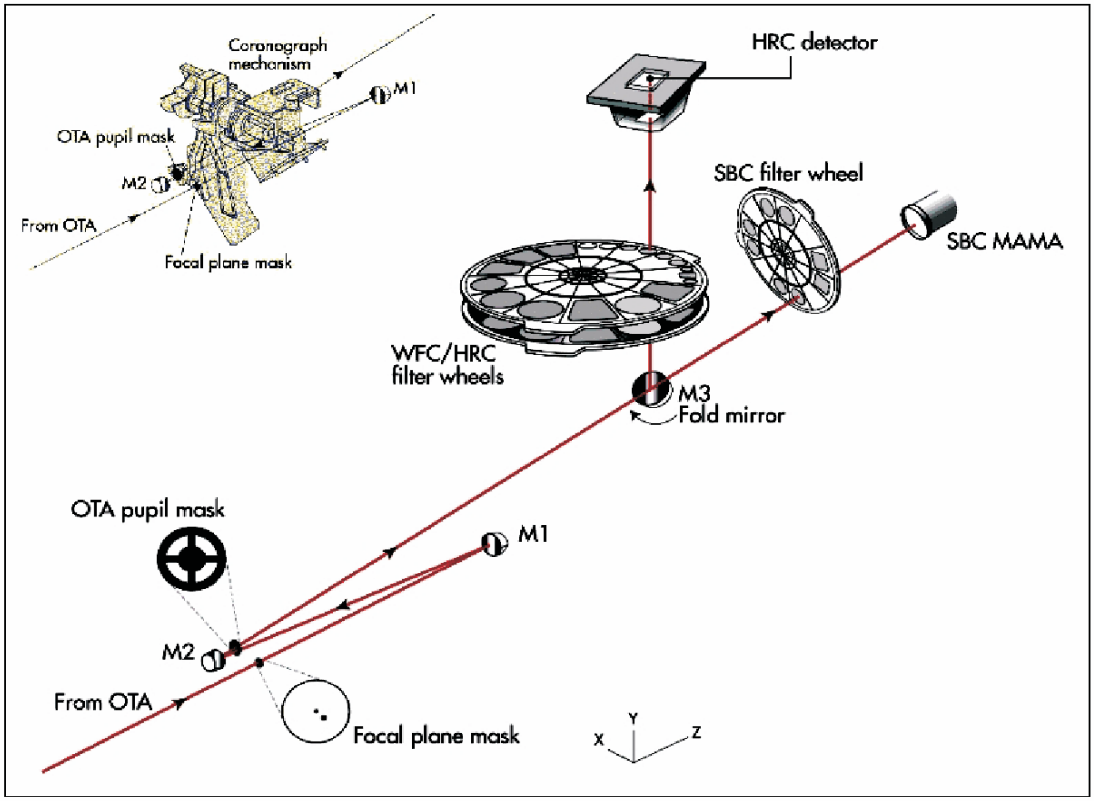

Figure 6.3: Simulated point spread functions at the plane of the occulting spots. For filters `F435W` and `F814W`, shown with logarithmic intensity scaling. The elliptical, cross-shaped patterns in the cores are due to astigmatism at the off-axis ACS aperture. The astigmatism is corrected later by the ACS optics. The sizes of the two occulting spots (D=1.8 arc seconds and 3.0 arc seconds) are indicated by the white circles.

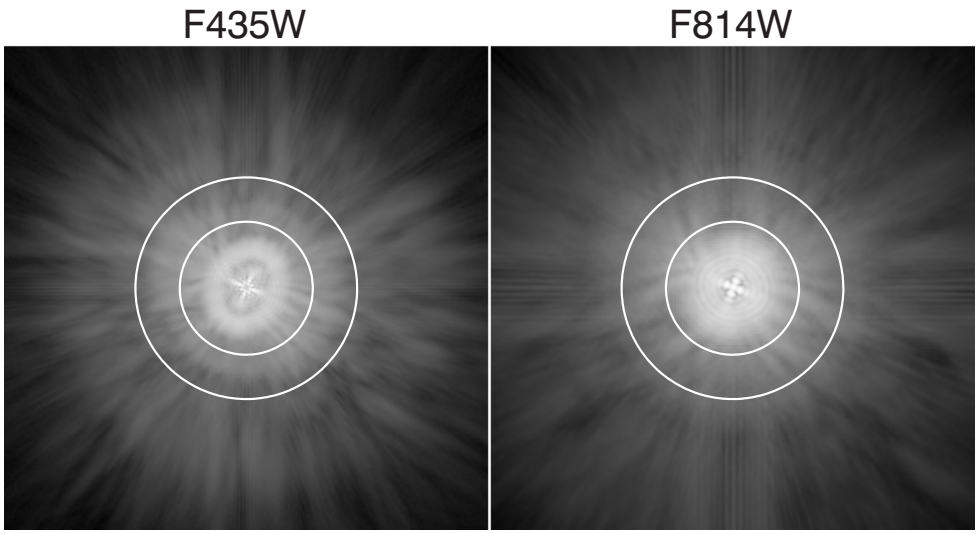

The occulting spots are solid (unapodized) metallic coatings deposited on a glass substrate that reduces the throughput by 4.5%. The smaller spot is 1.8 arcseconds in diameter and is at the center of the field. Its aperture name is `CORON-1.8`. The second spot, 3.0 arcseconds in diameter, is near the edge of the field (Figure 6.4) and is designated as aperture `CORON-3.0`. The smaller spot is used for the majority of the coronagraphic observations, as it allows imaging closer to the occulted source. The larger spot may be used for very deep imaging of bright targets with less saturation around the spot than would occur with the smaller spot. Its position near the edge of the field also allows imaging of material out to 20 arcseconds from the occulted source.

The Lyot stop is located just in front of the M2 aberration correction mirror, where an image of the *HST* primary is formed. The stop is a thin metal mask that covers all of the diffracting edges in the *HST* OTA (outer aperture, secondary mirror baffle, secondary mirror support vanes, and primary mirror support pads) at the reimaged pupil. The sizes of the Lyot stop and occulting spots were chosen to reduce the diffracted light below the level of the scattered light, which is unaltered by the coronagraph. The smaller aperture and larger central obscuration of the Lyot stop reduce the throughput by 48% and broaden the field PSF. The spots and Lyot stop are located on a panel attached to the ACS calibration door mechanism, which allows them to be flipped out of the beam when not in use. The inside surface of this door can be illuminated by a lamp to provide flat field calibration images for direct imaging. However, this configuration prevents the acquisition of internal coronagraphic flat fields.

In addition to the occulting spots and Lyot stop there is a 0.8 arcseconds x 5 arcseconds occulting finger (`OCCULT-0.8`) permanently located at the window of the CCD dewar. It does not suppress any diffracted light because it occurs after the Lyot stop. Its intended purpose was to allow imaging closer to stars than is possible with the occulting spots while preventing saturation of the detector. However, because the finger is located some distance from the image plane, there is significant vignetting around its edges, which reduces its effectiveness. It was originally aligned with the center of the 3.0 arcsecond spot, but shifting of the spots during launch ultimately placed the finger near the edge of the spot. Because of vignetting and the sensitivity of the occulted PSF to its position behind the finger, unocculted saturated observations of sources will likely be more effective than those using the occulting finger.

Figure 6.4: Region of the Orion Nebula imaged with the coronagraph and filter F606W.

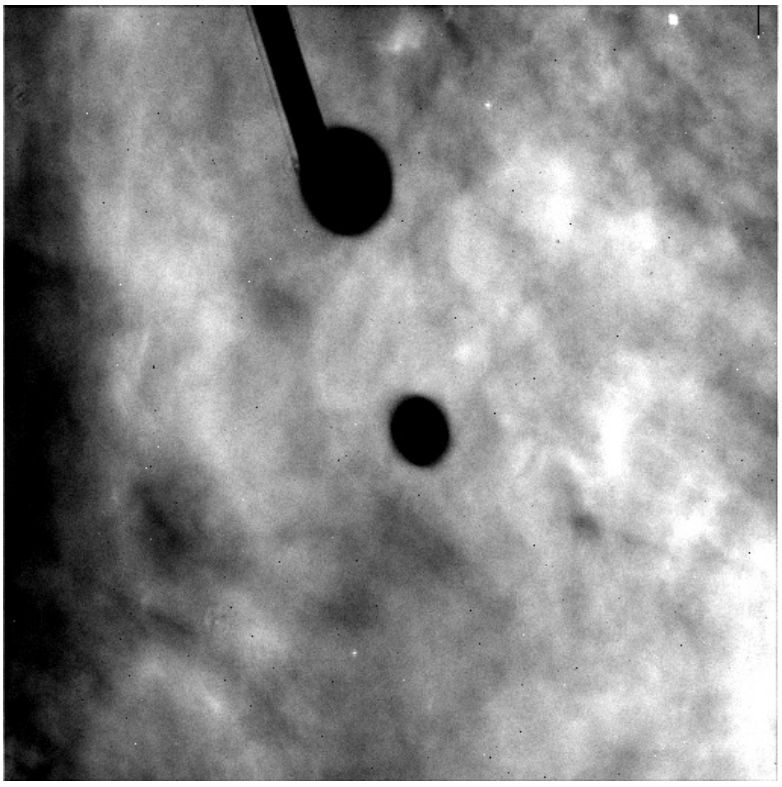

The silhouettes of the occulters can be seen against the background nebulosity. The 1.8 arc second spot is located at the center and the 3.0 arc second spot towards the top. The finger is aligned along one edge of the larger spot. This image has not been corrected for geometric distortion, so the spots appear elliptical.

6.2.2 Acquisition Procedure and Pointing Accuracy

The bright point source must be placed precisely behind the occulting spot to ensure the proper suppression of the diffracted light. The absolute pointing accuracy of *HST* is about 1 arcsecond, which is too crude to ensure accurate positioning behind the spot. An on-board acquisition procedure is used to provide better alignment. The observer must request an acquisition image immediately before using the coronagraph and must specify a combination of filter and exposure time that provides an unsaturated image of the source. To define an acquisition image in APT, specify HRC-ACQ as the aperture and ACQ as the *opmode*.

Acquisition images are taken with the coronagraph deployed. The bright source is imaged within a predefined 200 x 200 pixel (5 x 5 arcseconds) subarray near the small occulting spot. Two identical exposures are taken, each of the length specified by the observer (rather than each being half the length specified, as they would be for a conventional CR-SPLIT). From these two images, the on-board computer selects the minimum value for each pixel as a crude way of rejecting cosmic rays. The result is then smoothed with a 3 x 3 pixel boxcar and the maximum pixel in the subarray is identified. The centroid of the unsmoothed image is then computed within a 5 x 5

pixel box centered on this pixel. Based on this position, the telescope is then slewed to place the source behind the occulting spot.

Because the coronagraph is deployed during acquisition, throughput is decreased by 52.5% relative to a non-coronagraphic observation. Also, the Lyot stop broadens the PSF, resulting in a lower relative peak pixel value (see Section 6.2.6). Care must be taken to select a combination of exposure time and filter that avoids saturating the source but provides enough flux for a good centroid measurement. A peak pixel flux of 2000 e^- to 50,000 e^- is desirable. The HRC saturation limit is ~140,000 e^-. Narrowband filters can be used, but for the brightest targets crossed filters are required. Allowable filter combinations for acquisitions are F220W+F606W, F220W+F550M, and F220W+F502N, in order of decreasing throughput. Be warned that the calibration of these filter combinations is poor, so estimated count rates from ***synphot***[1] or the ETC may be high or low by a factor of two.

Multiple on-orbit observations indicate that the combined acquisition and slew errors are on the order of ±0.25 pixels (±6 milliarcseconds). While small, these shifts necessitate the use of subpixel registration techniques to subtract one coronagraphic PSF from another (Section 6.2.5). The position of the spots relative to the detector also varies over time. This further alters the PSF, resulting in subtraction residuals.

6.2.3 Vignetting and Flat Fields

ACS coronagraphic flat fields differ from the standard flats because of the presence of the occulting spots and alteration of the field vignetting by the Lyot stop. The large angular size of the aberrated PSF causes vignetting beyond one arcsecond of the spot edge (Figure 6.4), which can be corrected by dividing the image by the spot pattern (Figure 6.5). To facilitate this correction, separate flat fields have been derived that contain just the spot patterns (spot flats) and the remaining static features (P-flats). For a full discussion see ACS ISR 2004-16.

The ACS data pipeline will divide images by the P-flat. P-flats specific to the coronagraph have been derived from either ground-based or on-orbit data for filters F330W, F435W, F475W, F606W, and F814W. Other filters use the normal flats, which may cause some small-scale errors around dust diffraction patterns. The pipeline then divides images by the spot flat, using a table of spot positions versus date to determine the proper shift for the spot flat. However, there is a lag in determining the spot position, so it may be a month after the observation before the pipeline knows where the spot was on that date. So, coronagraph users should note that their data may be calibrated with an incorrect spot flat if they extract their data from the archive soon after they were taken. (Spot flats for the filters listed above are available for download from the ACS reference files Web page. For other filters, the available spot flat closest in wavelength should be used. The spot flat must be shifted by an amount listed on the reference files page to account for motions of the occulting spots.)

1. Synphot will soon be replaced by the pysynphot package, a significantly improved re-implementation of synphot written in Python. Please visit the pysynphot Web page at http://stsdas.stsci.edu/pysynphot.

Because coronagraphic P-flats and spot flats exist only for the few filters listed above, observers are encouraged to use those filters. It is unlikely that coronagraphic flat fields for other filters will be available in the future.

Figure 6.5: Region of the Orion Nebula around the D = 1.8 arc seconds spot.

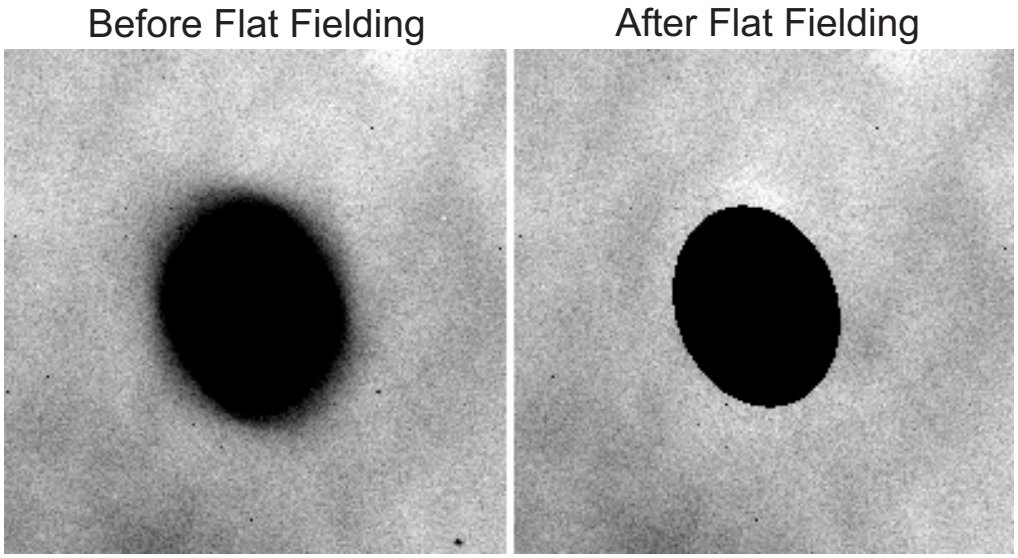

(Left) The spot edge appears blurred due to vignetting. The image has not been geometrically corrected. (Right) The same region after the image has been corrected by dividing by the flat field. The interior of the spot has been masked

6.2.4 Coronagraphic Performance

Early in Cycle 11, coronagraphic performance verification images were taken of the V = 0 star Arcturus (Figure 6.6 and Figure 6.7). This star has an angular diameter of 25 milliarcseconds and is thus unresolved by the coronagraph. The coronagraphic image of a star is quite unusual. Rather than appearing as a dark hole surrounded by residual light, as would be the case in an aberration-free coronagraph, the interior of the spot is filled with a diminished and somewhat distorted image of the star. This image is caused by the M2 mirror's correction of aberrated light from the star that is not blocked by the spot. The small spot is filled with light, while the large one is relatively dark. Broad, ring-like structures surround the spots, extending their apparent radii by about 0.5 arcseconds. These rings are due to diffraction of the wings of the aberrated PSF by the occulting spot itself. Consequently, coronagraphic images of bright stars may saturate at the interior and edges of the spot within a short time. Within the small spot, the brightest pixels will saturate in less than one second for a V = 0.0 star, while pixels at edge of the larger spot will saturate in about 14 seconds.

The measured radial surface brightness profiles (Figure 6.8) show that the coronagraph is well aligned and operating as expected. The light diffracted by the *HST* obscurations is suppressed below the level of the scattered light – there are no prominent diffraction spikes, rings, or ghosts beyond the immediate proximity of the spots. At longer wavelengths ($\lambda > 6000$ Å) the diffraction spikes appear about as

bright as the residual scattered light because the diffraction pattern is larger and not as well suppressed by the coronagraph. The spikes are more prominent in images with the large spot than the small one because the Lyot stop is not located exactly in the pupil plane but is slightly ahead of it. Consequently, the beam can "walk" around the stop depending on the field angle of the object. Because the large spot is at the edge of the field, the beam is slightly shifted, allowing more diffracted light to pass around the edges of the stop.

The coronagraphic PSF is dominated by radial streaks that are caused primarily by scattering from zonal surface errors in the *HST* mirrors. This halo increases in brightness and decreases in size towards shorter wavelengths. One unexpected feature is a diagonal streak or "bar" seen in both direct and coronagraphic images. It is about 5 times brighter than the mean azimuthal surface brightness in the coronagraphic images. This structure was not seen in the ground-test images and is likely due to scattering introduced by the *HST* optics. There appears to be a corresponding feature in STIS as well.

Figure 6.6: Geometrically corrected (29 arc seconds across) image of Arcturus observed in `F814W` behind the 1.8 arc seconds spot. This is a composite of short, medium, and long (280 seconds) exposures. The "bar" can be seen extending from the upper left to lower right. The shadows of the occulting finger and large spot can be seen against the scattered light background. Logarithmic intensity scale.

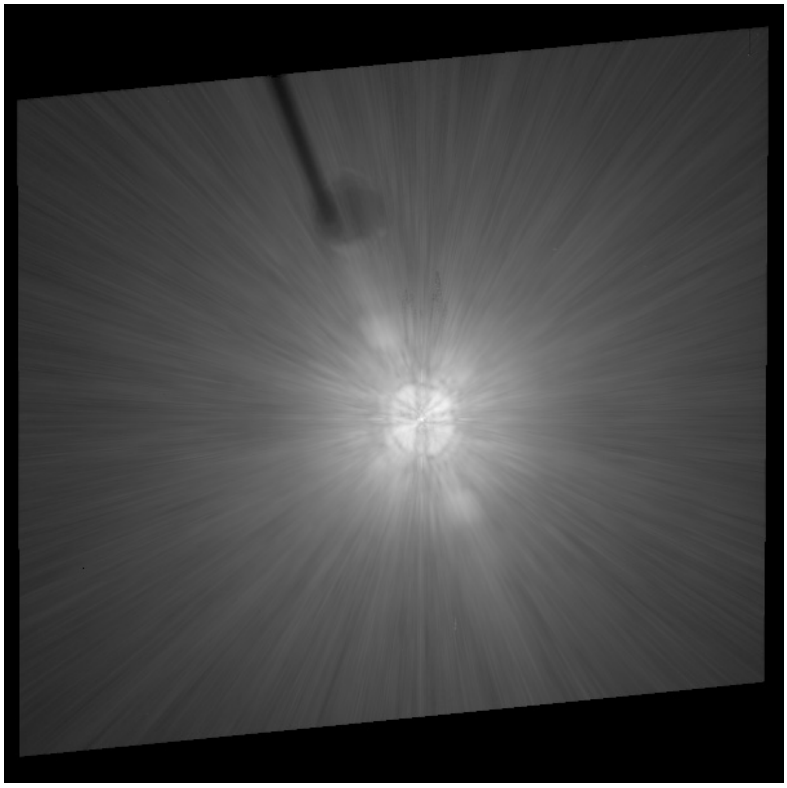

Figure 6.7: Regions around the occulting spots in different filters. The occulting finger can be seen in the 3 arc seconds spot images. Logarithmic intensity scaled.

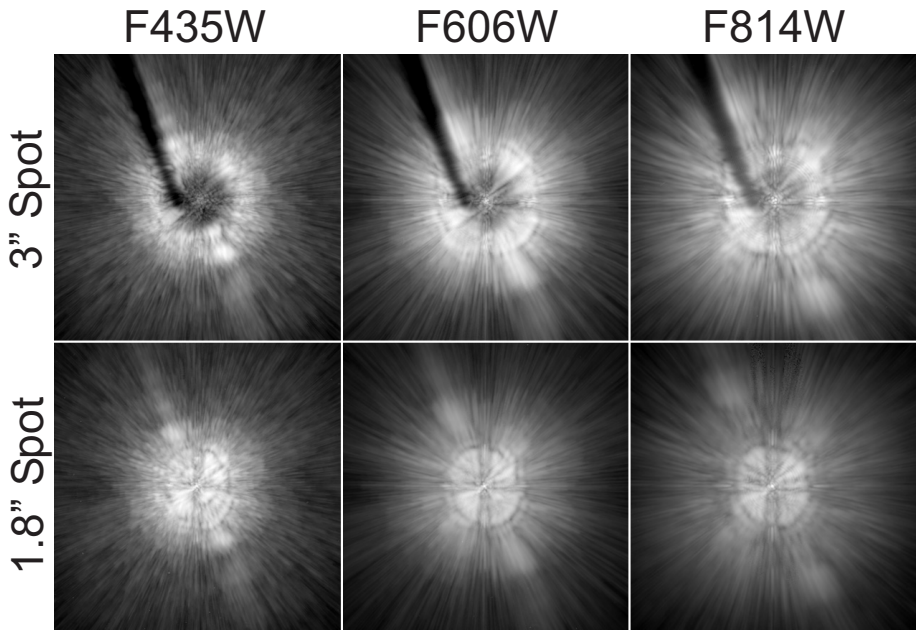

6.2.5 Subtraction of the coronagraphic PSF

While the coronagraph suppresses the diffracted light from a bright star, the scattered light still overwhelms faint, nearby sources. It is possible to subtract most of the remaining light using an image of another occulted star. PSF subtraction has been successfully used with images taken by other *HST* cameras, with and without a coronagraph. The quality of the subtraction depends critically on how well the target and reference PSFs match.

As mentioned above, for any pair of target and reference PSF observations, there is likely to be a difference of 5 to 20 milliarcseconds between the positions of the stars. Because the scattered light background is largely insensitive to small errors in star-to-spot alignment (it is produced before the coronagraph), most of it can be subtracted if the two stars are precisely registered and normalized. Due to the numerous sharp, thin streaks that form the scattered light background, subtraction quality is visually sensitive to registration errors as small as 0.03 pixels (0.75 milliarcseconds). To achieve this level of accuracy, the reference PSF may be iteratively shifted and subtracted from the target until an offset is found where the residual streaks are minimized. This method relies on the judgment of the observer, as any circumstellar material could unexpectedly bias a registration optimization algorithm. A higher-order sampling method, such as cubic convolution interpolation, should be used to shift the reference PSF by subpixel amounts; simpler schemes such as bilinear interpolation degrade the fine PSF structure too much to provide good subtractions.

Figure 6.8: Surface brightness plots derived by computing the median value at each radius. The brightness units are relative to the total flux of the star. The direct profile is predicted; the coronagraphic profiles are measured from on-orbit images of Arcturus. The label "Coronagraph-star" shows the absolute median residual level from the subtraction of images of the same star observed in separate visits.

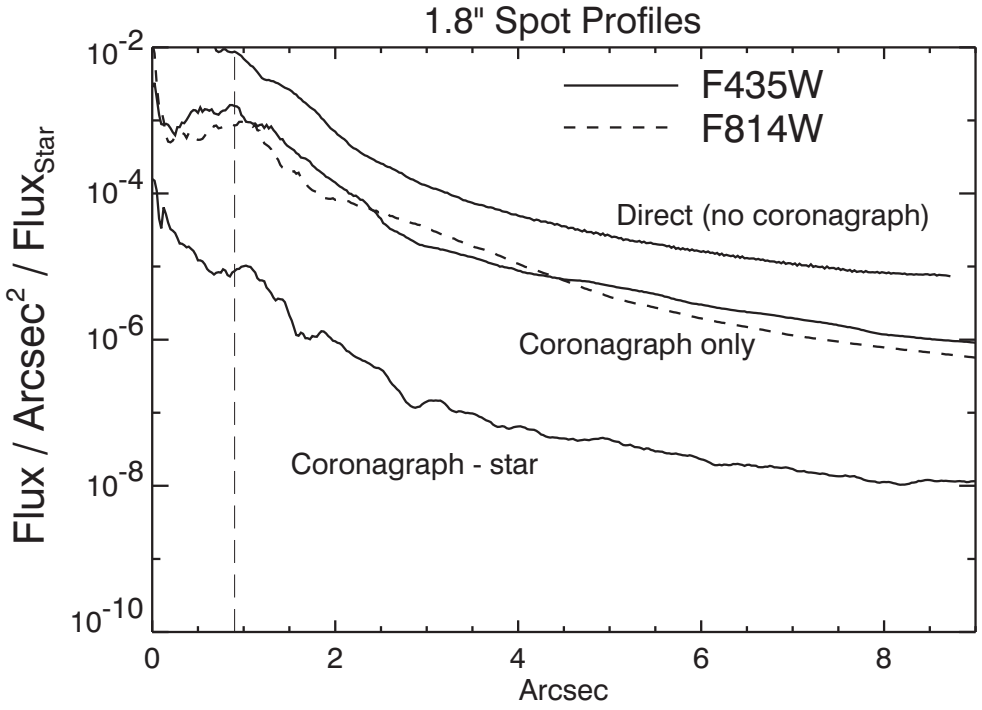

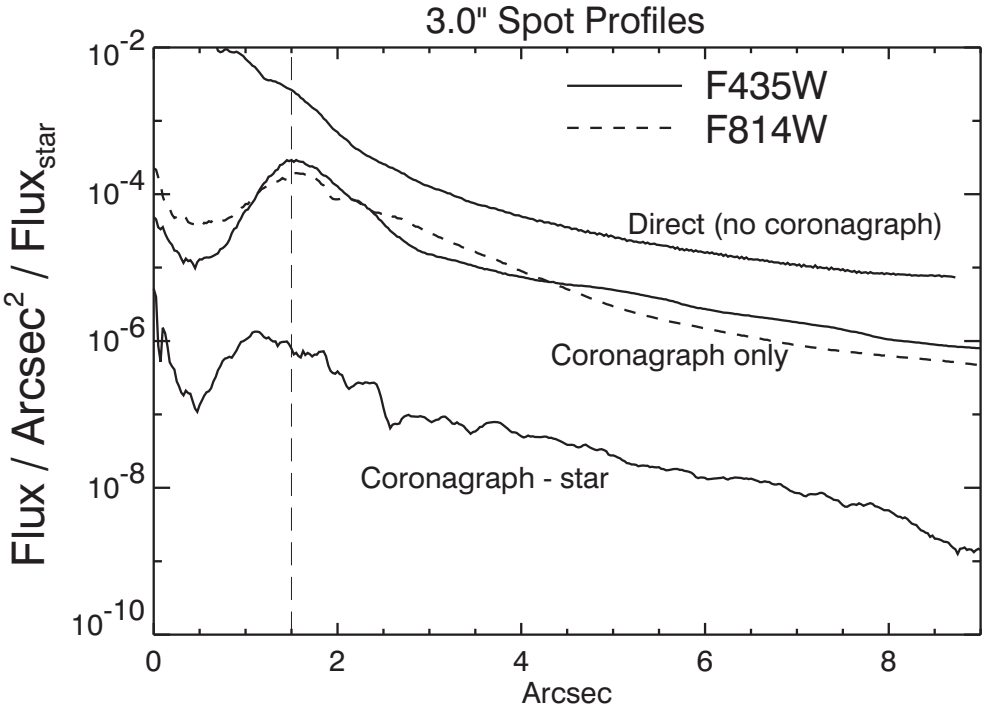

Normalization errors as small as 1% to 4% between the target and reference stars may also create significant subtraction residuals. However, derivation of the normalization factors from direct photometry is often not possible. Bright, unocculted stars will be saturated in medium or broadband filters at the shortest exposure time (0.1 seconds). An indirect method uses the ratio of saturated pixels in unocculted images (the accuracy improves with greater numbers of saturated pixels). A last-ditch effort would rely on the judgment of the observer to iteratively subtract the PSFs while varying the normalization factor.

In addition to registration offsets, positional differences can alter the diffraction patterns near the spots' edges. The shape and intensity of these rings are very sensitive to the location of the star relative to the spot. They cannot be subtracted by simply adjusting the registration or normalization. These errors are especially frustrating because they increase the diameter of the central region where the data are unreliable. The only solution to this problem is to observe the target and reference PSF star in adjacent orbits without flipping the masks out of the beam between objects.

Color differences between the target and reference PSFs can be controlled by choosing an appropriate reference star. As wavelength increases, the speckles that make up the streaks in the coronagraphic PSF move away from the center while their intensity decreases (Figure 6.7). The diffraction rings near the spot edges will expand as well. These effects can be seen in images through wideband filters – a red star will appear to have a slightly larger PSF than a blue one. Thus, an M-type star should be subtracted using a similarly red star – an A-type star would cause significant subtraction residuals. Even the small color difference between A0 V and B8 V stars, for example, may be enough to introduce bothersome errors (Figure 6.9).

A focus change can also alter the distribution of light in the PSF. *HST*'s focus changes over time scales of minutes to months. Within an orbit, the separation between the primary and secondary mirrors varies on average by 3 μm, resulting in 1/28 wave rms of defocus @ $\lambda = 5000$ Å. This effect, known as *breathing,* is caused by the occultation of the telescope's field of view by the warm Earth, which typically occurs during half of each 96-minute orbit. This heats *HST*'s interior structure, which expands. After occultation the telescope gradually shrinks. Changes relative to the sun (mostly anti-sun pointings) cause contraction of the telescope, which gradually expands to "normal" size after a few orbits. The main result of these small focus changes is the redistribution of light in the wings of the PSF (Figure 6.10).

Figure 6.9: Predicted absolute mean subtraction residual levels for cases where the target and reference stars have mismatched colors. The brightness units are relative to the total flux of the target star.

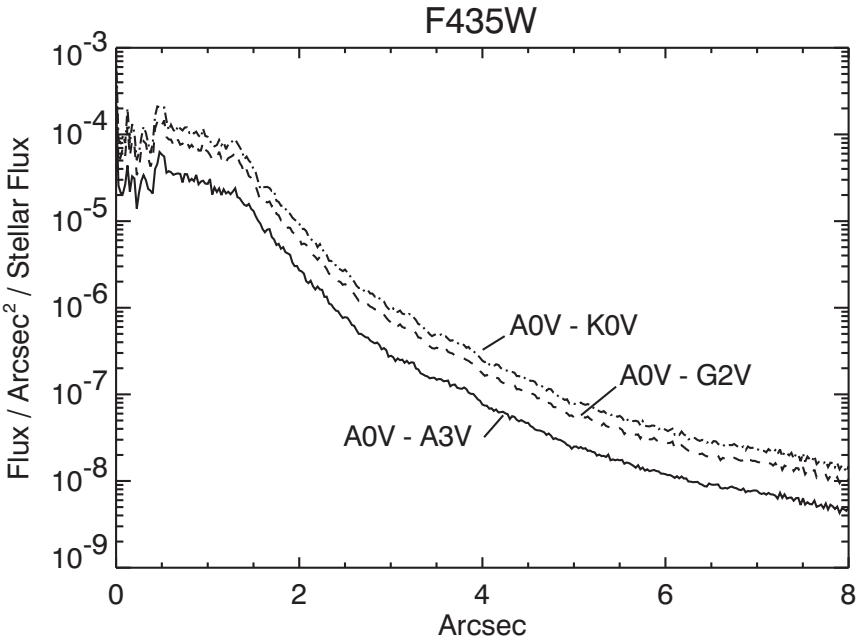

Figure 6.10: Predicted absolute mean subtraction residual levels for cases where the target and reference stars are imaged at different breathing-induced focus positions. The offset (0.75 or 2.5 mm) from perfect focus (0 mm) is indicated with respect to the change in primary-secondary mirror separation. The typical breathing amplitude is 3 to 4 mm within an orbit. The brightness units are relative to the total flux of the target star.

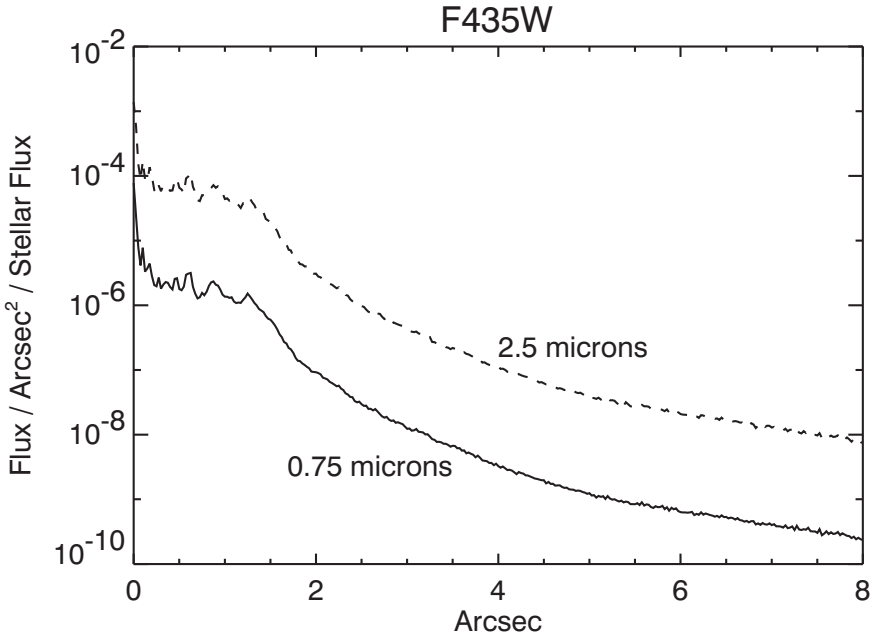

Plots of the azimuthal median radial profiles after PSF subtraction are shown in Figure 6.8. In these cases, images of Arcturus were subtracted from similar images of the star taken a day later. The images were registered as previously described. Combined with PSF subtraction, the coronagraph reduces the median background level by 250x to 2500x, depending on the radius and filter. An example of a PSF subtraction is shown in Figure 6.11. The mean of the residuals is not zero. Because of PSF mismatches, one image will typically be slightly brighter than the other over a portion of the field (Figure 6.12). The pixel-to-pixel residuals can be more than 10x greater than the median level (Figure 6.13). Note that these profiles would be worse if there were color differences between the target and reference PSFs.

One way to avoid both the color and normalization problems is to take images of the target at two different field orientations, and subtract one from the other. This technique, known as *roll subtraction*, can be done either by requesting a roll of the telescope about the optical axis (up to 30°) between orbits or by revisiting the target at a later date when the default orientation of the telescope is different. Roll subtraction only works when the nearby object of interest is not azimuthally extended. It is the best technique for detecting point source companions or imaging strictly edge-on disks (e.g. Beta Pictoris). It can also be used to reduce the pixel-to-pixel variations in the subtraction residuals by rotating and co-adding the images taken at different orientations. (This works for extended sources if another PSF star is used.) Ideally, the subtraction errors will decrease as the square root of the number of orientations.

The large sizes of the occulting spots severely limit how close to the target one can image. It may be useful to combine coronagraphic imaging with direct observations of the target, allowing the central columns to saturate. Additional observations at other rolls would help. PSF subtraction can then be used to remove the diffracted and scattered light.

Figure 6.11: Residual errors from the subtraction of one image of Arcturus from another taken in a different visit (filter = F435W, D = 1.8 arcseconds spot). The image is 29 arc seconds across and has not been geometrically corrected. Logarithmic intensity scaled.

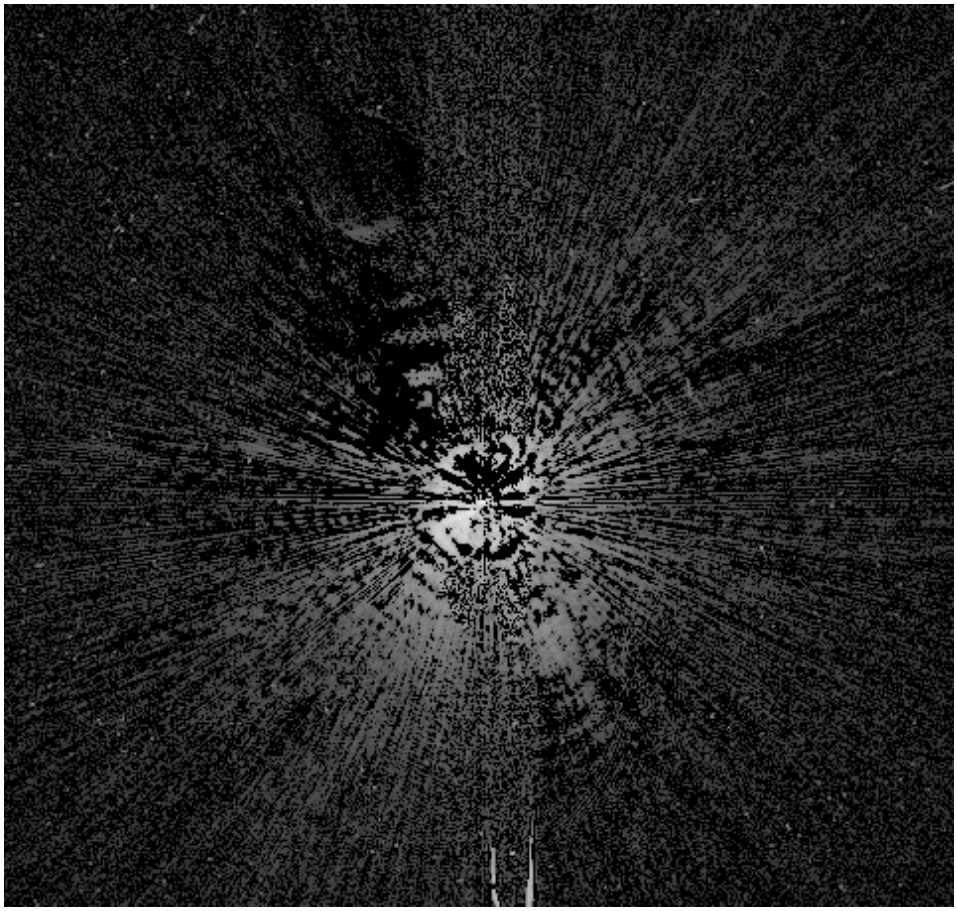

Figure 6.12: Subtraction of Arcturus from another image of itself taken during another visit using the large (D = 3.0 arc seconds) spot and `F435W` filter. The image has been rebinned, smoothed, and stretched to reveal very low level residuals. The broad ring at about 13 arc seconds from the star is a residual from some unknown source – perhaps it represents a zonal redistribution of light due to focus differences (breathing) between the two images. The surface brightness of this ring is 20.5 magnitudes/arcsecond^2 fainter than the star. The diameter, brightness, and thickness of this ring may vary with breathing and filter. The image has not been geometrically corrected.

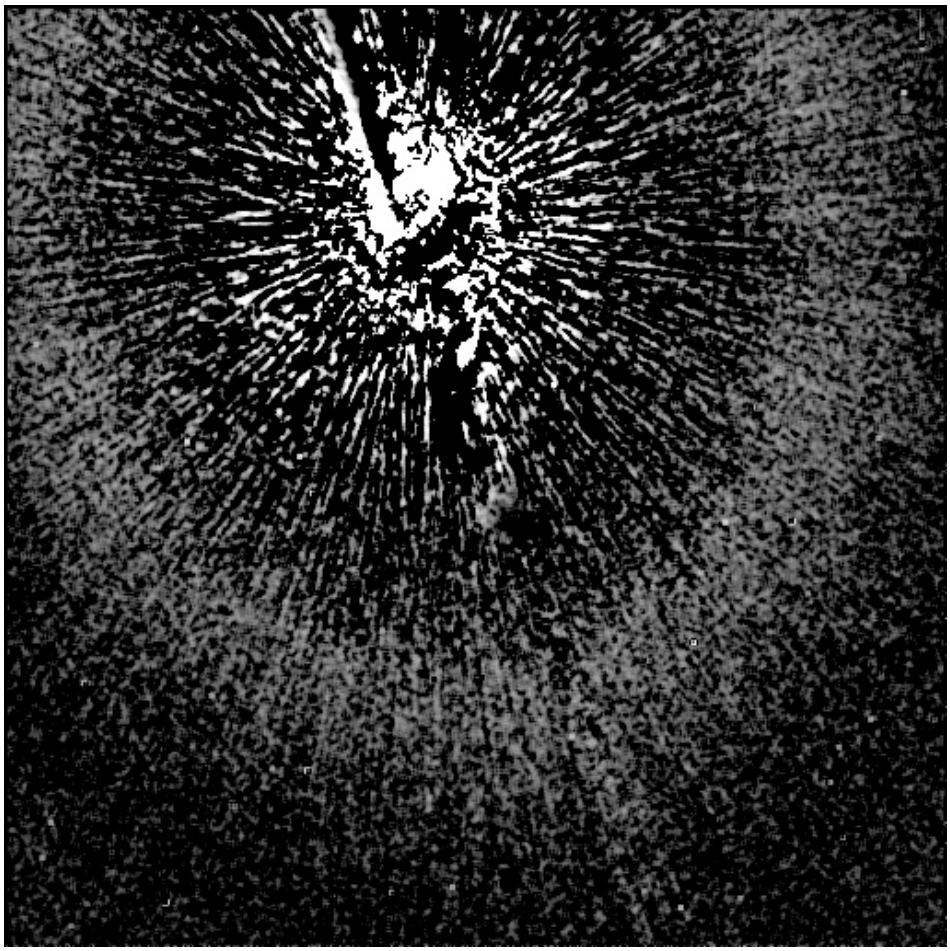

Figure 6.13: Plots of the azimuthal RMS subtraction residual levels at each radius for the large (3 arc seconds) spot. The flux units are counts per pixel relative to the total unocculted flux from the central source. These plots were derived from Arcturus-Arcturus subtractions represent the best results one is likely to achieve. The undistorted HRC scale assumed here is 25 milli arc seconds/pixel.

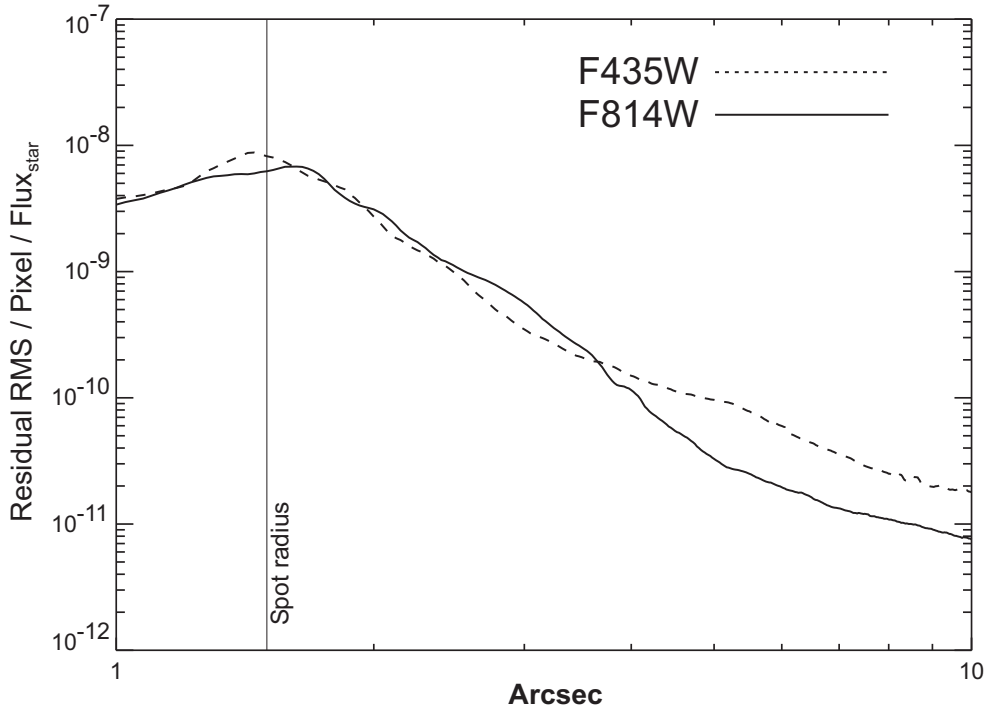

6.2.6 The Off-Spot PSF

Objects that are observed in the coronagraphic mode but that are not placed behind an occulting mask have a PSF that is defined by the Lyot stop. Because the stop effectively reduces the diameter of the telescope and introduces larger obscurations, this "off-spot" PSF is wider than normal, with more power in the wings and diffraction spikes (Figure 6.14). In addition, the Lyot stop and occulting spot substrate reduce the throughput by 52.5%. In F814W, the "off-spot" PSF has a peak pixel containing 4.3% of the total (reduced) flux and a sharpness (including CCD charge diffusion effects) of 0.010. (Compare these to 7.7% and 0.026, respectively, for the normal HRC PSF.) In F435W, the peak is 11% and the sharpness is 0.025 (compared to 17% and 0.051 for the normal F435W PSF). Observers need to take the reduced throughput and sharpness into account when determining detection limits for planned observations. Tiny Tim can be used to compute off-spot PSFs.

Figure 6.14: Image of Arcturus taken in coronagraphic mode with the star placed outside of the spot. The coronagraphic field PSF has more pronounced diffraction features (rings and spikes) than the normal HRC PSF due to the effectively larger obscurations introduced by the Lyot stop. The central portion of this image is saturated. It was taken through a narrowband filter (F660N) and is not geometrically corrected.

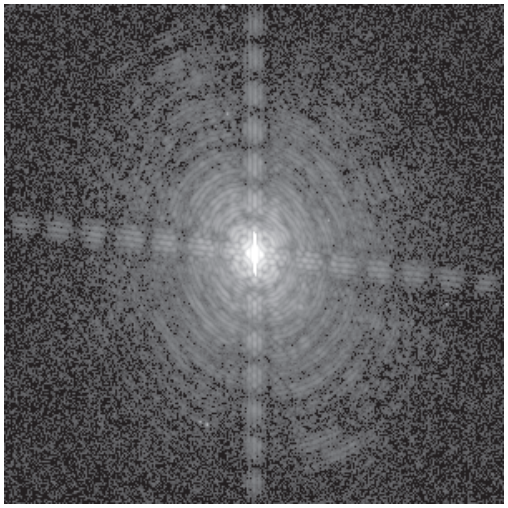

6.2.7 Occulting Spot Motions

STScI measures the positions of the occulting spots at weekly intervals using Earth flats. These measurements show that the spots move over daily to weekly time scales in an unpredictable manner. The cause of this motion is unknown. The spot positions typically vary by ~0.3 pixels (8 milliarcseconds) over one week, but they occasionally shift by 1 to 5 pixels over 1 to 3 weeks. During a single orbit, however, the spots are stable to within +/- 0.1 pixel when continuously deployed and they recover their positions within +/- 0.25 pixel when repeatedly stowed and deployed.

After the acquisition exposure, a coronagraphic target is moved to a previously measured position of an occulting spot. Unfortunately, ACS's configuration prevents automatic determination of the spot's position before a coronagraphic exposure, as can be done with NICMOS. Furthermore, unlike STIS, the target cannot be dithered until the flux around the occulter is minimized. Instead, STScI uploads the latest measured spot positions (which may be several days old) a few orbits before each coronagraphic observation. After acquisition, the target is moved to this appropriate spot position via a USE OFFSET special requirement. This procedure adds approximately 40 seconds to each visit and is required for all coronagraphic observations.

The uncertainties in the day-to-day spot positions can cause star-to-spot registration errors that affect coronagraphic performance. If the star is offset from the spot center by more than 3 pixels, then one side of the coronagraphic PSF will be brighter than expected and may saturate earlier than predicted. A large offset will also degrade the coronagraphic suppression of the diffraction pattern. Most importantly, slight changes in the spot positions can alter the coronagraphic PSFs of the target and reference stars enough to cause large PSF-subtraction residuals. Consequently, an observer cannot rely on reference PSFs obtained from other programs or at different times.

To reduce the impact of spot motion, observers should obtain a reference PSF in an orbit immediately before or after their science observation. A single reference PSF can be used for two science targets if all three objects can be observed in adjacent orbits and they have similar colors. (Note that SAA restrictions make it difficult to schedule programs requiring more than five consecutive orbits.) Otherwise, each target will require a distinct reference PSF. Additional orbits for reference PSFs must be included in the Phase 1 proposal.

6.3 Grism/Prism Spectroscopy

HRC has been unavailable since January 2007. Information about the HRC is provided for archival purposes.

The ACS filter wheels include four dispersing elements for low resolution slitless spectroscopy over the field of view of the three ACS channels. One grism (G800L) provides low resolution spectra from 5500 Å to 10,500 Å for both the WFC and HRC. A prism (PR200L) in the HRC covered 1700 Å to beyond 3900 Å, although reliable wavelength and flux calibration was guaranteed only up to 3500 Å. In the SBC a LiF prism (PR110L) covers the range 1150 Å to ~1800 Å and a CaF_2 prism (PR130L) is useful from 1250 Å to ~1800. The grism provides first order spectra with almost constant dispersion as a function of wavelength but with second order overlap beyond ~10,000 Å. The prisms have non-linear dispersion with maximum resolution at shorter wavelengths and much lower resolving power at longer wavelengths. Table 6.3 summarizes the essential features of the four ACS dispersers in the five supported modes.

Table 6.3: Optical parameters of ACS dispersers.

Disperser	Channel	Wavelength range (Å)	Resolving power	Å/pixel	Tilt[1] (deg)
G800L	WFC	1st order: 5500 to 10500	100 @ 8000 Å	39.8[2]	-2
G800L	WFC	2nd order: 5000 to 8500	200 @ 8000 Å	20.7[2]	-2
G800L	HRC	1st order: 5500 to 10500	140 @ 8000 Å	23.9[3]	-38
G800L	HRC	2nd order: 5500 to 8500	280 @ 8000 Å	12.0[3]	-38
PR200L	HRC	1700 to 3900	59 @ 2500 Å	21.3	-1
PR110L	SBC	1150 to 1800	79 @ 1500 Å	9.5	0
PR130L	SBC	1250 to 1800	96 @ 1500 Å	7.8	0

1. Tilt with respect to the positive X-axis of the data frame.
2. The dispersion varies over the field by ±11%; the tabulated value refers to the field center.
3. The dispersion varies over the field by ±2%; the tabulated value refers to the field center.

6.3.1 WFC G800L

The G800L grism provides two-pixel resolving power from 69 (at 5500 Å) to 131 (at 10,500 Å) for first order spectra over the whole accessible WFC field of 202 x 202 square arc seconds. Figure 6.15 shows the wavelength range and sensitivity for the zeroth, first, and second order WFC spectra. Figure 6.16 shows the same plot as a function of pixel range, where pixel 0 is the position of the direct image.

Figure 6.17 shows the full G800L spectrum of the white dwarf GD153 (V=13.35 mag) obtained in one 60 second exposure. The first order is contaminated by the second order beyond ~10,000 Å. The total flux in the zeroth order is 2.5% of that in the first order, so locating the zeroth order is a less effective method of obtaining the wavelength zero point of weak spectra than using a matched pair of direct and grism images. The third and fourth orders contain about 1% of the flux in the first order, and the negative orders contain about 0.5% of that flux. When bright objects are observed, the signal in fainter orders may be mistaken for the spectra of fainter objects. In crowded fields, many spectral orders from different objects may overlap.

Table 6.3 lists the linear dispersion for the first and second order spectra, but their dispersions are better described with second order fits (ISR ACS 2005-08). Because the grism is tilted with respect to the optical axis, the wavelength solutions are field dependent. This dependence has been calibrated within 0.5 pixels over the whole field; the linear dispersion varies by ±11% from center to corner. The full extent of the spectrum of a bright source (orders -2, -1, 0, 1, 2, 3) is 1200 pixels (60 arcseconds). The higher spectral orders are not in focus, so their spectral resolutions are smaller than expected from their nominally higher dispersions.

Figure 6.15: Sensitivity versus wavelength for WFC G800L.

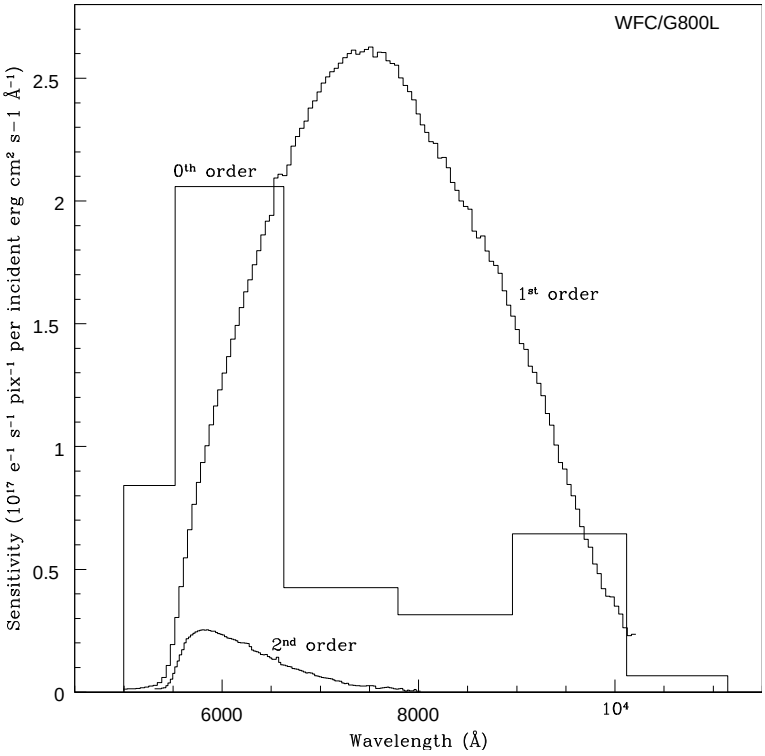

Figure 6.16: Sensitivity versus pixel position for WFC G800L.

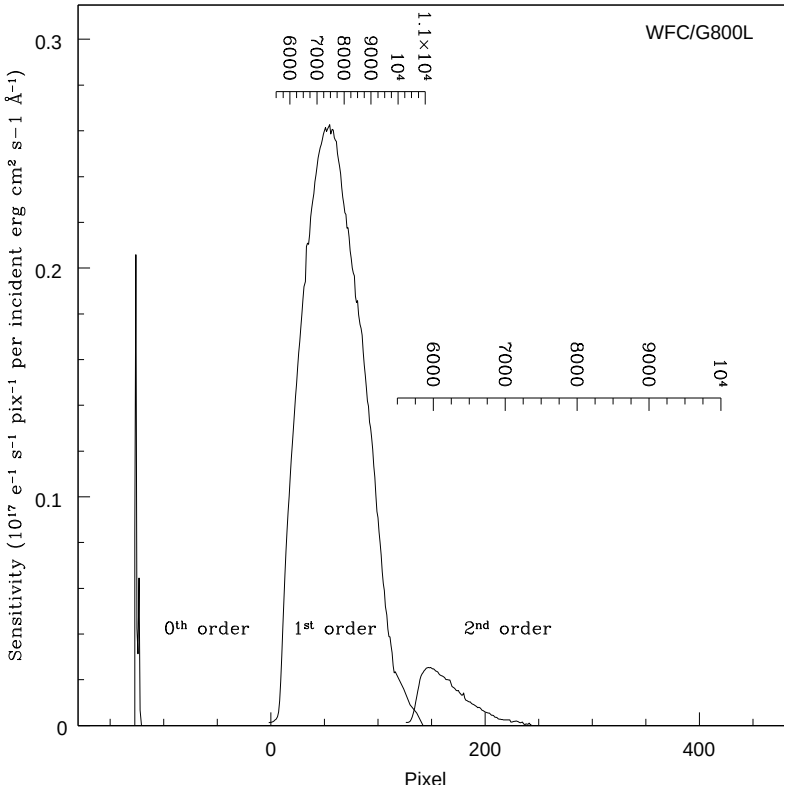

Figure 6.17: Fully dispersed spectrum for white dwarf GD153 with WFC/G800L. The numbers indicate the different grism orders.

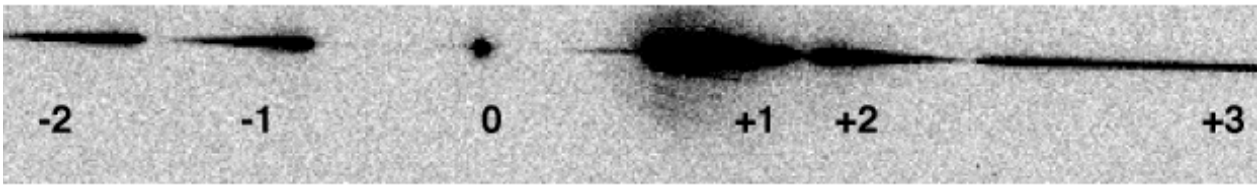

6.3.2 HRC G800L

G800L provided higher spatial resolution with the HRC than with the WFC, but the spectra were tilted at −38° with respect to the HRC's X axis. Figure 6.18 and Figure 6.19 show the ranges and sensitivities of the zeroth, first, and second orders as a function of wavelength and pixel, respectively. Figure 6.20 shows the spectrum of the standard star GD153. Orders -1 through +2 span about 70% of the 1024 detector columns, and the +2 order overlaps the +1 order beyond ~9500 Å. The dispersion varies by ±2% from the center to the corners of the detector. Because of the HRC's limited FOV, many G800L spectra were truncated by the edges of the detector or originated from objects located outside the corresponding direct image.

Figure 6.18: Sensitivity versus wavelength for HRC G800L.

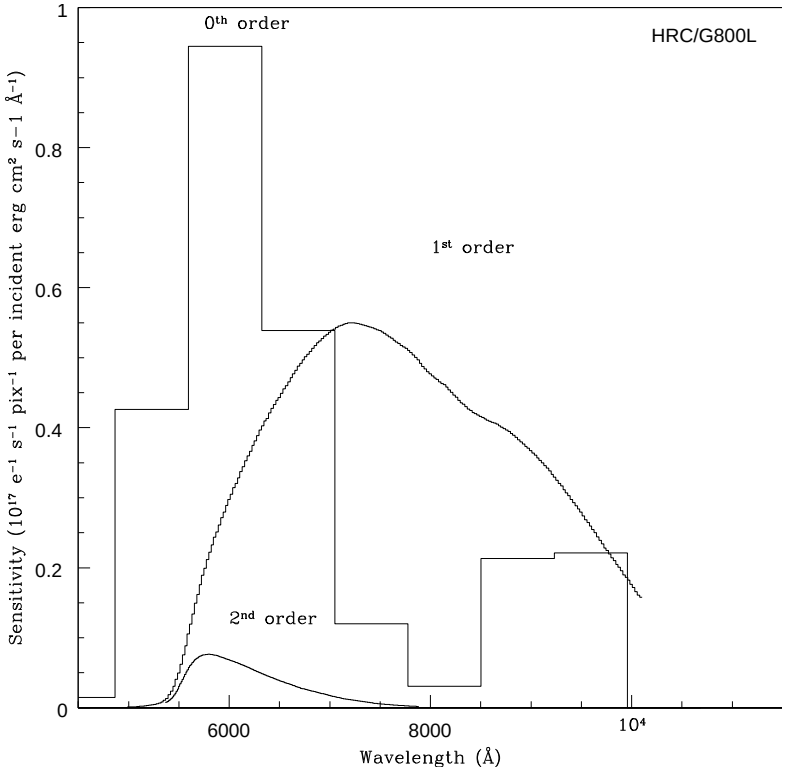

Figure 6.19: Sensitivity versus pixel position for HRC G800L.

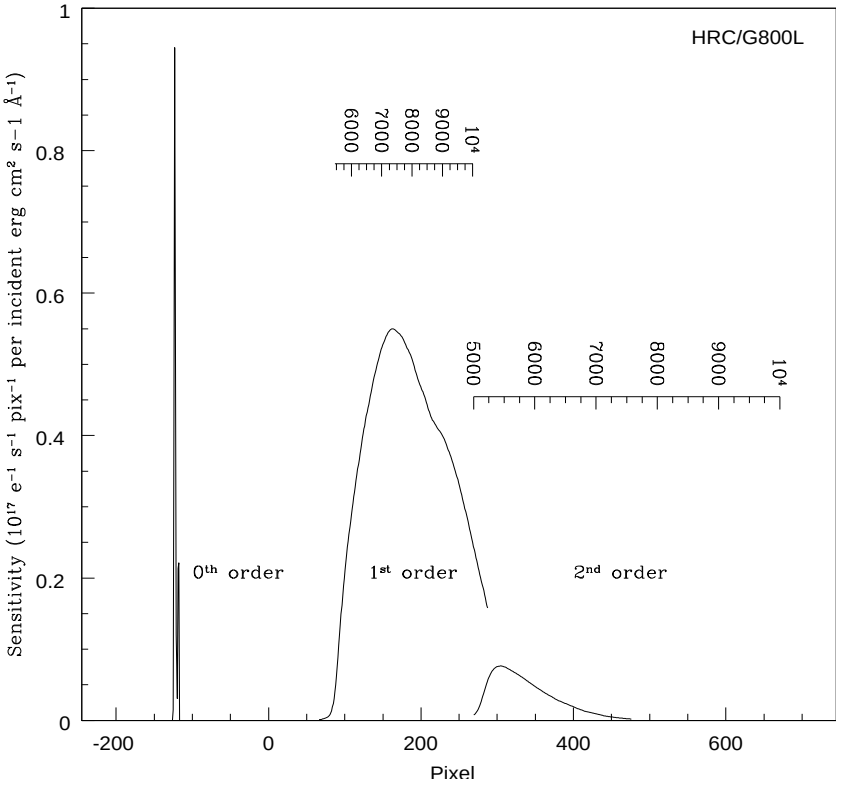

Figure 6.20: Fully dispersed spectrum of white dwarf GD153 with HRC/G800L. The numbers indicate the different grism orders.

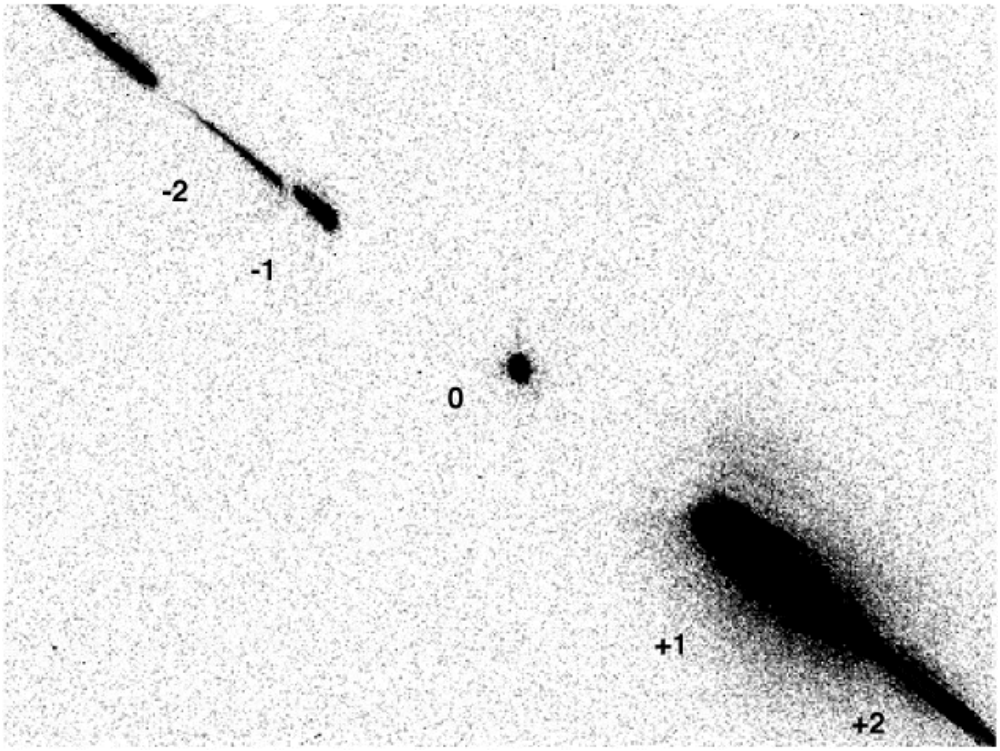

6.3.3 HRC PR200L

Figure 6.21 shows the sensitivity versus wavelength and the wavelength range of the HRC pixels for prism PR200L. The dispersion peaked at 5.3 Å/pix at 1800 Å, but dropped to 105 Å/pix at 3500 Å and then to 563 Å/pix at 5000 Å. Consequently, the spectrum piled up at longer wavelengths, where 1500 Å of spectrum was spanned by only 8 pixels. For bright objects, this effect could lead to saturation and blooming of the CCD, which could affect other spectra. The dispersion also varied by ±4% at 2000 Å between opposite corners of the detector. The tilt of the prism caused an offset of up to ~250 pixels between the CCD positions of the direct image and the PR200L spectrum of an object (Figure 6.21), and caused a similar amount of vignetting along the low-x side of the HRC image. Consequently, an additional prism aperture was defined with a reference point offset by 7.4 arc seconds from the geometric center of the CCD. The wavelength solution used by the aXe data reduction software (see Section 6.3.7) accounts for this aperture offset.

Figure 6.21: Sensitivity versus wavelength for HRC/PR200L. The numbers indicate the resolving power (R) and the offset from the direct image in pixels (Δx) as functions of wavelength.

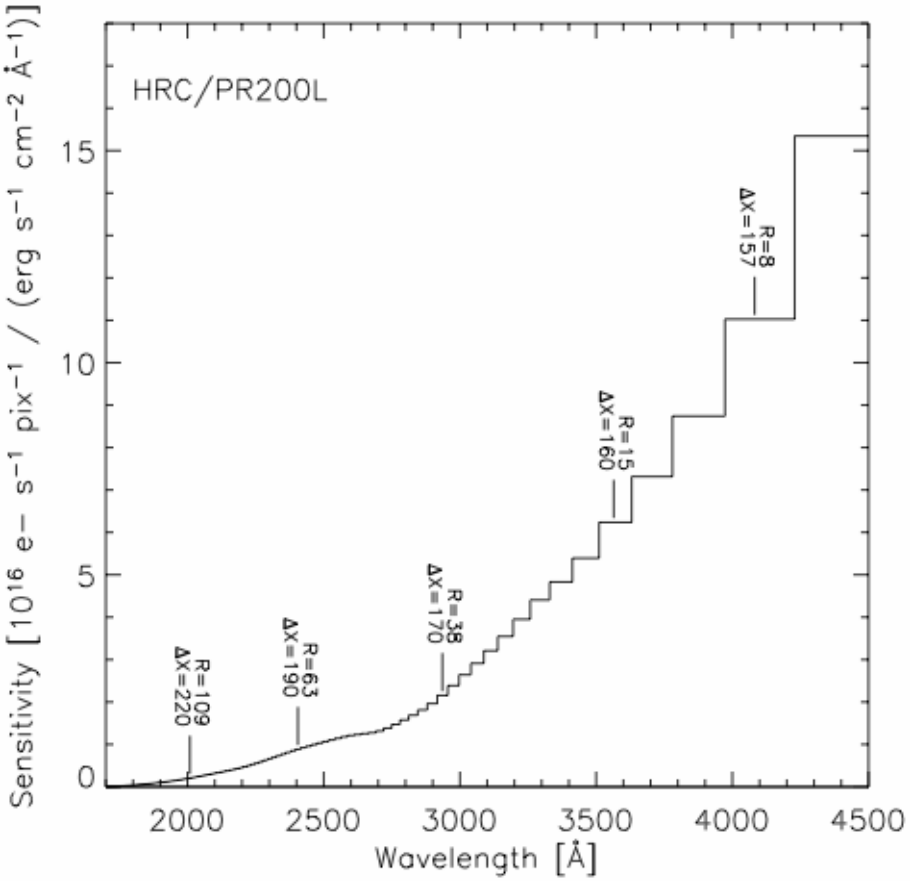

6.3.4 SBC PR110L

Figure 6.22 shows the sensitivity with wavelength and the wavelength range of the pixels for PR110L. This prism is sensitive below 1200 Å and includes the geocoronal Lyman α line, so it is subject to large background signal. The dispersion is 2.6 Å/pix at Lyman α and decreases to 21.6 Å/pix at 1800 Å. The declining efficiency of the CsI MAMA detector beyond ~1800 Å occurs before the long wavelength pile-up, but observations of standard stars indicate that the throughput is ~1000 times higher at 4000 Å than indicated in Figure 4.12. Observations of stars redder than spectral type F experience significantly higher counts between 2000 Å and 6000 Å, with a peak count rate at ~3500 Å. For G stars, this peak can be ~3 times larger than the maximum UV count rate. This red leak and the geo-coronal Lyman α must not exceed the MAMA Bright Object Protection (BOP) limits (see Section 4.6). The prism's optical tilt causes an offset of up to ~250 pixels between the positions of the direct image and the PR110L spectrum of an object (Figure 6.22), and causes a similar amount of vignetting along the high-x side of the SBC image. Figure 6.23 demonstrates this offset with the summed direct image and PR110L image of the standard star WD1657+343. An appropriately offset aperture is automatically implemented by the planning software for all PR110L observations. The wavelength solution used by aXe (Section 6.3.7) accounts for this aperture offset.

Figure 6.22: Sensitivity versus wavelength for SBC `PR110L`. The numbers indicate the resolving power (R) and the offset from the direct image in pixels (Δx) as functions of wavelength.

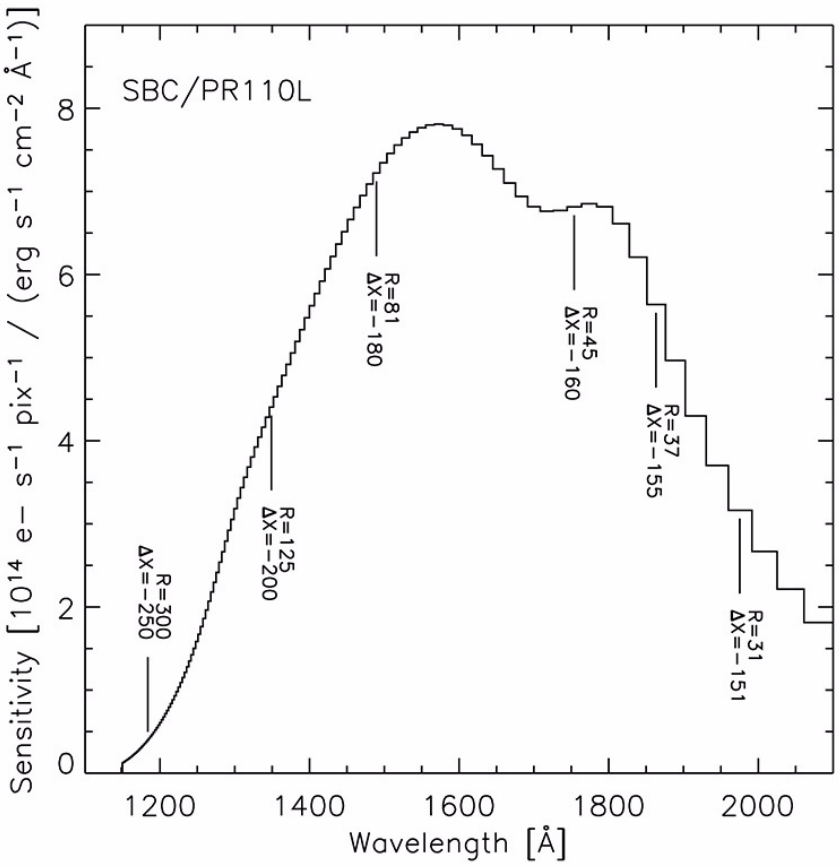

Figure 6.23: Sum of direct (F122M) and PR110L prism exposure of the standard star WD1657+343. The direct image exposure was scaled prior to combination for representation purposes. The cutout shown covers 400 x 185 pixels, where the wavelength increases from left to right for the dispersed image.

6.3.5 SBC PR130L

The short wavelength cut-off of the PR130L prism at 1250 Å excludes the geo-coronal Lyman α, so PR130L is the preferred disperser for faint object detection between 1250 Å and 1800 Å. The dispersion varies from 1.65 Å/pixel at 1250 Å to 20.2 Å/pixel at 1800 Å. Figure 6.24 shows the sensitivity versus wavelength, along with the resolving power (R) and the offset from the direct image in pixels (Δx) as functions of wavelength. As for PR110L, Bright Object Protection must be considered when using this prism, even though the background count rate is lower (see Section 4.6). As for the other prisms, the direct and dispersed images use different apertures with a small angle maneuver between them.

Figure 6.24: Sensitivity versus wavelength for SBC/PR130L. The numbers indicate the resolving power (R) and the offset from the direct image in pixels (Δx) as functions of wavelength.

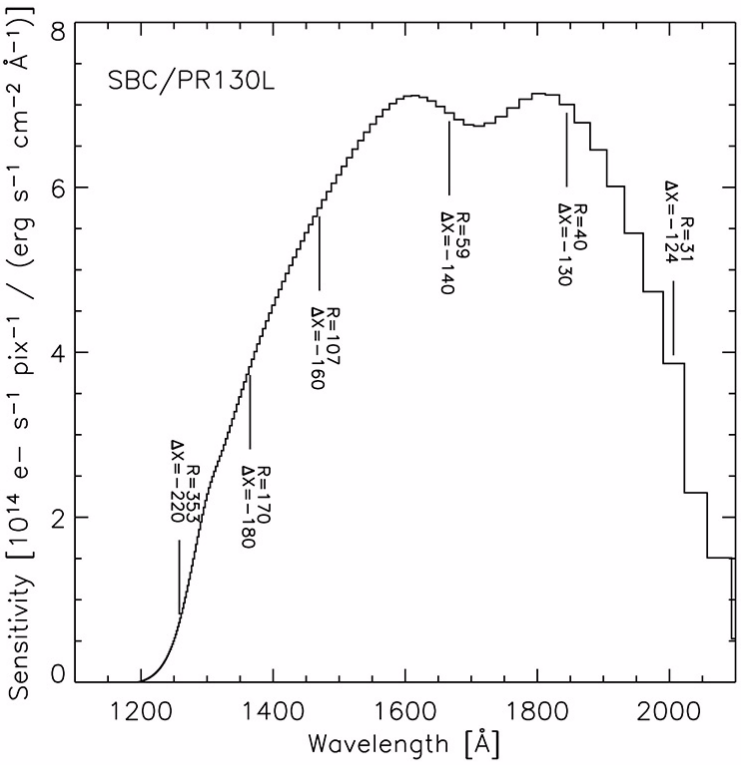

6.3.6 Observation Strategy

The normal observing technique for all ACS spectroscopy is to obtain a direct image of the field followed by the dispersed grism/prism image. This technique allows the user to determine the wavelength zero points from the positions of the sources in the corresponding direct images. For WFC and HRC, the scheduling system automatically inserts a default direct image for each spectroscopic exposure, e.g., a 3 minute F606W exposure for G800L and a 6 minute F330W exposure for PR200L. The user may override the default image by setting the optional parameter AUTOIMAGE=NO. A direct image can then be manually defined with a different filter and/or exposure time or it can be eliminated entirely if the spectroscopic exposures are repeated or if no wavelength calibration is required. No default direct images are obtained for SBC prism exposures because of Bright Object Protection requirements (Section 7.2). The direct image must always be specified manually and satisfy the BOP limits, which will be more stringent than for the dispersed image. Because of the offsets between the direct imaging and prism apertures, the SAME POS AS option will generally not have the desired effect for prism spectroscopy. Users who wish to specify offsets from the field center by means of the POS-TARG option should do so by explicitly specifying the same POS-TARG for the direct imaging and prism exposures.

Table 6.4 lists the V detection limits for the ACS grism/prism modes for unreddened O5 V, A0 V, and G2 V stars generated by the ETC. These limits were computed for WFC and HRC using the parameters CR-SPLIT=2 and GAIN=2. An average sky background was used, but users should be aware that limiting magnitudes are sensitive to background levels, e.g., the limiting magnitude of an A0 V star in the WFC using the F606W filter changes by ±0.4 magnitudes at the background extremes.

Table 6.4: V detection limits for the ACS grism/prism modes.

Mode	V limit (S/N = 5, exposure time = 1 hour)			Reference wavelength (Å)
	O5 V (Kurucz model)	A0 V (Vega)	G2 V (Sun)	
WFC/G800L	24.2	24.4	24.9	7000
HRC/G800L	23.4	23.6	24.2	7000
HRC/PR200L	25.6	22.7	18.8	2500
SBC/PR110L	24.9	20.9	9.3	1500
SBC/PR130L	25.6	21.5	9.9	1500

Chapter 9 provides details of the calculations. Depending on the wavelength region, the background must also be taken into account in computing the signal to noise ratio. The background at each pixel consists of the sum of all the dispersed light in all the orders from the background source. For complex fields, the background consists of the dispersed spectrum of the unresolved sources; for crowded fields, overlap in the spectral direction and confusion in the direction perpendicular to the dispersion may limit the utility of the spectra.

The ACS ETC supports all the available spectroscopic modes of the ACS and is available for more extensive calculations at:

`http://etc.stsci.edu/etc`

The current version employs the on-orbit determinations of the dispersion solution and sensitivity where available.

For more detailed, two-dimensional simulations of ACS slitless spectra, an IRAF/PyRAF package called aXeSIM is available. aXeSIM generates slitless images and their associated direct images using object shapes and spectra given as input. In the most primitive form, aXeSIM uses Gaussians as object shapes and direct imaging magnitudes as "spectra", however, more realistic object shapes (e.g. a PSF from TinyTim) and high resolution spectra can be provided. aXeSIM is described in Kuemmel, Kuntschner & Walsh (2007, ST-ECF Newsletter 43, 8) and Kuemmel et al. (2009, PASP 121, 59).

Online

Please refer to the ACS Web page and http://www.stsci.edu/resources/software_hardware/stsdas/axe for the aXeSIM software and related information.

6.3.7 Extraction and Calibration of Spectra

Because ACS spectroscopy is slitless, the point spread function of the target modulates the spectral resolution. For extended sources, the size of the target in the dispersion direction limits the achievable resolution (ACS ISR 2001-02). The dispersions of the grism and prisms are well characterized, but the zeroth order of grism spectra are generally too weak to reliably set the wavelength zero point. For typical spacecraft jitter, wavelength zero points to ±0.4 pixels should be routinely achievable using a direct image taken just before or after the grism or prism image. The jitter information can be used to obtain more accurate coordinates for the center of the FOV. These coordinates allow one to determine better relative offsets between the direct and the spectroscopic images. The red wavelength range of each pixel in G800L images is small enough that fringing can modulate the spectra. The peak-to-peak fringe amplitude was about 30% at 9500 Å for the HRC, and it is about 25% for the WFC. Models of the fringing in the WFC and HRC are described in ACS ISR 2003-12. In practice, the fringing is significantly reduced by the smoothing effects of the PSF and intrinsic object size in the dispersion direction. ACS ISR 2008-01 shows that the errors due to fringing are less than 0.1% for continuum sources and can therefore be neglected. For narrow emission lines, however, fringing can cause line flux variations of 12% and more. For realistic scenarios like Wolf Rayet emission lines, variations of ~4% are seen.

The STSCI pipeline does not provide an extracted spectral count rate vs. wavelength, but the software package aXe is available to extract, wavelength calibrate, flat field, and flux calibrate ACS grism and prism spectra. Full details are presented by Kuemmel et al. 2009, PASP 121, 59 and at:

`http://www.stsci.edu/resources/software_hardware/stsdas/axe.`

ACS grism extraction for 47,919 sources were performed by ST-ECF and are available via the Hubble Legacy Archive. A good starting point for information about these extractions is available at:

`http://hla.stsci.edu/STECF.org/archive/hla/`

CHAPTER 7:

Observing Techniques

In this chapter . . .

7.1 Designing an ACS Observing Proposal

In this section, we describe the sequence of steps you should follow when designing your ACS observing proposal. The sequence is an iterative one, as trade-offs are made between signal-to-noise ratio and the limitations of the instrument itself. The basic sequence of steps in defining an ACS observation are:

- Identify science requirements and select the basic ACS configuration to support those requirements.
- Estimate exposure time to achieve the required signal-to-noise ratio, CR-SPLIT, dithering, and mosaic strategies, and check feasibility, including saturation and bright-object limits.
- Identify any additional target acquisition and calibration exposures needed.
- Calculate the total number of orbits required, taking into account the overheads.

Figure 7.1: Defining an ACS observation.

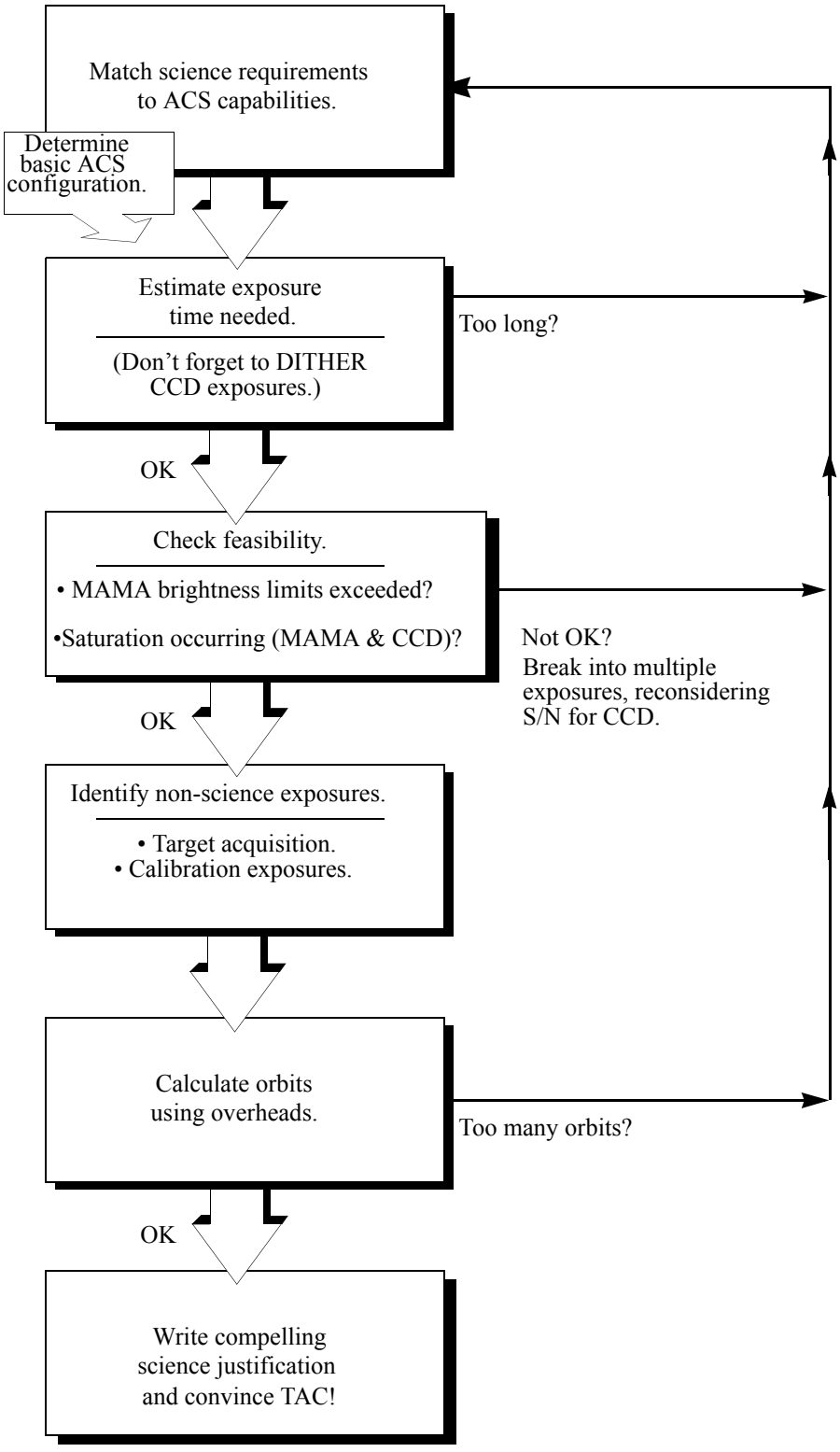

7.1.1 Identify Science Requirements and Define ACS Configuration

First, you must identify the science goals you wish to achieve with ACS. Basic decisions you must make are:

- Nature of target
- Filter selection

As you choose your science requirements and match them to the instrument's capabilities, keep in mind that the capabilities depend on whether you are observing in the optical with the WFC, or in the far-UV with the SBC. Trade-offs involving only ACS modes are described in Table 7.1. A discussion of trade-offs between different instruments can be found in Section 2.2.

Table 7.1: Science decision guide. .

Decision	Choices	Trade-offs
Field of view	Camera Filter selection	WFC: 202 x 202 arcseconds SBC: 35 x 31 arcseconds
Spectral response	Camera Filter selection	WFC: 3700-11,000 Å SBC: 1150-1700 Å
Spatial resolution	Camera	WFC: ~50 milliarcsecond pixels SBC: ~32 milliarcsecond pixels
Filter selection	Camera	WFC: broad, medium & narrow band, ramps SBC: broad band
Spectroscopy	Camera Spatial resolution Field of view Wavelength range	Grism (G800L): WFC Prism (PR110L, PR130L): SBC
Polarimetry	Filters	UV polarizers combine with Wheel 2 filters VIS polarizers combine with Wheel 1 filters

Imaging

For imaging observations, the basic configuration consists of detector, operating mode (MODE=ACCUM), and filter. Chapter 5 presents detailed information about each ACS imaging mode.

Special Uses

We refer you to Chapter 6 if you are interested in slitless spectroscopy or polarimetry.

7.1.2 Available but Unsupported Modes

Please check for updates on the ACS Web site.

STScI provides full calibration and user support for most of ACS's operational modes. However, there are some "available but unsupported" modes accessible to observers in consultation with an ACS Instrument Scientist. These unsupported modes include a few apertures, limited- interest optional parameters, some GAIN options, and filterless (CLEAR) operation. If your science cannot be obtained using fully supported modes, or would be much better with use of these special cases, then you may consider using an unsupported mode.

Unsupported modes should only be used if the technical requirements and scientific justifications are particularly compelling. The following caveats apply:

- STScI does not provide calibration reference files for available-but-unsupported modes. It is the observer's responsibility to obtain any needed calibrations.
- Requests to repeat failed observations taken with unsupported modes will not be honored if the failure is related to use of this mode.
- User support from STScI will be more limited.

Phase I proposals that include unsupported ACS modes must include the following:

- Explanation of why supported modes don't suffice.
- A request for any observing time needed for calibration purposes.
- Justification for added risk of use in terms of scientific payback.
- Demonstration that the observers are able to analyze such data.

During the Phase II proposal submission process, use of unsupported modes require formal approval from the ACS/WFPC2 Team at STScI. To request an unsupported mode, send a brief e-mail to your Program Coordinator (PC) that addresses the above four points. The PC will relay the request to the contact scientist or relevant ACS instrument scientist, who will then decide whether the use will be allowed. This procedure ensures that any potential technical problems have been taken into account. Note also that archival research may be hindered by use of these modes. Requests for unsupported modes that do not adequately address the above four points or that will result in only marginal improvements in the quality of the data obtained may be denied, even if the request was included in your approved Phase I proposal.

The current list of available-but-unsupported items are:

- Targets: `BIAS`

- Optional parameters: SIZEAXIS1, SIZEAXIS2, CENTERAXIS1, CENTERAXIS2, COMPRESSION, AMP, FLASHEXP, WFC: GAIN=0.5, 1.0, 1.4
- Spectral elements: CLEAR (WFC)
- ACQ mode: optional parameter GAIN
- Apertures: WFC2-2K, WFC2-MRAMPQ, WFC2-SMFL, WFC2-POL0V, WFC2-POL0UV

7.1.3 Determine Exposure Time and Check Feasibility

Once you've selected your basic ACS configuration, the next steps are:

- Estimate the exposure time needed to achieve your required signal-to-noise ratio, given your source brightness. (You can use the ETC for this; see also Chapter 9 and the plots in Chapter 10).
- For observations using the CCD detectors, ensure that you do not exceed the pixel full well.
- For observations using the MAMA detector, ensure that your observations do not exceed brightness (count rate) limits.
- For observations using the MAMA detector, ensure that for pixels of interest, your observations do not exceed the limit of 65,535 accumulated counts per pixel per exposure imposed by the ACS 16 bit buffer.

To determine your exposure-time requirements, consult Chapter 9 where an explanation of how to calculate a signal-to-noise ratio and a description of the sky backgrounds are provided. To assess whether you are close to the brightness, signal-to-noise, and dynamic-range limitations of the detectors, refer to Chapter 4.

If you find that the exposure time needed to meet your signal-to-noise requirements is too large, or that you are constrained by the detector's brightness or dynamic-range limitations, you must adjust your basic ACS configuration. Table 7.2 summarizes the available options and actions for iteratively selecting an ACS configuration that is suited to your science and is technically feasible.

Table 7.2: Science feasibility guide.

Action	Outcome	Recourse
Estimate exposure time.	If too long, re-evaluate instrument configuration.	Consider another filter.
Check full-well limit for CCD observations.	If full well exceeded and you wish to avoid saturation, reduce time per exposure.	Divide total exposure time into multiple, short exposures.[1]
Check bright-object limits for MAMA observations.	If source is too bright, re-evaluate instrument configuration.	Consider another filter or change detectors and wavelength regime.
Check 65,535 counts-per pixel limit for MAMA observations.	If limit exceeded, reduce time per exposure.	Divide total exposure time into multiple, short exposures

1. Splitting CCD exposures affects the exposure time needed to achieve a given signal-to-noise ratio because of the read noise.

7.1.4 Identify Need for Additional Exposures

Having identified a sequence of *science* exposures, you need to determine what additional exposures you may require to achieve your scientific goals. Specifically, if the success of your science program requires calibration to a higher level of precision than is provided by STScI calibration data, and if you are able to justify your ability to reach this level of calibration accuracy yourself, you will need to include the necessary calibration exposures in your program, including the orbits required for calibration in your total orbit request.

7.1.5 Data Volume Constraints

ACS data taken at the highest possible rate for more than a few orbits or in the Continuous Viewing Zone (CVZ) may accumulate data faster than they can be transmitted to the ground. High data volume proposals will be reviewed and, on some occasions, users may be requested to break the proposal into different visits. Consider using sub-arrays, or take other steps to reduce data volume.

7.1.6 Determine Total Orbit Request

In this step, you place all of your exposures (science and non-science, alike) into orbits, including tabulated overheads, and determine the total number of orbits required. Refer to Chapter 8 when performing this step. If you are observing a small target and find your total time request is significantly affected by data-transfer overheads (which will be the case *only* if you are taking many separate exposures under 339 seconds with the WFC), you can consider the use of CCD subarrays to lessen the data volume. Subarrays are described in Section 7.3.1 and Section 8.2.1.

If you are unhappy with the total number of orbits required, you can adjust your instrument configuration, lessen your acquisition requirements, or change your target

signal-to-noise or wavelength requirements, until you find a combination which allows you to achieve your science goals. If you are happy with the total number of orbits required, you are done!

7.1.7 Charge Transfer Efficiency

All CCDs operated in a radiative environment are subject to a significant degradation in charge transfer efficiency (CTE). The degradation is due to radiation damage of the silicon, inducing the creation of traps that impede an efficient clocking of the charge on the CCD. Since reading out the ACS WFC requires 2048 parallel transfers and 2048 serial transfers, it is not surprising that CTE effects have begun to manifest themselves since first years of ACS operation.

Special CTE monitoring programs show that CTE degradation proceeds linearly with time. For the current Cycle a star with 100 electrons, a nominal sky background of 30 electrons, and a placement at row 1024 (center) in one of the WFC chips would experience a loss of about 19% for an aperture of 3 pixel radius. A target placed at the WFC aperture reference point, near the maximum number of parallel shifts during readout, would have approximately twice the loss. Expected absolute errors after calibration of science data, at these low-loss levels, is expected to be of order 10% the relative loss.

When observing a single target significantly smaller than a single detector, it is possible to place it near an amplifier to reduce the impact of imperfect CTE. This is easy to accomplish by judicious choice of aperture and target position, or by utilizing POS TARG commands. However, be aware that large POS TARGs are not advisable because they change the fractional pixel shifts of dither patterns due to the geometric distortion of ACS. An alternative means to achieve the placement of a target near the amplifier is by using some of the subarray apertures. For example, `WFC1-512` (target will have 256 transfers in X and Y), `WFC1-1K`, and `WFC1-2K` place the target near the B amplifier. The aperture WFC1-CTE is available to mitigate CTE loss. This aperture has the same area as the WFC1 aperture except that the reference position is 200 pixels from the upper right corner of chip 1, in both the chips x- and y- direction. Therefore, WFC1-CTE is not appropriate for highly extended targets.

Recently there have been efforts to correct WFC images for CTE charge-trailing at the pixel level (Massey et al. 2010, MNRAS, 401, 371; Anderson & Bedin 2010, PASP, 122, 1035) as an alternative to photometric corrections a posteriori. The Anderson & Bedin algorithm has been made available by the ACS Team as a stand-alone tool incorporated into the STSDAS software package. The ACS/WFPC2 Team is also working on implementing and testing the CTE de-trailing software in the WFC calibration pipeline. Please check for updates on the ACS Web site.

7.1.8 Image Anomalies

The ACS was designed with a requirement that no single straylight feature may contain more than 0.1% of the detected energy in the object producing it. This goal has generally been met, but during the extensive ground and SMOV test programs a few

exceptions have been identified (Hartig et al. 2002, Proc. SPIE 4854; HLA ISR 2008-01) such as the WFC elliptical haloes and the F660N ghosts.

More details about the ACS image anomalies can be found in the *ACS Data Handbook*[1] and at:

`http://www.stsci.edu/hst/acs/performance/anomalies/`

While some of these anomalies exceed the specified intensity, some judicious planning of your science observations is recommended to help alleviate their effect on your data, especially if bright sources are expected in the field of view. For instance, the impact of diffraction spikes (which for ACS lie along x and y axes) and of CCD blooming (which occurs along the y direction) due to saturation of a bright star(s), can be reduced by choosing an ORIENT which prevents the source of interest from being connected to the bright star along either of these axes, Alternatively, a suitable ORIENT could move the bright star(s) into the interchip gap or off the field of view altogether. Similarly, the impact of WFC elliptical haloes can be minimized by avoiding a bright star in the quadrant associated with amplifier D.

SBC observations of bright objects may show optical ghosts possibly due to reflection between the back and front sides of the filter.

Subsequent to the replacement of the ACS CCD Electronics Box during SM4, all WFC images show horizontal striping which is constant across the full row (for both amplifiers) of each chip. This striping is the result of a *1/f* noise on the bias reference voltage, and has a standard deviation of 0.9 $\mathbf{e}^-$. The contribution of the stripes to the global read noise statistics is small, but the correlated nature of the noise may affect photometric precision for very faint sources and very low surface brightnesses. Please see Section 5.2.6 for additional details, and mitigation strategy. Destriping will be performed in the automated WFC data reduction pipeline starting during Cycle 20. Further information can be found in ACS ISR 2011-05.

7.2 SBC Bright Object Protection

7.2.1 How Do You Determine if You Violate a Bright Object Limit for SBC Exposures?

High global and local count rates can cause catastrophic damage to the SBC detector. Therefore, targets should be checked to verify that their fluxes do not exceed the defined SBC safety limits. As a first step, you can check your source V magnitude and peak flux against the bright-object screening magnitudes in Table 7.4 for your chosen observing configuration. In many cases, your source properties will be much fainter than these limits, and you need not worry further.

However, the magnitudes in this table are hard screening limits that correspond to the count rate limits in Table 7.3 and the output of the ETC. In earlier editions of this

1. Please check the ACS Web site for the most recent version of the *ACS Data Handbook*.

Handbook, these magnitudes were made fainter by arbitrary 1 or 2 magnitude pads, depending on the spectral-type range, which have now been removed. If your target is near these limits (within 2 magnitudes or a factor of 6.3 of the flux limits), then you need to carefully consider whether your source will be observable in the chosen configuration. Remember that the limits in these tables assume zero extinction. Thus, you will want to correct the limits appropriately for your source reddening due to interstellar dust.

Table 7.3: Absolute SBC count rate screening limits for nonvariable and variable objects.

Target	Limit type	Screening limit
Nonvariable	Global	200,000 counts/second
Nonvariable	Local	50 counts/second/pixel
Irregularly variable[1]	Global	80,000 counts/second
Irregularly variable[1]	Local	20 counts/second/pixel

1. Applies to the brightest state of the target.

The limits for irregular variable sources are a factor 2.5 more conservative than for sources with predictable fluxes. Predictable variables are treated as nonvariable for this purpose. Examples of sources whose variability is predictable are Cepheids or eclipsing binaries. Irregularly variable sources are, for instance, cataclysmic variables or AGN.

You can use the information presented in Section 9.2 to calculate peak and global count rates. You can also use the ETC to calculate the expected count rate from your source. The ETC has a host of template stellar spectra. If you have a spectrum of your source (e.g., from IUE, FOS, GHRS, or STIS) you can also use it directly in the calculator. As implied by the footnotes to Table 7.4, the model spectra in the ETC cannot be used for bright-object checking at the solar spectral type and later; the UV spectra of such stars are dominated by emission lines and continua not reproduced by the models. For these types, more realistic theoretical or observational input spectra (e.g., from the IUE or *HST* archives) must be used. The calculator will evaluate the global and per pixel count rates, and will warn you if your exposure exceeds the absolute bright-object limits. We recommend you use the ETC if you have *any concern* that your exposure may exceed the bright-object MAMA limits.

7.2.2 Policy and Observers' Responsibility in Phase I and Phase II

It is the responsibility of the observer to ensure that observations do not exceed the bright-object count rate limits stated in Table 7.3. Please address this issue in your Phase I proposal.

It is your responsibility to ensure that you have checked your planned observations against the brightness limits prior to proposing for Phase I. If your proposal is accepted and we, or you, subsequently determine in Phase II that your source violates the absolute limits, then you will either have to change the configuration or target, if allowed, or lose the granted observing time. We request that you address the safety of your SBC targets by means of the ACS ETC; you may consult with an ACS Instrument Scientist via the Help Desk if needed. For SBC target-of-opportunity proposals, please include in your Phase I proposal an explanation of how you will ensure your target can be safely observed.

In Phase II, proposers of SBC observations are required to check their targets and fields in detail for excessively bright sources, by the Phase II deadline. The relevant policies and procedures are described here.

STScI has developed bright object tools (BOT) to conduct detailed field checking prior to SBC program implementation. These tools are based on automated analysis of the fields by means of data from the second Guide Star Catalogue (GSC2) and displays of the Digital Sky Survey (DSS). GSC2 provides two magnitudes (photographic J and F), hence one color, for most fields down to about 22nd magnitude, which, combined with conservative spectral-type vs. color relationships, supports determinations of safety or otherwise for individual objects. In the best cases, these procedures allow expeditious safety clearing, but in some cases the GSC2 is inadequate because of crowding or absence of one of the filters, for instance. Then supplementary information must be provided by the proposers to support the bright object protection (BOP) process. The target should always be checked directly in the ETC with the more detailed information generally available for it, rather than relying on its field report data.

Subsequently, automated GALEX screening has been added as a selectable option in the BOT. The AIS (all-sky) sources are screened as unreddened O5 stars and reported as either safe or unsafe. This is a powerful tool because it is based directly on UV fluxes; e.g., previously unknown hot companions to late-type stars will be revealed. The target should still be checked using the ETC. Unsafe objects require further investigation; the GALEX fluxes are upper limits in crowded regions because of the relatively low spatial resolution, or the source may clear with more specific parameter information.

Table 7.4: Bright limit V-band magnitudes for observations with the SBC filters and prisms (no reddening).

Spectral type[1]	Log T_{eff}	F122M	F115LP	F125LP	F140LP	F150LP	F165LP	PR110L	PR130L
O5 V	4.648	16.1	19.2	19.0	18.5	18.0	16.6	15.8	15.5
B1 V	4.405	15.2	18.4	18.2	17.7	17.1	15.7	15.0	14.7
B3 V	4.271	14.3	17.6	17.5	17.0	16.4	15.2	14.2	14.0
B5 V	4.188	13.5	17.0	16.9	16.5	15.9	14.7	13.7	13.4
B8 V	4.077	12.0	15.9	15.9	15.5	15.0	13.8	12.7	12.5
A1 V	3.965	9.4	14.0	13.9	13.8	13.6	12.6	11.1	11.0
A3 V	3.940	8.2	13.0	13.0	12.9	12.8	12.2	10.5	10.3
A5 V	3.914	6.8	11.9	11.9	11.9	11.9	11.6	9.9	9.8
F0 V	3.857	4.8	10.1	10.0	10.0	10.0	9.9	8.3	8.3
F2 V	3.838	4.0	9.3	9.3	9.2	9.2	9.1	7.6	7.5
F5 V	3.809	2.2	7.7	7.6	7.6	7.6	7.5	5.9	5.9
F8 V	3.792	0.9	6.8	6.8	6.7	6.7	6.7	4.7	4.7
G2 V[2]	---	2.2	6.3	6.0	6.0	5.9	5.8	3.2	3.1
G8 V[3]	---	---	5.6	5.6	5.4	5.2	4.8	2.2	2.1
K2 V[4]	---	---	5.7	5.7	5.2	5.0	4.3	3.2	3.0
KM III[5]	---	---	4.5	4.5	4.2	4.0	3.6	2.7	2.3
Binary[6]	---	14.4	17.5	17.3	16.8	16.3	14.9	14.1	13.8

1. O5 V through F8 V values are based on Kurucz models.
2. The magnitudes listed for G2 V are for the Solar template in the ETC.
3. The magnitudes listed for G8 V are from IUE data for the star Tau Ceti.
4. The magnitudes listed for K2 V are from IUE data for the star Epsilon Eri.
5. The magnitudes listed for KM III are from IUE data for 8 stars of these types.
6. System made of a late-type star with an O5 companion contributing 20% to the total light in the V band. In the UV, the O5 component dominates and sets the same magnitude limit for companion types A to M.

STScI will check all targets and fields before any SBC observations are cleared. However, by policy GOs must provide screened, safe targets for SBC programs, and supplementary data as needed to verify target and field safety. The APT/BOT, including an Aladin interface, makes the BOP procedures accessible for GO use. Extensive help files and training movies are available. While the procedures may appear complex on first exposure, their convenience and straightforward application rapidly become apparent. All SBC proposers must conduct BOP reviews of their targets and fields in conjunction with their Phase II preparations. Thus, they will become aware of any problems earlier, such as the need for supplementary data, which may otherwise entail lengthy implementation delays following the Phase II deadline. (An exception is moving target fields, which must be cleared after the scheduling windows have been established.) To assist with these procedures, a Contact Scientist

(CS) who is an SBC/BOP specialist will be assigned to each SBC program, to interact with the GO as necessary and requested during the Phase II preparations, and through program execution.

Briefly, for a single default SBC pointing with unconstrained orientation, a field of 70 arcseconds in diameter must be cleared. The APT/BOT automatically reports on all GSC2 stars or GALEX sources within that field. If any displacements from the default pointing (e.g., POS TARGs, patterns, or mosaics) are specified, the field to be cleared increases commensurately. POS TARG vectors and the enlarged, rotated field circles are conveniently displayed in APT/Aladin. No unsafe or unknown star may lie within 5 arcseconds of the detector edge at any orientation. Conversely, POS TARGs and orientation restrictions may be introduced to avoid bright objects in the fields. In case a single guide-star implementation becomes necessary, the field to be cleared increases to 140 arcseconds in diameter, but usually that will not become known until scheduling is attempted after the Phase II deadline.

An SBC GO must send his/her CS, by the Phase II deadline, ETC calculations for each discrete target, and reports on any unsafe or unknown stars from APT/BOT for each field, either showing that the observations are in fact safe, or documenting any unresolved issues. In the latter case, including inadequacy of BOT/GSC2 to clear the observations, other photometric or spectroscopic data sources must be sought by the GO to clear the fields. Many of these are available directly through the APT/Aladin interface (although automatic BOP calculations are available only with GSC2 and GALEX), including the STScI Multimission Archive (MAST), which contains the IUE and GALEX in addition to the *HST* data. An existing UV spectrum of the target or class may be imported directly into the ETC; IUE data must be low resolution, large aperture for BOP. If model spectra are used, the original Kurucz (not Castelli & Kurucz) set should be used for early-type stars. None of the provided models is adequate for stars later than the Sun, since they lack chromospheric emission lines; actual UV data must be used for them. In worst cases, new ground based data or *HST* CCD UV exposures may be required to clear the fields for BOP; in general, the latter must be covered by the existing Phase I time allocation.

If a given star has only a V magnitude, it must be treated as an unreddened O5 star. (The older Kurucz O5 model with higher Teff in the ETC should be used for BOP purposes.) If one color is available, it may be processed as a reddened O5 (which will always have a greater UV flux than an unreddened star of the same color). If two colors are available, then the actual spectral type and reddening can be estimated separately. The APT/BOT now clears automatically stars with only a single GSC2 magnitude, if they are safe on the unreddened O5 assumption. Any other "unknowns" must be cleared explicitly.

In some cases, the 2MASS JHK may be the only photometry available for an otherwise "unknown" star. It is possible to estimate V and E(B-V) from those data on the assumption of a reddened O5 star, and thus determine its count rates in the ETC. F. Martins & B. Plez, A&A, 457, 637 (2006), derive $(J-H)_0 = -0.11$ for all O stars; and $(V-J)_0 = -0.67$, $(V-H)_0 = -0.79$ for early O types. (The K band should be avoided for BOP because of various instrumental and astrophysical complications.) M.S. Bessell & J.M. Brett, PASP, 100, 1134 (1988), Appendix B, give relationships between the

NIR reddenings and E(B-V). These data determine the necessary parameters. Note that the ETC also supports direct entry of observed J, H magnitudes with E(B-V).

It is not expected that all such issues will be resolved by the Phase II deadline, but they should at least be identified and have planned resolutions by then. Another possible resolution is a change to a less sensitive SBC configuration. Any SBC targets or fields that cannot be demonstrated to be safe to a reasonable level of certainty in the judgement of the CS will not be observed. It is possible that equivalent alternative targets may be approved upon request in that case; but any observations that trigger the onboard safety mechanisms will not be replaced.

A related issue is SBC pointing specification changes after the targets and fields have been cleared by the STScI BOP review. Any such changes must be approved by the ACS Team on the basis of a specific scientific justification and a new BOP review by the GO, which may be submitted via the CS if absolutely necessary. However, in general such requests should be avoided by ensuring that submitted SBC specifications are final, to prevent a need for multiple BOP reviews.

GOs planning SBC observations of unpredictably variable targets, such as cataclysmic variables, are reminded of the special BOP procedures in effect for them, which are detailed in ACS ISR 2006-04.

Policy on Observations Which Fail Because they Exceed Bright-Object Limits

If your source passes screening, but causes the automatic flight checking to shutter your exposures or shut down the detector voltage causing the loss of your observing time, *then that lost time will not be returned to you*; it is the observer's responsibility to ensure that observations do not exceed the bright-object limits.

7.2.3 Bright-Object Protection for Solar System Observations

Observations of planets with the SBC require particularly careful planning due to very stringent overlight limits. In principle, Table 7.3 and Table 7.4 can be used to determine if a particular observation of a solar-system target exceeds the safety limit. In practice, the simplest and most straightforward method of checking the bright object limits for a particular observation is to use the ETC. With a user-supplied input spectrum, or assumptions about the spectral energy distribution of the target, the ETC will determine whether a specified observation violates any bright object limits.

Generally speaking, for small (< ~0.5 to 1 arc seconds) solar-system objects the local count rate limit is the more restrictive constraint, while for large objects (> ~1 to 2 arc seconds) the global limit is more restrictive.

As a first approximation, small solar system targets can be regarded as point sources with a solar (G2 V) spectrum, and if the V magnitude is known, Table 7.3 and Table 7.4 can be used to estimate whether an observation with a particular SBC prism or filter is near the bright-object limits. V magnitudes for the most common solar-system targets (all planets and satellites, and the principal minor planets) can be found in the *Astronomical Almanac*. This approximation should provide a conservative estimate, particularly for the local limit, because it is equivalent to

assuming that all the flux from the target falls on a single pixel, which is an overestimate, and because the albedos of solar-system objects in the UV are almost always significantly less than their values in the visible part of the spectrum. A very conservative estimate of the global count rate can be obtained by estimating the peak (local) count rate assuming all the flux falls on one pixel, and then multiplying by the number of pixels subtended by the target. If these simple estimates produce numbers near the bright-object limits, more sophisticated estimates may be required to provide assurance that the object is not too bright to observe in a particular configuration.

For large solar-system targets, checking of the bright-object limits is most conveniently done by converting the integrated V magnitude (V_0, which can be found in the *Astronomical Almanac*) to V magnitude/arc seconds^2 as follows:

$$V/(\text{arcsec}^2) = V_0 - 2.5\log(1/\text{area})$$

where *area* is the area of the target in arc seconds^2. This surface brightness and the diameter of the target in arc seconds can then be input into the ETC (choose the solar template spectrum for the spectral energy distribution) to test whether the bright-object limits are satisfied.

7.2.4 Prime and Parallel Observing with the SBC

STScI will perform screening of all SBC exposures prior to scheduling. Targets not established as safe for the configuration in which they are being observed will not be scheduled. Observations that pass screening but are lost in orbit due to a bright-object violation will not be rescheduled. Observers are responsible for ensuring that their observations do not violate the SBC count-rate limits.

To ensure that STScI can adequately screen observations, special constraints are imposed on parallel observing with the SBC. In particular:

- No pure or coordinated parallels are allowed using the SBC
- SNAPSHOT observations with the SBC are not allowed
- GO Survey programs using the SBC are not permitted

Table 7.5: Bright object protection policy for SBC observations.

Type of observing	Policy
Prime	Allowed if target passes screening
Snapshots	Not allowed
Coordinated parallel	Not allowed
Pure parallel	Not allowed

Targets that are one magnitude or more fainter than the magnitude limits in the screening tables generally automatically pass screening. For a target that is within one magnitude of the screening limits, observers must provide a calibrated spectrum of the

source at the intended observing wavelength. If such a spectrum is not available, the prospective GO must request an orbit in Phase I for a pre-qualification exposure, during which the target spectrum must be determined by observation in an allowed configuration.

Please note that if you are proposing SBC target-of-opportunity observations, we ask you to provide an explanation in your Phase I proposal of how you will ensure that your target can be safely observed.

7.3 Operating Modes

HRC has been unavailable since January 2007.

ACS supports two types of operating modes:

- `ACCUM` for each of the cameras. This is the standard data taking mode used by observers.
- `ACQ` (acquisition). This was the mode used to acquire a target for coronagraphic observations. `ACQ` was only available with the HRC.

7.3.1 WFC ACCUM Mode

In this mode the WFC CCD accumulates signal during the exposure in response to photons. The charge is read out at the end of the exposure and translated by the A-to-D converter into a 16 bit data number (DN), ranging from 0 to 65,535. The number of electrons per DN can be specified by the user as the GAIN value. The full well of the WFC CCD is about 85,000 electrons and consequently, all GAIN values larger than 1 will allow the observer to count up to the full well capacity. For GAIN=1 only 75% of full well capacity is reached when the DN value saturates at 65,535. The read-out noise of the WFC CCD is about 4 electrons rms and thus it is critically sampled even at GAIN=2. WFC can make use of a user-transparent, lossless, on-board compression algorithm, the benefits of which will be discussed in the context of parallel observations. The algorithm is more effective with higher GAIN values (i.e., when the noise is undersampled). Note that only GAIN=2 is supported by STScI.

Several supported apertures (see Table 7.6) are accessible to WFC users. `WFC1-FIX` and `WFC2-FIX` select the geometric centers of the two WFC camera chips. `WFCENTER` corresponds to the geometric center of the combined WFC field, and will be useful for facilitating mosaics and obtaining observations at multiple orientations. Due to maximal CTE loss, WFCENTER is not recommended for a single

compact target. `WFC, WFC1,` and `WFC2` are located near the field of view center and the centers of chips 1 and 2, respectively (see Figure 7.3), Their locations were chosen to be free of detector blemishes and hot pixels, and they are the preferred apertures for typical observations. See Section 7.7 for more details about ACS apertures, including subarray apertures.

Usually each CCD is read from two amplifiers to minimize charge transfer efficiency (CTE) problems and read-out time. As a result, the two 2K by 2K portions in a single chip may have slightly different read-out noise. The WFC chips have both physical and virtual overscans that can be used to estimate the bias level and the read-out noise on each single image.

The present flight software does not allow reading an ACS frame directly into the *HST* on-board recorder. Images have to be first stored in the internal buffer. The ACS internal buffer can store only a single full frame WFC image. When this image is compressed, the buffer can store additional SBC images, depending on the compression factor. Regardless of the compression strategy, no more than one full frame WFC image can be stored in the buffer. It is STScI's policy not to compress primary WFC observations. When more than one WFC image is obtained during an orbit, a buffer dump must occur during the visibility period so as to create space in the buffer for a new WFC image.

If each exposure is longer than approximately 339 seconds, buffer dumps can occur during the integration of the following image with no impact on observing efficiency.

Conversely, short, full frame, integrations with the WFC during the same orbit will cause buffer dumps to be interleaved with observations and will negatively affect the observing efficiency. See Chapter 8 for more details about ACS overheads.

WFC CCD Subarrays

It is possible to read-out only a portion of a detector with subarrays, which have a smaller size than the full frame. Subarrays are used to reduce data volume, to store more frames in the internal buffer (thus avoiding the efficiency loss due to buffer dumps), or to read only the relevant portion of the detector when imaging with ramp filters or with HRC filters (which produce a vignetted field of view on WFC). WFC subarrays have some limitations:

1. They can be specified only on a single WFC chip;
2. They may have physical but no virtual overscan;
3. They cannot include the CCD edge (i.e. the maximum subarray size is 4140 by 2046); and
4. They are read through a single amplifier and may take longer to readout than a full-frame image, depending on size and location.

Users can use WFC subarrays either by specifying a supported pre-defined subarray (which is recommended) or by defining their own general subarrays. Calibration frames will be provided for supported subarrays only. Users who define general subarrays that cross amplifier boundaries or do not include a corner (not advised) must request their own subarray bias images, and these will typically be scheduled during the following occultation.

Pre-defined subarrays are the appropriate choice for observing a small target when lessening the data volume is desired. On `WFC1`, at the amplifier B corner there are supported square apertures `WFC1-512`, `WFC1-1K`, and `WFC1-2K` with light collecting areas being squares with sides of length 512, 1024, and 2048 pixels. These apertures incorporate 22 columns of the physical overscan pixels. Placing the subarrays at the amplifier corner mitigates the impact of degraded CTE on source photometry, astrometry, and morphology. The reference pixel and extent of the subarrays are listed in Table 7.6. More information about pre-defined subarrray apertures can be found in Section 7.7

To define a general subarray, the available-but-unsupported parameters `SIZEAXIS1`, `SIZEAXIS2`, `CENTERAXIS1`, and `CENTERAXIS2` can be used. More practical information about defining subarrays can be found at:

`http://www.stsci.edu/hst/acs/faqs/subarrays.html`.

When polarizers or the small HRC filter F892N are used with the WFC, the aperture `WFC` must be selected and a subarray is forced by the system. If the user chooses to use a polarizer with a ramp filter, then they may select an available-but-unsupported ramp aperture, but a subarray is still read out.

Ramp Filters

Unlike WFPC2, ACS ramp filter observations at different wavelengths are obtained at the same location on the CCD, thus simplifying data processing. In practice the observer specifies a ramp filter and a central wavelength; the filter wheel is automatically rotated to place the central wavelength at the reference point of the relevant aperture. The different ramp apertures and their reference points on the WFC CCDs are shown in Table 7.6 and Figure 7.4.

To select the desired wavelength, the ramp filter is rotated to move the appropriate part of the filter over the specified pointing. Observations with different ramp filters do not generally occur at the same pointing. The precise location where a given observation will be performed can be found from Table 7.6 where for each ramp filter we list the fiducial pointing for the inner IRAMP, middle MRAMP, and outer ORAMP filter segment. The inner segment corresponds to the WFC1 CCD, while the outer segment corresponds to the WFC2 CCD. The middle segment can be used with either of the WFC CCDs but only the WFC1 aperture is supported.

For any ramp filter observation three ramp filters will end up in the FOV even though the target is properly positioned only for the requested one. However, the user can define a general subarray to read out only the relevant portion of the CCD. Table 5.1 and Table 5.2 can be used to determine if the remaining two ramp filter segments are useful for serendipitous observations. While all fifteen ramp segments can be used with the WFC, only the five middle ramp segments were available with the HRC. Ramps used with the HRC cover the region defined by the `HRC` aperture (Table 7.8). Please refer to Section 7.7 and Section 5.3.1 for further information.

7.3.2 SBC ACCUM Mode

The SBC ACCUM mode accumulates photons into a 1024 by 1024 array, with 16 bits per pixel. The data are sent to the onboard recorder via the internal ACS memory buffer at the end of the exposure. ACCUM is the only mode available for SBC observations; the Time Tag mode of the STIS MAMAs is not available on ACS. The minimum SBC exposure time is 0.1 seconds and the maximum is 1.0 hour. The minimum time between SBC exposures is 40 seconds. Note that the SBC, like the STIS MAMAs, has no read-out noise. As a consequence there is no scientific driver for longer exposure times apart from the small overhead between successive images, described in Section 8.2.

Up to 16 SBC images can be stored in the internal buffer. SBC images can also share the buffer with a single, compressed WFC image.

7.4 Patterns and Dithering

A number of dither patterns are available for ACS that automatically shift the target pointing between exposures. The size of the shifts depends on the purpose of dithering between exposures. It is useful to distinguish between *mosaicing* and *dithering*. Mosaicing is done with the aim of increasing the area covered by a particular set of exposures, while providing a seamless joining of contiguous frames. Dithering is done for a variety of reasons, such as:

- Better removal of detector blemishes,
- Straightforward removal of hot pixels,
- Improving the PSF sampling,
- Improving the photometric accuracy by averaging over flat fielding errors and
- Obtaining a contiguous field of view for the WFC (filling in the interchip gap).

Patterns have been defined that easily implement mosaicing and dithering. These patterns allow exposures to be automatically associated in ***calacs*** pipeline processing with the following restrictions: only exposures obtained within a single visit and exposures whose cumulative offset is under the ~100 arcsecond guide star limitation can be associated. The latter condition includes the dither patterns for all three cameras, the SBC mosaic patterns, the 2-point ACS-WFC-MOSAIC-LINE pattern, and all patterns designed with POS TARGs. These are described in detail on the ACS Dither Web page:

http://www.stsci.edu/hst/acs/proposing/dither.

The plate scale for the WFC varies by about ±5%, so a one pixel dither near the center will be 0.95 or 1.05 pixels near the corners. For this reason, dither patterns should strike a balance between being large enough to reject detector artifacts, and being as compact as possible to maintain the integrity of the pattern over the entire field-of-view. Large displacements will have varying sub-pixel properties across the image.

In addition to the plate scale variation associated with the significant ACS geometric distortion, there can also be a temporal variation of overall image alignment. Some CR-SPLIT images taken during SMOV (SM3B) testing, in which the two components were separated by the scheduling system across orbital occultations (about a one hour gap), showed registration differences of about 0.5 pixels corner-to-corner. Thus, to combine multiple images to create oversampled images at the resolution ACS is capable of providing, the user may need to allow for the general problem of combining distorted, misregistered images. A number of tools are available to help users align and combine dithered data. For information on how best to reduce dithered ACS data we recommend users obtain the *MultiDrizzle Handbook* available at:

http://stsdas.stsci.edu/multidrizzle.

7.5 A Road Map for Optimizing Observations

Dithering and CR-SPLITing more than the minimum recommended values tends to yield higher quality images with fewer residual detector defects, hot pixels or CR signatures in the final combined image. Dithering is recommended over CR-SPLITs since it allows the removal of both detectors artifacts (hot pixels, bad columns, etc.) and cosmic rays. Unfortunately, splitting a given exposure time into several exposures reduces its signal-to-noise when an image is read noise limited. WFC images with exposure times longer than about 500 seconds are background limited, while shorter exposures and narrow band images are read noise limited for all practical exposure times. Thus, the optimal number of CR-SPLITs and dithering positions is a result of a trade-off between completeness of the hot pixel elimination, CR-rejection, final image quality, and optimal S/N. A schematic flow chart of this trade-off is given in Figure 7.2. The main steps in this, possibly iterative, process are the following:

1. Determine the exposure time required to achieve the desired S/N
2. Determine the maximum number of acceptable residual CR in the final combined image. This number depends critically on the scientific objective. For example, for a survey of distant galaxies or a globular cluster color magnitude diagram, a few residual CR will not compromise the scientific output of the observations. In contrast, for a search for an optical counterpart of some radio or gamma ray selected object even one residual CR would not be acceptable over the region of interest. In this latter case, since we expect about ~4% to 7% of the pixels to be affected by CR hits during a one orbit exposure on the WFC, the requirement that no pixel in the final image is affected by CR hits would force one to use at least 4 sub-exposures. For an experiment in which the number of allowed false alarms is zero (e.g., a search for cosmological supernovae), observers may wish to consider using at least twice the number of sub-exposures required to formally avoid coincidences. Note also that given the large number of pixels in the WFC even a few thousand residual CR hits would correspond to only a small fraction of the total number of pixels. In

general, the number of pixels affected by coincident CR hits for a given total exposure time and number of sub-exposures N will be:

$$\left(0.05 \times \frac{ExposureTime}{2400s \times N}\right)^{N} \times 4096^{2}$$

3. Determine whether dithering is required. CR-SPLITs do not mitigate hot pixels, which result from CCD radiation damage and which may persist for weeks if not indefinitely. If such features would critically affect the science, then dithering is required to remove them. For some imaging programs the spatial resolution provided by the WFC and the presence of some detector defects and hot pixels in the final image are acceptable. For such observations, dithering would not be required and one would simply split the exposure time for CR correction. For observations where several orbits worth of data are obtained with each filter, the best strategy is to observe using a sub-pixel dither pattern *without* obtaining multiple images at each position. Since each CR will now influence more than one output pixel the requirement on the number of separate exposures is more stringent than in the simple CR-SPLIT case. If the total exposure time with each filter is short, one will have to compromise between S/N and image quality. In general, dithering with sub-pixel steps increases the number of individual exposures required to eliminate CR hits. Given that the geometric distortion of WFC makes any dithering step non-integer somewhere in the field of view (unless the dither steps are very small, less than 2 pixels), the size of the high image quality field of view also comes into play. If the high quality area being considered is small, the observer may use integer pixel dithers. In this case a few CR-SPLITs may be obtained at each dithering position and the combined images may then be combined together using ***drizzle*** or ***multidrizzle***. On the edges of the field the CR-rejection quality will be lower than in the field center. A minimum of 4 images for a two position dither, and 8 for a four position dither are then required.
4. Once the required number of individual exposures has been established on the basis of CR rejection and dithering requirements, the observer will need to verify whether the resulting read-out noise affects the achieved S/N.

Figure 7.2: Schematic flow-chart of the CR-split vs. dithering vs. S/N trade-off.

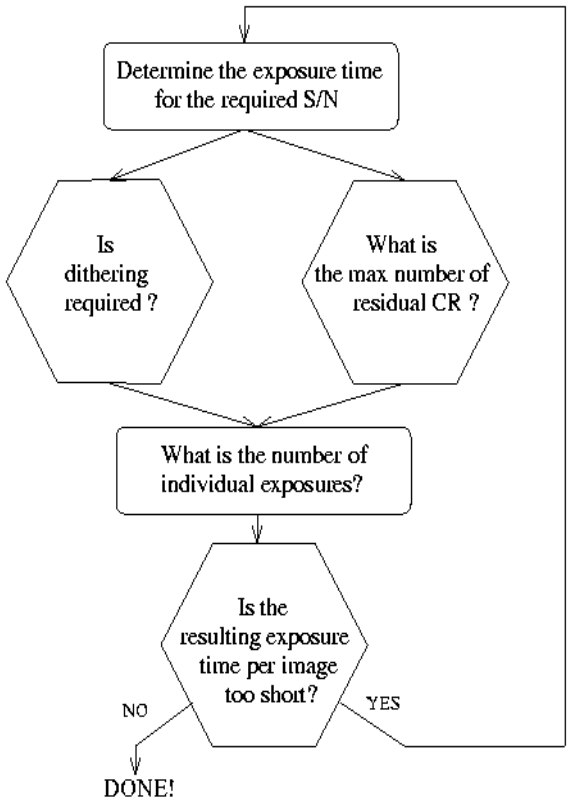

7.6 CCD Gain Selection

Please check for updates on the ACS Web site.

As quantified in Table 4.1, the WFC CCDs have selectable gain values of 0.5, 1.0, 1.4, and 2.0 electrons per digital number. Various factors should influence the gain selected in Phase II for your science program: level of support and calibrations provided, influence of associated readout noise on data quality, dynamic range on the bright end, and data compressibility for WFC in limited applications.

As of Cycle 18, only GAIN 2.0 is fully supported for the WFC. Calibration support will not be provided for the GAIN=0.5, 1.0, and 1.4 settings; users proposing their use should provide special justification and discussion of calibrations to be used. Please note that post-SM4 WFC images appear to have substantial (> 10^{-3} fractional) amplifier crosstalk when the ADC saturates.

GAIN=2 completely samples the full well depth of nearly 85,000 e^-. Furthermore, charge is conserved even beyond filling the full well depth; for point sources at

GAIN=2 it is possible to obtain valid aperture photometry several magnitudes beyond saturation by summing over all pixels affected by the bleeding due to saturation (see Section 4.3.1). GAIN= 2 provides critical sampling of the readout noise, supporting robust background sky-level determination even at low values.

7.7 ACS Apertures

7.7.1 WFC Apertures

The active image area of each WFC detector is 4096 by 2048 pixels. The mean scale is 0.049 arc seconds/pixel, and the combined detectors cover an approximately square area of 202 arc seconds on a side. In establishing reference pixel positions we have to consider the overscan pixel areas which extend 24 pixels beyond the edges in the long direction. So each CCD must be regarded as a 4144 by 2048 pixel area. The gap between the two CCDs is equivalent to 50 pixels. In Figure 7.3 the letters A, B, C, and D show the corner locations of the four readout amplifiers.

We define apertures named `WFC1` and `WFC2` which represent the two CCDs, with their reference points near the geometric center of each chip. The positions have been moved about 50 pixels from the center line to avoid a discontinuity at the amplifier readout boundary. However, we keep two other apertures named `WFC1-FIX` and `WFC2-FIX` at the original central locations (2072,1024). For extended sources, choosing new positions may not be of any advantage and it may be more effective to use these fixed positions.

The aperture `WFC` encompasses both detectors, and has its reference point near the overall center but about 10 arcseconds away from the inter-CCD gap. This reference point is (2124,200) on the WFC1 CCD. Again, this point has been moved away from the center line, but the reference point for `WFC-FIX` remains at (2073,200). Selection of `WFC1`, `WFC2` or `WFC` only changes the pixel where the target will be positioned. In all three cases data is normally delivered in a file containing two science image extensions, one for each detector. See the *ACS Data Handbook* for details of the ACS data format. Reading out a subarray, which consists of part of only one of the CCDs, is done only if requested.

Figure 7.3: WFC aperture definitions.

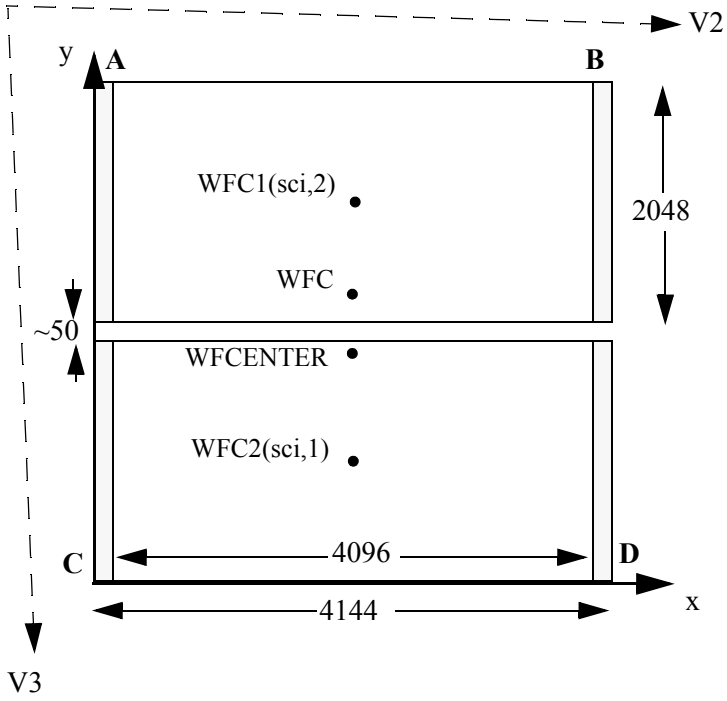

WFCENTER is similar to WFC, but is placed at the center of the combined WFC full field. The center is defined as the average of the four corners in the distortion corrected space. Because of the scale variation this does not appear at the center in pixel space, but rather is on WFC2 about 20 pixels from the edge. Selection of WFCENTER can be of use in obtaining observations with maximum overlap at unique orientations and for mosaics.

For sets of observations which take place over a substantial part of a year, the telescope roll limitations will require measurements to be taken over most of the angular range. On sky, the WFC aperture is roughly square, and it is natural to design observations in steps of 90° to consistently cover the same area. There will be some region at the edges not covered at all four orientations. However, a square area of side 194.8 arcseconds centered on WFCENTER, and with edges parallel to the V2 and V3 axes, is overlapped at all four positions. In designing a mosaic which combines observations at 90° steps, a translation of about 190 arcseconds between pointings would provide continuous coverage.

Figure 7.4: Schematic WFC apertures and ramp filters.

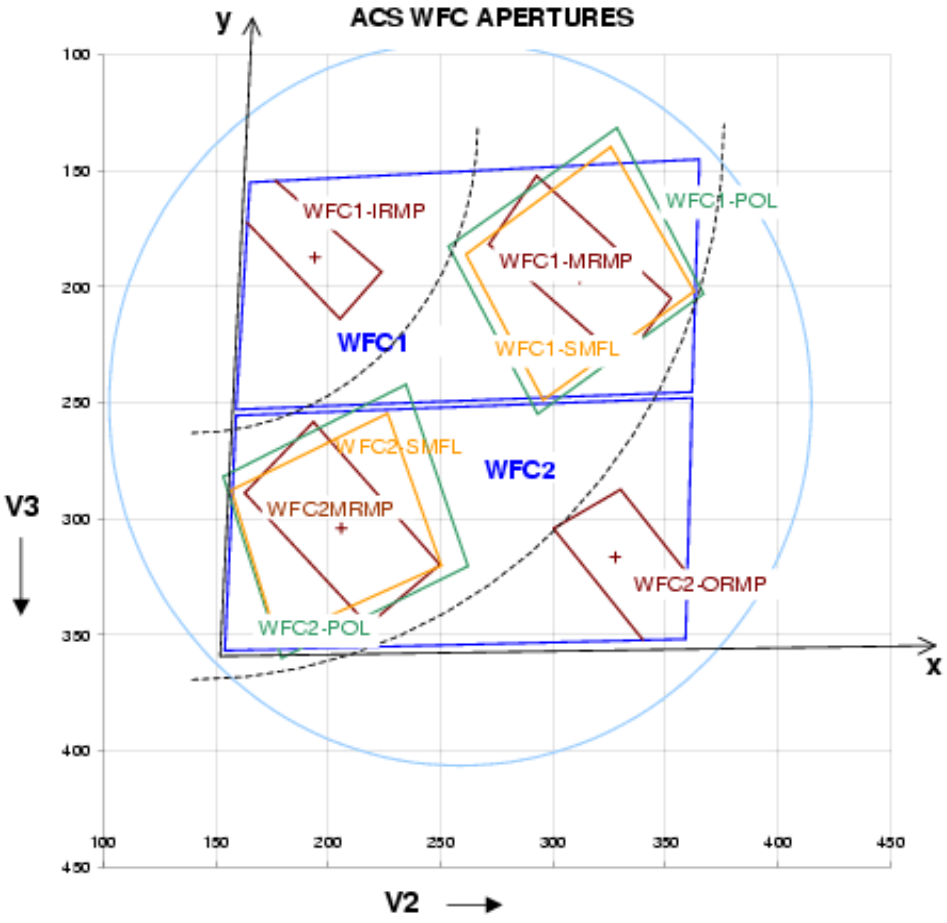

Shown are the approximate active areas defined by the filters. The actual readout areas are the quadrants for the polarizers and small (HRC) filters, and either the quadrant or the full chip for the ramp filters.

7.7.2 Ramp Filter Apertures

WFC Ramp Filter Apertures

There are five ramp filters. Each ramp filter consists of three segments (inner, middle, outer) that can be rotated across the WFC field of view as indicated in Figure 7.4. The IRAMP filters can only be placed on `WFC1` in a location which will define the aperture `WFC1-IRAMP` and the ORAMP filters only on WFC2 creating the aperture `WFC2-ORAMP`. The MRAMP filters can lie on WFC1 or WFC2 with corresponding apertures `WFC1-MRAMP` and `WFC2-MRAMP`. The approximate aperture locations are indicated in Figure 7.4, while actual data obtained during ground calibrations are overlayed on an image of a ramp filter in Figure 7.5. Operationally, a fixed reference point will be defined for each detector and filter combination. Then the ramp filter will be rotated to place the required wavelength at the reference position.

The reference positions for all defined apertures are given in Table 7.6 in pixels, and in the telescope V2,V3 reference frame where values are measured in arc seconds. The values given here are based on in-flight calibration results. The x and y axis angles are measured in degrees from the V3 axis towards the V2 axis. This is in the same sense as measuring from North to East on the sky. The "extent" of the ramp filter apertures given in Table 7.6 are the FWHM of the monochromatic patches (visible in Figure 7.4) measured from a small sample of ground calibration data. To use a ramp filter in a Phase II program, specify the filter name, the central wavelength, and the aperture. The scheduling software will then automatically rotate the filter to the appropriate wavelength, and point at the reference point of the aperture chosen.

The aperture chosen may either be the full CCD or just the quadrant on which the ramp filter lies. This second choice was new as of Cycle 15, and requires that the aperture be specified. The apertures matching each filter are given in Table 7.6. Those with names ending in Q are the quadrants. It will normally be preferable to choose the quadrant aperture to save data volume and buffer dumping time. All apertures may be used with non-ramp filters. A target may thereby be put at the same position using a ramp and a non-ramp filter. Note that the WFC2-MRAMPQ aperture is available but not supported. Please see the footnotes to Table 7.6 for a complete list of available but unsupported apertures.

HRC Ramp Filter Apertures

HRC has been unavailable since January 2007.

Only the middle segments of the five ramp filters could be used with the HRC. They are FR914M, FR459M, FR505N, FR388N and FR656N. All five middle segments could be used with any of the HRC apertures listed in Table 7.7 (see Table 7.8 for the aperture reference positions). There were no special ramp apertures with the HRC because when a ramp filter is used with the HRC it covered the entire HRC CCD. This region was defined by the HRC aperture in Table 7.8. To use the HRC-512 or HRC-SUB1.8 subarray apertures with a ramp filter, POS TARGs had to be used to align the aperture correctly.

As with the WFC, the fixed reference point of the ramp aperture was defined operationally depending on the detector, aperture and filter combination. Please refer to Section 7.3.1, Section 5.3.1, and ACS ISR 02-01 for further information.

Figure 7.5: Monochromatic patches in ground calibration data showing actual aperture sizes through ramp filters (superimposed on photo of ramp filters).

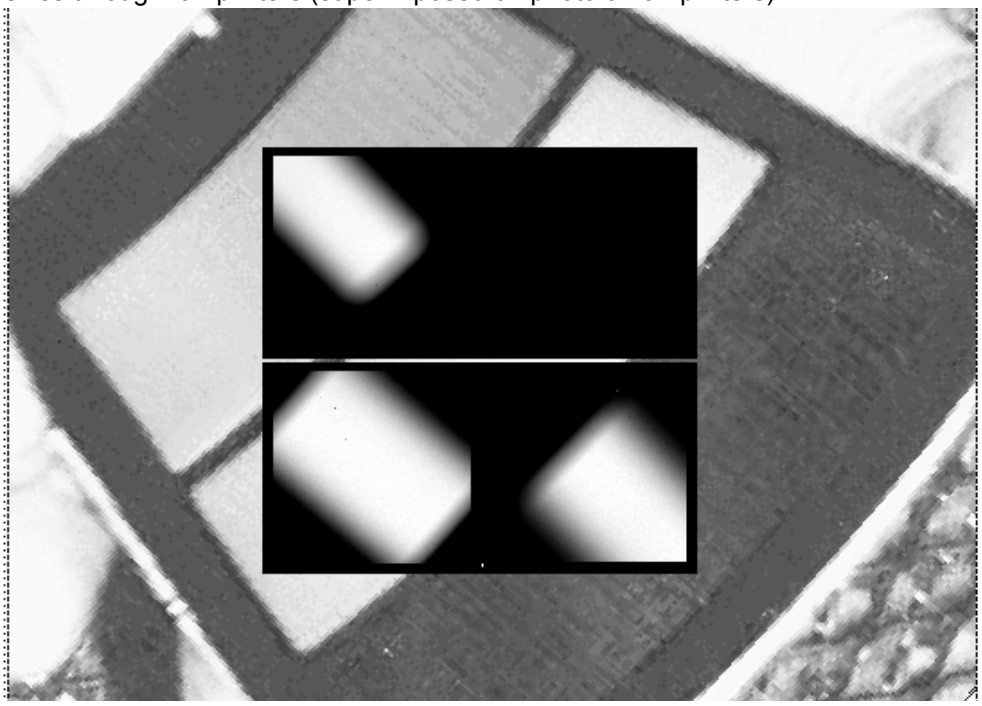

7.7.3 The Small Filter Apertures

When a filter designed for the HRC is used with the WFC, it only covers a small area on either WFC1 or WFC2. The projected filter position may be placed on either chip by selection of the filter wheel setting. Figure 7.4 shows how the filter projection may be placed so as to avoid the borders of the CCDs. When a WFC observation is proposed using a HRC filter spacecraft commanding software automatically uses internal built-in apertures designed for these observing scenarios, called WFC1-SMFL and WFC2-SMFL. Reference positions at or near the center of these apertures are defined so that a target may be placed in the region covered by the chosen filter. Note that WFC2 SMFL is available but not supported.

The axis angles given in Table 7.6 do not refer to the edges of the apertures as drawn, but rather to the orientation of the x and y axes at the WFC reference pixel. These angles vary slightly with position due to geometric distortion.

For the polarizers and F892N used with WFC, the default will be to read out a subarray. The subarray will be a rectangular area with sides parallel to the detector edges which encompasses the indicated filtered areas. For ramp filters the default will be to readout the entire WFC detector, unless a polarizer is used with the ramp filter, in which case a subarray is read out. Users cannot override the small filter subarrays.

Table 7.6: WFC aperture parameters.

APT Aperture Name	Readout area	Extent[1] (arcsec)	Reference pixel	Reference V2,V3 (arcsec)	x-axis angle	y-axis angle
					(degrees from V3 through V2)	
WFC	4096 × 4096	202 × 202	(2124,200) *on WFC1*	(262,239)	92.2	177.5
WFC-FIX	4096 × 4096	202 × 202	(2073,200)	(261,198)	92.5	177.3
WFCENTER	4096 × 4096	202 × 202	(2114,2029) *on WFC2*	(261,252)	92.1	177.5
WFC1	4096 × 4096	202 × 202	(2124, 1024)	(263,198)	92.5	177.4
WFC1-FIX	4096 × 4096	202 × 202	(2072, 1024)	(261,198)	92.5	177.4
WFC2	4096 × 4096	202 × 202	(2124, 1024)	(259,302)	91.7	177.8
WFC2-FIX	4096 × 4096	202 × 202	(2072, 1024)	(257,302)	91.7	177.8
WFC1-IRAMP	4096 × 4096	25 × 65	(680,1325)	(194,187)	93.1	176.6
WFC1-MRAMP	4096 × 4096	35 × 80	(3096,1024)	(312,196)	92.2	177.8
WFC2-MRAMP	4096 × 4096	40 × 80	(1048,1024)	(206,304)	91.9	177.5
WFC2-ORAMP	4096 × 4096	35 × 65	(3494,708)	(328,316)	91.4	178.2
WFC1-SMFL[2]	2048 × 2048	70 × 80	(3096,1024)	(312,196)	92.2	177.8
WFC2-SMFL[2 3]	2048 × 2048	70 × 80	(1048,1024)	(206,304)	91.9	177.5
WFC1-POL0UV [4]	2048 × 2048	90 × 80	(3096,1024)	(312,196)	92.1	177.8
WFC1-POL0V [4]	2048 × 2048	90 × 80	(3096,1024)	(312,196)	92.2	177.8
WFC2-POL0UV [3 4]	2048 × 2048	90 × 80	(1048,1024)	(206,304)	91.9	177.5
WFC2-POL0V [3 4]	2048 × 2048	90 × 80	(1048,1024)	(206,304)	91.9	177.5
WFC1-512	512 × 512	25 × 25	(3864,1792)	(352,158)	92.1	178.0
WFC1-1K	1024 × 1024	50 × 50	(3608,1536)	(338,170)	92.1	177.9
WFC1-2K	2048 × 2048	101 × 101	(3096,1024)	(312,196)	92.2	177.8
WFC2-2K [3]	2048 × 2048	101 × 101	(1048,1024)	(206,304)	91.9	177.5
WFC1-IRAMPQ	2048 × 2048	25 × 65	(680,1325)	(194,187)	93.1	176.6
WFC1-MRAMPQ	2048 × 2048	35 × 80	(3096,1024)	(312,196)	92.2	177.8
WFC2-MRAMPQ [3]	2048 × 2048	40 × 80	(1048,1024)	(206,304)	91.9	177.5
WFC2-ORAMPQ	2048 × 2048	35 × 65	(3494,708)	(328,316)	91.4	178.2
WFC1-CTE	4096 × 4096	202 × 202	(3920,1848)	(354,155)	92.1	178

1. Extent (arcsec) is the smaller of actual pixel domain readout and the area actively exposed to sky. For RAMP associated apertures the leading dimension is size yielding coverage at the specified wavelength.
2. Apertures are automatically created by commanding software when a HRC filter is used in WFC observations. (Apertures are not listed in the APT aperture pull-down menu.)
3. **These are available but unsupported modes.**
4. Apertures are automatically created by commanding software when a polarizer filter is used. Same parameters apply for POL60 and POL120 in V and UV. (Apertures are not listed in the APT aperture pull-down menu.)

Table 7.7: Ramp filter apertures.

Detector	Filter	Ramp Segment	Full-frame apertures	Quadrant or subarray aperture
WFC	FR423N FR716N FR853N FR5551N FR647M	Inner	WFC1-IRAMP	WFC1-IRAMPQ
	FR388N FR656N FR459M FR505N FR914M	Middle	WFC1-MRAMP	WFC1-MRAMPQ
	FR462N FR782N FR931N FR1016N FR601N	Outer	WFC2-ORAMP	WFC2-ORAMPQ
HRC	FR914M FR459M FR505N FR388N FR656N	Middle	HRC HRC-FIX	HRC-CORON1.8 HRC-CORON3.0 HRC-OCCULT08 HRC-ACQ HRC-SUB1.8

7.7.4 Polarizer Apertures

Apertures have been provided for use with the polarizer sets similar to the SMFL apertures. These apertures are selected automatically when a polarizing spectral element is used, and a single WFC chip quadrant readout is obtained. The aperture parameters given in Table 7.6 are valid for all three polarizing filters in each polarizer set, UV or visible, to the stated significant figures.

7.7.5 HRC Apertures

Information regarding the HRC is provided for archival purposes only.

The HRC has an area of 1062 pixels by 1024 pixels including 19 physical overscan pixels at each end in the x direction. The active area is 1024 by 1024 pixels. The mean scales along the x and y directions are 0.028 and 0.025 arcseconds/pixel, thus providing a field of view of about 29 by 26 arcseconds in extent. The anisotropy and variation of scales is discussed in Section 10.3 of this Instrument Handbook. The reference point for the aperture labelled HRC-FIX, and initially for HRC, is at the

geometric center, (531,512). As with the WFC apertures, there may be reason to move the HRC reference point later.

Figure 7.6: HRC coronagraphic finger and spots (left), coronagraphic finger always in data (right)

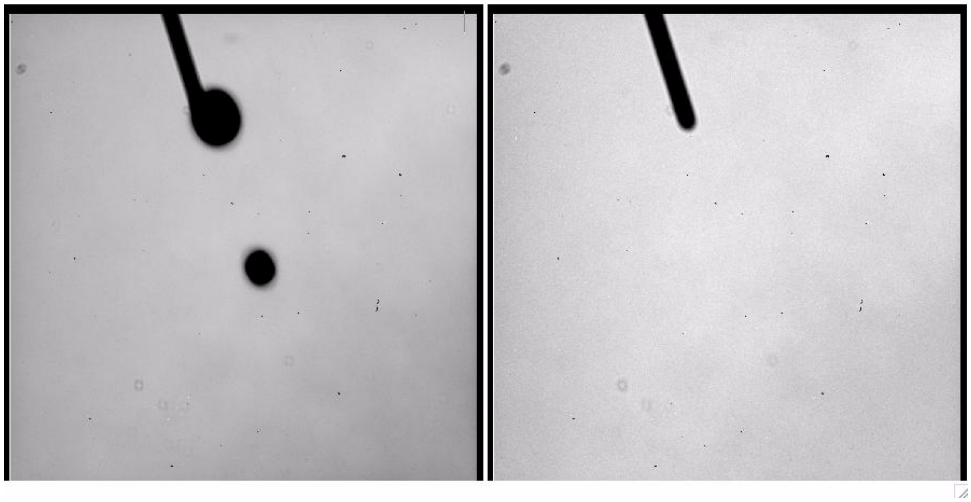

The HRC is equipped with two coronagraphic spots, nominally 1.8 and 3.0 arcseconds in diameter and a coronagraphic finger, 0.8 arcseconds in width. Apertures HRC-CORON1.8, HRC-CORON3.0, and HRC-OCCULT0.8 are defined to correspond to these features. The coronagraphic spots are only in the optical train and thus in the data if HRC-CORON1.8 or HRC-CORON 3.0 are specified. Their positions are shown in Figure 7.6 (left panel). In addition we define a target acquisition aperture, HRC-ACQ designed for acquiring targets which are subsequently automatically placed behind a coronagraphic spot or the occultation finger. The positions of the coronagraphic spots have been found to fluctuate. Observations will need to incorporate a USE OFFSET special requirement to allow current values to be inserted at the time of the observation.

A substantial region masked out by the occulting finger will be present in the HRC data (Figure 7.6, right panel). The occulting finger is not retractable. It will be in every HRC exposure. However as with any other detector feature or artifact, the "lost" data can be recovered by combining exposures which were suitably shifted with respect to each other. A dither pattern, ACS-HRC-DITHER-LINE has been defined for this purpose and spans the area flagged for the HRC occulting finger (~1.6 arcseconds or ~56 pixels wide), with an extra ~0.3 arcseconds or ~10 pixels of overlap.

Table 7.8: HRC aperture parameters.

APT Aperture Name	Active area	Extent (arcsec)	Reference pixel	Reference V2,V3 (arcsec)	x-axis angle	y-axis angle
HRC	1024 × 1024	29 × 26	(531, 512)	(206,472)	-84.1	0.1
HRC-FIX	1024 × 1024	29 × 26	(531, 512)	(206,472)	-84.1	0.1
HRC-CORON1.8	200 × 200	6 × 5	(564,466)[1]	(205,471)[1]	-84.1	0.1
HRC-CORON3.0	200 × 200	6 × 5	(467,794)[1]	(208,479)[1]	-84.2	0.1
HRC-OCCULTO.8	200 × 200	6 × 5	(443,791)	(209,477)	-84.2	0.2
HRC-ACQ	200 × 200	6 × 5	(735,575)	(200,474)	-84.1	0.0
HRC-512	512 × 512	15 × 13	(276,256)	(214,465)	-84.1	0.2
HRC-SUB1.8	512 × 512	15 × 13	(570,468)	(205,471)	-84.1	0.1
HRC-PRISM [2]	744 × 1024	21 × 26	(671,512)	(214,471)	-84.2	0.2

1. These values fluctuate and will be updated at the time of the observation.
2. HRC-PRISM is automatically created by commanding software when spectral element PR200L and aperture HRC are selected in APT.

Use of the prism PR200L requires specifying aperture HRC, but results in a reference point of (671,512) to optimally center the target coordinates within the somewhat vignetted prism field of view. Although the HRC direct imaging and PR200L prism apertures have the same name in APT, they are actually distinct, and *HST* executes a small angle maneuver between observations of a given target with them, to compensate for the positional deflection by the prism. One consequence is that the Special Requirement SAME POS AS cannot be used among mixed direct and prism exposures, as always with different apertures.

7.7.6 SBC Apertures

The SBC aperture is 1024 pixels square. There are no overscan pixels to consider. The x and y scales are 0.034 and 0.030 arcseconds/pixel leading to a coverage on the sky of 35 by 31 arcseconds. The reference point has been moved to (512,400) to place targets further from a bad anode which disables several rows of the detector near y = 600. As with the CCDs we maintain an SBC-FIX aperture which will always have position (512,512). MAMA detectors slowly lose efficiency with each exposure, therefore the SBC reference point may be shifted again if the chosen position shows this effect to a measurable degree.

The (512,512) reference point falls near to the same position in (V2,V3) as the HRC, namely (205, 470), and the x and y axis angles are –85.4° and –0.9°.

Use of either prism PR110L or PR130L requires use of aperture SBC and results in a reference point of (425,400) to optimally center the target coordinates with respect to vignetting on the right side of the field and to avoid a set of bad rows at 599 to 605.

Although the SBC direct imaging and prism apertures have the same name in APT, they are actually distinct, and *HST* executes a small angle maneuver between observations of a given target with them, to compensate for the positional deflection by the prisms. One consequence is that the Special Requirement `SAME POS AS` cannot be used among mixed direct and prism exposures. Figure 7.7 shows a direct and prism observation of the same field. The prism now is vignetted on the positive x side. The reference points and the small angle maneuver place the same target near the reference point of each view.

Table 7.9: SBC aperture parameters

APT Aperture Name	Active area	Extent (arcsec)	Reference pixel	Reference V2,V3 (arcsec)	x-axis angle	y-axis angle
SBC	1024 × 1024	34 × 31	(512, 400)	(205, 467)	-84.7	-0.2
SBC-FIX	1024 × 1024	34 × 31	(512, 512)	(205, 470)	-84.7	-0.2
SBC-PRISM[1]	1024 × 1024	28 × 31	(425, 400)	(203, 467)	-84.7	-0.2

1. SBC-PRISM is automatically created by commanding software when spectral elements PR110L and PR130L, and aperture SBC, are selected in APT.

Figure 7.7: Direct and prism observations of NGC6681.

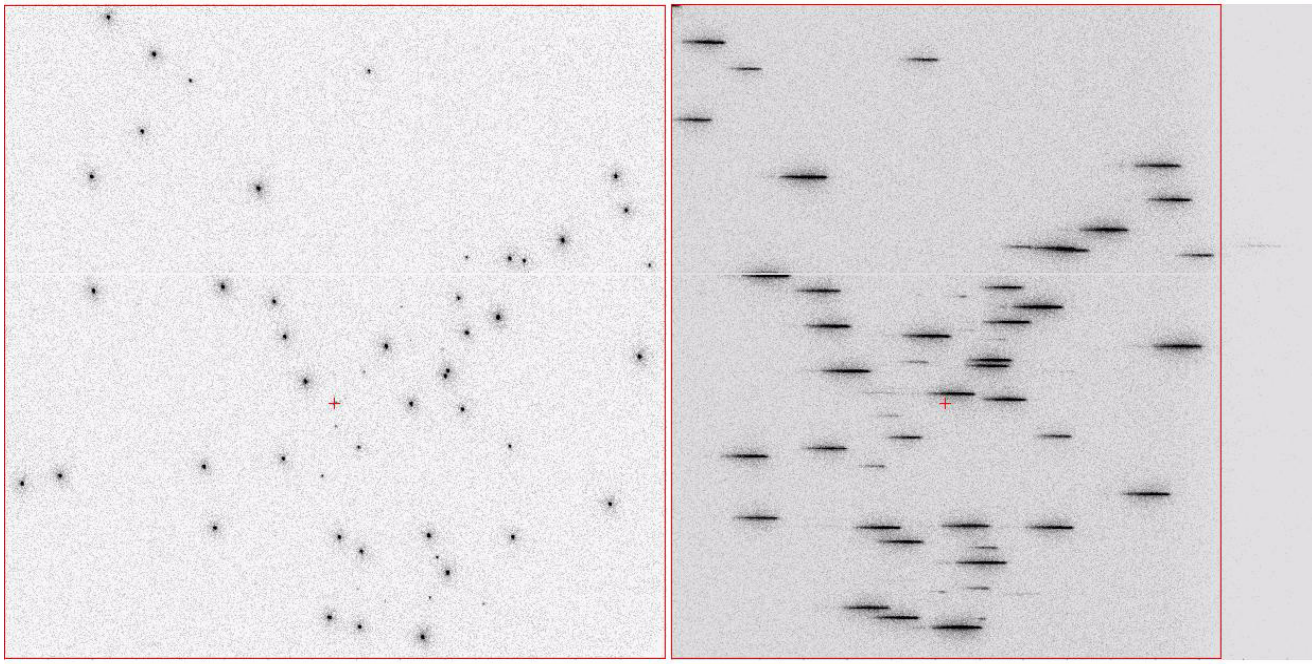

Direct and prism observations of NGC6681. The reference point is defined to be at the center of each aperture in the x direction but below the center in the y direction to avoid the bad rows.

7.8 Specifying Orientation on the Sky

Determining the orientation of an image requires knowledge of the telescope roll and the angle of the aperture relative to the *HST* coordinate frame. A target may need to be oriented in a preferred direction on a detector, particularly when spectroscopy is to be performed.

To specify an ORIENT in Phase II, note that this parameter is just the usual PA (Position Angle) of the *HST* U3 axis (= −V3, see below); see Figure 3.1 and Figure 7.9 in this Handbook, as well as the *Phase II Proposal Instructions*. APT provides a convenient interactive display of the aperture and orientations in your field. The ORIENT parameter is related to the following discussion of ACS geometry.

All *HST* aperture positions and orientations are defined within an orthogonal coordinate system labeled V1,V2,V3, in which V1 is nominally along the telescope roll axis. Apertures are therefore in the V2,V3 plane. For more information about *HST* instrument aperture locations and axes in the *HST* FOV, please visit the Observatory Support Web page section on apertures at:

http://www.stsci.edu/hst/observatory/apertures.

The V3 position angle *p* is defined as the angle of the projection of the V3 axis on the sky, measured from North towards East with the aperture denoting the origin. This is almost identical to the telescope roll angle. (There is a small difference between roll angles measured at the V1 axis and those measured at the aperture. This can amount to several tenths of a degree depending on the target declination.) When the position angle is zero, V3 points North and V2 points East. In the V2V3 coordinate system, as shown in Figure 7.8, aperture orientations are defined by β_x and β_y, the angles their x and y axes make with the V3 axis, measured in an anti-clockwise direction. (The value of β_x as illustrated in Figure 7.8, would be considered negative.) Hence, the angles these axes make with North are found by adding the axis angles to the position angle.

Figure 7.8: Aperture and image feature orientation.

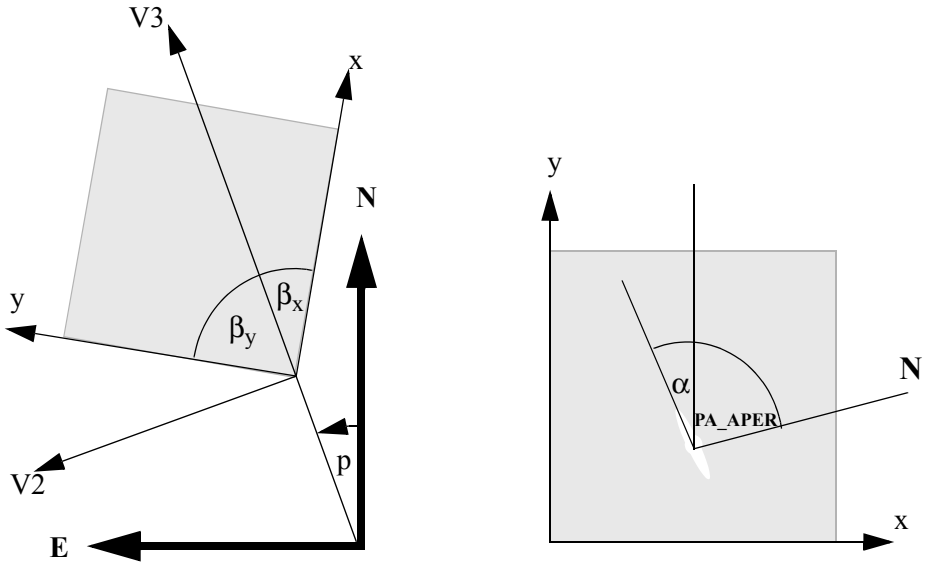

The science image header supplies the value of ORIENTAT, the angle the detector y axis makes with North, which is equal to $p + \beta_y$. Another angle keyword supplied is PA_APER which is the angle the aperture y axis makes with North. Both angles are defined at the aperture so using them does not involve the displacement difference. Normally the aperture and detector y axes are parallel, and so PA_APER = ORIENTAT. Several STIS slit apertures were not aligned parallel to the detector axes, so this distinction was meaningful, but ACS has no slit apertures so this difference will probably not arise. In any case, we recommend using PA_APER.

Beyond establishing the direction of the aperture axes, it will often be necessary to know the orientation of a feature, such as the plane of a galaxy, within an image. Conversely, we need to know what direction within an image corresponds to North. To this end we define a feature angle α within the aperture as measured on the science image, anti-clockwise from the y-axis so that it is in the same sense as the previously defined angles. For an orthogonal set of aperture axes the direction of this feature would be PA_APER + α and the image direction of North would be the value of α which makes this angle zero, namely −PA_APER, still measured in an anti-clockwise direction from the y axis.

Figure 7.9: ACS apertures in the V2/V3 reference frame.

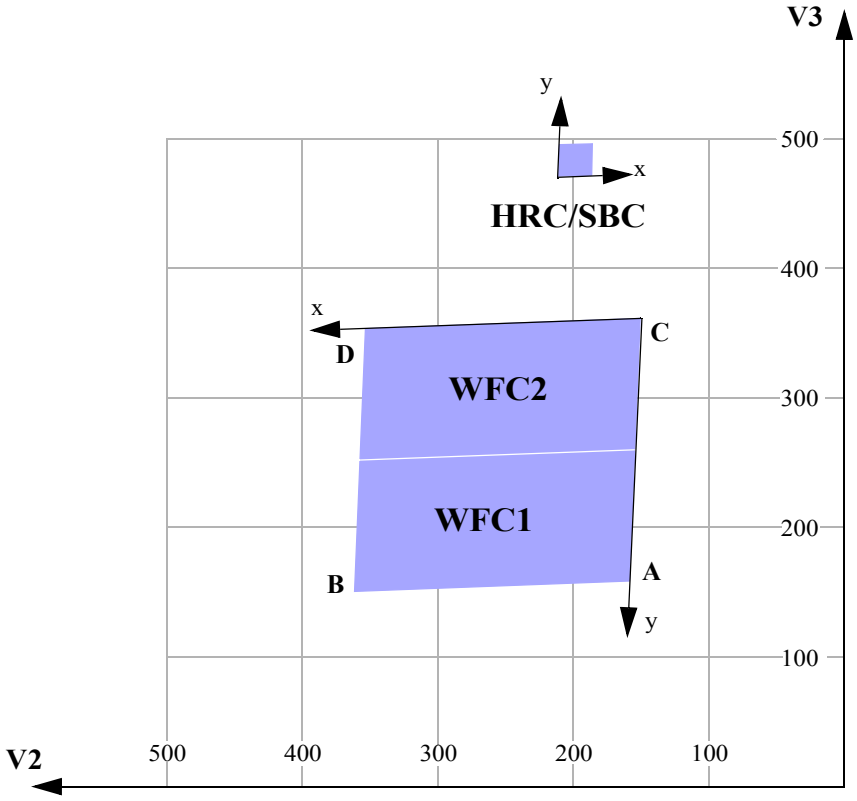

The readout amplifiers (A,B,C,D) are indicated on the figure. The WFC data products from the calibration pipeline will be oriented so that WFC1 (chip 1, which uses amps A and B) is on top. The HRC data products will also be oriented such that amps A and B are on top, but they will be inverted from WFC images with respect to the sky

The x and y axes projected on the sky are not necessarily orthogonal. For all instruments prior to the ACS the departure from orthogonality has been negligible, but for the ACS the angle between the axes is about 85°. Figure 7.9 realistically represents the alignment of the ACS apertures and shows that the apertures are not square. The x and y axes indicated are those that will be used for the science images. The V2,V3 coordinates can be calculated from the x, y coordinates according to

$$V2 = V2_0 + s_x \sin\beta_x x + s_y \sin\beta_y y$$

$$V3 = V3_0 + s_x \cos\beta_x x + s_y \cos\beta_y y$$

where s_x and s_y are scales in arcseconds per pixel along the image x and y axes. $V2_0$ and $V3_0$ are the coordinates of the aperture origin, but they do not enter into the angle calculations. Figure 7.9 shows that a rotation from x to y is in the opposite sense to a rotation from V2 to V3. This will be the arrangement for ACS apertures. This is significant in defining the sense of the rotation angles. For a direction specified by displacements Δx and Δy in the image, the angle α is $\arctan(-\Delta x/\Delta y)$.

Because of the oblique coordinates, the angle α_s on the sky will not be equal to α. To calculate the sky angle, it is convenient to define another set of orthogonal axes x_s, y_s, similar to the V2V3 but rotated so that y_s lies along y, and x_s is approximately in

the x direction. Let $\omega = \beta_y - \beta_x$ be the angle between the projected detector axes and for simplicity let their origins be coincident.Then the transformation is

$$x_s = s_x \sin\omega x$$

$$y_s = s_x \cos\omega x + s_y y$$

By comparing differentials and defining α_s as arctan($-\Delta x_s/\Delta y_s$) we find

$$\tan\alpha_s = \frac{s_x \sin\omega \sin\alpha}{s_y \cos\alpha - s_x \cos\omega \sin\alpha}$$

The equation as written will place the angle in the proper quadrant if the ATAN2 Fortran function or the IDL ATAN function is used. To get the true angle East of North, for a feature seen at angle α in the image, calculate α_s and add to PA_APER.

The inverse relation is

$$\tan\alpha = \frac{s_y \sin\alpha_s}{s_x \sin(\alpha_s + \omega)}$$

To find the value of α corresponding to North we need the value of α_s such that PA_APER $+ \alpha_s = 0$. So substitute $-$PA_APER for α_s in the equation to get the angle α in the image which corresponds to North. The values of the scales and axis angles for all instruments are maintained on an Observatory Science Group Web page.

For the ACS apertures, the values in Table 7.10 have been derived from results of operating the ACS in the Refractive Aberrated Simulator. These should not be considered as true calibrations but they indicate some aperture features, such as the non-orthogonality of the aperture axes, and the x and y scale differences for HRC and SBC.

Table 7.10: Plate scales and axis angles for the 3 ACS channels.

	s_x	s_y	β_x	β_y	$\beta_y - \beta_x$
	arcsec/pixel		degrees		
WFC	.0494	.0494	92.2	177.528	85.3
HRC	.0284	.0248	-84.1	0.081	84.2
SBC	.0338	.0301	-84.6	-0.1	84.5

7.8.1 Determining Orientation for Phase II

A particular orientation is specified in an *HST* Phase II proposal using yet another coordinate system: U2,U3. These axes are opposite to V2 and V3, so, for example, U3 = –V3. The angle ORIENT, used in a Phase II proposal to specify a particular spacecraft orientation, is the position angle of U3 measured from North towards East. The direction of the V3 axis with respect to North is PA_APER $- \beta_y$ and so

$$\text{ORIENT} = \text{PA\_APER} - \beta_y \pm 180°.$$

The IRAF task ***rotate*** in the package ***images.geom*** takes a drizzled image and rotates it counter-clockwise by a specified angle. To orient the image so that its y axis becomes North, the angle to specify is `PA_APER`. The x axis of the coordinate system will then point East. Orientations can be checked by using APT.

7.9 Parallel Observations

7.9.1 Parallel Observing

Parallel observing allows *HST* to operate several other instruments while the prime instrument is executing its observations. While the primary instrument observes a fixed target at user-specified coordinates, the parallel instrument observes at coordinates 5 to 10 arcminutes away, depending on the parallel instrument. The *HST* field of view following SM4 (Figure 3.1) shows the general locations of the instrument apertures adjacent to one another on the sky. Accurate relative positions for all instruments can be found on STScI's Observatory Web page in the Pointing section.

The recommended method of determining the field of view for any instrument is to use APT. A Digital Sky Survey (or user supplied) image of the primary target area is displayed with an *HST* field of view overlay. Any desired coordinate and `ORIENT` combination for the primary target will then display the possible pointings of any instrument operated in parallel. If the primary exposure will execute at a known (absolute) orientation, APT will display the exact field of view for any instrument executed in parallel. If the primary exposure will execute at a random (nominal) orient or range of orient values, APT allows the *HST* field of view to be rotated interactively about the primary pointing. APT can be a valuable resource for parallel observing programs, especially those designed for, or restricted to specific pointings for the parallel FOV.

Certain operating limits are in place to restrict use of configurations, modes, parameters, elements, and requirements allowed for each instrument while used in parallel. Details on these limits are documented in the *Call for Proposals* and *Primer*. General information on ACS specific parallel operations are documented in the following sections for each of the three types of ACS parallel observing: coordinated, auto, and pure.

ACS Coordinated Parallels

Coordinated parallel observations are specified in the same Phase II observing program as the primary observations via the prime and parallel group containers in APT. A single ACS channel may be used for a coordinated parallel observation, with, and only with, another instrument. Coordinated parallels cannot be used to operate any of the ACS channels simultaneously. ACS exposures may not be used as both the prime and parallel exposures within the same parallel container.

In order to protect the ACS SBC detector from inadvertent over-illumination, the ACS/SBC configuration is no longer supported as a coordinated parallel.

Users frequently wish to employ ACS and WFC3 in parallel. Because users also generally want to dither their observations, exposures of these two cameras are generally taken synchronously. However, both ACS and WFC3 images must first be loaded into and then transferred from the camera buffers to the solid state data recorders (SSDRs). The ACS buffer can only hold one image, while the WFC3 buffer can hold two optical images and two or more NIR images, depending on the number of NIR readouts per image. However images from these cameras cannot be transferred to the SSDRs simultaneously, and each transfer takes about 350 seconds. It is possible to take at least three images per orbit in each of the two cameras.

ACS Pure Parallels

In ACS pure parallel observations, an observation is taken with ACS on an essentially random area of the sky while another instrument is making prime observations. No SBC pure parallels will be allowed due to bright object concerns.

Unlike the previous two types of parallel programs, pure parallels contain only parallel visits. Use of the GO/PAR proposal category will make any visit in the program a pure parallel.

The ACS default (archival) pure parallel program continued to execute for the community until midway through Cycle 13 when all of the "Default" *HST* archival pure parallel programs were discontinued to prolong the lifetime of transmitters on *HST*. This non-proprietary data came from programs 9575, 9584, and 9701. A list of all pure parallel datasets in the *HST* archive is at:

`http://www.stsci.edu/instruments/parallels/retrieve.html.`

Observers can request ACS pure parallels; however, there are many constraints which can render pure parallels unselectable in any given orbit. Pure parallels will always be given lower priority than primaries, and are thus scheduled only on a non-interference basis. Users should consult the *Call for Proposals* for more information about pure parallel opportunities with ACS.

7.10 Pointing Stability for Moving Targets

Observations of Solar System targets are subject to some special limitations on the achievable pointing stability during a visit. These limitations apply to both two-gyro and three-gyro operations.

For moving targets, the *HST* ground system assumes that the position of the target as seen from the center of the Earth can be approximated as a linear function of time. This is done using rates of motion calculated from the object's ephemeris for a time near the start of each orbit. If the target's geocentric ephemeris departs significantly from this linear approximation over the course of an orbit, this can lead to small but noticeable pointing offsets. If you think this may adversely affect your science, please consult with your PC about possible strategies for ameliorating this effect.

The correction for the variable parallax to a Solar System object due to *HST*'s orbit around the Earth is calculated on-orbit using the best ephemeris for *HST*'s orbit that

was available at the time the detailed weekly schedule was created. However, the real position of *HST* along its orbit often differs by up to 1 to 2 seconds (7 to 15 kilometers) from the predicted ephemeris position. This leads to small errors in the phasing of the calculated parallax correction. For example, when observing a Solar System object at a distance of 0.5 AU from the Earth, this can cause typical pointing offsets over the course of an orbit of order 20 to 40 milliarcseconds. As these offsets depend on unpredictable changes in *HST*'s orbit, such drifts are unavoidable when observing near-Earth objects.

CHAPTER 8:

Overheads and Orbit-Time Determination

In this chapter. . .

8.1 Overview

After you establish a set of scientific exposures, as well as any additional target acquisition or calibration exposures required for your program, you are ready to determine the total number of orbits to request. Generally, this straightforward exercise involves compiling the overheads for individual exposures, packing exposure plus overhead time into individual orbits, and tallying up the results to determine the total number of orbits needed. It may be an iterative process as you refine your exposures to better use the orbit visibility times.

The Phase I Call for Proposals includes instructions that provide information on the Observatory policies and practices with respect to orbit time requests. The *HST Primer* provides specific advice on orbit determination. Below, we provide a summary of the ACS specific overheads, and give several examples that illustrate how to calculate your orbit requirements for a Phase I Proposal.

8.2 ACS Exposure Overheads

Please check for updates on the ACS Web site.

Exposure overheads are summarized in Table 8.1 and Table 8.2. All numbers given are approximate; they do not make detailed differentiations between overheads for different ACS modes and configurations. These overhead times are to be used (in conjunction with the actual exposure times and the instructions in the *HST Primer* to estimate the total number of orbits for your proposal. After your *HST* proposal is accepted, you will be asked to submit a Phase II proposal to support scheduling of your approved observations. At that time you will be presented with actual, up-to-date overheads by the APT scheduling software. *Allowing sufficient time for overhead in your Phase I proposal is important; additional time to cover unplanned overhead will not be granted later.*

The following list presents important points for each type of overhead:

- ***Generic (Observatory Level) Overheads:***
  - The first time you acquire an object you must include overhead for the guide-star acquisition (6 minutes).
  - In subsequent contiguous orbits you must include the overhead for the guide-star reacquisition (6 minutes); if you are observing in the Continuous Viewing Zone (see the *Phase I Proposal Instructions*), no guide-star *reacquisitions* are required.
  - Allocate some time for each deliberate movement of the telescope; e.g., if you are performing a target acquisition exposure on a nearby star and then offsetting to your target, or if you are taking a series of exposures in which you move the target on the detector, you must allow time for the moves (20 seconds to 60 seconds, depending on the size of the slew (see Table 8.1 and Table 8.2).

Table 8.1: Science exposure overheads: general.

Action	Overhead
	Generic (observatory level)
Guide-star acquisition	Initial acquisition overhead = 6 minutes. Reacquisitions on subsequent orbits = 6 minutes per orbit.
Spacecraft moves	For offsets less than 1.5 arcminutes and more than 10 arcseconds = 1 minute. For offsets between 10 arcseconds and 1 arcseconds = 0.5 minutes. For offsets less than 1 arcseconds in size = 20 seconds.

Table 8.2: ACS science exposure overhead times (minutes).

Exposure type	WFC	SBC
Mode: ACCUM		
Single exposure or the first exposure in a series of identical exposures.	4.0	1.4
Subsequent identical exposures in series (within an orbit).	2.5	0.6
Additional overhead for each serial buffer dump (added when WFC exposures are less than 339 seconds long, or the buffer fills with short SBC exposures).	5.8	5.8
Predefined imaging exposure for prism spectroscopy.	N/A	N/A
Predefined imaging exposure for grism spectroscopy.	7	N/A

Onboard Target-Acquisition Overheads:

HRC has been unavailable since January 2007.

- On board target acquisitions only need to be done to place the target under one of the coronagraphic spots.
- An on board target acquisition needs to be done only once for a series of observations in contiguous orbits (i.e., once per visit).
- The drift rate induced by the observatory is less than 10 milliarcseconds per hour. Thermal drifts internal to ACS are even smaller.

- ***Scientific Exposures:***
  - The overhead times are dominated by the time to move the filter wheel, the CCD readout time, and any necessary serial buffer dumps. Again, it should be stressed that in Phase II, the overheads will frequently be less, but it is important to plan Phase I using the conservative overheads given in Table 8.2 to ensure adequate time for the proposal's scientific goals.
- ***Spectroscopy:***
  - Each CCD spectroscopic observation is preceded by an imaging exposure used for calibration, with exposure times of 3 and 6 minutes, respectively, for grism and prism observations. SBC prism exposures are not preceded by an automatic calibration exposure. Technically this is an individual single exposure requiring all regular science exposure overheads. For the observer, however, it represents an additional overhead in the observation time budget, so it has been included in the table of instrument overhead times for science exposures. However, if the observing

program is already taking an appropriate broadband image, the automatic imaging and associated overheads preceding the spectroscopic grism or prism observations can be avoided by invoking the Optional Parameter AUTOIMAGE=NO during the Phase II preparations. More details can be found in the *Phase II Proposal Instructions*.

Note that identical exposures are generated automatically if the observer specifies the proposal optional parameters CR-SPLIT (for n > 1), or PATTERN, or if Number_of_Iterations > 1. If it is not specified, CR-SPLIT defaults to n = 2. In general, identical exposures are defined here as exposures of the same target, with the same detector and filter(s). For identical exposures in PATTERNS, this also involves slews and therefore slew overheads.

The overhead time for serial buffer dumps arises in certain cases from the overheads associated with the onboard data management and switching over the cameras. The on-board buffer memory can hold no more than one WFC image. The next WFC image can be placed into the buffer only after the buffer has dumped the previous image, which takes 349 seconds.

If the next exposure time is longer than 339 seconds, the buffer dump will occur during that exposure, and no overhead is imposed. However, if the next exposure time is shorter than 339 seconds, then the dump must occur between the two exposures.

Sequences of many short SBC exposures can also lead to serial dumps when the buffer becomes full. In this case the buffer dump time becomes an overhead to be included into the orbit time budget. This overhead can severely constrain the number of short exposures one can squeeze into an orbit. Subarrays can be used to lower the data volume for some applications.

8.2.1 Subarrays

At the end of each exposure, data are read out into ACS's internal buffer memory where they are stored until they are dumped into *HST*'s solid state data recorder. The ACS internal buffer memory holds 34 MB or the equivalent of 1 full WFC frame, or 16 SBC frames. Thus, after observing a full WFC frame, the internal buffer memory must be dumped before the next exposure can be taken. The buffer dump takes 349 seconds and may not occur while ACS is being actively commanded. Of this time, 339 seconds is spent dumping the image. The buffer dump cannot be done during the next exposure if the latter is shorter than 339 seconds. If, however, the next exposure is less than 339 seconds the buffer dump will create an extra 5.8 minutes of overhead.

If your science program is such that a smaller FOV can be used, then one way of possibly reducing the frequency and hence overheads associated with buffer dumps is to use WFC subarrays. With subarrays, only the selected region of the detector is read

out at a normal speed and stored in the buffer, and a larger number of frames can be stored before requiring a dump. Using subarrays not only reduces the amount of time spent dumping the buffer but in some cases may reduce the readout time. See Chapter 7 for a discussion of some of the limitations of subarrays. If the user elects to define a subarray of arbitrary size and location, allowed on an available-but-unsupported basis, then matching bias frames will not be automatically provided by STScI. Any bias frames specified by the user will typically be scheduled during the following occultation (i.e., they do not add to the overheads during visibility time). Dark frames and flat fields will be extracted from full frame images.

8.3 Orbit Use Determination Examples

The easiest way to learn to compute total orbit time requests is to work through a few examples. Below we provide five different examples:

- Example in Section 8.3.1 is a simple WFC image in one filter.
- Example in Section 8.3.2 is a set of short WFC exposures that may require large overheads associated with buffer dumps.
- Example in Section 8.3.3 is a two-orbit observation using dithering.
- Example in Section 8.3.4 is a one orbit WFC grism spectroscopic observation.
- Example in Section 8.3.5 is a 2-orbit SBC observation.

These examples represent fairly typical uses of ACS.

8.3.1 Sample Orbit Calculation 1:

Consider a target to be imaged with WFC in a given filter in one orbit. Using the ETC, we find that we need 2400 seconds of exposure time to reach the desired level of signal-to-noise ratio. Given that the observation must be split into a series of two exposures by CR-SPLIT (`CR-SPLIT=2`), we map the overheads and the science exposure times onto the orbit as follows:

Table 8.3: Orbit calculation for example 1.

Action	Time (minutes)	Explanation
Orbit 1		
Initial guide-star acquisition	6.0	Needed at start of observation of a new target
WFC overhead for the first exposure	4.0	Includes filter change, camera set-up, and readout
First science exposure	20.0	
WFC overhead for the subsequent science exposure in the series	2.5	Includes readout
The next science exposure in the series	20.0	
Total time for science exposures	40.0	
Total used time in the orbit	52.6	

Thus, the two WFC exposures totaling 2400 seconds make full use of the typically available time in one orbit. The exposure times can be adjusted if the actual target visibility time differs from the derived total used time.

8.3.2 Sample Orbit Calculation 2:

This example illustrates the impact of short WFC exposures on the useful time in the orbit. We have one orbit to observe a target with WFC in two filters, so the observation consists of two series, each with two identical CR-SPLIT exposures. The ETC has shown that at the minimally accepted signal-to-noise ratio the exposure time must be 540 seconds for each of the filters, so each of the CR-SPLITs must be at least 270 seconds long. For the target declination, we find that the visibility time is 55 minutes. The time budget for the orbit is then as follows:

Table 8.4: Orbit calculation for example 2.

Action	Time (minutes)	Explanation
Orbit 1		
Initial guide-star acquisition	6.0	Needed at start of observation of a new target
WFC overhead for the first exposures in two series	$2 \times 4 = 8.0$	Includes filter change, camera set-up, and readout
WFC overhead for subsequent exposures in each of the two series	$2 \times 2.5 = 5.0$	Includes readout
Additional overhead for all but the last exposures in the orbit	$5.8 \times 3 = \sim 17$	Needed to dump the buffer because the next exposure is too short (> 339 seconds) to accommodate the dump time.
Science exposures	$4 \times 4.5 = 18$	
Total time for science exposures	18	
Total used time in the orbit	54	

Comparing with the previous example, we see that although with the adopted minimum exposure times we can squeeze the observation into one orbit, the efficiency of the orbit use is very low because of the large overheads associated with buffer dumps. However, if we increase each of the four exposure times so that they are larger than 339 seconds, we avoid these additional overheads. This would free ~17 minutes of the orbit time for science, which allows us to almost double the science exposure time (35 minutes instead of 18 minutes) and thus significantly improve signal-to-noise.

Similarly, a subarray can be used to readout only a fraction of the detector, allowing more frames to be stored in the buffer before requiring a dump. In this example, using four `WFC1-1K` subarrays for 4 short ($t < 339$ seconds) exposures would save 176 seconds in readout time and 1047 seconds in dump time. This frees up ~20 minutes of orbit time to be used for science.

8.3.3 Sample Orbit Calculation 3:

This example illustrates the orbit calculation for a WFC observation with the ACS box pattern, which implements imaging at four offset pointings. The goal of the observation is to obtain a dithered image of a field in such a way that would allow us to bridge the 50 pixel interchip gap between the WFC CCDs in the combined image. Given the WFC plate scale of 0.05 arcseconds/pixel, this requires that the offsets in the dithering pattern are larger than 2.5 arcseconds. Each offset will then take 0.5 minutes to move the spacecraft from one pointing in the pattern to another. We have determined that the exposure time necessary to reach the desired signal-to-noise ratio is 80 minutes. The visibility time at our target declination is 58 minutes. In this observation we do not want to rely on cosmic ray removal provided by the dithering data reduction package, and set `CR-SPLIT=2` to be able to remove cosmic rays from

the four individual images separately. As a result, the orbit calculation will involve a series of 8 exposures (two exposures at each of the four pointings in the dithering pattern) split across two orbits:

Table 8.5: Orbit calculation for example 3.

Action	Time (minutes)	Explanation
Orbit 1		
Initial guide-star acquisition	6.0	Needed at start of observation of a new target
WFC overhead for the first exposures in the series	4.0	Includes filter change, camera set-up, and readout
WFC overhead for the subsequent 3 exposures in the series	$3 \times 2.5 = 7.5$	Includes readout
Spacecraft slew	0.5	To offset from the first to the second pointing
Four science exposures	$4 \times 10 = 40$	Exposures at the first two pointings in the dither pattern
Total time for science exposures	40	
Total used time in the orbit	58	
Orbit 2		
Guide-star re-acquisition	~6.0	Needed at start of a new orbit to observe the same target
WFC overhead for the remaining exposures in the series	$4 \times 2.5 = 10$	Includes readout
Spacecraft slews	$2 \times 0.5 = 1.0$	To offset to the third and fourth pointings
Four science exposures	$4 \times 10 = 40$	Exposures at the second two pointings in the dither pattern
Total time for science exposures	40	
Total used time in the orbit	57	

The total used time in the first orbit comes out a little bit larger than the visibility time. However, given the conservative nature of the adopted overhead times as well as a bit of flexibility in the adopted signal-to-noise ratio, the difference is not significant. It should be remembered that the purpose of the above exercises is to estimate how many orbits to request for our science program rather than to exactly design the observation.

8.3.4 Sample Orbit Calculation 4:

This example illustrates the orbit calculation for a simple 30 minutes WFC grism spectroscopic observation broken down by `CR-SPLIT=2` into a series of two exposures.

Table 8.6: Orbit calculation for example 4.

Action	Time (minutes)	Explanation
Orbit 1		
Initial guide-star acquisition	6.0	Needed at start of observation of a new target
Predefined imaging exposure for grism spectroscopy	7.0	Needed to co-locate the targets and their spectra in the FOV
WFC overhead for the first science exposure in the series	4.0	Includes filter change, camera set-up, and readout
WFC overhead for the subsequent science exposure in the series	2.5	Includes readout
Two science exposures	$2 \times 15.0 = 30$	
Total science exposure time	30.0	
Total used time in the orbit	49.5	

Unlike similar imaging exposures, here we have to take into account an additional imaging exposure before the sequence of spectroscopic exposures, which takes 10 minutes. off the available orbit time.

8.3.5 Sample Orbit Calculation 5:

This example deals with the orbit calculation for an observation of a relatively faint extended object using the SBC. The target has to be observed using two filters, F150LP and F165LP. The ETC shows that the required S/N for the observations are achieved in 3200 seconds and 2000 seconds for the F150LP and the F165LP filters, respectively. There is no readout noise associated with SBC exposures; therefore, the observations can be split into four equally long dither pointings. Since the average visibility time for the target is ~55 minutes, the images can be taken in two orbits, as shown in Table 8.7. The standard ACS-SBC-DITHER-BOX pattern, which allows for the rejection of most artifacts, is suitable for these observations. Here are the details of the orbit calculation:

Table 8.7: Orbit calculation for example 5.

Action	Time (minutes)	Explanation
Orbit 1		
Initial guide-star acquisition	6	Needed at start of observation of a new target
SBC overhead for the first exposure	1.4	Includes filter change and camera setup
SBC overhead for each of the following 3 exposures	3×1	Includes filter change (3 x 0.4min)
Telescope slew time	0.3	Slew performed between the 2nd and the 3rd exposure in this orbit
Exposures with F150LP filter	$2 \times 13.3 = 26.6$	Exposures at the first two pointings of the dither pattern
Exposures with F165LP filter	$2 \times 8.3 = 16.6$	Exposures at the first two pointings of the dither pattern
Total time used in this orbit	53.9	
Orbit 2		
Guide-star re-acquisition	~6	Needed at start of a new orbit to observe the same target
SBC overhead for each of the following 3 exposures	4×1	Includes filter change (4 x 0.4min)
Telescope slew time	0.3	Slew performed between the 2nd and the 3rd exposure in this orbit
Exposures with F150LP filter	$2 \times 13.3 = 26.6$	Exposures at the first two pointings of the dither pattern
Exposures with F165LP filter	$2 \times 8.3 = 16.6$	Exposures at the first two pointings of the dither pattern
Total used time in the orbit	53.5	

The total time is slightly shorter in the second orbit because of the shorter time required for guide star re-acquisition and SBC overheads. There is also ~1min of visibility available in the first orbit that can be used for the observations. However, we recommend dithered observations in each filter using the same exposure time for each pointing.

CHAPTER 9:

Exposure-Time Calculations

In this chapter...

9.1 Overview

In this chapter we explain how to use sensitivities and throughputs to determine the expected count rate from your source and how to calculate exposure times to achieve a given signal-to-noise ratio for your ACS observations taking all background contributions into account. At the end of this chapter you will find examples to guide you through specific cases.

9.1.1 The ACS Exposure Time Calculator

The ACS ETC is available to help with proposal preparation at:

http://etc.stsci.edu/etc

This ETC calculates count rates for given source and background parameters, signal-to-noise ratios for a given exposure time, or count rates and exposure time for a given signal-to-noise ratio for imaging, spectroscopic, and coronagraphic observations. A variety of apertures are now available, both circular and square, allowing the user to either select a radius in arcseconds or a size in pixels. The current default are a 0.2 arcseconds radius for the WFC, and a 0.4 arcseconds radius for SBC observations, which enclose approximately 80% of the PSF flux. Square and circular apertures are available between 0.1 and 2.0 arcseconds. For extended sources the S/N calculation is based on counts summed over one resolution element of 2 x 2 pixels, as the source size is assumed to be larger than the ACS resolution. A calibrated spectrum of your source can be provided directly to the ETC. The ETC also determines peak per-pixel count rates and total count rates to aid in feasibility assessment. Warnings appear if the source exceeds the local or global brightness limits for SBC observations (see Section 7.2). The ETC has online help for its execution and interpretation of results. Alternatively, users can use **synphot**[1] in STSDAS to calculate count rates and the wavelength distribution of detected counts.

9.2 Determining Count Rates from Sensitivities

In this Chapter, specific formulae appropriate for imaging and spectroscopic modes are provided to calculate the expected count rates and the signal-to-noise ratio from the flux distribution of a source. The formulae are given in terms of sensitivities, but we also provide transformation equations between the throughput (QT) and sensitivity (S) for imaging and spectroscopic modes.

Throughputs are presented in graphical form as a function of wavelength for the prisms and for the imaging modes in Chapter 10. Given your source characteristics and the sensitivity of the ACS configuration, calculating the expected count rate over a given number of pixels is straightforward, since the ACS PSF is well characterized. The additional required information is the encircled energy fraction (ε_f) in the peak pixel, the plate scale, and the dispersions of the grisms and prisms. This information is summarized in Table 9.1 and Table 9.2 for Side 1. For updates please see the ACS Web page.

1. Synphot will soon be replaced by the pysynphot package, a significantly improved re-implementation of Synphot written in Python. Please visit the pysynphot Web page at http://stsdas.stsci.edu/pysynphot for updates.

Table 9.1: Useful quantities for the ACS WFC, at -81° C

Filter	Pivot λ (Å)	$\int Q_\lambda T_\lambda d\lambda/\lambda$	$\int S_\lambda d\lambda$	ABMAG zero point	Encircled Energy	Flux in Central Pixels	Background sky rate (per pixel)
F435W	4318.9	0.0739	3.14E+18	25.66	0.85	0.22	0.0302
F475W	4746.9	0.1070	5.49E+18	26.06	0.86	0.21	0.0566
F502N	5023.0	0.0033	1.87E+17	22.27	0.86	0.21	0.0019
F550M	5581.4	0.0366	2.60E+18	24.90	0.85	0.22	0.0275
F555W	5361.0	0.0782	5.12E+18	25.72	0.86	0.21	0.0538
F606W	5921.1	0.1593	1.27E+19	26.49	0.85	0.22	0.1270
F625W	6311.4	0.0930	8.44E+18	25.91	0.85	0.22	0.0827
F658N	6584.0	0.0051	5.05E+17	22.76	0.85	0.22	0.0047
F660N	6599.4	0.0019	1.89E+17	21.68	0.85	0.22	0.0018
F775W	7692.4	0.0744	1.00E+19	25.67	0.85	0.21	0.0779
F814W	8057.0	0.0962	1.42E+19	25.94	0.84	0.19	0.1026
F850LP	9033.1	0.0349	6.48E+18	24.84	0.74	0.15	0.0390
F892N	8914.8	0.0036	6.50E+17	22.37	0.77	0.15	0.0040
G800L	7467.8	0.1611	2.05E+19	26.50	--	--	--
CLEAR	6272.4	0.3857	3.46E+19	27.45	0.85	0.22	0.2934

Table 9.2: Useful quantities for the ACS SBC.

Filter	Pivot λ (Å)	$\int Q_\lambda T_\lambda d\lambda/\lambda$	$\int S_\lambda d\lambda$	ABMAG zero point	Encircled Energy	Flux in Central Pixel	Background sky rate (per pixel)
F115LP	1406.6	0.0149	6.70E+16	23.92	0.82	0.11	0.0479
F122M	1273.7	0.0010	3.56E+15	20.95	0.82	0.09	0.0085
F125LP	1438.2	0.0123	5.81E+16	23.71	0.83	0.11	0.0053
F140LP	1528.0	0.0069	3.69E+16	23.09	0.83	0.13	0.0001
F150LP	1612.2	0.0038	2.28E+16	22.45	0.84	0.14	0.0000
F165LP	1762.5	0.0010	7.35E+15	21.03	0.85	0.16	0.0000
PR110L	1430.1	0.0121	5.62E+16	23.69	--	--	--
PR130L	1439.4	0.0120	5.67E+16	23.69	--	--	--

In each Table, the following quantities are listed:

- The pivot wavelength, a source-independent measure of the characteristic wavelength of the bandpass, defined such that it is the same if the input spectrum is in units of F_λ or F_ν:

$$\lambda_p = \sqrt{\frac{\int Q(\lambda)T(\lambda)d\lambda}{\int Q(\lambda)T(\lambda)((d\lambda)/\lambda)}}$$

- The integral $\int Q_\lambda T_\lambda \, d\lambda/\lambda$, used to determine the count rate when given the astronomical magnitude of the source.
- The sensitivity integral, defined as the count rate that would be observed from a constant F_λ source with flux 1 erg/cm^2/second/Å.
- The ABmag zero point, defined as the AB magnitude of a source with a constant F_ν that gives 1 count/second with the specified configuration.
- The encircled energy, defined as the fraction of PSF flux enclosed in the default photometry aperture, 0.2 arcseconds for the WFC and 0.5 arcseconds for the SBC. These correspond approximately to 5×5 and 15×15 box-sizes respectively.
- The fraction of PSF flux in the central pixel, useful for determining the peak count rate to check for overflow or bright object protection possibilities.
- The sky background count rate, which is the count rate that would be measured with average zodiacal background, and average earthshine. It does not include the contribution from the detectors, tabulated separately in Table 3.1

Here, we describe how to determine two quantities:

1. The counts/second (C) from your source over some selected area of N_{pix} pixels, where a signal of an electron on a CCD is equivalent to one count.
2. The peak counts/second/pixel (P_{cr}) from your source, which is useful for avoiding saturated CCD exposures, and for assuring that SBC observations do not exceed the bright-object limits.

We consider the cases of point sources and diffuse sources separately in each of the imaging and spectroscopy sections following.

9.2.1 Imaging

Point Source

For a point source, the count rate, C, can be expressed as the integral over the bandpass of the filter:

$$C = A\int F_\lambda \frac{\lambda}{hc} Q_\lambda T_\lambda \varepsilon_f d\lambda = \int F_\lambda S_\lambda \varepsilon_f d\lambda$$

Where:

- A is the area of the unobstructed 2.4 meter telescope (i.e., 45,239 cm^2)
- F_λ is the flux from the astronomical source in erg/second/$cm^{2/}$Å
- h is Planck's constant
- c is the speed of light
- The factor λ/hc converts ergs to photons.
- $Q_\lambda T_\lambda$ is the system fractional throughput, i.e., the probability of detecting a count per incident photon, including losses due to obstructions of the full 2.4 meter OTA aperture. It is specified this way to separate out the instrument sensitivity Q_λ and the filter transmission T_λ.
- ε_f is the fraction of the point source energy encircled within N_{pix} pixels.
- S_λ is the total imaging point source sensitivity with units of counts/second/Å per incident erg/second/cm^2/Å.

The peak counts/second/pixel from the point source, is given by:

$$C_{peak} = \int F_\lambda S_\lambda \varepsilon_f(1) d\lambda$$

Where:

- F_λ and S_λ are as above.
- $\varepsilon_f(1)$ is the fraction of energy encircled within the peak pixel.

Again, the integral is over the bandpass.

If the flux from your source can be approximated by a flat continuum (F_λ = constant) and ε_f is roughly constant over the bandpass, then:

$$C = F_\lambda \varepsilon_f \int S_\lambda d\lambda$$

We can now define an equivalent bandpass of the filter (B_λ) such that:

$$\int S_\lambda d\lambda = S_{peak} B_\lambda$$

Where:

- S_{peak} is the peak sensitivity.
- B_λ is the effective bandpass of the filter.

The count rate from the source can now be written as:

$$C = F_\lambda \varepsilon_f S_{peak} B_\lambda$$

In Tables 9.1 to 9.2, we give the value of $\int S_\lambda d\lambda$ for each of the filters. Alternatively, we can write the equation in terms of V magnitudes:

$$C = 2.5 \times 10^{11} \varepsilon_f (\int QT d\lambda / \lambda) \times 10^{-0.4(V + AB_v)}$$

where V is the visual magnitude of the source, the quantity under the integral sign is the mean sensitivity of the detector+filter combination, and is tabulated in Tables 9.1 to 9.2, and AB_v is the filter-dependent correction for the deviation of the source spectrum from a constant F_v spectrum. This latter quantity is tabulated for several different astronomical spectra in Tables 10.1 to 10.3 in Chapter 10.

Diffuse Source

For a diffuse source, the count rate (C) per pixel, due to the astronomical source can be expressed as:

$$C = \int I_\lambda S_\lambda m_x m_y d\lambda$$

Where:

- I_λ = the surface brightness of the astronomical source, in erg/second/cm^2/Å/ arcseconds^2.
- S_λ as above.
- m_x and m_y are the plate scales along orthogonal axes.

Emission Line Source

For a source where the flux is dominated by a single emission line, the count rate can be calculated from the equation

$$C = 2.23 \times 10^{12} \cdot (QT)_\lambda \cdot F(\lambda) \cdot \lambda$$

where C is the observed count rate in counts/second, (QT) is the system throughput at the wavelength of the emission line, $F(\lambda)$ is the emission line flux in units of erg/cm^2/second, and λ is the wavelength of the emission line in Angstroms. $(QT)_\lambda$ can be determined by inspection of the plots in Chapter 10. See Section 9.6.4 for an example of emission-line imaging using ACS.

9.2.2 Spectroscopy

Point Source

For a point source spectrum with a **continuum flux distribution**, the count rate, C, is per pixel in the dispersion direction, and is integrated over a fixed extraction height N_{spix} in the spatial direction perpendicular to the dispersion:

$$C = F_\lambda S'_\lambda \varepsilon'_{Nspix} = F_\lambda A \frac{\lambda}{hc} T_\lambda \varepsilon'_{Nspix} d$$

Where:

- S'_λ is the total point source sensitivity in units of counts/second per incident erg/second/cm^2/Å; and $S'_\lambda = S_\lambda \cdot d$
- d is the dispersion in Å/pixel.
- ε'_{Nspix} is the fraction of the point source energy within N_{spix} in the spatial direction.
- the other quantities are defined above.

For an **unresolved emission line** at $\lambda = L$ with a flux of F_L in erg/second/cm^2 the total counts recorded over the N_{spix} extraction height is:

$$C = F_\lambda S'_\lambda / d$$

These counts will be distributed over pixels in the wavelength direction according to the instrumental line spread function.

In contrast to the case of imaging sensitivity S_λ, the spectroscopic point source sensitivity calibration ($S'_\lambda \times \varepsilon'_{Nspix}$) for a default extraction height of N_{spix} is measured directly from observations of stellar flux standards after insertion of ACS into *HST*. Therefore, the accuracy in laboratory determinations of T_λ for the ACS prisms and grisms is NOT crucial to the final accuracy of their sensitivity calibrations.

The peak counts/second/pixel from the point source, is given by:

$$P_{cr} = \varepsilon'_f(1) F_\lambda S'_\lambda$$

Where:

- $\varepsilon'_f(1)$ is the fraction of energy contained within the peak pixel.
- the other quantities are as above.

9.3 Computing Exposure Times

To derive the exposure time to achieve a given signal-to-noise ratio, or to derive the signal to noise ratio in a given exposure time, there are four principal ingredients:

- Expected counts *C* from your source over some area.
- The area (in pixels) over which those counts are received (N_{pix}).
- Sky background (B_{sky}) in counts/pixel/second.
- The detector background (B_{det}) or dark count in units of counts/second/pixel and the read noise (*R)* in counts of the CCD.
- Section 9.4 provides the information for determining the sky-plus-detector background.

9.3.1 Calculating Exposure Times for a Given signal-to-noise

The signal-to-noise ratio, Σ is given by:

$$\Sigma = \frac{Ct}{\sqrt{Ct + N_{pix}(B_{sky} + B_{det})t + N_{pix}N_{read}R^2}}$$

Where:

- *C* = the signal from the astronomical source in counts/second, or electrons/second from the CCD. The actual output signal from a CCD is *C/G* where *G* is the gain. You must remember to multiply by *G* to compute photon events in the raw CCD images.
- *G* = the gain is always 1 for the SBC, and 0.5, 1, 1.4, or 2 for the WFC after SM4, depending on `GAIN`. For archival purposes, gains prior to SM4 for WFC and HRC were ~ 1, 2, 4, or 8.
- N_{pix} = the total number of detector pixels integrated over to achieve *C*.
- B_{sky} = the sky background in counts/second/pixel.
- B_{det} = the detector dark current in counts/second/pixel.
- *R* = the read noise in electrons; it is equal to zero electrons for SBC observations. See Table 4.1 for WFC after SM4. For archival purposes, see Table 4.2 and Table 4.3 for WFC and HRC prior to SM4.
- N_{read} = the number of CCD readouts.
- *t* = the integration time in seconds.

This equation assumes the optimistic (and often realistic) condition that the background zero point level under the object is sufficiently well known (and subtracted) to not significantly contribute; in crowded fields this may not be true.

Observers using the CCD normally take sufficiently long integrations that the CCD read noise is not important. This condition is met when:

$$Ct + N_{pix}(B_{sky} + B_{det})t > 2N_{pix}N_{read}R^2$$

For the CCD in the regime where read noise is not important and for all SBC observations, the integration time to reach a signal-to-noise ratio Σ, is given by:

$$t = \frac{\Sigma^2[C + N_{pix}(B_{sky} + B_{det})]}{C^2}$$

If your source count rate is much brighter than the sky plus detector backgrounds, then this expression reduces further to:

$$t = \frac{\Sigma^2}{C}$$

i.e., the usual result for Poisson statistics of $\Sigma = \sqrt{totalcounts}$.

More generally, the required integration time to reach a signal-to-noise ratio Σ is given by:

$$t = \frac{\Sigma^2[C + N_{pix}(B_{sky} + B_{det})] + \sqrt{\Sigma^4[C + N_{pix}(B_{sky} + B_{det})]^2 + 4\Sigma^2C^2[N_{pix}N_{read}R^2]}}{2C^2}$$

9.3.2 Exposure Time Estimates for Red Targets in F850LP

At wavelengths greater than 7500 Å (HRC) and about 9000 Å (WFC) ACS CCD observations are affected by a red halo due to light scattered off the CCD substrate. An increasing fraction of the light as a function of wavelength is scattered from the center of the PSF into the wings. This problem particularly affects the very broad z-band F850LP filter, for which the encircled energy mostly depends on the underlying spectral energy distribution. The encircled energy fraction is calculated at the effective wavelength which takes into account the source spectral distribution. This fraction is then multiplied by the source counts. (The effective wavelength is the weighted average of the system throughput AND source flux distribution integrated over wavelength). However, this does not account for the variation in enclosed energy with wavelength.

As a consequence, in order to obtain correct estimated count rates for red targets, observers are advised to use the **synphot** package in IRAF/STSDAS for which the proper integration of encircled energy over wavelength has now been incorporated. To quantify this new **synphot** capability, we compare the ETC results with **synphot** for a set of different spectral energy distributions and the observation mode WFC/F850LP. In Table 9.3, the spectral type is listed in the first column. The fraction of light with respect to the total integrated to infinity is listed in the other two columns, for the ETC

and **synphot** calculations respectively. These values are derived for a 0.2 arcsecond aperture for the ETC calculations and **synphot.**

Table 9.3: Encircled energy comparison for WFC/F850LP.

Spectral type	APT ETC	Synphot
O	0.76	0.74
M	0.71	0.7
L	0.69	0.68
T	0.61	0.6

The ETC results are off by 3% (O star), 2% (M star), 2% (L star), and 1% (T star). If this small effect is relevant to particular observations, then the ***synphot*** software package can be used. To learn how to use the **synphot** tool, we refer the reader to the instructions provided in the April 2003 STAN at:

http://www.stsci.edu/hst/acs/documents/newsletters/stan0302.html,

and in ACS ISR 2003-08.

9.4 Detector and Sky Backgrounds

When calculating expected signal-to-noise ratios or exposure times, the background from the sky, and the background from the detector must be taken into account.

9.4.1 Detector Backgrounds

See Table 3.1 for read noise and dark current characteristics of the detectors, including variations by amplifier and GAIN for the CCDs.

9.4.2 Sky Background

The sources of sky background which will affect ACS observations include:

- Earth shine (ES).
- Zodiacal light (ZL).
- Geocoronal emission (GC).

The background in counts/second/pixel for **imaging observations** can be computed as:

$$B_{sky} = \int I_\lambda S_\lambda m_x m_y d\lambda$$

Where:

- I_λ is the surface brightness of the sky background, in erg/second/cm^2/Å/arcseconds^2.
- S_λ is the point source sensitivity for the imaging mode.
- m_x and m_y are the plate scales along orthogonal axes.

The image of the sky through a disperser is not uniform, since some wavelengths fall off the detector for regions of sky near the edge of the field of view (FOV). Since the ACS grism spectra are of order 200 pixels long, the regions of lower sky will be strips at the long and short wavelength edges of the FOV. The maximum width of the strips from where the signal starts to decline to the edge, where the signal is down by roughly 2x, is about half the total length of a spectrum of a point source, i.e., roughly 100 pixels in the case of a sky background with a **continuum** of wavelengths. In the case of the HRC, the sky for the dispersed mode will not have the low background strips, since the FOV is not masked to the detector size. These small strips of lower sky background in the SBC and the WFC are ignored in the following formulae. Furthermore in the SBC and the WFC, since the spectra do not lie along the direction of the anamorphic distortion, the plate scales of m_x and m_y above must be replaced by the plate scales m_s and m_λ in the orthogonal spatial and dispersion directions, respectively. Interior to the strips, a point on the detector sees a region of sky over the full wavelength coverage of the disperser. Thus, for **spectroscopic observations**:

$$B^{\lambda}_{sky} = \int I_\lambda S'_\lambda m_s m_\lambda d\lambda$$

For a **monochromatic** sky emission line at $\lambda = L$ like Lyman-α, which will dominate the background through the LiF prism:

$$B^{L}_{sky} = I_L S'_\lambda m_s m_\lambda / d$$

where

- I_L is the monochromatic intensity of a line at wavelength L in erg/second/cm^2/ arcseconds^2.

The total sky background is:

$$B_{sky} = B^{\lambda}_{sky} + B^{L}_{sky}$$

Figure 9.1 and Table 9.6 show "high" sky background intensity as a function of wavelength, identifying the separate components which contribute to the background. The "shadow" and "average" values of the Earthshine contribution in the ETC correspond, respectively, to 0 and 50% of the "high" values in Figure 9.1 and Table 9.6.

"Extremely high" Earthshine corresponds to twice the "high" value. For the zodiacal sky background, the values in Figure 9.1 and Table 9.6 and the ETCs correspond to the

high value of $m_v = 22.1$ from Table 9.4, while the "low" and "average" zodiacal light is scaled to $m_v = 23.3$ and 22.7, respectively.

Figure 9.1: High sky background intensity as a function of wavelength.

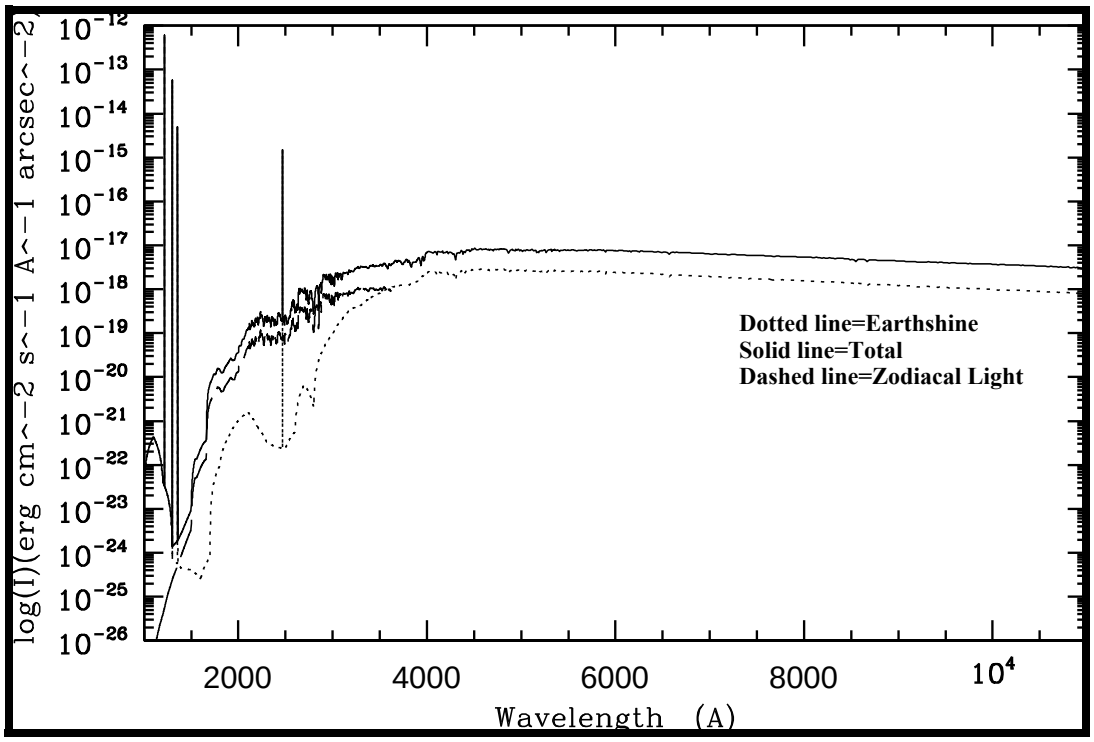

The zodiacal contribution (ZL) is at ecliptic latitude and longitude of 30°,180°, and corresponds to $m_v = 22.1$ per square arcseconds. The Earthshine (ES) is for a target which is 38° from the limb of the sunlit Earth. Use Figure 9.2 to estimate background contributions at other angles. The daytime geocoronal line intensities are in erg/cm^2/ second/arcseconds^2 (see Table 9.5).

Background Variations and LOW-SKY

In the ultraviolet, the background contains bright airglow lines, which vary from day to night and as a function of *HST* orbital position. The airglow lines may be the dominant sky contributions in the UV both for imaging-mode and spectroscopic observations. Away from the airglow lines, at wavelengths shortward of ~3000 Å, the background is dominated by zodiacal light, where the small area of sky that corresponds to a pixel of the high resolution *HST* instrumentation usually produces a signal that is much lower than the intrinsic detector background. The contribution of zodiacal light does not vary dramatically with time, and varies by only a factor of about three throughout most of the sky. Table 9.4 gives the variation of the zodiacal background as a function of ecliptic latitude and longitude. For a target near ecliptic coordinates of (50,0) or (-50,0), the zodiacal light is relatively bright at $m_v = 20.9$, i.e. about 9 times the faintest values of $m_v = 23.3$. Deep imaging applications must carefully consider expected sky values!

On the other hand, Earthshine varies strongly depending on the angle between the target and the bright Earth limb. The variation of the Earthshine as a function of limb angle from the sunlit Earth is shown in Figure 9.2. This figure also shows the

contribution of the Moon, which is typically much smaller than the zodiacal contribution, for which the upper and lower limits are shown. For reference, the limb angle is approximately 24° when the *HST* is aligned toward its orbit pole (i.e., the center of the CVZ), this limb angle corresponds to "Extremely High" Earthshine. The Earthshine contribution shown in Figure 9.1 and Table 9.6 corresponds to a limb angle of 30°, High Earthshine.

For observations taken longward of 3500 Å, the Earthshine dominates the background at small (< 22°) limb angles. In fact, the background increases exponentially for limb angles < 22°. The background near the bright limb can also vary by a factor of ~2 on timescales as short as two minutes, which suggests that the background from Earthshine also depends upon the reflectivity of the terrain over which *HST* passes during the course of an exposure. Details of the sky background as it affects ACS, as well as STIS, are discussed by Shaw, et al. (STIS ISR 98-21). The impact of Earthshine on ACS observations is discussed by Biretta, et al., (ACS ISR 03-05).

Figure 9.2: Background contributions in V magnitude per arcseconds^2

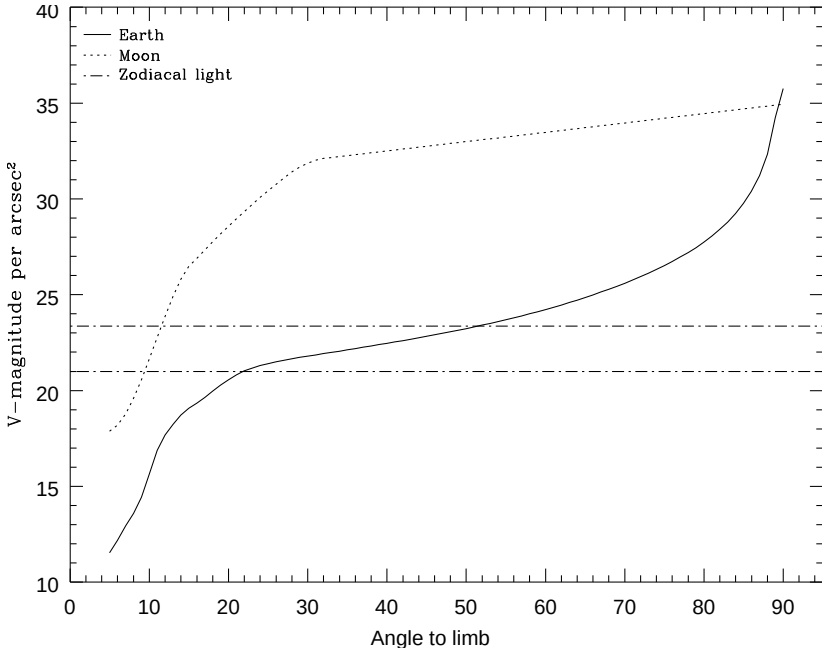

Background due to the zodiacal light, Moon, and the sunlit Earth, as a function of angle between the target and the limb of the Earth or Moon. The two zodiacal light lines show the extremes of possible values.

Table 9.4: Approximate zodiacal sky background as a function of ecliptic latitude and ecliptic longitude. (In V magnitudes per square arcseconds.)

Ecliptic longitude (degrees)	Ecliptic latitude (degrees)			
	0	30	60	90
180	22.1	22.7	23.2	23.3
145	22.4	22.9	23.3	23.3
110	22.3	22.9	23.3	23.3
50	20.9	22.2	22.9	23.3

Observations of the faintest objects may need the special requirement LOW-SKY in the Phase II observing program. LOW-SKY observations are scheduled during the part of the year when the zodiacal background light is no more than 30% greater than the minimum possible zodiacal light for the given sky position. LOW-SKY in the Phase II scheduling also invokes the restriction that exposures will be taken only at angles greater than 40° from the bright Earth limb to minimize Earthshine and the UV airglow lines. The LOW-SKY special requirement limits the times at which targets within 60° of the ecliptic plane will schedule, and limits visibility to about 48 minutes per orbit. The use of LOW-SKY must be requested and justified in the Phase I Proposal.

The ETC provides the user with the flexibility to separately adjust both the zodiacal (low, average, high) and Earthshine (shadow, average, high, extremely high) sky background components in order to determine if planning for use of LOW-SKY is advisable for a given program. However, the absolute sky levels that can be specified in the ETC may not be achievable for a given target; e.g., as shown in Table 9.4 the zodiacal background minimum for an ecliptic target is $m_v = 22.4$ which is still brighter than both the low and average options with the ETC. By contrast, a target near the ecliptic pole would always have a zodiacal = low background in the ETC. The user is cautioned to carefully consider sky levels as the backgrounds obtained in *HST* observations can cover significant ranges.

Geocoronal Emission and Shadow

Background due to geocoronal emission originates mainly from hydrogen and oxygen atoms in the exosphere of the Earth. The emission is concentrated in the four lines listed in Table 9.5. The brightest line is Lyman–α at 1216 Å. The strength of the Lyman-α line varies between about 2 and ~30 kilo-Rayleighs (i.e., between 6.1×10^{-14} and 6.1×10^{-13} erg/second/cm^2/arcseconds^2 where 1 Rayleigh = 10^6 photons/second/cm per 4π steradian) depending on the position of *HST* with respect to the day-night terminator and the position of the target relative to the Earth limb. The next strongest line is the OI line at 1304 Å, which rarely exceeds 10% of Lyman-α. The typical strength of the OI 1304 Å line is about 1 kilo-Rayleighs (which corresponds to about 2.85×10^{-14} erg/second/cm^2/arcseconds^2) on the daylight side and about 75 times fainter on the night side of the *HST* orbit. OI 1356 Å and

OI 2471 Å lines may appear in observations on the daylight side of the orbit, but these lines are ~10 times weaker than the OI 1304 Å line. The width of the lines also vary with temperature, the line widths given in Table 9.5 are representative values assuming a temperature of 2000 °K.

Except for the brightest objects (e.g., planets), a filter or prism mode which does not transmit at Lyman-α should be employed. To minimize geocoronal emission the special requirement `SHADOW` can be requested. Exposures using this special requirement are limited to roughly 25 minutes per orbit, exclusive of the guide-star acquisition (or reacquisition), and can be scheduled only during a small percentage of the year. `SHADOW` reduces the contribution from the geocoronal emission lines by roughly a factor of ten while the continuum Earthshine is set to zero. `SHADOW` requirements must be included and justified in your Phase I proposal (see the *Call for Proposals*).

Table 9.5: Geocoronal emission lines.

Wavelength (Å)	ID	Line width (Å)	Intensity			
			Day		Night	
			kilo-Rayleighs	erg/s/cm^2/arcsec^2	kilo-Rayleighs	erg/s/cm^2/arcsec^2
1216	Ly-α	0.04	~20	6.1 x 10^{-13}	2	6.1 x 10^{-14}
1304	OI	0.013	~2	5.7 x 10^{-14}	0.013	3.8 x 10^{-16}
1356	OI	0.013	~0.2	~5 x 10^{-15}	~ 0.001	~3 x 10^{-17}
2471	OI	0.023	< 0.2	< 3 x 10^{-15}	< 0.001	< 1.5 x 10^{-17}

9.5 Extinction Correction

Extinction can dramatically reduce the counts expected from your source, particularly in the ultraviolet. Figure 9.3 shows the average $A_V/E(B–V)$ values for our galaxy, taken from (Seaton, *MNRAS*, **187**, 73P, 1979). Large variations about the average are observed (Witt, Bohlin, & Stecher, *ApJ*, 279, 698, 1984).

Extinction curves have a strong metallicity dependence, particularly in the UV wavelengths. Sample extinction curves can be seen in Koornneef and Code, *ApJ*, 247, 860 1981 (LMC); Bouchet et al., *A&A*, 149, 330 1985 (SMC); and Calzetti, Kinney and Storchi-Bergmann, *ApJ*, 429, 582, 1994, and references therein. At lower metallicities, the 2200 Å bump which is so prominent in the Galactic extinction curve disappears; and $A_V/E(B–V)$ may increase monotonically at UV wavelengths.

Figure 9.3: Extinction versus wavelength.

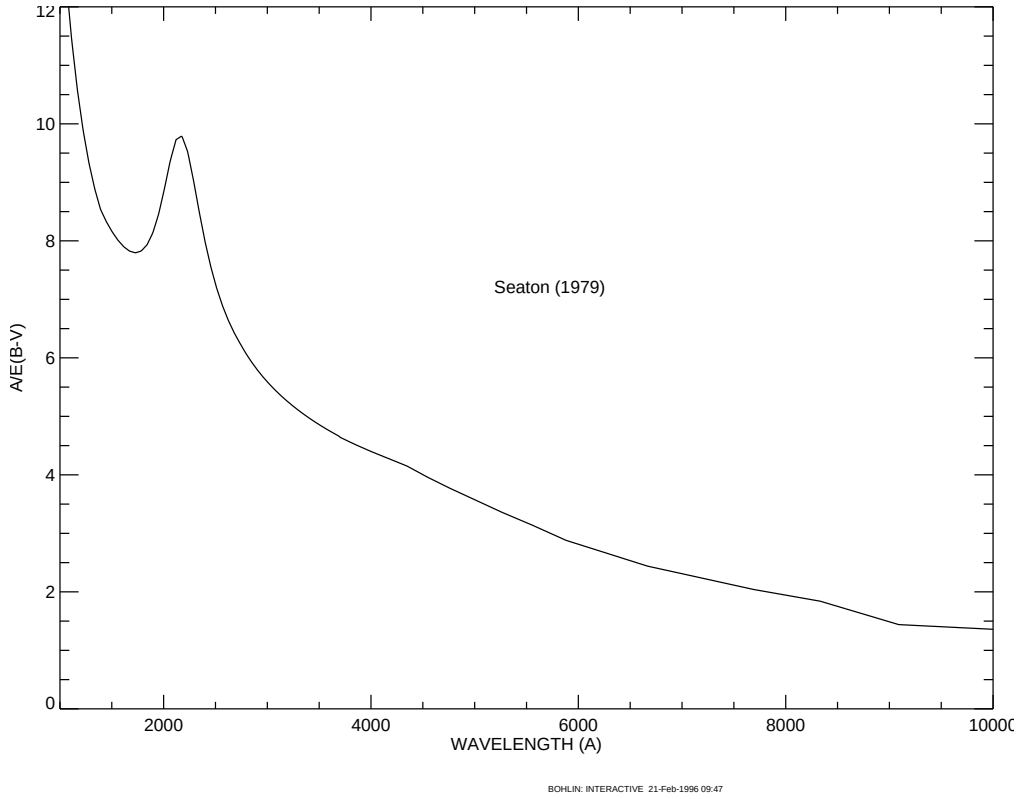

9.6 Exposure-Time Examples

In the following you will find a set of examples for the three different channels and for different types of sources. The examples were chosen in order to present typical objects for ACS and also to present interesting cases that may arise with the use of ACS.

Actual ETC calculation results may differ slightly from these published values due to recent improvements in the ETC tables.

9.6.1 Example 1: WFC Imaging a Faint Point Source

What is the exposure time needed to obtain a signal-to-noise of 10 for a point source of spectral type F2 V, normalized to V = 26.5, when using the WFC, F555W filter? Assume a GAIN of 1 and a photometry box size of 11 x 11 pixels, and average sky values.

The ETC gives a total exposure time of 4410 seconds to obtain this S/N in a single exposure. Since such an exposure would be riddled with cosmic rays and essentially useless, it is necessary to specify how many exposures to split the observation into. ACS WFC observations generally should be split if the exposure time is larger than about 11 minutes, but for multi-orbit observations, splitting into 2 exposures per orbit is generally sufficient.

For a typical object visibility of 53 minutes, after applying the requisite overheads, there is time for two 1200 seconds exposures per orbit. The required exposure time can thus be reached in 4 exposures, but re-running the ETC using `CR-SPLIT=4` raises the required exposure time to 5303 seconds (because of the extra noise introduced by the four extra readouts). To achieve the required exposure time would require `CR-SPLIT=5`, or three orbits.

Using the pencil and paper method, Table 9.1 gives the integral $QT d\lambda/\lambda$ as 0.0775, and the AB_ν correction term can be retrieved from Table 10.1 as 0.040. According to Figure 5.11, a circular aperture of radius 0.3 arcseconds (which has an area of 116 pixels, close to the 121 pixel box specified) encloses about 90% of the light from a star. The count rate is then $2.5x10^{11}*0.0775*0.9*10^{-0.4(26.5+0.040)} = 0.423$ counts/second, which agrees with the ETC-returned value of 0.42. The exposure time can then be found by using the equation

$$t = \frac{\Sigma^2[C + N_{pix}(B_{sky} + B_{det})]}{C^2}$$

to give $t = 4172$ seconds, which is close to the ETC-derived value of 4410 seconds. We have inserted the background rate from Table 9.1 ($B_{sky} = 0.055$) and Table 9.4 ($B_{det} = 0.0032$), and assumed that the noise on the background is much greater than the readout noise.

Note that this can be greatly shortened by specifying a smaller analysis box (for example, 5 x 5) and using `LOW-SKY`. Dropping the aperture size to 5 x 5 at average sky which still encloses 81% of the light requires 1532 seconds. Including both the smaller 5 x 5 box and `LOW-SKY` (Zodiacal = `LOW`, Earthshine = `AVERAGE`), using the ETC gives the required exposure time as only 1306 seconds (using `CR-SPLIT=1`), or 1540 seconds with `CR-SPLIT=2`. The `LOW-SKY` visibility per orbit is 47 minutes, which allows a total on-target exposure time of 2000 seconds in one orbit with `CR-SPLIT=2`.

9.6.2 Example 2: SBC Objective Prism Spectrum of a UV Spectrophotometric Standard Star

What is the peak count rate using the PR110L prism in the SBC for the *HST* standard star HS2027+0651 (V = 16.9) that was used for the STIS prism calibration (this spectrum is not in the ETC list, therefore we quote below the flux which could be found by dearchiving the STIS spectrum)?

The sensitivity peaks in the 1500 Å to 1600 Å region. To find the count rate at 1537 Å, inspection of Figure 6.22 gives the sensitivity of 9.9×10^{14} counts/second per erg/cm^2/s/Å. Multiplying by the stellar flux of 5.3587×10^{-14} gives 53.0 counts/second, summed in the cross dispersion direction. For the fraction of light in the central pixel $\varepsilon = 0.31$, the brightest pixel at 1437.6 Å is 17.6 counts/second/pixel, well below the bright object limit.

The SBC has no readout noise, and the dark current rate is negligible, while the main sky contribution for PR110L is from Lyman-α. For daytime Ly-α intensity of 20kR = 6.1×10^{-13} ergs/cm^2/second/arcseconds^2, S′ = 1.7×10^{14}, and *d*, the dispersion in Å/pixel, is 2.58. Therefore, the background count rate is:
$6.1 \times 10^{-13} * 1.7 \times 10^{14} * 0.032^2 / 2.58 = 0.041$counts/second/pixel.
This value varies somewhat over the field, as the plate scale varies from the nominal 0.032 arcseconds/pixel. For faint source spectroscopy, it is better to use PR130L, which is on a CaF_2 substrate to block Ly-α.

9.6.3 Example 3: WFC VIS Polarimetry of the Jet of M87

What signal-to-noise ratio is reached in three one orbit exposures (~2400 seconds each) for M87, when using the WFC, F555W for one orbit each in the three VIS polarizers? Gain is 2, box size is 5 x 5 pixels, `CR-SPLIT=2`, and average sky.

If the M87 jet region has $\mu_V = 17$ magnitudes/arcseconds^2, using the ETC with a flat continuum spectral distribution and an exposure time of 2400 seconds (`CR-SPLIT=2`), gives S/N = 131.6 for an observation with each VIS polarizer filter (which is an average of the polarizer at the 3 available position angles 0°, 60°, and 120°). If the polarization P is 20%, then P*S/N = 26.3, so using

$$\log\left(\frac{\sigma_P}{P}\right) = -0.102 - 0.9898 \log\left(P \langle \mathrm{S/N} \rangle_i\right)$$

from Chapter 6, $\sigma_P/P = 0.031$, or $\sigma_P = 6.2 \times 10^{-3}$, which is the error on the fractional polarization. The error on the position angle should be ~1.0°using the formula, again from Chapter 6, of

$$\log \sigma_\theta = 1.514 - 1.068 \log\left(P \langle \mathrm{S/N} \rangle_i\right)$$

9.6.4 Example 4: SBC imaging of Jupiter's Aurora at Lyman-alpha

What signal-to-noise ratio is reached in a one orbit exposure (2000 seconds) observing Jupiter's aurora in Ly-α using the SBC and F122M filter?

The equation from Section 9.2.1 can be used to calculate the expected count rate. The aurora is variable, up to ~100kR. The value of (QT) for the SBC+F122M filter at 1216 Å is 0.0009, from inspection of Figure 10.106. For a surface brightness of 40kR

$= 1.22 \times 10^{-12}$ erg/cm^2/second/arcseconds^2 (see Section 9.4.2 for conversion), the total counts per pixel are given by the following calculation:

$2.23 \times 10^{1\,2} * 0.009 * 1.22 \times 10^{-12} * 1216 * (0.032)^2 * 2000 = 61.0.$

The background contributions are the detector dark of 1.2×10^{-5} counts/pixel/second (which can be ignored in this case) and a sky background which is dominated by geocoronal Lyman-α. During the daytime, the geocoronal background is 20kR, or 30.5 counts, while at night the background drops to one tenth of this, or 3.05 counts.

Finally, we calculate the signal-to-noise ratio Σ for a 2 x 2 pixel resolution element: in the daytime, $\Sigma = 61.0 \cdot 4 / \sqrt{(61.0 + 30.5) \cdot 4} = 12.7$, while at night, $\Sigma = 61.0 \cdot 4 / \sqrt{(61.0 + 3.05) \cdot 4} = 15.2$

9.6.5 Example 5: Coronagraphic imaging of the Beta-Pictoris Disk (The HRC is no longer available)

In the final example we shall consider the case where we are trying to determine the S/N achieved on the Beta Pictoris disk, assuming a disk surface brightness of R magnitude of 16 arcseconds^2 at a distance of 6 arcseconds from the central star with a V magnitude of 3.9, for an exposure time of 1000 seconds with an F435W filter. Assume that the star and disk have an A5 V-type spectrum. Using the ETC and considering the case for the 3.0 arcseconds occulting mask:

- Disk count rate = 4.98 e^-/second for a 2 x 2 aperture (including 47.5% throughput of coronagraph) Sky count rate = 0.010 e^-/second/pixel, Detector dark rate = 0.015 e^-/second/pixel
- In 1000 seconds, this gives 4,980 e^-/2 x 2 aperture in the disk region.
- Central star count rate = 3.63×10^8 e^-/second for a 101 x 101 aperture (101 x 101 aperture used to estimate total integrated flux)
- At a distance 6 arcseconds from the central star, the fraction of flux per square arcsecond in the PSF wings is 2.6×10^{-6}.
  $B_{PSF} = 3.63 \times 10^{11} * 2.6 \times 10^{-6} = 943.8$ e^- per square arcsecond. The counts collected in 4 pixels are $4 \times 0.027^2 \times 943.8 = 2.752$.
- The S/N in a 2 x 2 box is then $4980 / \sqrt{4980 + 2.8} \cong 70.5$.

9.7 Tabular Sky Backgrounds

We provide Table 9.6 of the "high" sky background numbers as plotted in Figure 9.1. See the text and the caption in Figure 9.1 for more details. These high sky values are defined as the earthshine at 38° from the limb and the high zodiacal light of m_v = 22.1 magnitude/arcseconds^2.

Table 9.6: High sky backgrounds.

Wavelength	Earthshine	Zodiacal light	Total background
Å	erg/sec/cm^2/Å/arcsec^2	erg/sec/cm^2/Å/arcsec^2	erg/sec/cm^2/Å/arcsec^2
1000.	2.41E-23	1.26E-28	2.41E-23
1100.	4.38E-22	1.02E-26	4.38E-22
1200.	4.01E-23	1.05E-25	4.02E-23
1400.	4.29E-25	2.50E-24	2.93E-24
1500.	4.16E-25	9.12E-24	9.54E-24
1600.	2.55E-25	2.30E-22	2.30E-22
1700.	7.89E-23	7.06E-21	7.14E-21
1800.	9.33E-23	1.50E-20	1.51E-20
1900.	4.39E-22	2.20E-20	2.24E-20
2000.	1.01E-21	3.49E-20	3.59E-20
2100.	1.60E-21	1.21E-19	1.23E-19
2200.	7.49E-22	2.16E-19	2.17E-19
2300.	3.32E-22	1.75E-19	1.75E-19
2400.	2.50E-22	1.79E-19	1.79E-19
2500.	2.39E-22	2.47E-19	2.47E-19
2600.	5.62E-22	2.93E-19	2.94E-19
2700.	6.77E-21	9.95E-19	1.00E-18
2800.	2.03E-21	2.82E-19	2.91E-19
2900.	4.32E-20	2.04E-18	2.08E-18
3000.	9.34E-20	1.20E-18	1.29E-18
3100.	2.07E-19	1.46E-18	1.67E-18
3200.	3.60E-19	2.25E-18	2.61E-18
3400.	6.40E-19	2.81E-18	3.45E-18

Table 9.6: High sky backgrounds.

Wavelength	Earthshine	Zodiacal light	Total background
Å	erg/sec/cm^2/Å/arcsec^2	erg/sec/cm^2/Å/arcsec^2	erg/sec/cm^2/Å/arcsec^2
3500.	8.20E-19	2.73E-18	3.55E-18
3600.	1.06E-18	2.68E-18	3.74E-18
3700.	1.22E-18	3.25E-18	4.47E-18
3800.	1.23E-18	3.05E-18	4.28E-18
3900.	1.52E-18	3.27E-18	4.79E-18
4000.	2.38E-18	4.54E-18	6.92E-18
4250.	2.33E-18	4.48E-18	6.81E-18
4500.	2.78E-18	5.32E-18	8.10E-18
5000.	2.55E-18	4.92E-18	7.47E-18
5250.	2.69E-18	5.28E-18	7.97E-18
5500.	2.56E-18	5.20E-18	7.76E-18
5750.	2.56E-18	5.33E-18	7.89E-18
6000.	2.40E-18	5.11E-18	7.51E-18
6250	2.27E-18	4.94E-18	7.21E-18
6500.	2.20E-18	4.88E-18	7.08E-18
6750.	2.07E-18	4.69E-18	6.76E-18
7000.	1.90E-18	4.40E-18	6.30E-18
7250.	1.85E-18	4.34E-18	6.19E-18
7500.	1.73E-18	4.13E-18	5.86E-18
7750.	1.63E-18	3.95E-18	5.58E-18
8000.	1.57E-18	3.85E-18	5.42E-18
8250.	1.48E-18	3.68E-18	5.16E-18
8500.	1.37E-18	3.46E-18	4.83E-18
8750.	1.31E-18	3.36E-18	4.67E-18

CHAPTER 10:

Imaging Reference Material

In this chapter. . .

10.1 Introduction

This chapter provides reference material to help you select your filter and detector configuration, and determine your observing plan (e.g., total required exposure time, and number of exposures). This chapter is, for the most part, organized by *filter* and *detector*. For each imaging mode the following are provided:

- Plots of integrated system throughput as a function of wavelength.
- Plots of the time needed to achieve a desired signal-to-noise ratio vs. magnitude for all filters for a point source and a one arcsecond^2 extended source.
- Tables of color corrections AB_V to go from Johnson V magnitude to AB magnitude.

The Tables and Figures that are provided in this Chapter may slightly differ from the current results obtained using SYNPHOT. This is due to the fact that several Tables in SYNPHOT have been updated to reflect the latest calibration results. Please contact the STScI Help Desk if you have any questions regarding this subject.

10.2 Using the Information in this Chapter

10.2.1 Sensitivity Units and Conversions

This chapter contains plots of throughputs for each imaging mode. Section 9.2 explains how to use these throughputs to calculate expected count rates from your source.

The first figure for each imaging mode gives the integrated system throughput. This is the combination of the efficiencies of the detector and of the optical elements in the light path. The throughputs in this handbook are based in part on ground test data, although, at the time of writing the overall detector efficiency curve and most filter throughputs have been adjusted based on in-flight data. The throughput is defined as the number of detected counts/second/cm^2 of telescope area relative to the incident flux in photons/cm^2/second. For the CCD, "counts" is the number of electrons detected. For the MAMA, "counts" is the number of valid events processed by the detector electronics after passing through the various pulse-shape and anti-coincidence filters. In both cases the detected counts obey Poisson statistics. The

throughput includes all obscuration effects in the optical train (e.g., due to the *HST* secondary).

To recalculate the throughput with the most recent CCD QE tables in ***synphot***[1], you can create total-system-throughput tables (instrument plus OTA) using the ***synphot calcband*** task. ***calcband*** takes any valid obsmode command string as input and produces an STSDAS table with two columns of data called "wavelength" and "throughput" as its output. For example, to evaluate the throughput for the F475W filter and the WFC detector, chip 1, you would use the command

calcband acs,wfc1,f475w sdssg_thpt.

The resulting throughput table is stored in ***sdssg_thpt***.

The ramp filters are not included in this chapter because the passband will change depending on the chosen central wavelength. The width of the passband and available range of central wavelengths for each ramp segment are listed in Table 5.2. Additionally, the passband for a ramp segment can be obtained with ***synphot***[1] using the following command ***calcband acs,wfc1,fr388n#3880 sdssg_thpt*** where the #3880 is the desired central wavelength in Angstroms.

10.2.2 Signal-to-Noise

For each imaging mode, plots are provided to estimate the signal-to-noise ratio (S/N) for a representative source. The first figure shows S/N for point sources (GAIN=1). The second figure shows S/N for uniform extended sources of area 1 arcsecond^2.

The different line styles in the S/N figures delineate regions where different sources of noise dominate. A particular source of noise (read noise for example) is presumed to dominate if it contributes more than half the total noise in the observations.

The point- and extended-source S/N figures are shown for average and low sky levels. For point sources, an aperture size of 5 x 5 pixels has been used for the WFC, 9 x 9 pixels for HRC, and 15 x 15 pixels for the SBC S/N evaluation. For extended sources, a 1 arcsecond^2 aperture was used. For the CCD the read noise has been computed assuming a number of readouts `NREAD`= integer (t / 1000 seconds), where t is the exposure time, with a minimum `NREAD=2`. That is, each exposure has a minimum `CR-SPLIT=2`. Different line styles in the figures are used to indicate which source of noise dominates.

To the left of the vertical line in the SBC S/N plots, the count rate from the source exceeds the 150 counts/second/pixel local count rate limit. This is computed from the model PSF, which gives 14% to 22% of the flux in the central pixel.

1. Synphot will soon be replaced by the pysynphot package, a significantly improved re-implementation of Synphot written in Python. Please visit the pysynphot Web page at http://stsdas.stsci.edu/pysynphot.

In situations requiring more detailed calculations (non-stellar spectra, extended sources, other sky background levels, unknown target V magnitude, etc.), the ACS ETC should be used.

Follow these steps to use the signal-to-noise plots:

1. Determine the AB magnitude of your source at the wavelength of interest. There are several ways to do this.
   - Examine Table 10.1, 10.2, or 10.3 and find AB_ν for the desired spectral type and filter. Sum the V magnitude of the target and AB_ν derived from the table.
   - Alternatively, compute ABMAG (=V+ABν) from the source flux, using the relation $ABMAG = -2.5\log f_\nu - 48.60$, or $ABMAG = -2.5\log f_\lambda - 5\log\lambda - 2.406$.
2. Find the appropriate plot for the filter in question, and locate $V+AB_\nu$ on the horizontal axis. Then read off the signal-to-noise ratio for the desired exposure time, or vice-versa.

The "x" characters at the top of each plot indicate the onset of saturation, in the case of the CCD. The "x" shows where the total number of counts exceeds the 16 bit buffer size of 65,535.

Note that the plots show the S/N as a function of source magnitude for exposure times as short as 0.1 seconds, although the minimum exposure time for the WFC CCD channel is 0.5 seconds.

10.2.3 Point Spread Functions

All information about the PSF are based on the modeled encircled energy data presented in ACS Point Spread Functions in Section 5.6

WFC/F435W

Description

Johnson B filter.

Figure 10.1: Integrated system throughput for WFC/F435W.

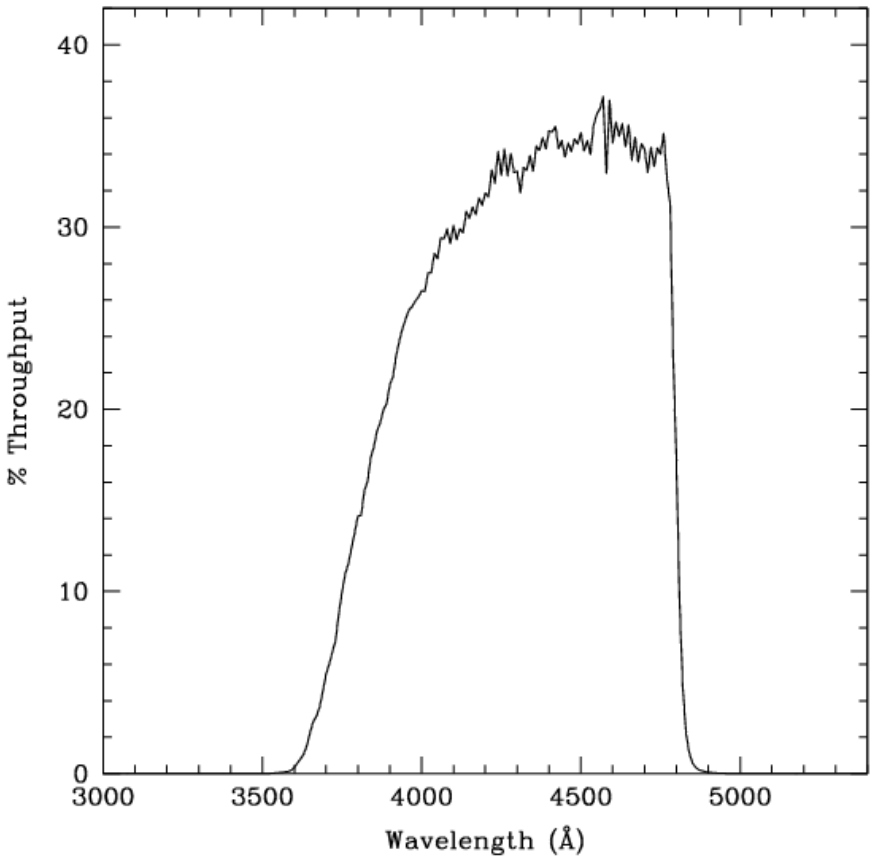

Figure 10.2: Point source S/N vs. V+ABν for the WFC/F435W filter. Top curves are for low sky; bottom curves are for average sky.

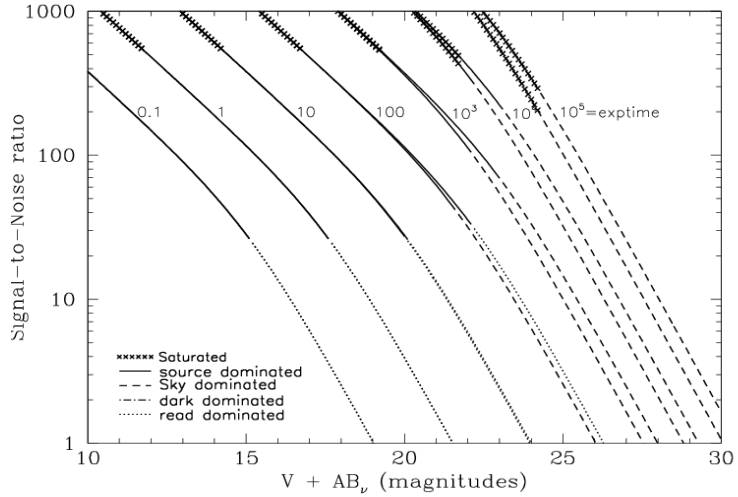

Figure 10.3: Extended source S/N vs. V+ABν for the WFC/F435W filter. Top curves are for low sky and bottom curves are for average sky for a 1 arcsec^2 area.

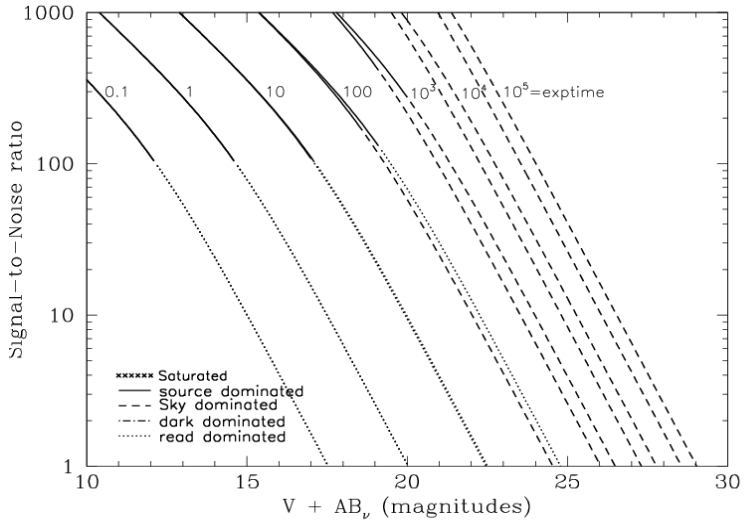

WFC/F475W

Description

Sloan Digital Sky Survey g filter.

Figure 10.4: Integrated system throughput for WFC/F475W.

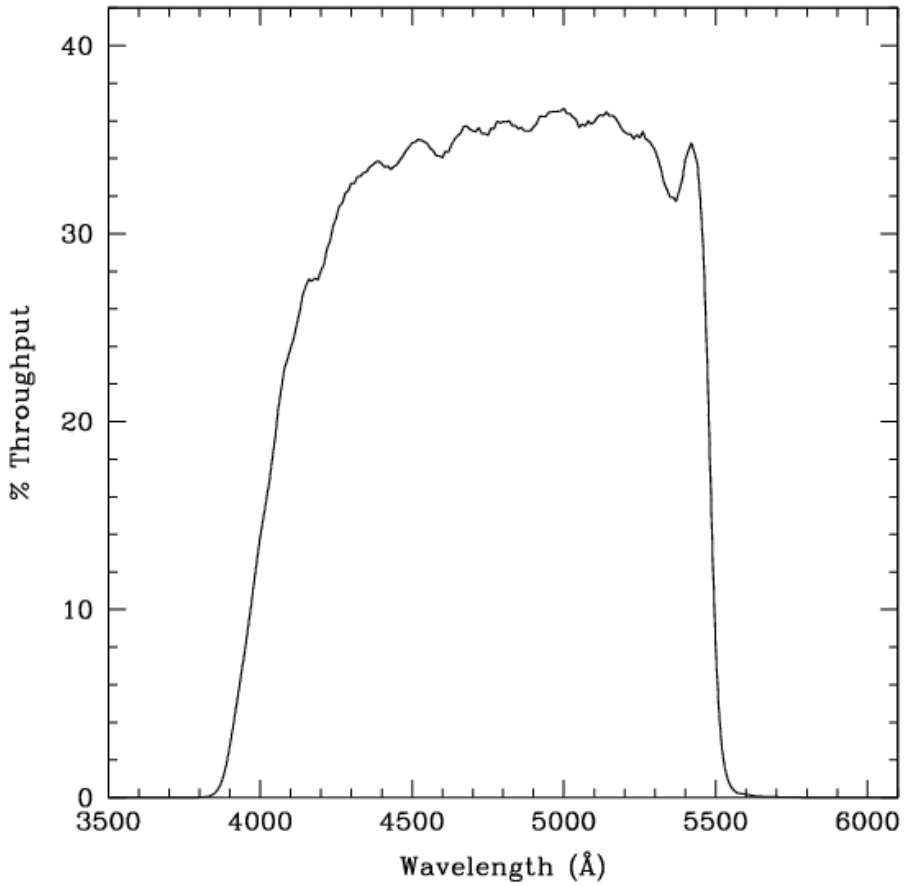

Figure 10.5: Point source S/N vs. V+ABν for the WFC/F475W filter. Top curves are for low sky; bottom curves are for average sky.

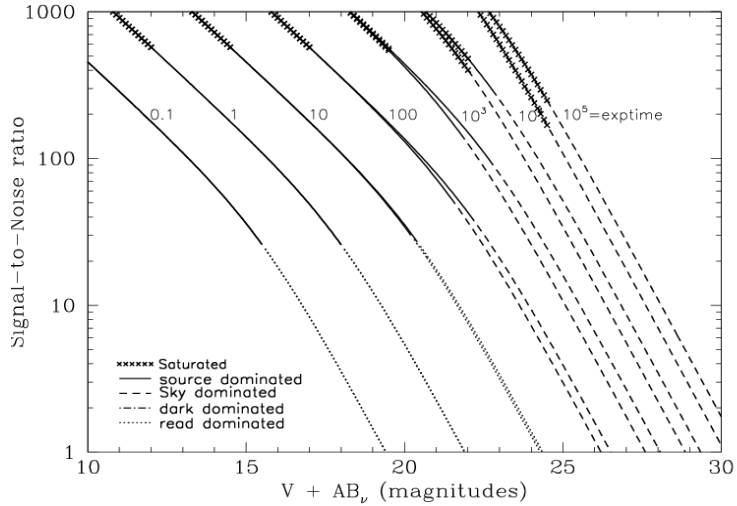

Figure 10.6: Extended source S/N vs. V+ABν for the WFC/F475W filter. Top curves are for low sky and bottom curves are for average sky for a 1 arcsec^2 area.

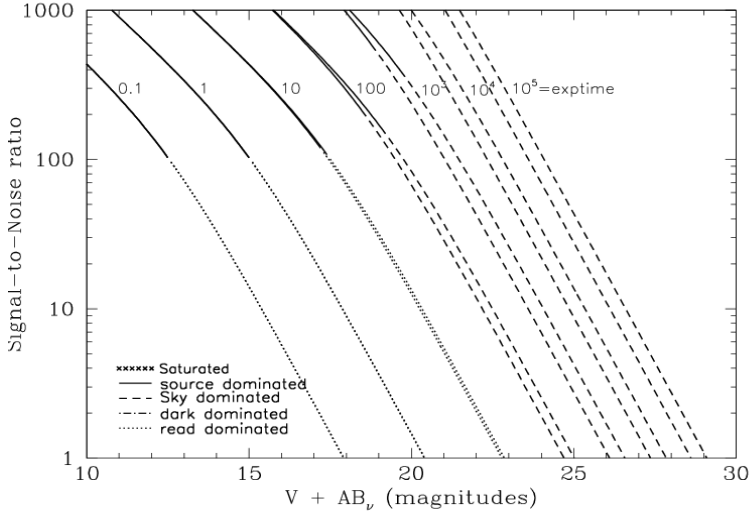

WFC/F502N

Description

OIII filter.

Figure 10.7: Integrated system throughput for WFC/F502N.

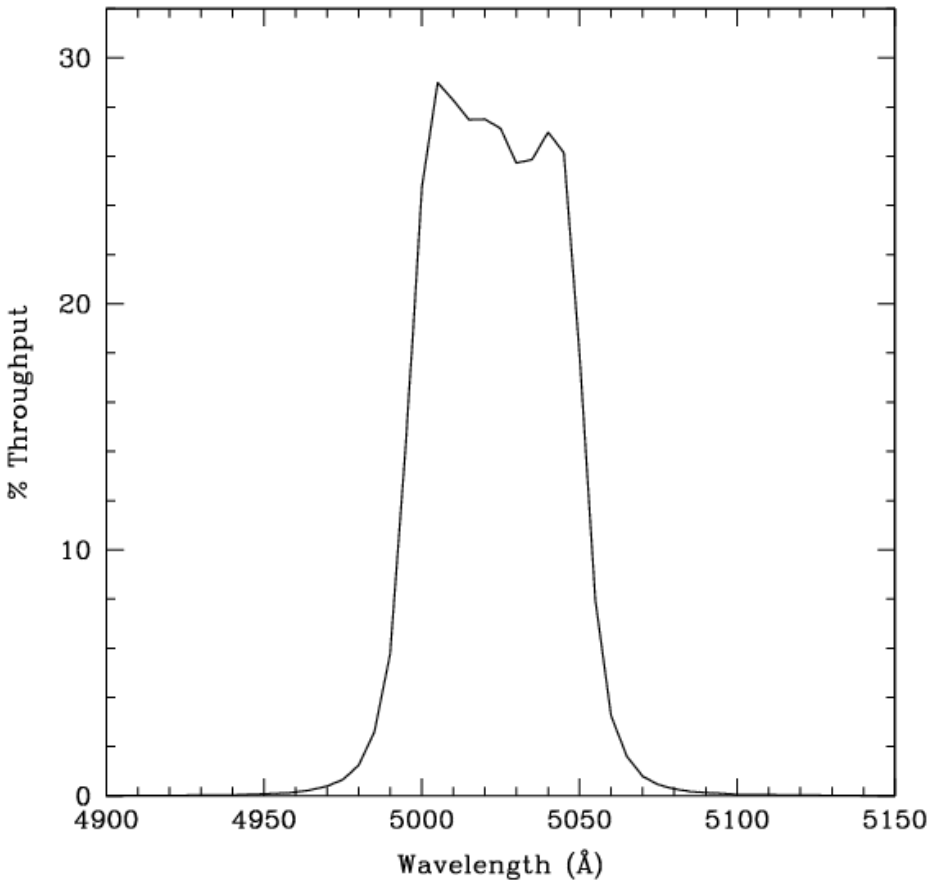

Figure 10.8: Point source S/N vs. V+ABν for the WFC/F502N filter. Top curves are for low sky; bottom curves are for average sky.

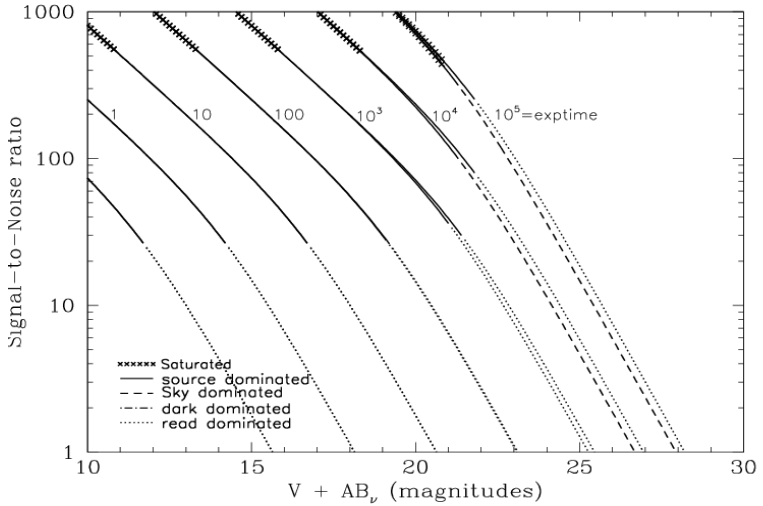

Figure 10.9: Extended source S/N vs. V+ABν for the WFC/F502N filter. Top curves are for low sky and bottom curves are for average sky for a 1 arcsec^2 area.

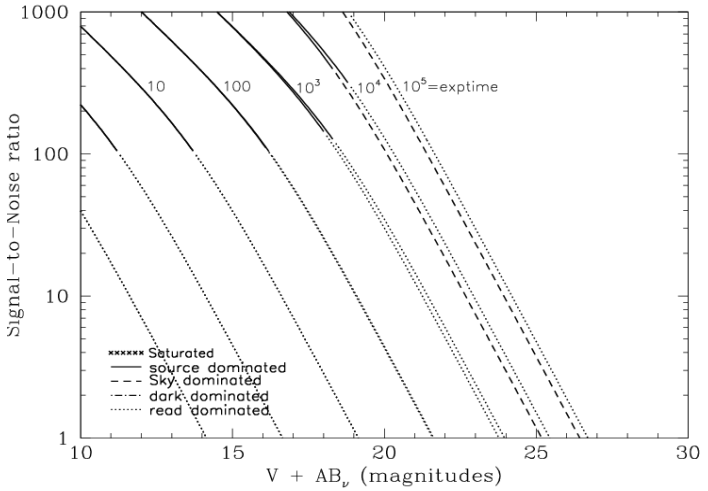

WFC/F550M

Description

Narrow V filter.

Figure 10.10: Integrated system throughput for WFC/F550M.

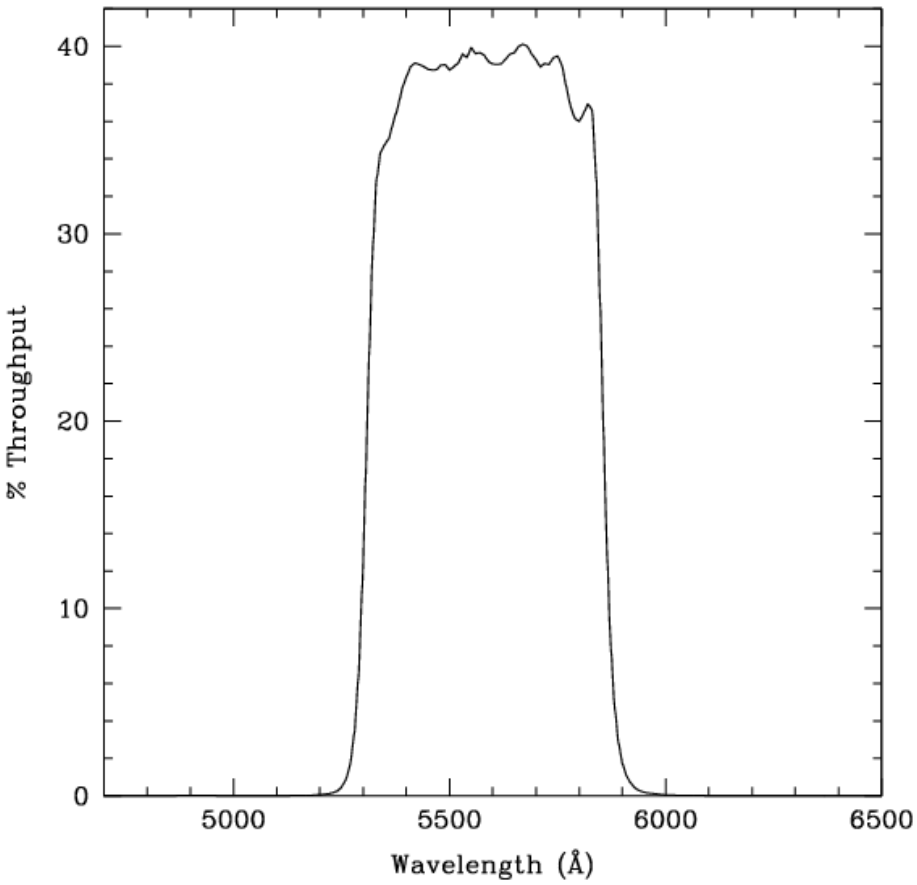

Figure 10.11: Point source S/N vs. V+ABν for the WFC/F550M filter. Top curves are for low sky; bottom curves are for average sky.

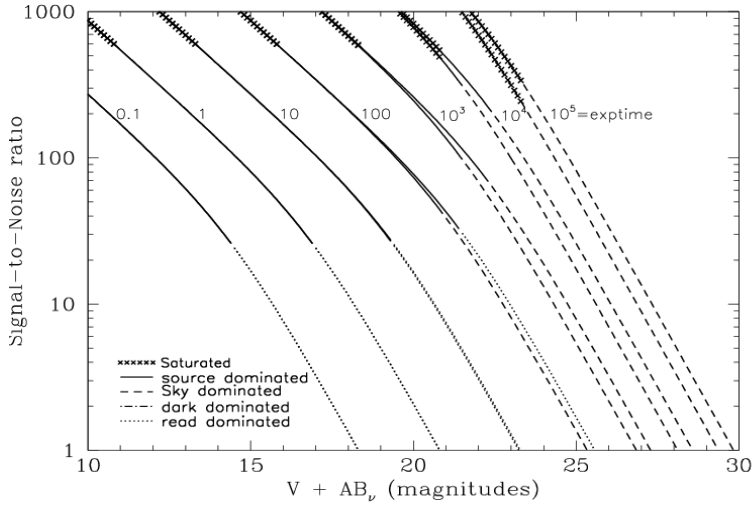

Figure 10.12: Extended source S/N vs. V+ABν for the WFC/F550M filter. Top curves are for low sky and bottom curves are for average sky for a 1 arcsec^2 area.

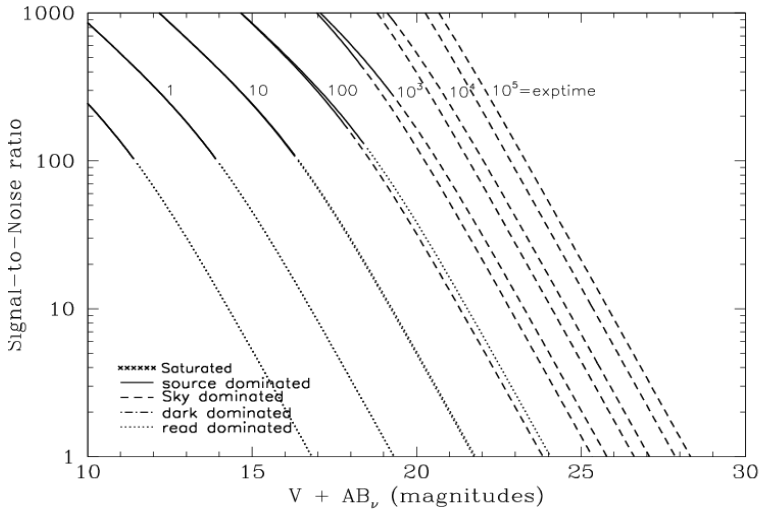

WFC/F555W

Description

Johnson V filter.

Figure 10.13: Integrated system throughput for WFC/F555W.

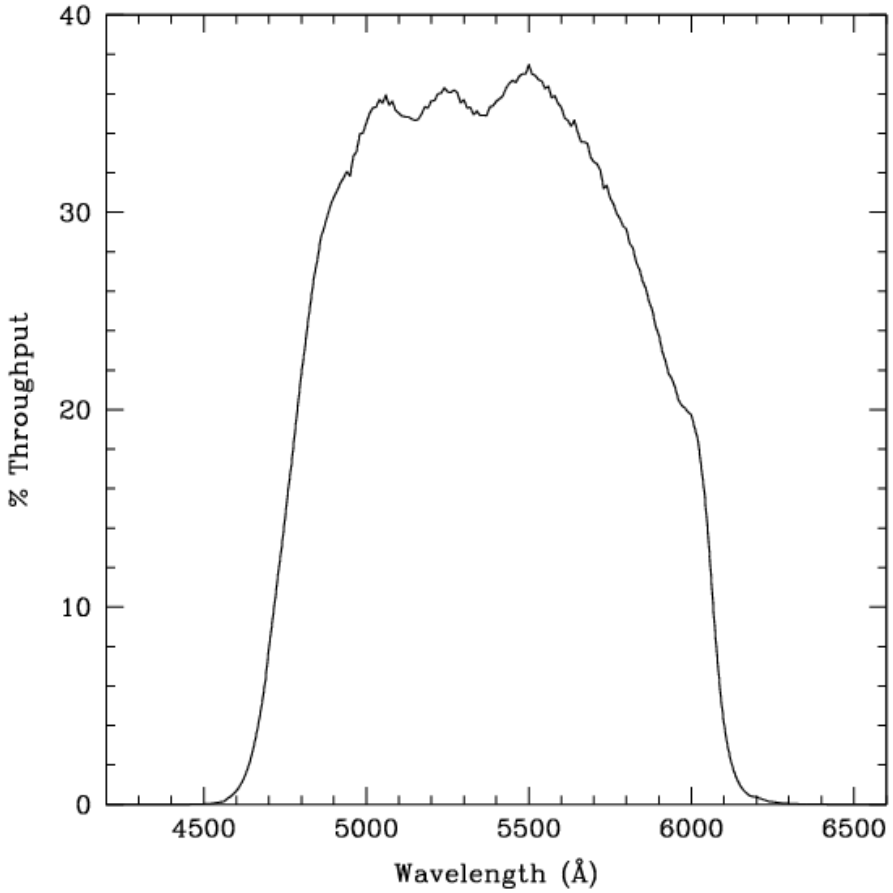

Figure 10.14: Point source S/N vs. V+ABν for the WFC/F555W filter. Top curves are for low sky; bottom curves are for average sky.

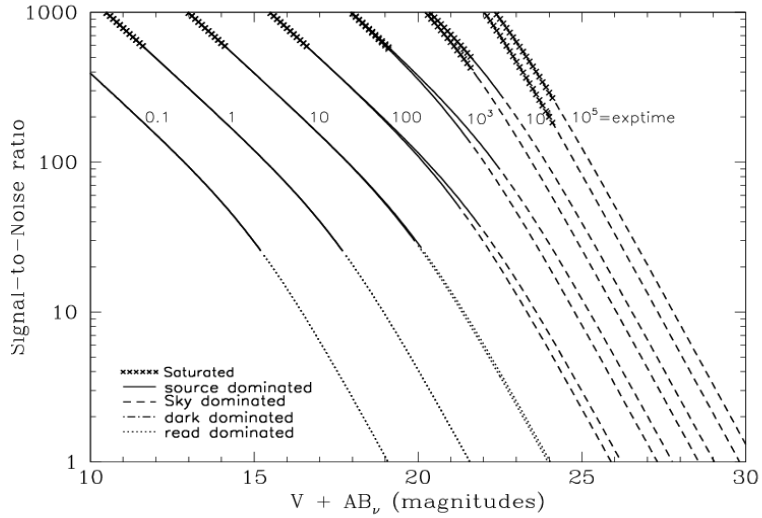

Figure 10.15: Extended source S/N vs. V+ABν for the WFC/F555W filter. Top curves are for low sky and bottom curves are for average sky for a 1 arcsec^2 area.

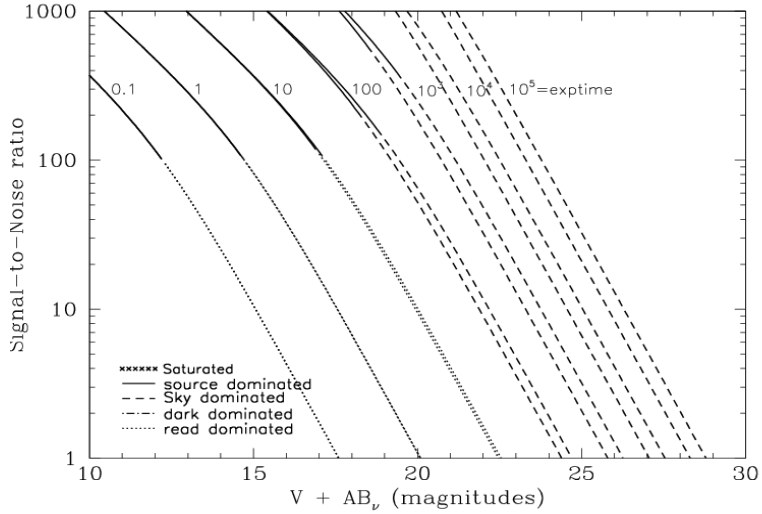

WFC/F606W

Description

Broad V filter.

Figure 10.16: Integrated system throughput for WFC/F606W.

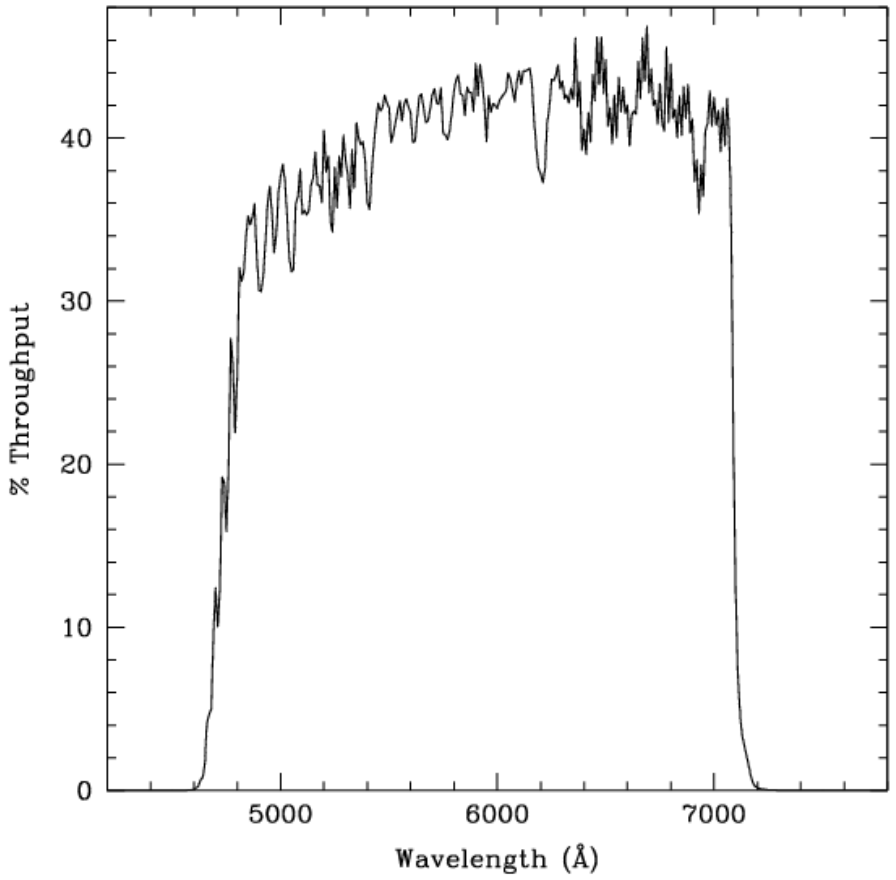

Figure 10.17: Point source S/N vs. V+ABν for the WFC/F606W filter. Top curves are for low sky; bottom curves are for average sky.

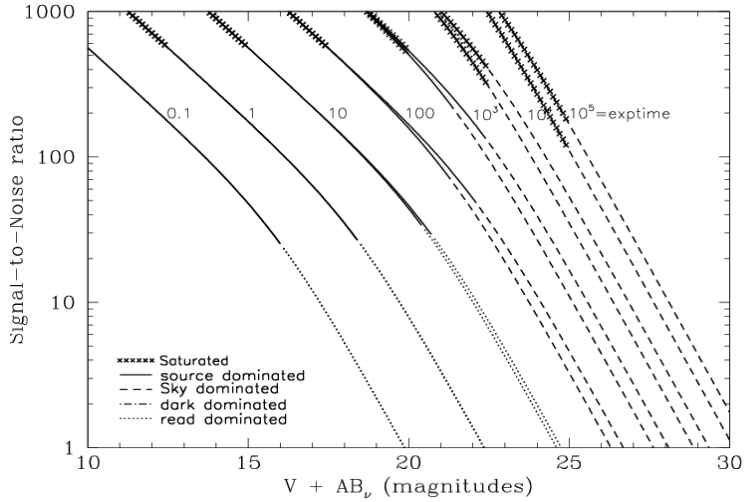

Figure 10.18: Extended source S/N vs. V+ABν for the WFC/F606W. Top curves are for low sky and bottom curves are for average sky for a 1arcsec^2 area.

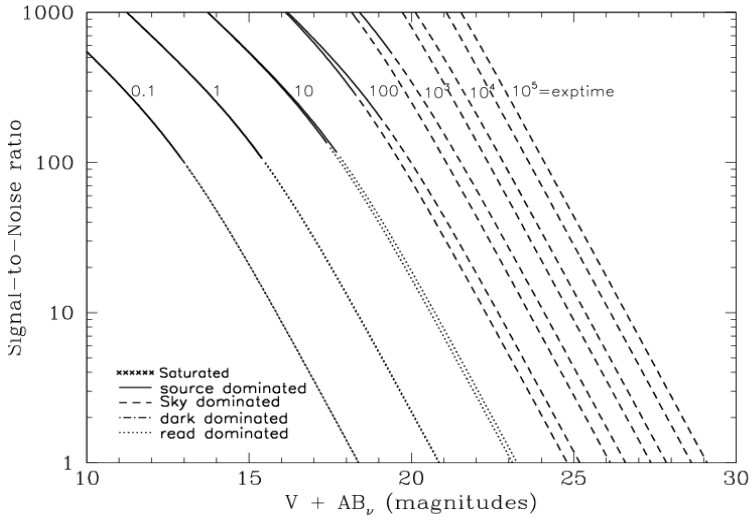

WFC/F625W

Description

Sloan Digital Sky Survey r filter.

Figure 10.19: Integrated system throughput for WFC/F625W.

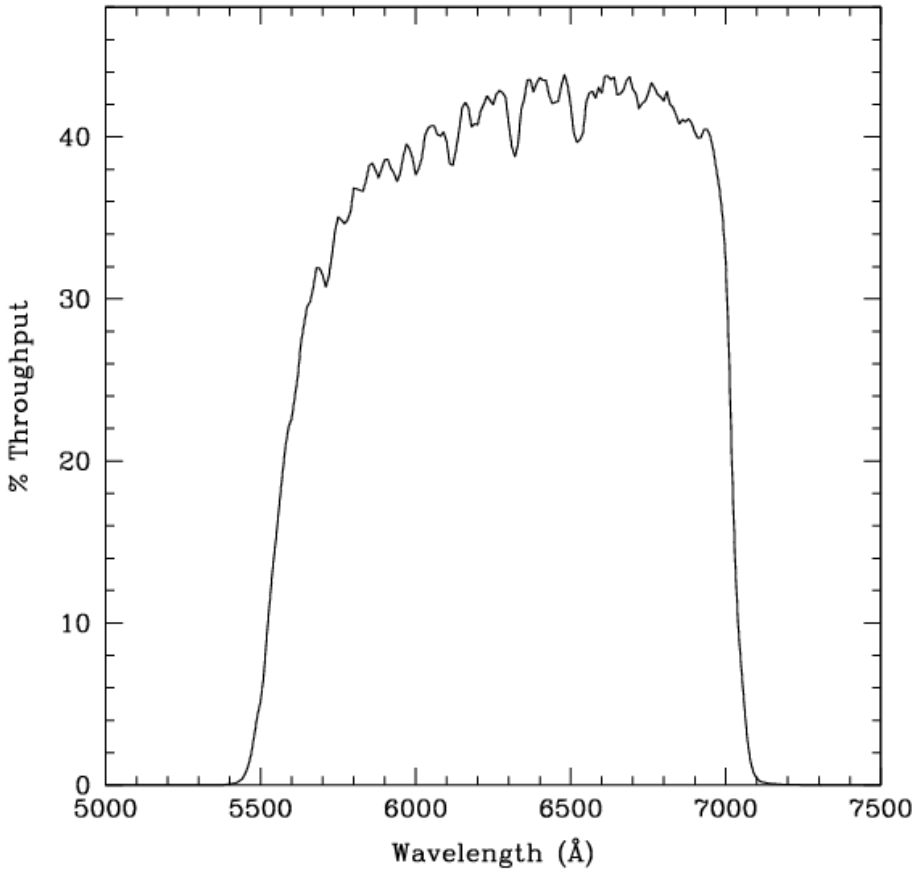

Figure 10.20: Point source S/N vs. V+ABν for the WFC/F625W filter. Top curves are for low sky; bottom curves are for average sky.

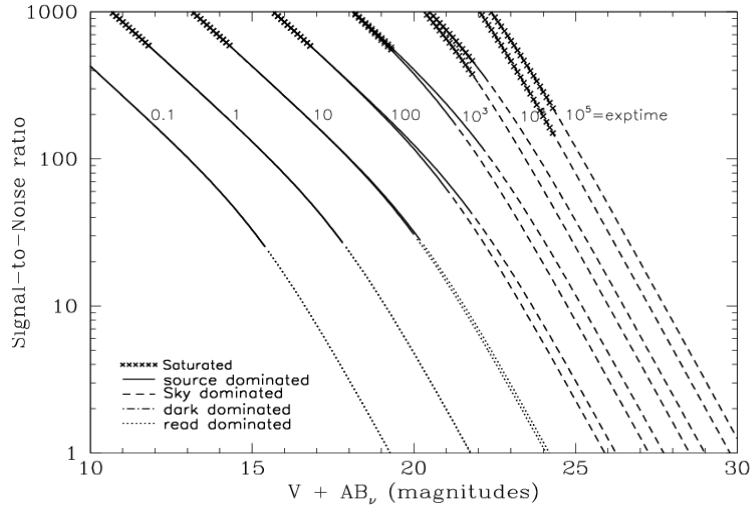

Figure 10.21: Extended source S/N vs. V+ABν for the WFC/F625W filter. Top curves are for low sky and bottom curves are for average sky for a 1 arcsec^2 area.

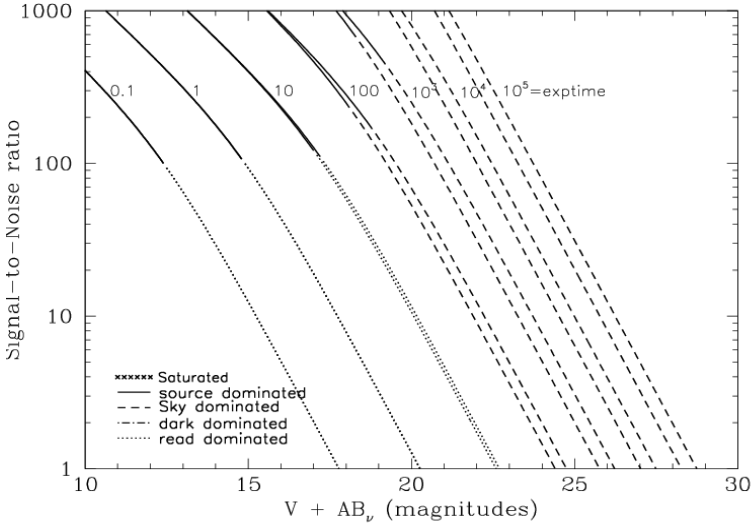

WFC/F658N

Description

Hα filter.

Figure 10.22: Integrated system throughput for WFC/F658N.

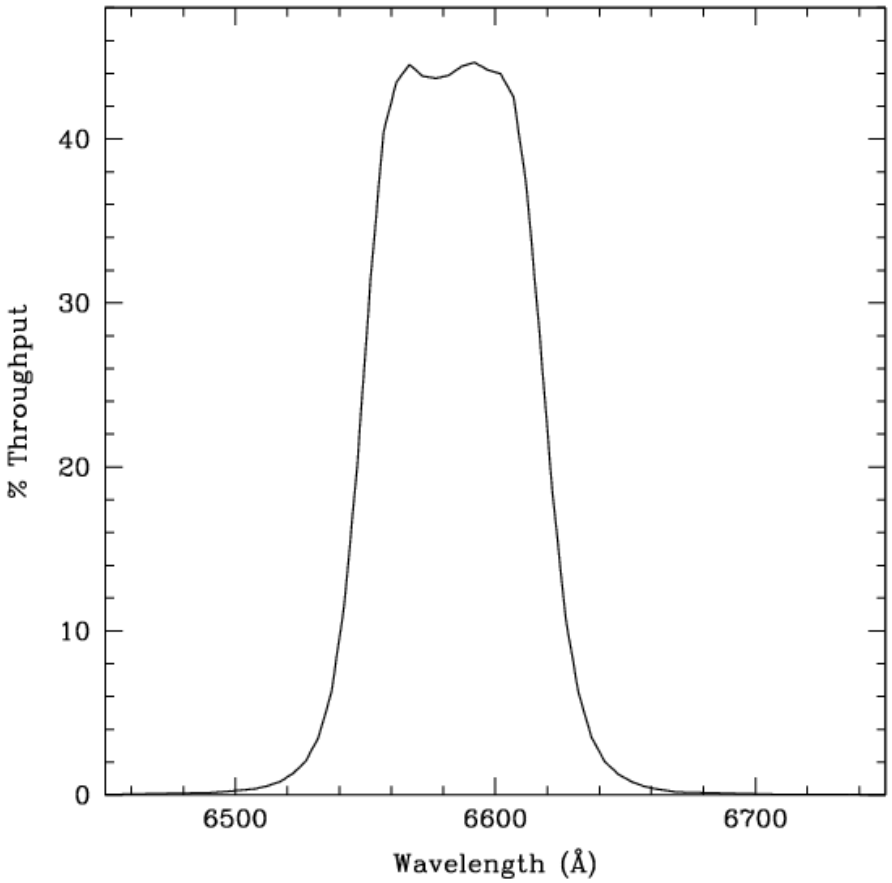

Figure 10.23: Point source S/N vs. V+ABν for the WFC/F658N filter. Top curves are for low sky; bottom curves are for average sky.

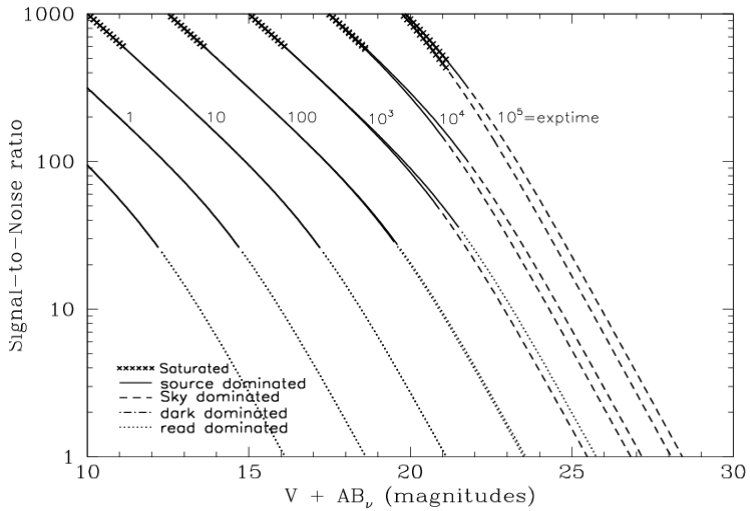

Figure 10.24: Extended source S/N vs. V+ABν for the WFC/F658N filter. Top curves are for low sky and bottom curves are for average sky for 1 arcsec^2 area.

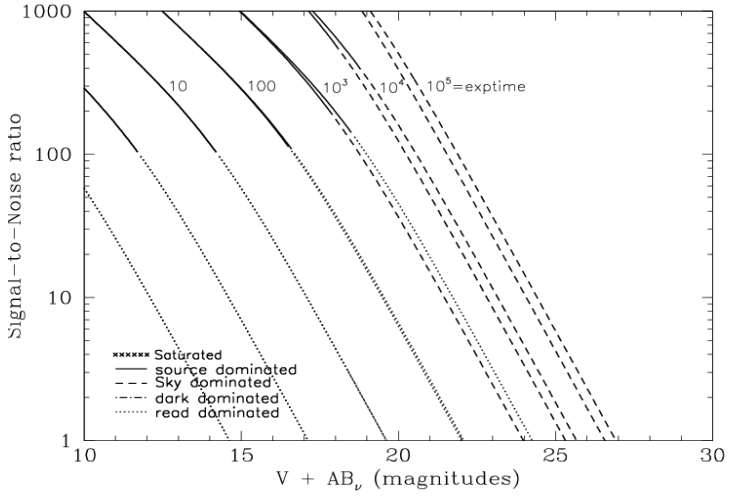

WFC/F660N

Description

NII filter.

Figure 10.25: Integrated system throughput for WFC/F660N.

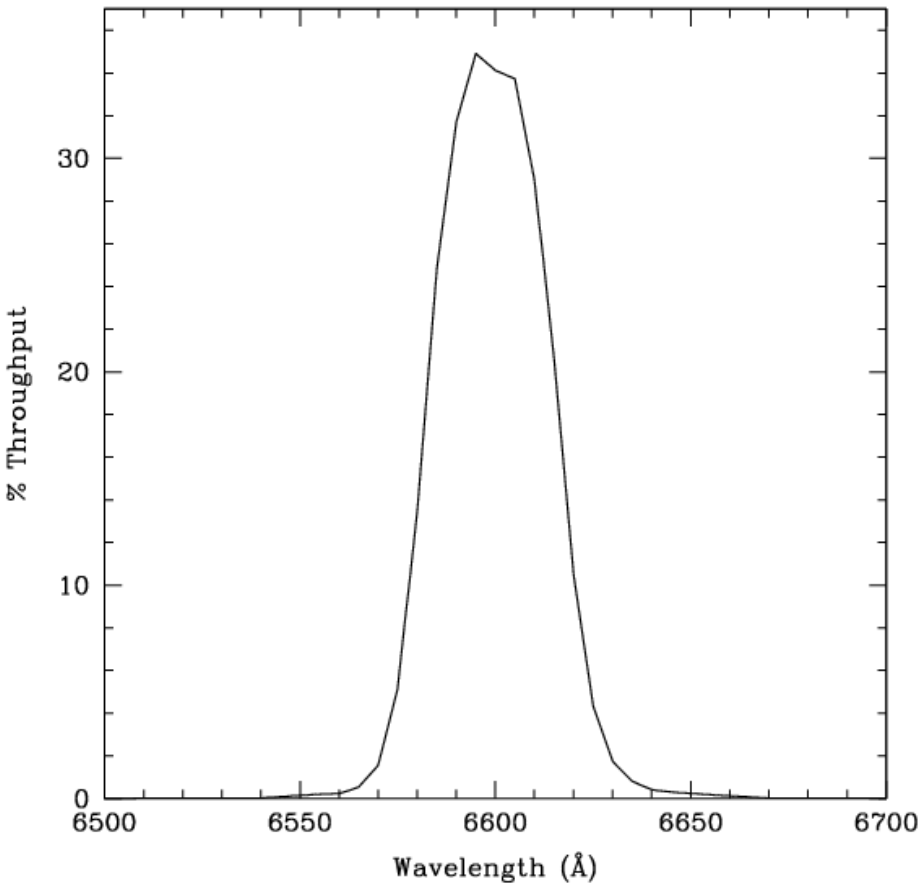

Figure 10.26: Point source S/N vs. V+ABν for the WFC/F660N filter. Top curves are for low sky; bottom curves are for average sky.

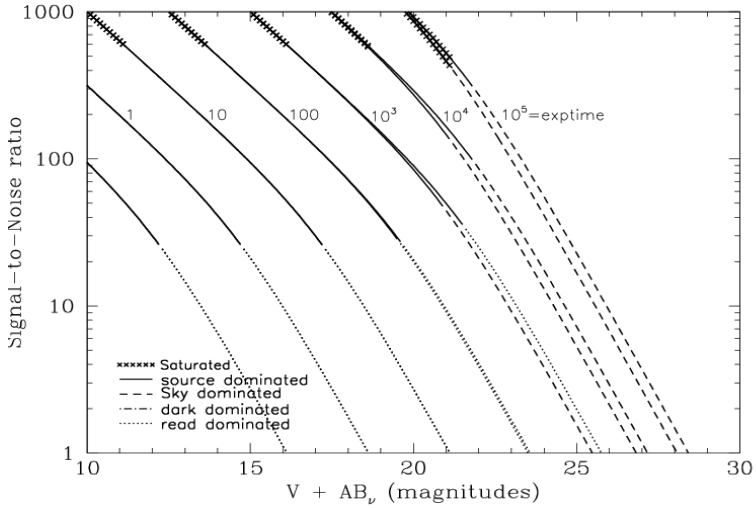

Figure 10.27: Extended source S/N vs. V+ABν for the WFC/F660N filter. Top curves are for low sky and bottom curves are for average sky for a 1 arcsec^2 area.

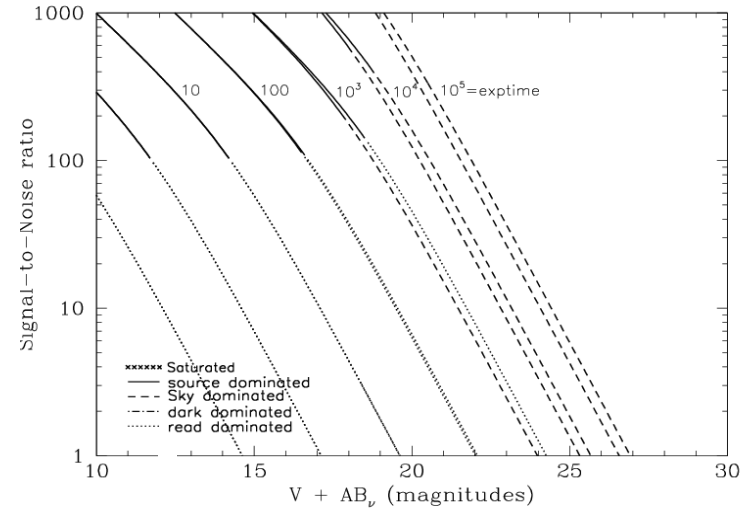

WFC/F775W

Description

Sloan Digital Sky Survey i filter

Figure 10.28: Integrated system throughput for WFC/F775W.

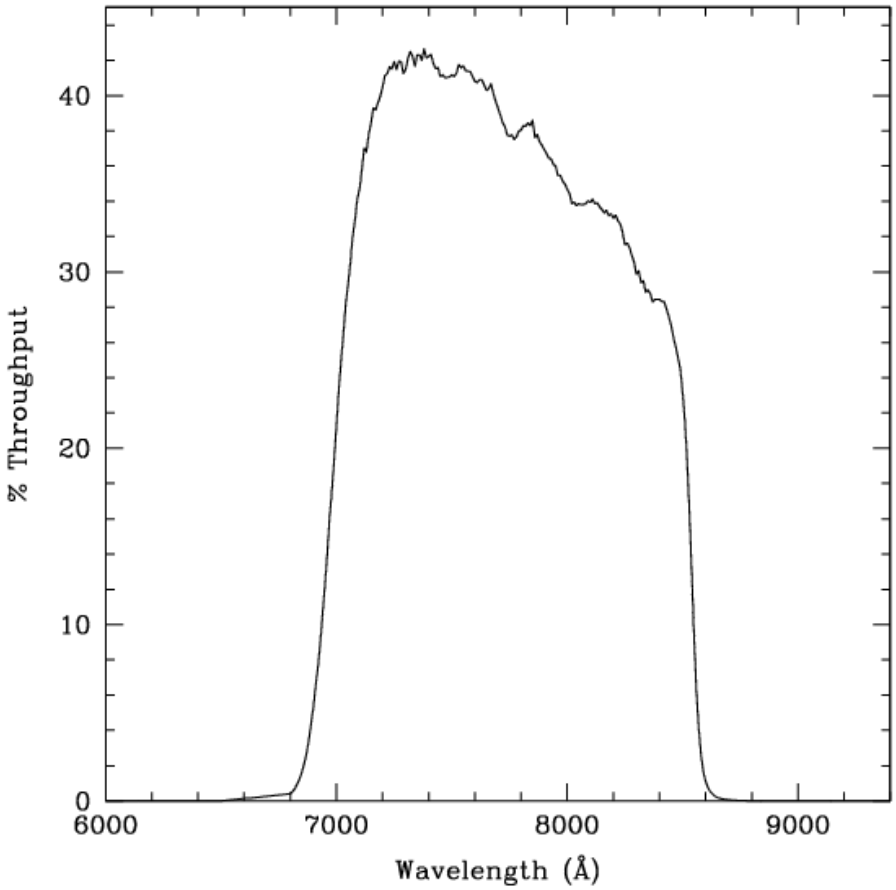

Figure 10.29: Point source S/N vs. V+ABν for the WFC/F775W filter. Top curves are for low sky; bottom curves are for average sky.

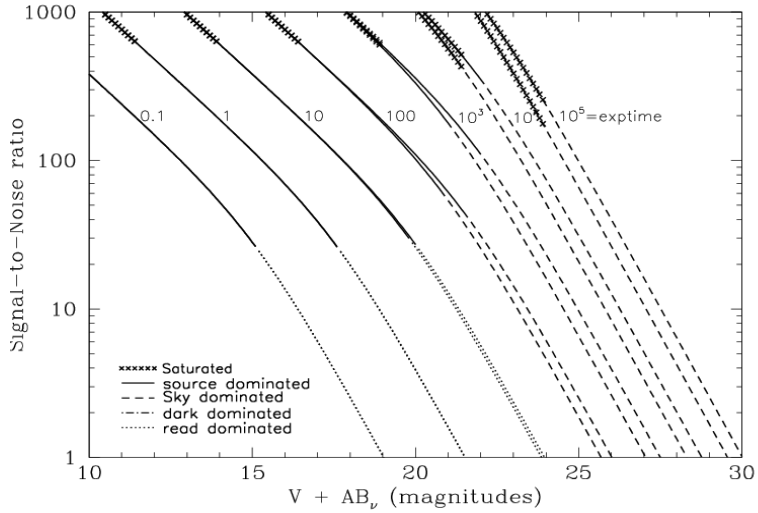

Figure 10.30: Extended source S/N vs. V+ABν for the WFC/F775W filter. Top curves are for low sky and bottom curves are for average sky for a 1 arcsec^2 area.

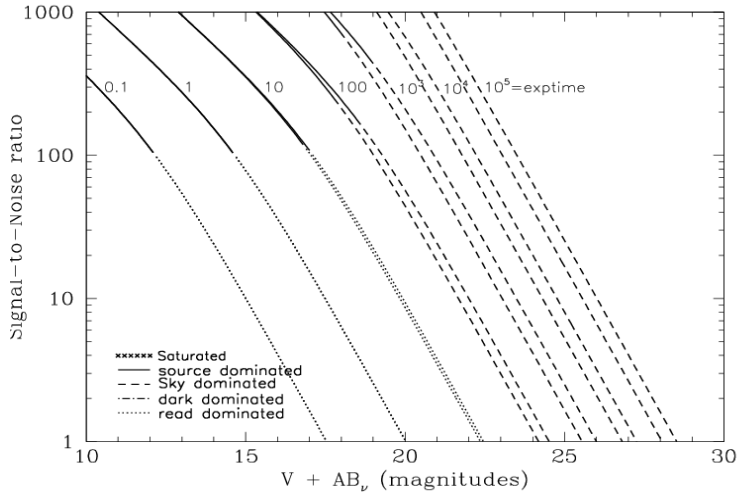

WFC/F814W

Description

Broad I filter.

Figure 10.31: Integrated system throughput for WFC/F814W.

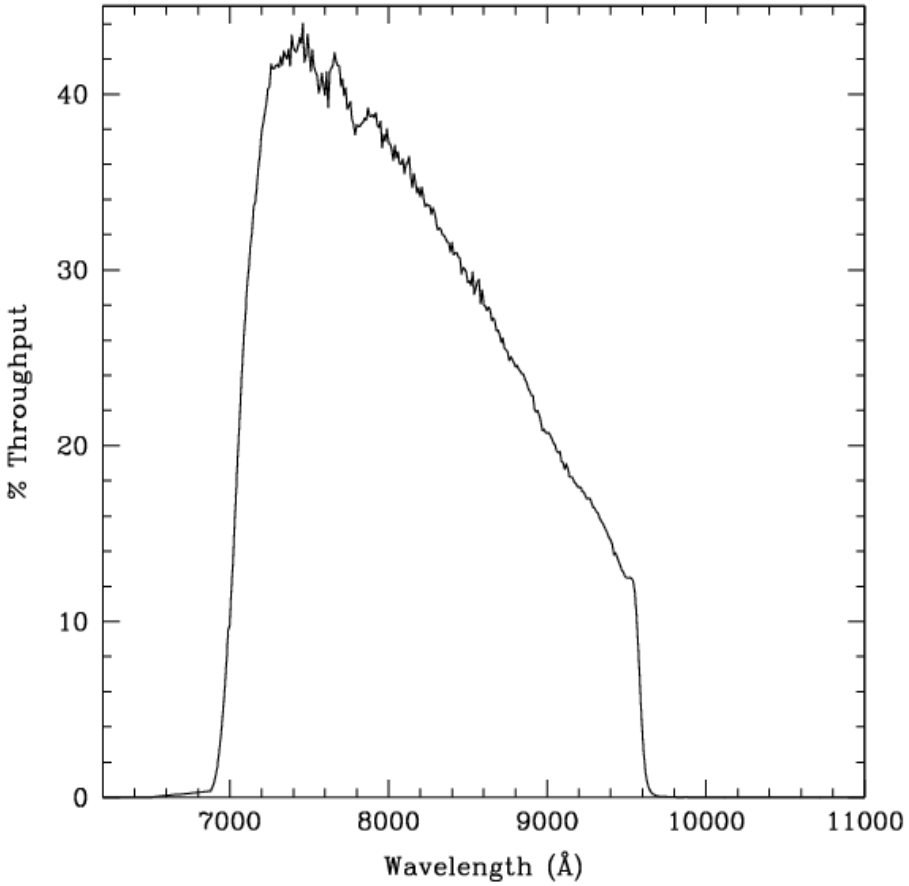

Figure 10.32: Point source S/N vs. V+ABν for the WFC/F814W filter. Top curves are for low sky; bottom curves are for average sky.

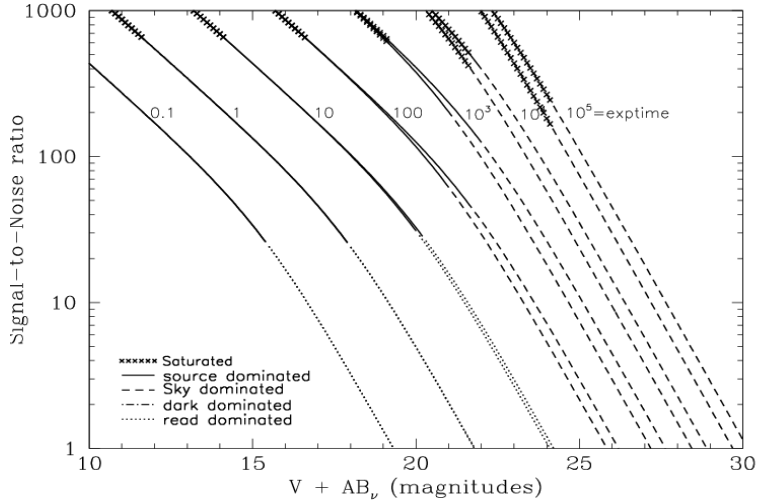

Figure 10.33: Extended source S/N vs. V+ABν for the WFC/F814W filter. Top curves are for low sky and bottom curves are for average sky for a 1 arcsec^2 area.

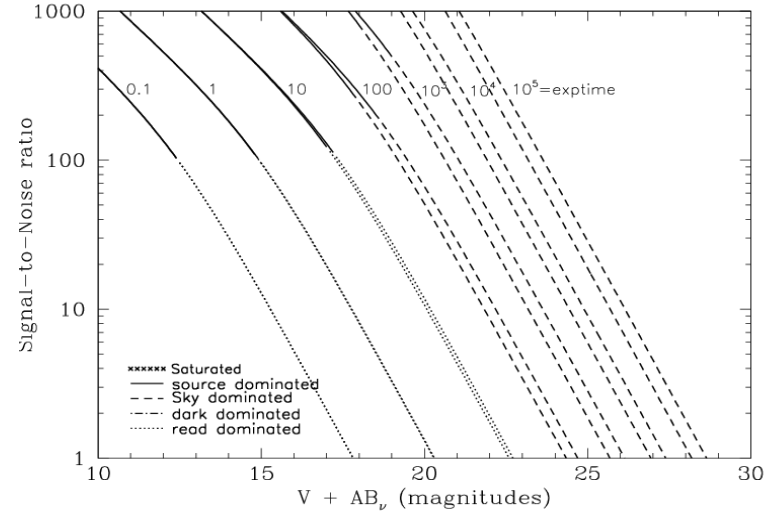

WFC/F850LP

Description

Sloan Digital Sky Survey z filter.

Figure 10.34: Integrated system throughput for WFC/F850LP.

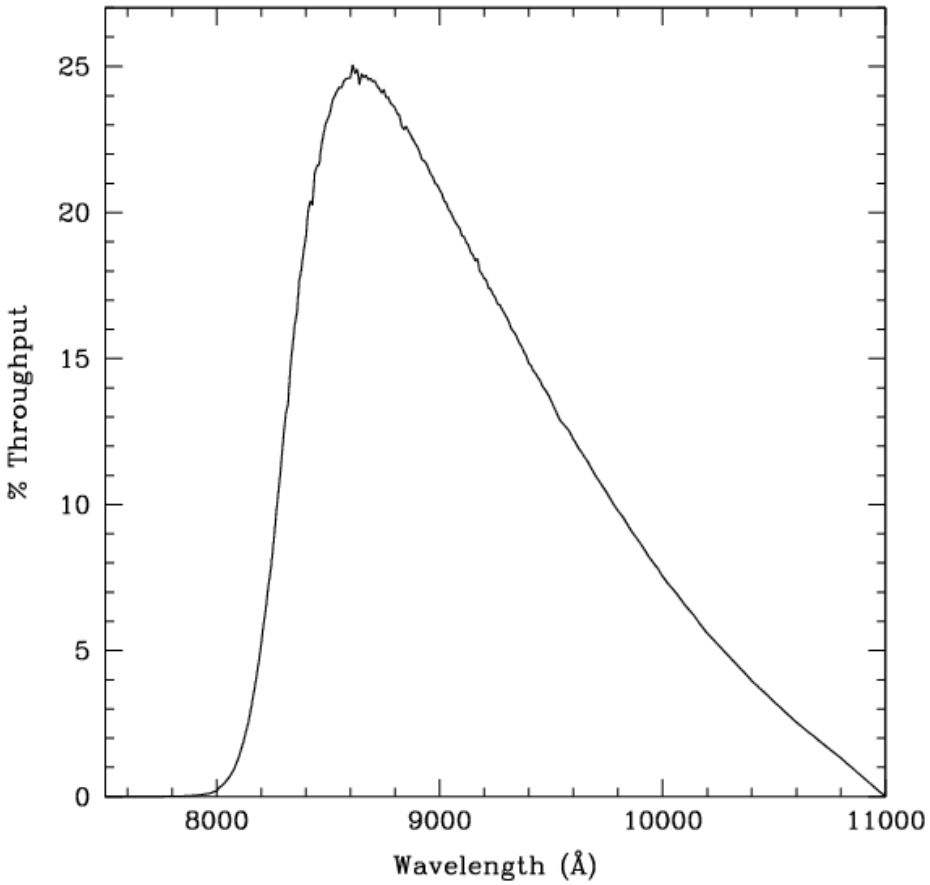

Figure 10.35: Point source S/N vs. V+ABν for the WFC/F850LP filter. Top curves are for low sky; bottom curves are for average sky.

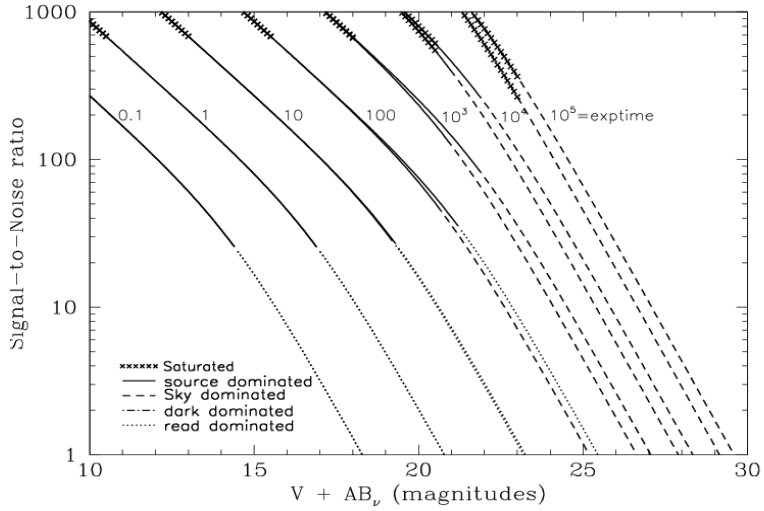

Figure 10.36: Extended source S/N vs. V+ABν for the WFC/F850LP filter. Top curves are for low sky and bottom curves are for average sky for a 1arcsec^2 area.

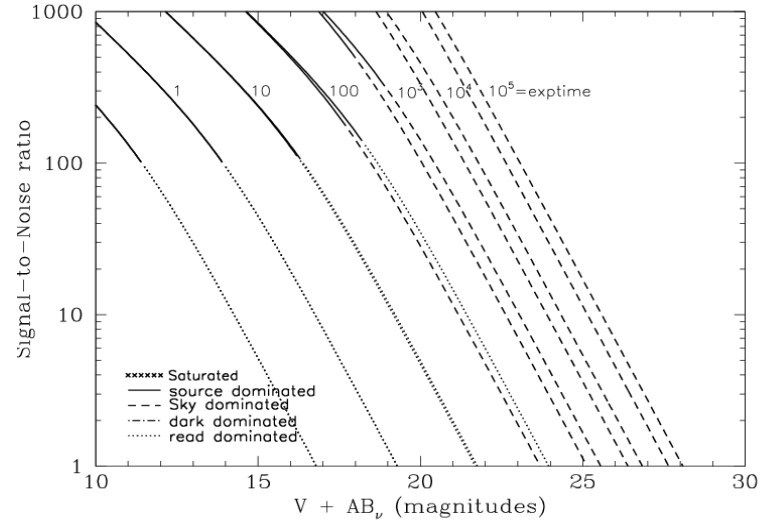

WFC/G800L

Description

Grism.

Figure 10.37: Integrated system throughput for WFC/G800L.

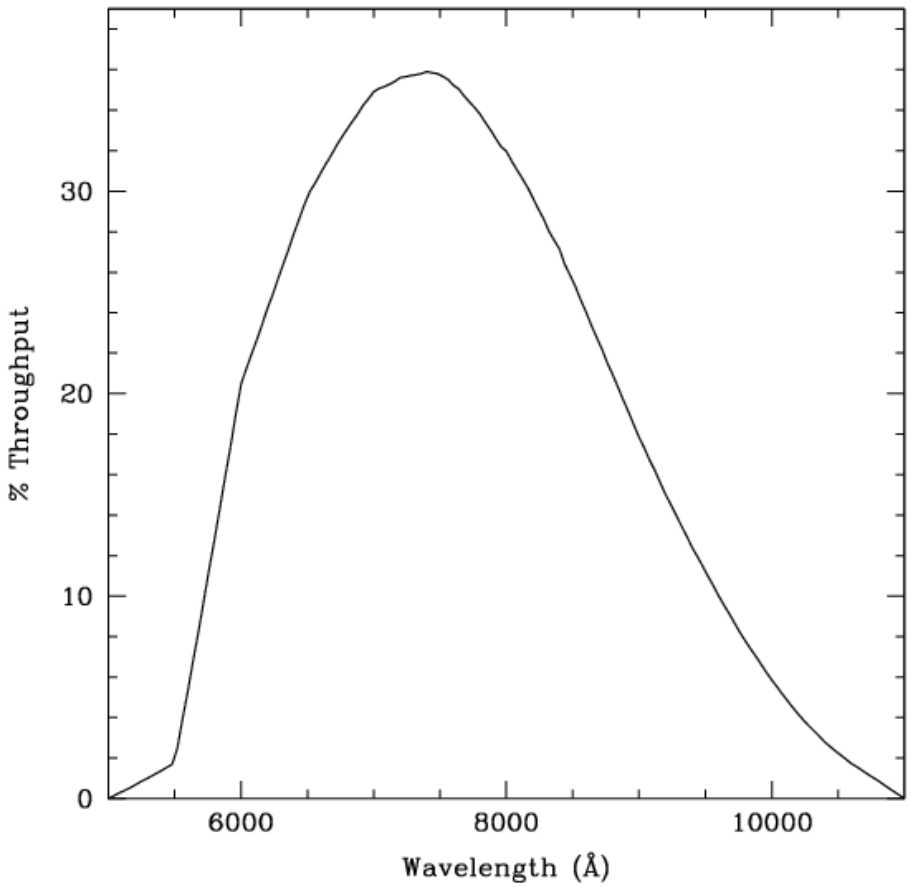

Figure 10.38: Point source S/N vs. V+ABν for the WFC/G800L filter. Top curves are for low sky; bottom curves are for average sky.

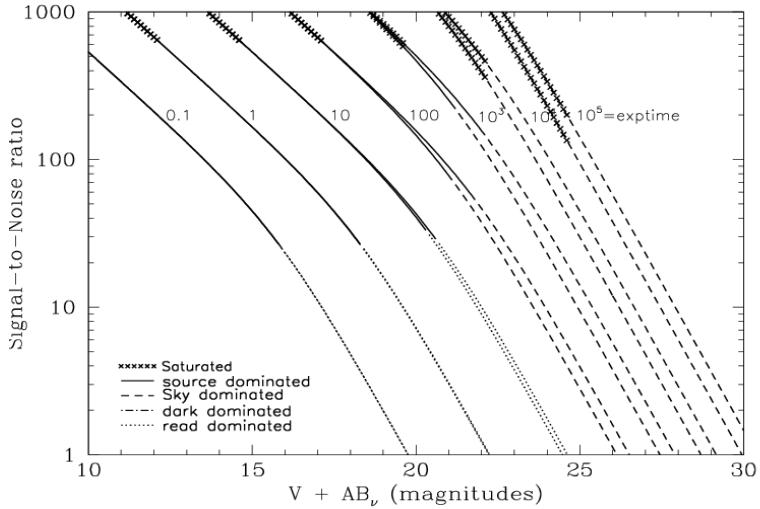

Figure 10.39: Extended source S/N vs. V+ABν for the WFC/G800L filter. Top curves are for low sky and bottom curves are for average sky for a 1arcsec^2 area.

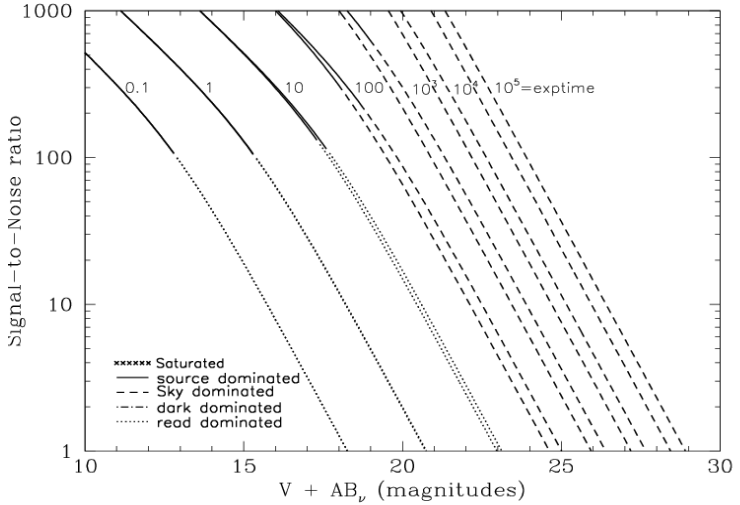

WFC/CLEAR

Description

Clear filter.

Figure 10.40: Integrated system throughput for WFC/Clear.

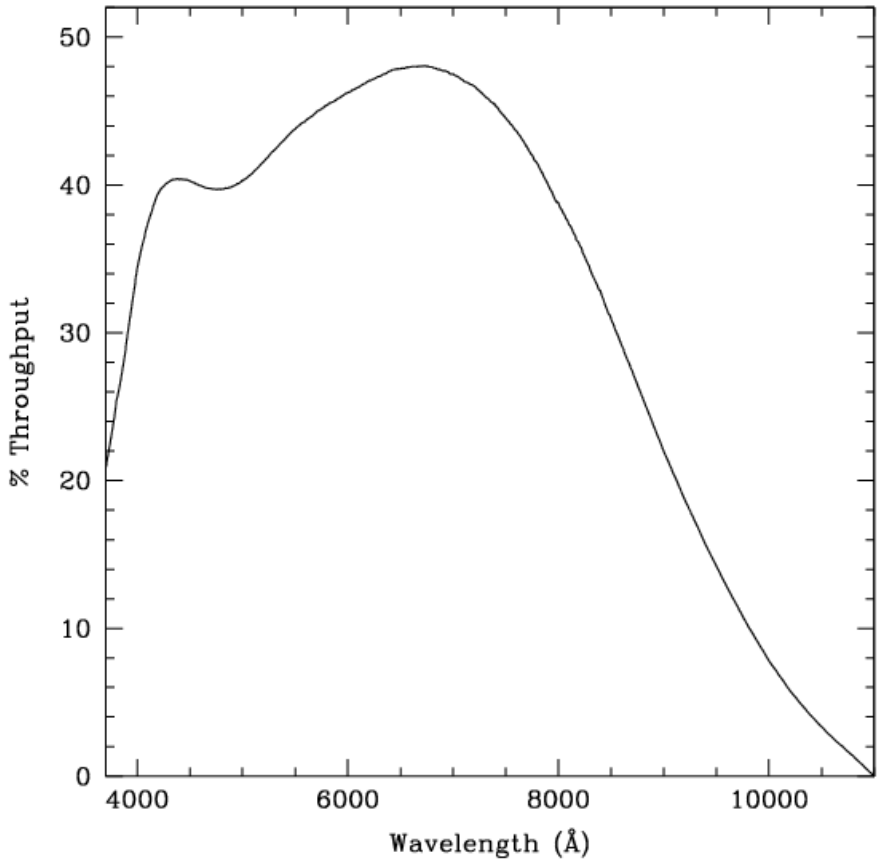

Figure 10.41: Point source S/N vs. V+ABν for the WFC/Clear filter. Top curves are for low sky; bottom curves are for average sky.

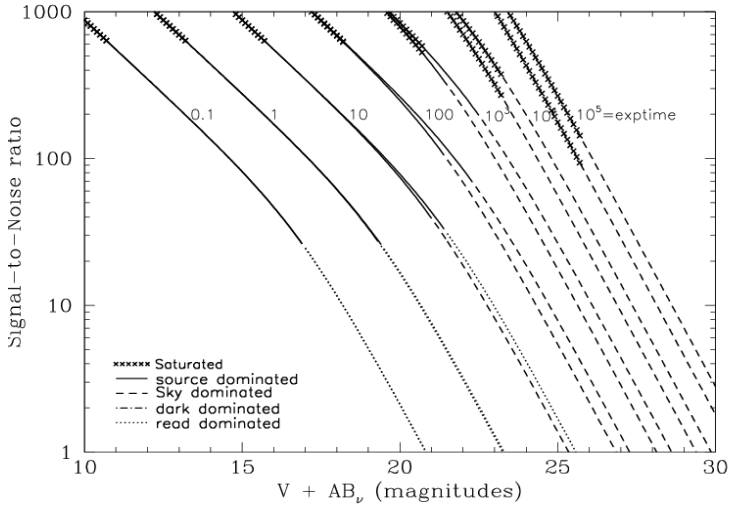

Figure 10.42: Extended source S/N vs. V+ABν for the WFC/Clear filter. Top curves are for low sky and bottom curves are for average sky for a 1 arcsec^2 area.

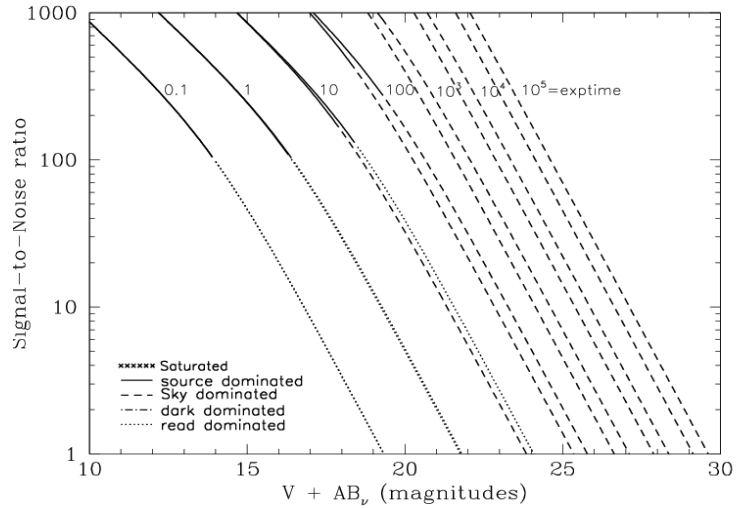

HRC/F220W

Description

Near-UV filter.

Figure 10.43: Integrated system throughput for HRC/F220W.

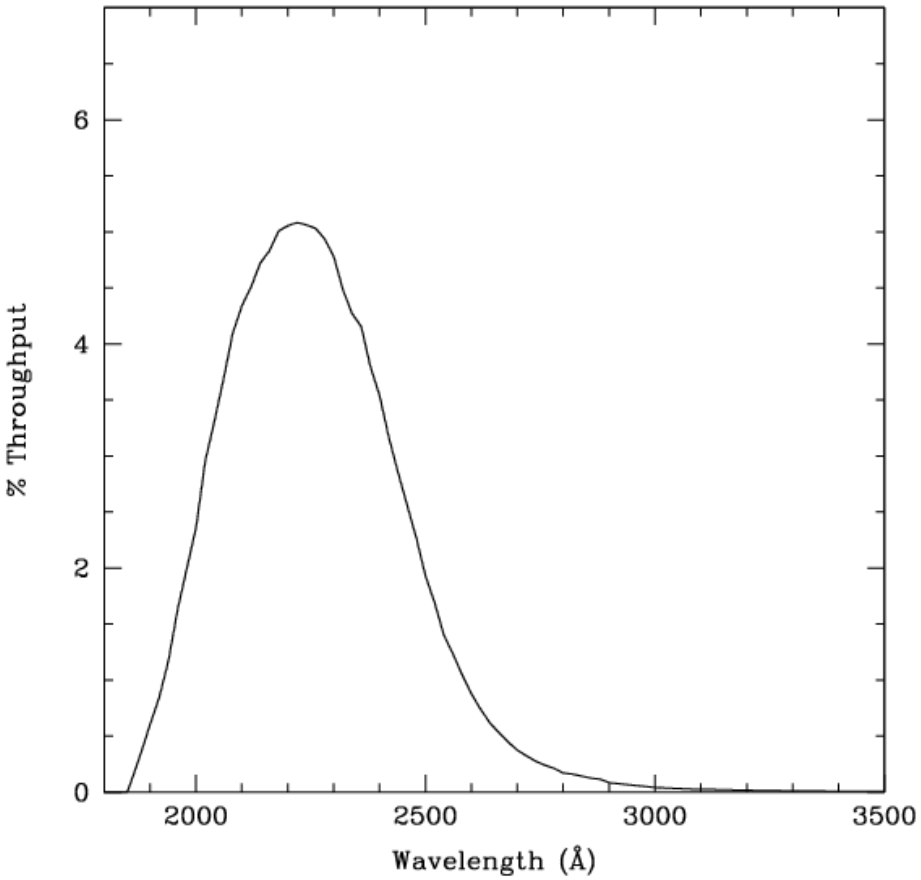

Figure 10.44: Point source S/N vs. V+ABν for the HRC/F220W filter. Top curves are for low sky; bottom curves are for average sky.

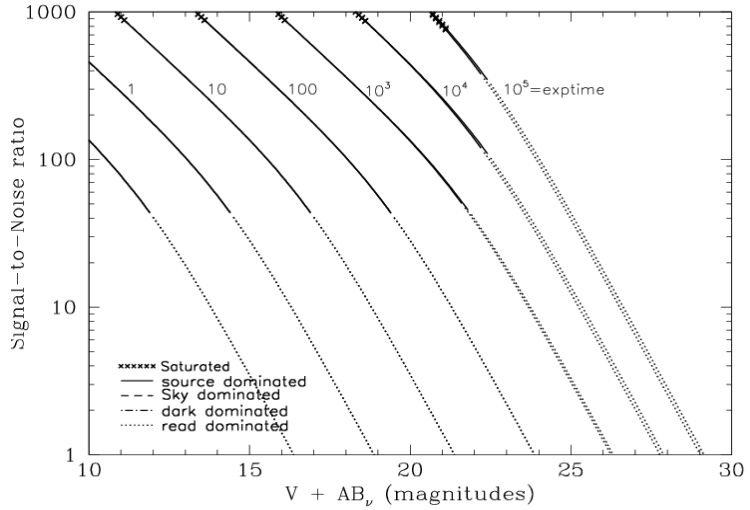

Figure 10.45: Extended source S/N vs. V+ABν for the HRC/F220W filter. Top curves are for low sky and bottom curves are for average sky for a 1 arcsec^2 area.

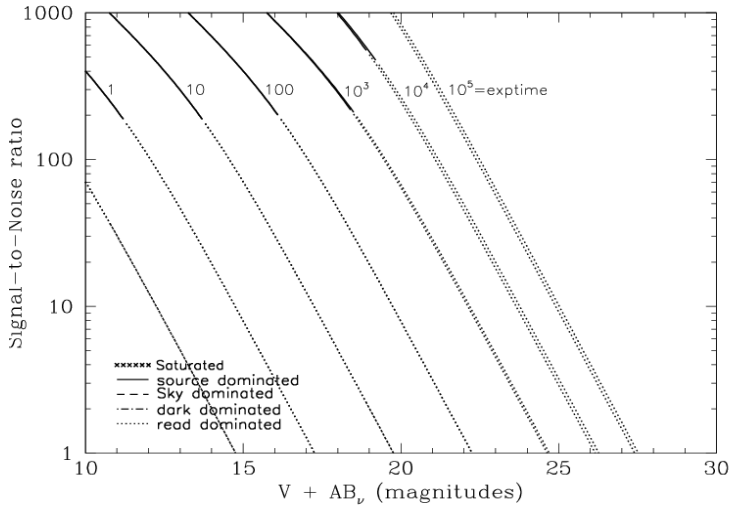

HRC/F250W

Description

Near-UV filter.

Figure 10.46: Integrated system throughput for HRC/F250W.

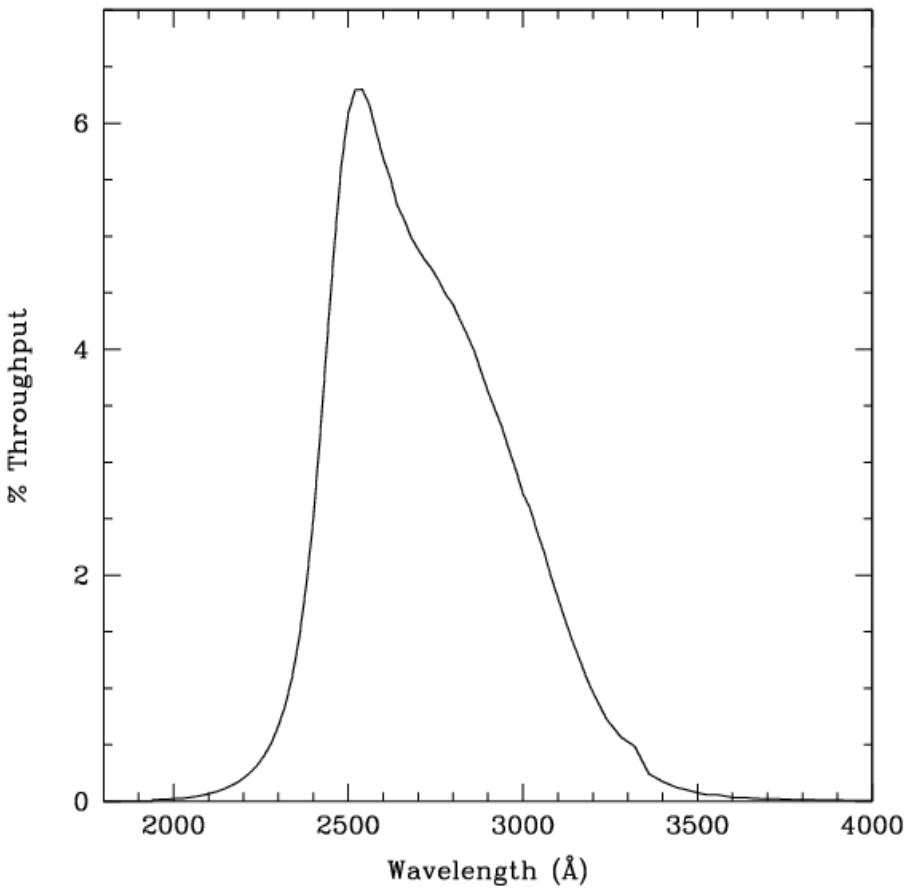

Figure 10.47: Point Source S/N vs. V+ABν for the HRC/F250W filter. Top curves are for low sky; bottom curves are for average sky.

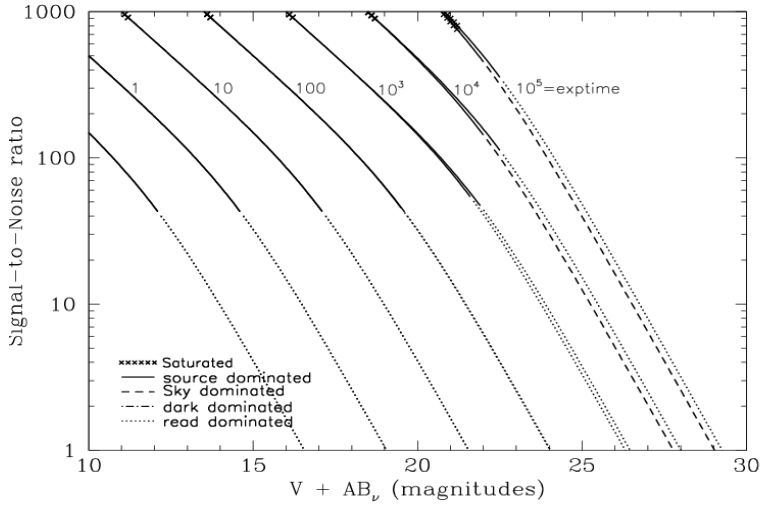

Figure 10.48: Extended Source S/N vs. V+ABν for the HRC/F250W filter. Top curves are for low sky and bottom curves are for average sky for a 1 arcsec^2 area.

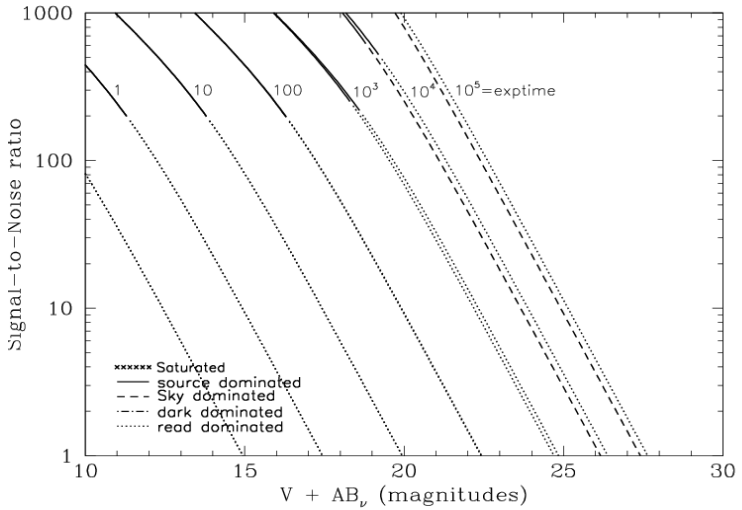

HRC/F330W

Description

HRC u filter.

Figure 10.49: Integrated system throughput for HRC/F330W.

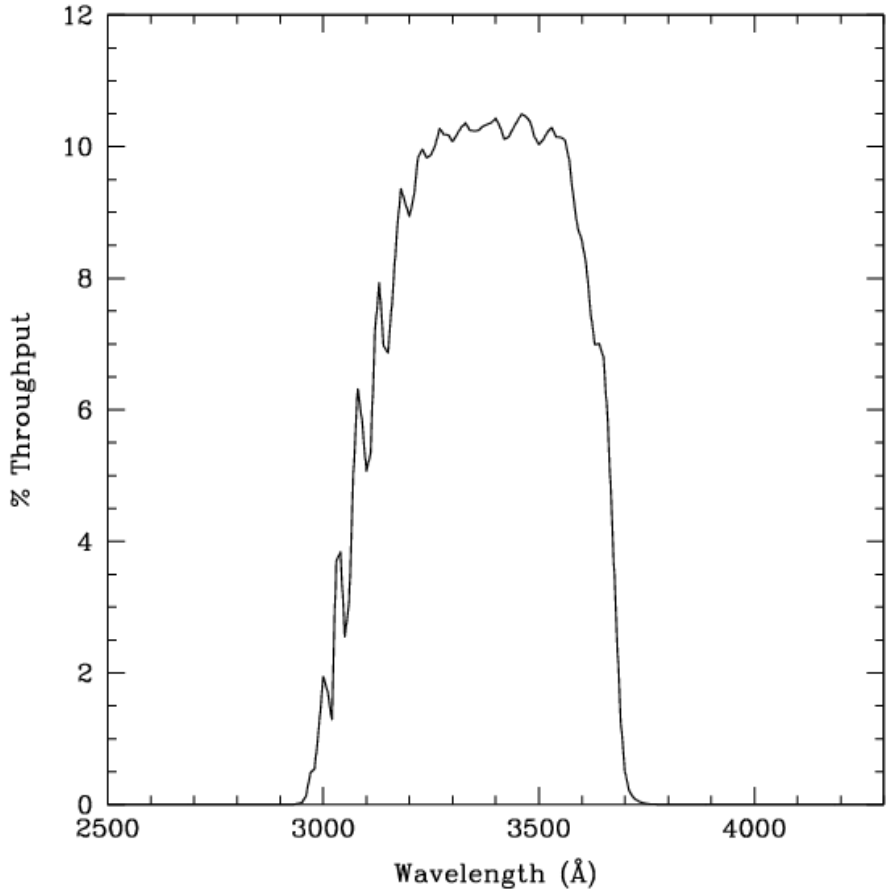

Figure 10.50: Point source S/N vs. V+ABν for the HRC/F330W filter. Top curves are for low sky; bottom curves are for average sky.

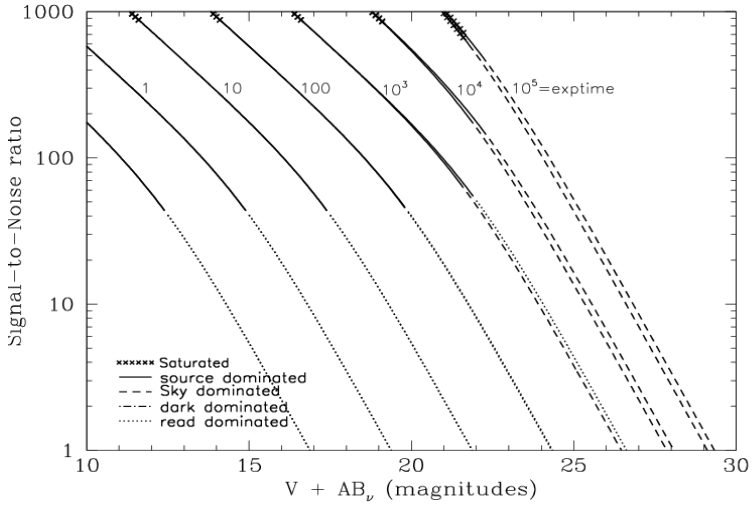

Figure 10.51: Extended source S/N vs. V+ABν for the HRC/F330W filter. Top curves are for low sky and bottom curves are for average sky for a 1 arcsec^2 area.

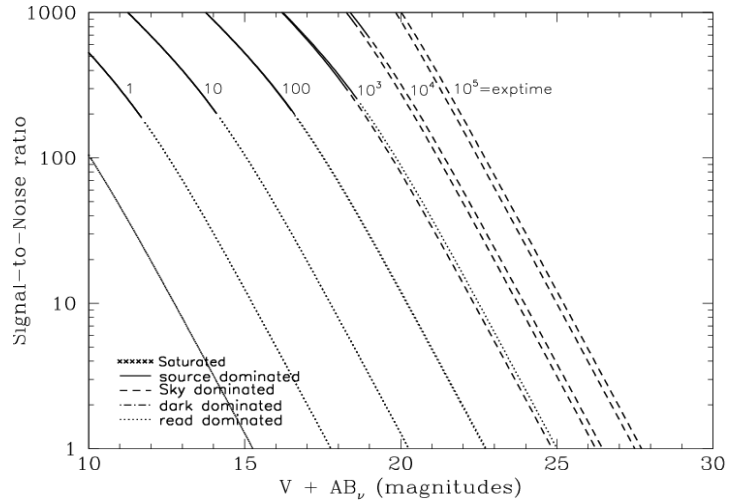

HRC/F344N

Description

NeV filter.

Figure 10.52: Integrated system throughput for HRC/F344N.

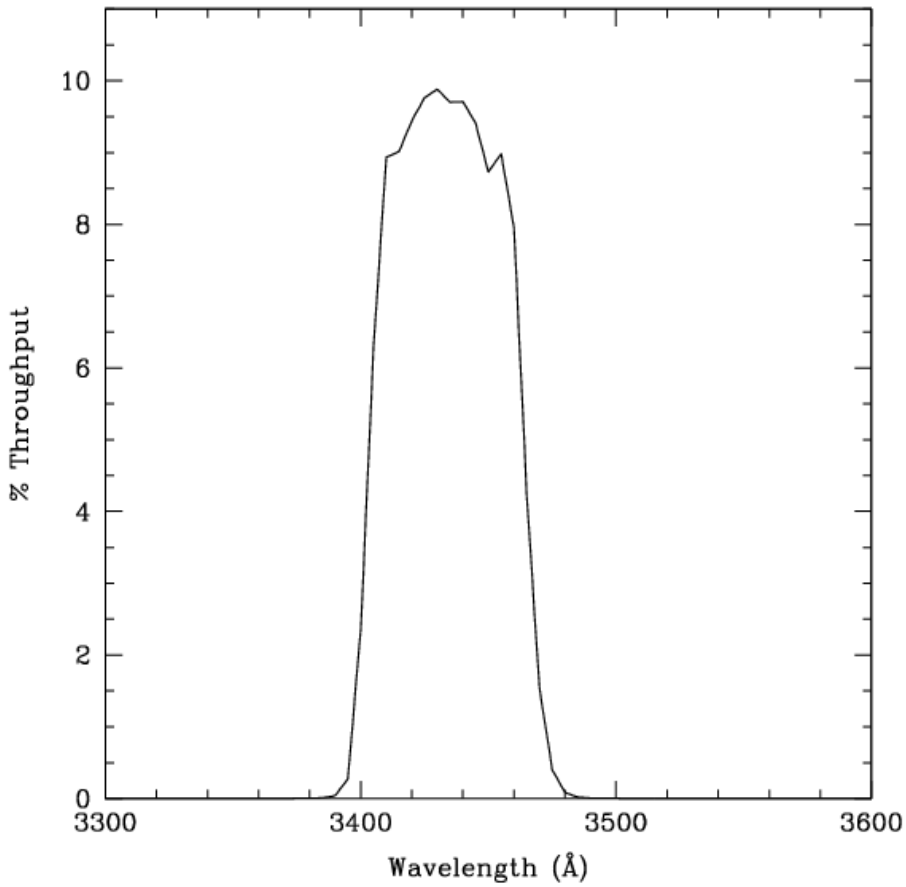

Figure 10.53: Point source S/N vs. V+ABν for the HRC/F344N filter. Top curves are for low sky; bottom curves are for average sky.

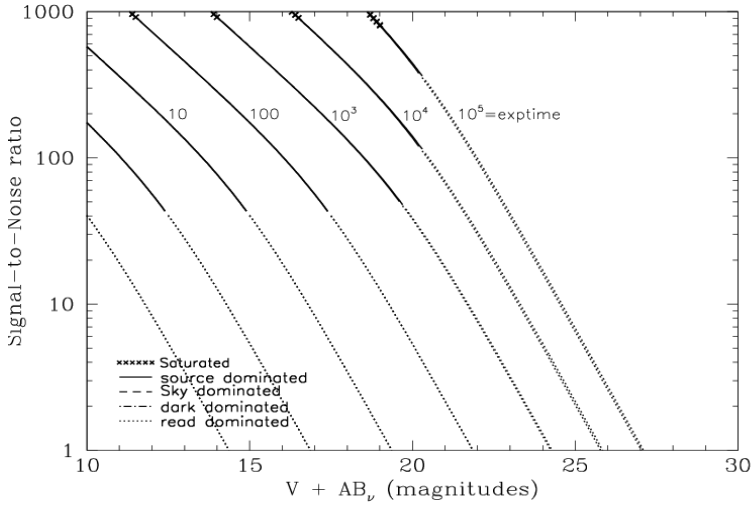

Figure 10.54: Extended source S/N vs. V+ABν for the HRC/F344N filter. Top curves are for low sky and bottom curves are for average sky for a 1 arcsec^2 area.

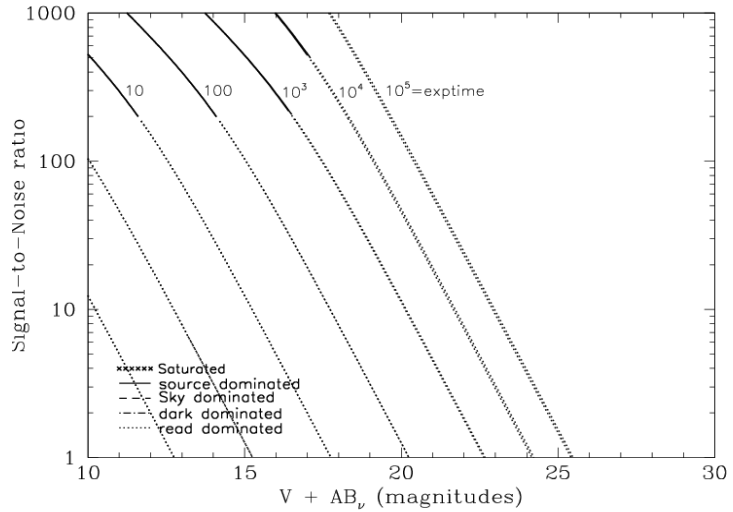

HRC/F435W

Description

Johnson B filter.

Figure 10.55: Integrated system throughput for HRC/F435W.

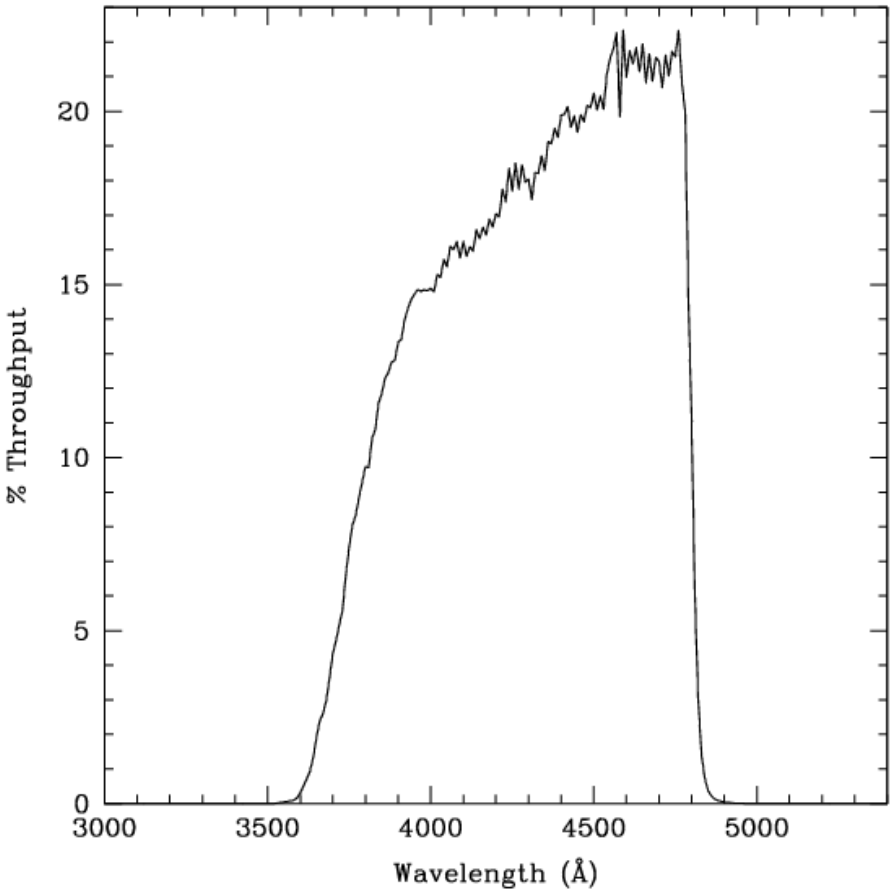

Figure 10.56: Point source S/N vs. V+ABν for the HRC/F435W filter. Top curves are for low sky; bottom curves are for average sky.

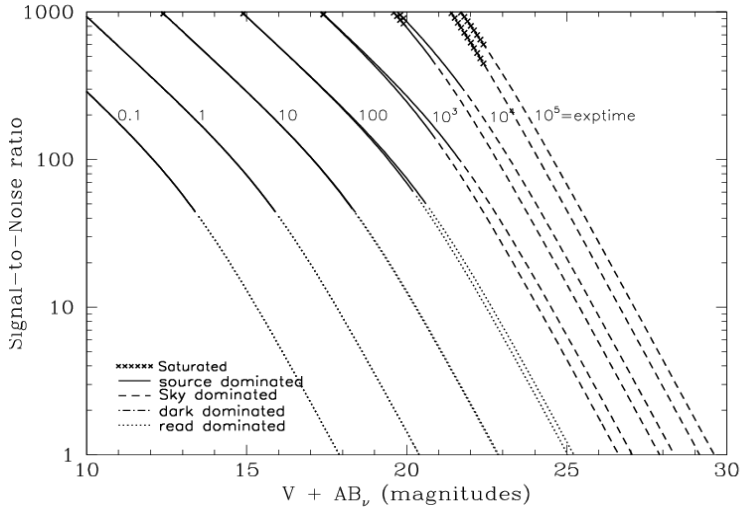

Figure 10.57: Extended source S/N vs. V+ABν for the HRC/F435W filter. Top curves are for low sky and bottom curves are for average sky for a 1 arcsec^2 area.

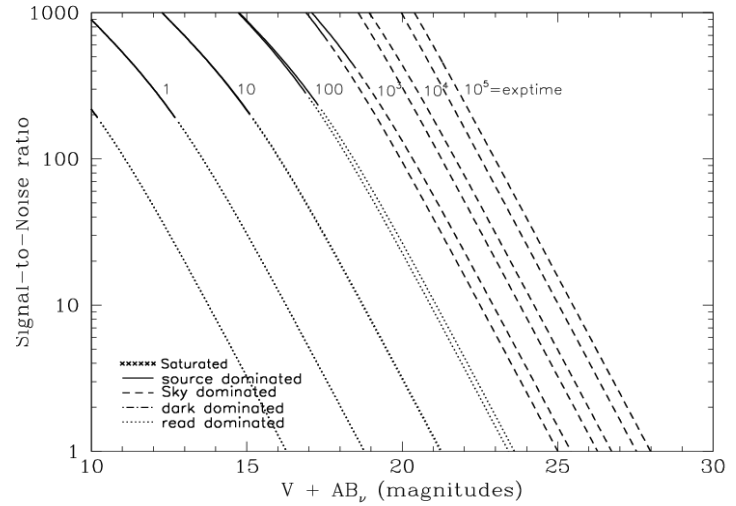

HRC/F475W

Description

Sloan Digital Sky Survey g filter.

Figure 10.58: Integrated system throughput for HRC/F475W.

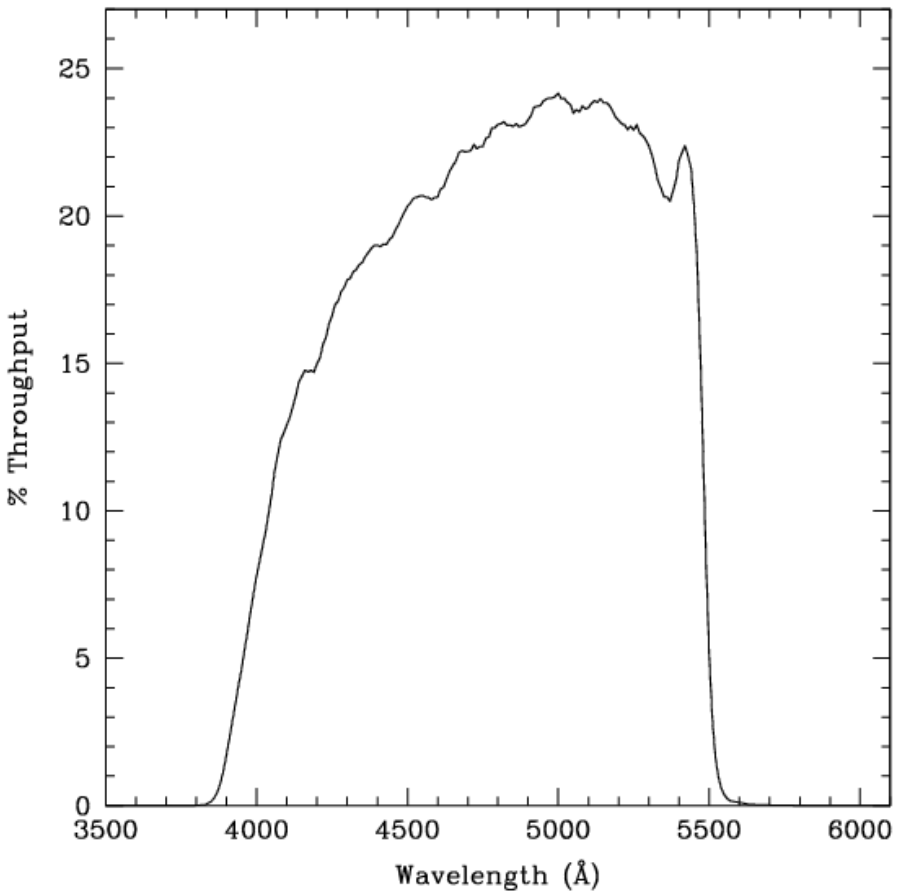

Figure 10.59: Point source S/N vs. V+ABν for the HRC/F475W filter. Top curves are for low sky; bottom curves are for average sky.

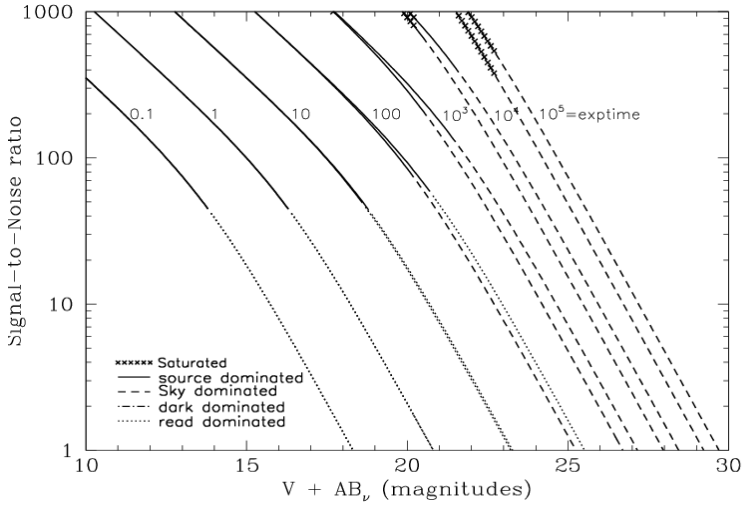

Figure 10.60: Extended source S/N vs. V+ABν for the HRC/F475W filter. Top curves are for low sky and bottom curves are for average sky for a 1 arcsec^2 area.

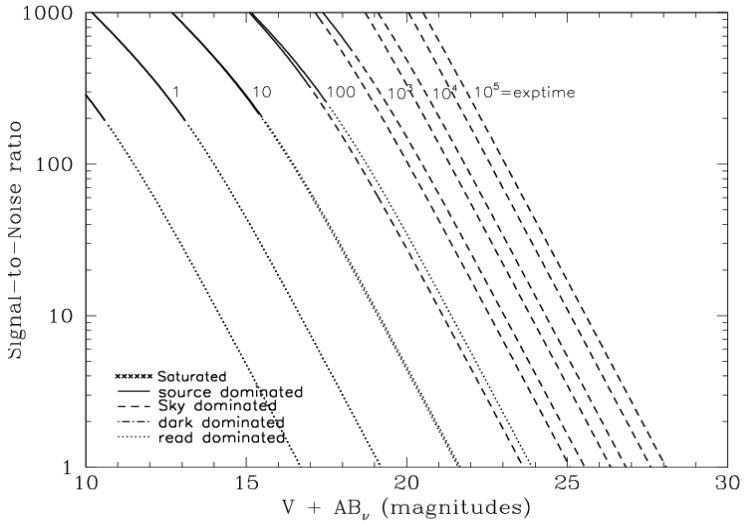

HRC/F502N

Description

OIII filter.

Figure 10.61: Integrated system throughput for HRC/F502N.

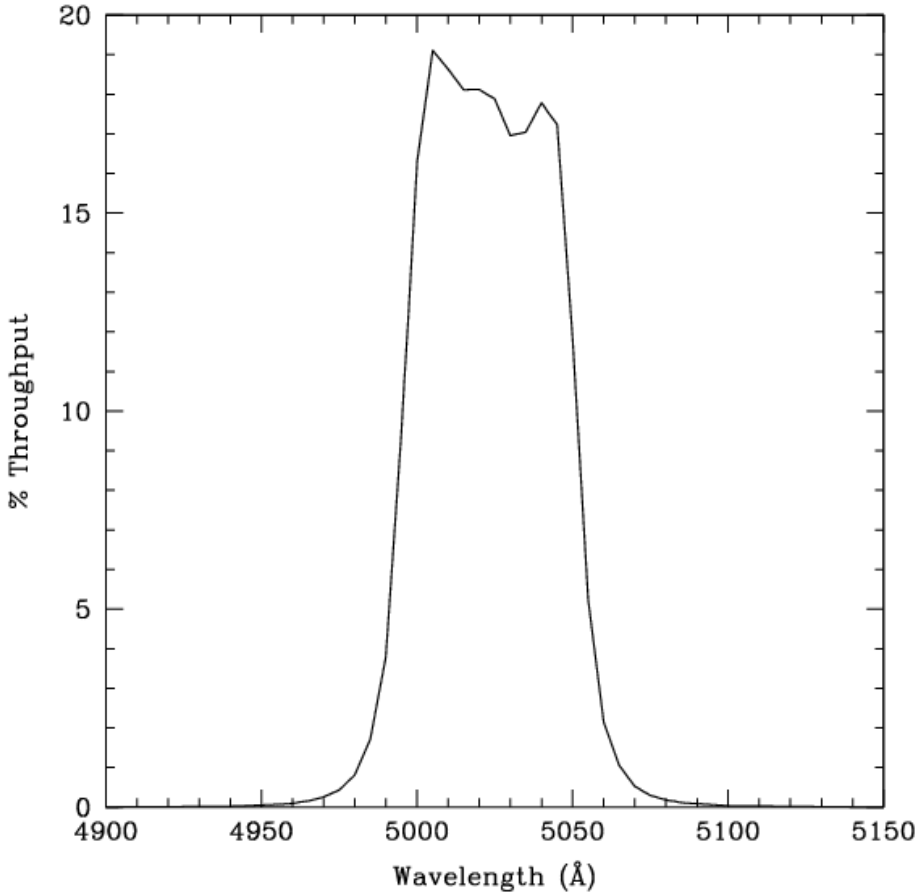

Figure 10.62: Point source S/N vs. V+ABν for the HRC/F502N filter. Top curves are for low sky; bottom curves are for average sky.

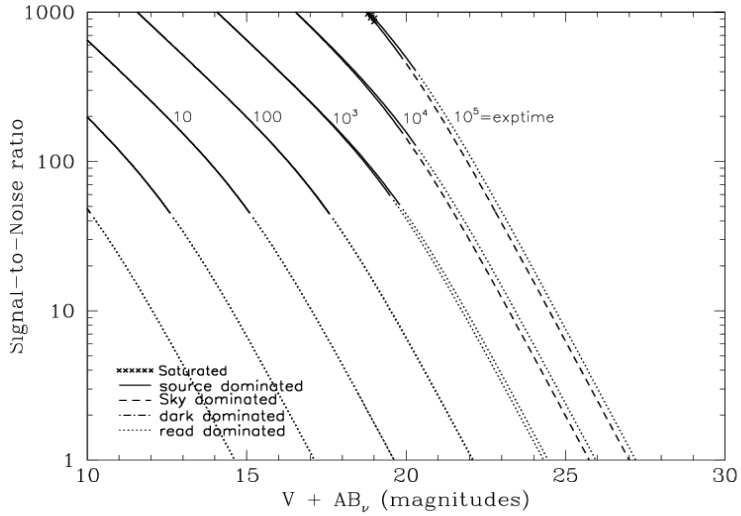

Figure 10.63: Extended source S/N vs. V+ABν for the HRC/F502N filter. Top curves are for low sky and bottom curves are for average sky for a 1 arcsec^2 area.

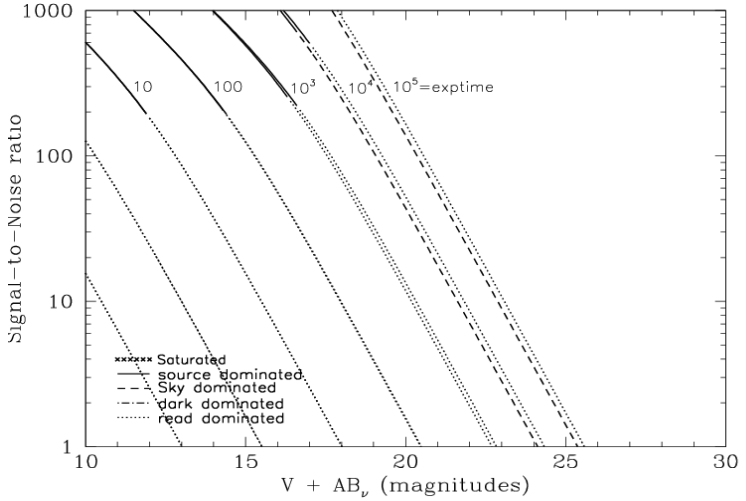

HRC/F550M

Description

Narrow V filter.

Figure 10.64: Integrated system throughput for HRC/F550M.

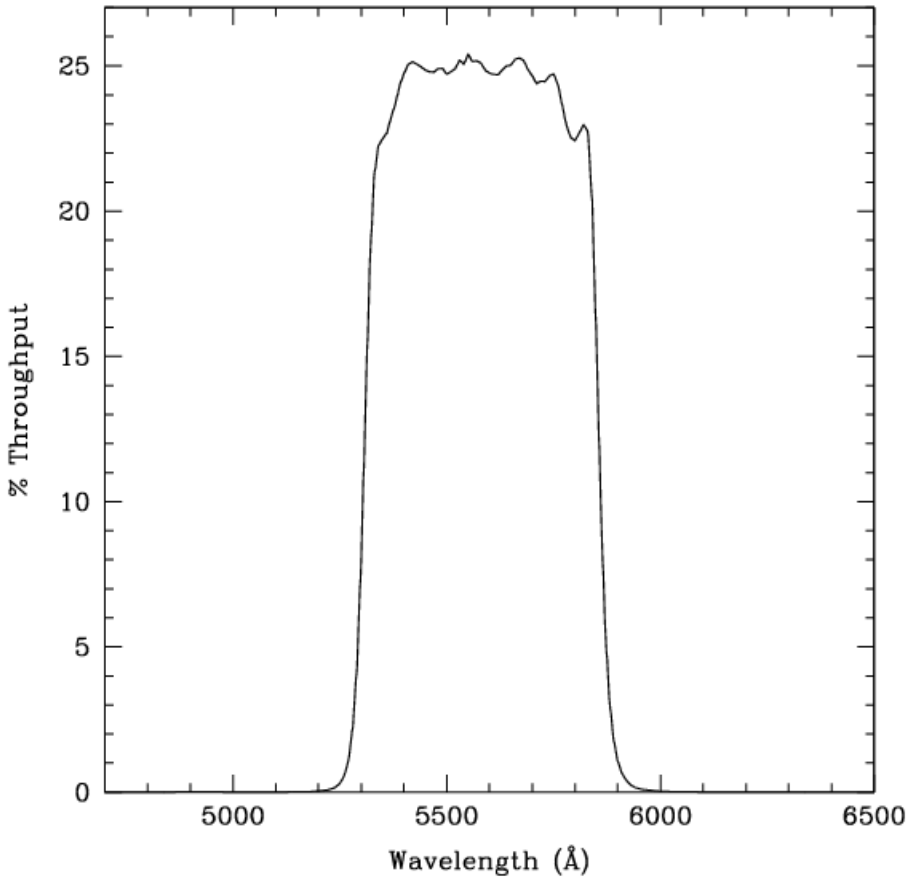

Figure 10.65: Point source S/N vs. V+ABν for the HRC/F550M filter. Top curves are for low sky; bottom curves are for average sky.

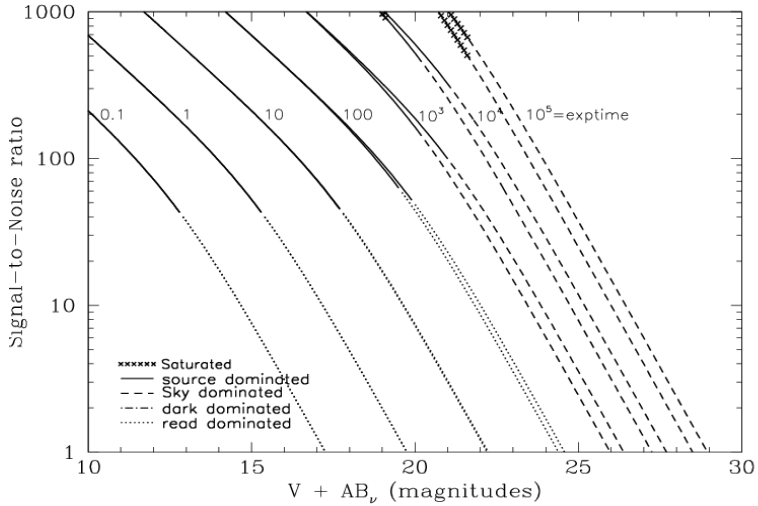

Figure 10.66: Extended source S/N vs. V+ABν for the HRC/F550M filter. Top curves are for low sky and bottom curves are for average sky for a 1 arcsec^2 area.

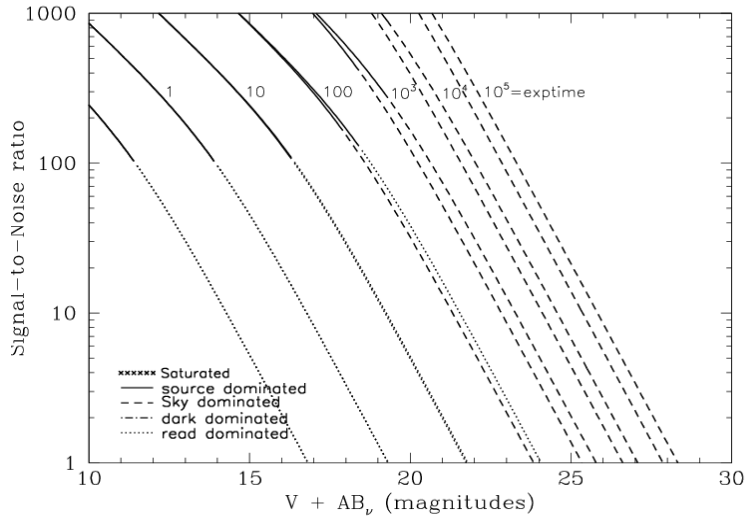

HRC/F555W

Description

Johnson V filter.

Figure 10.67: Integrated system throughput for HRC/F555W.

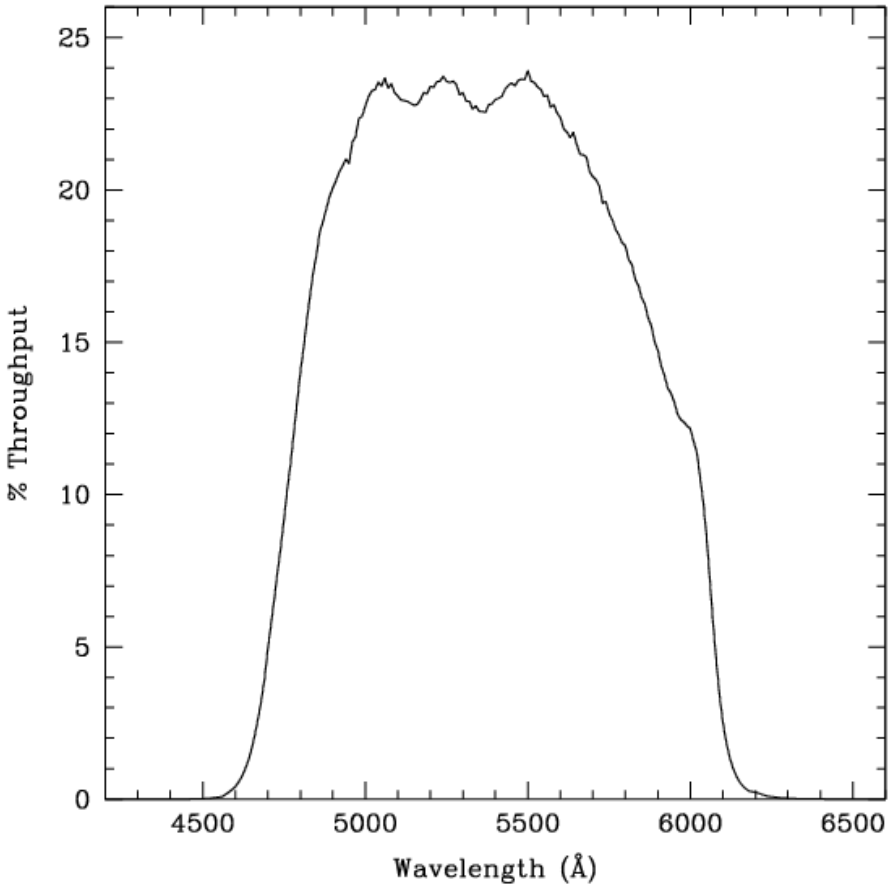

Figure 10.68: Point source S/N vs. V+ABν for the HRC/F555W filter. Top curves are for low sky; bottom curves are for average sky.

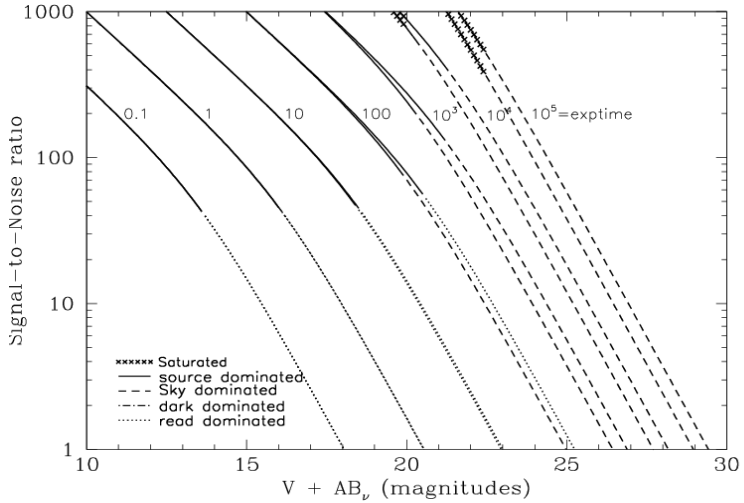

Figure 10.69: Extended source S/N vs. V+ABν for the HRC/F555W filter. Top curves are for low sky and bottom curves are for average sky for a 1 arcsec^2 area.

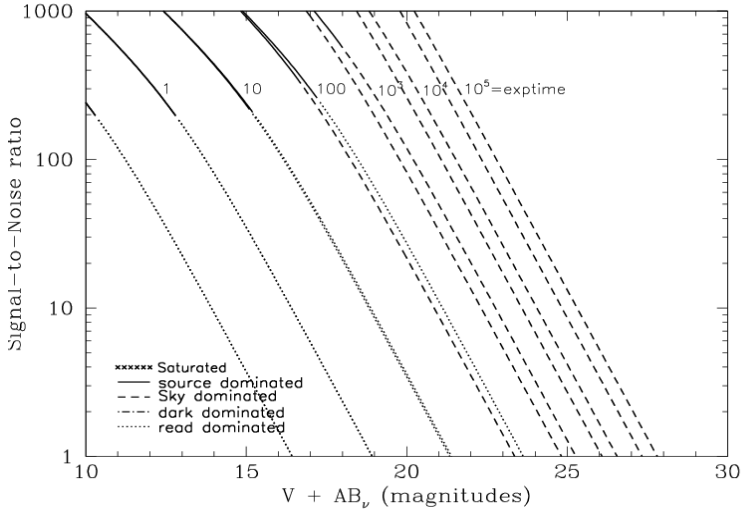

HRC/F606W

Description

Broad V filter.

Figure 10.70: Integrated system throughput for HRC/F606W.

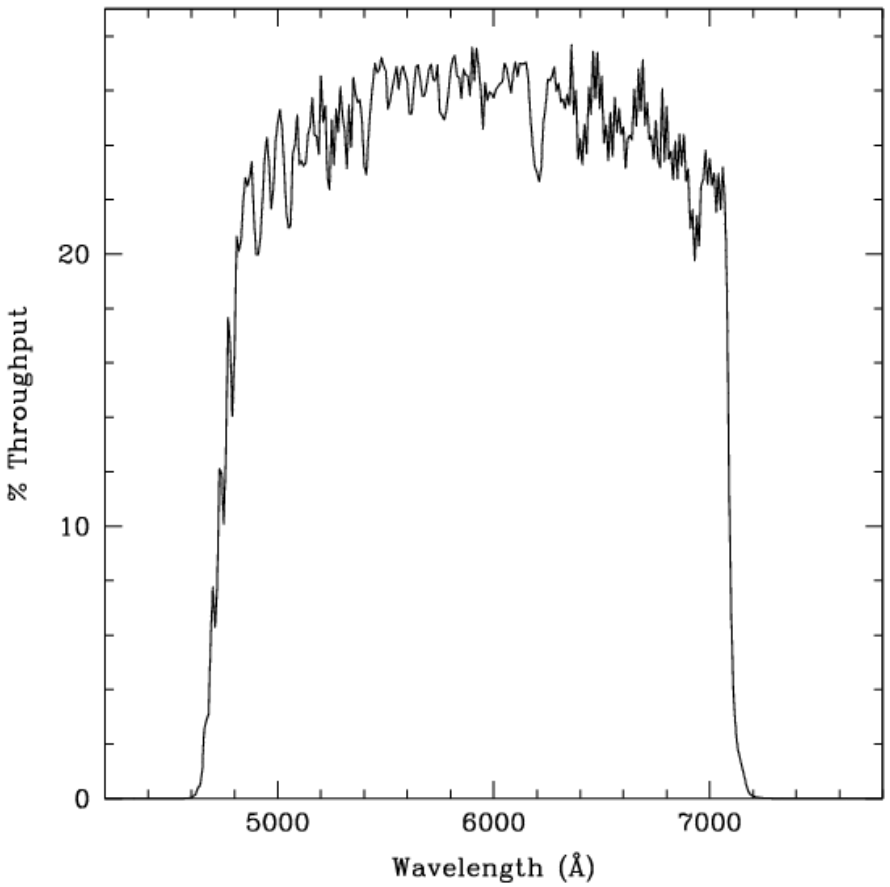

Figure 10.71: Point source S/N vs. V+ABν for the HRC/F606W filter. Top curves are for low sky; bottom curves are for average sky.

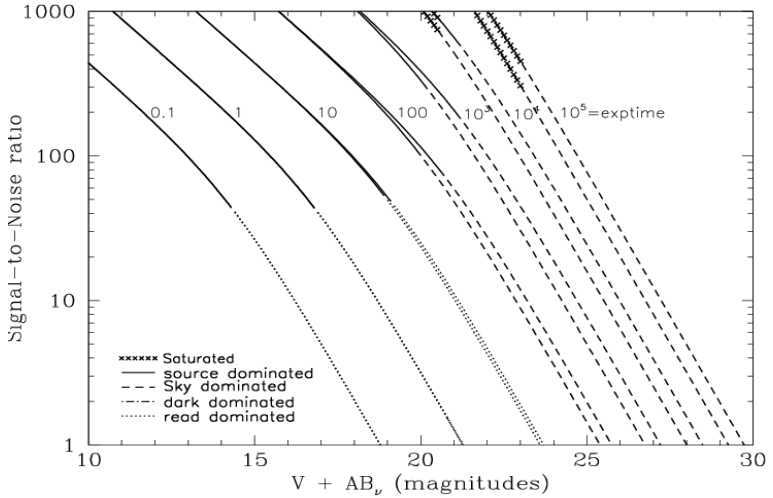

Figure 10.72: Extended source S/N vs. V+ABν for the HRC/F606W filter. Top curves are for low sky and bottom curves are for average sky for a 1 arcsec^2 area.

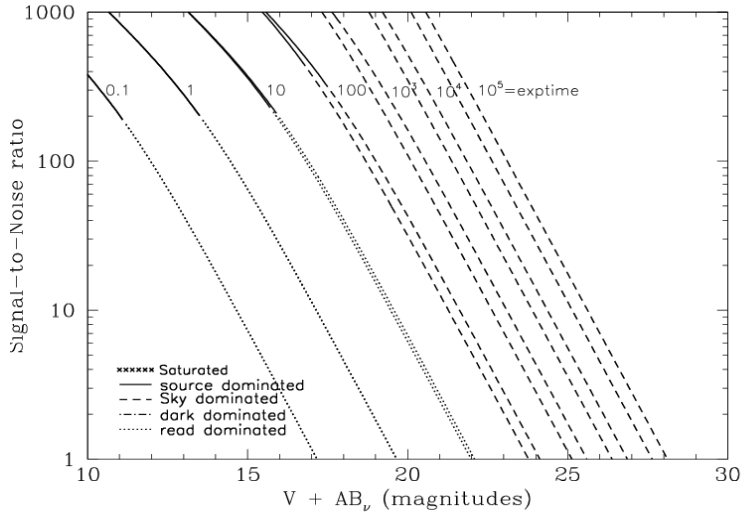

HRC/F625W

Description

Sloan Digital Sky Survey r filter.

Figure 10.73: Integrated system throughput for HRC/F625W.

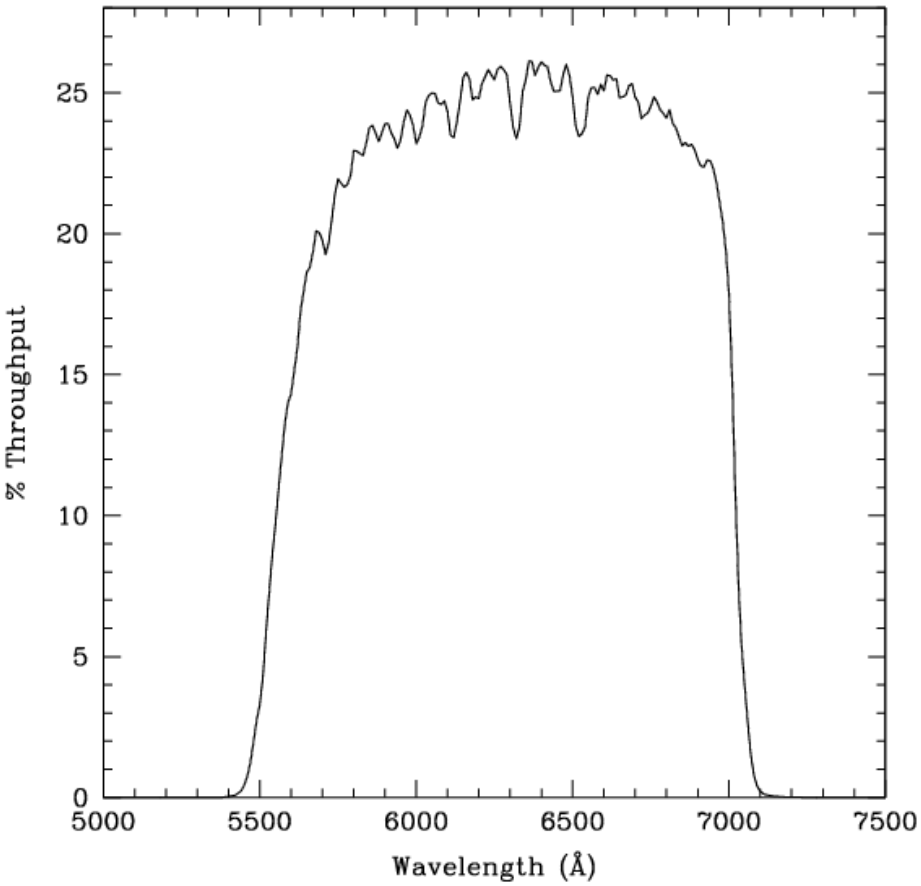

Figure 10.74: Point source S/N vs. V+ABν for the HRC/F625W filter. Top curves are for low sky; bottom curves are for average sky.

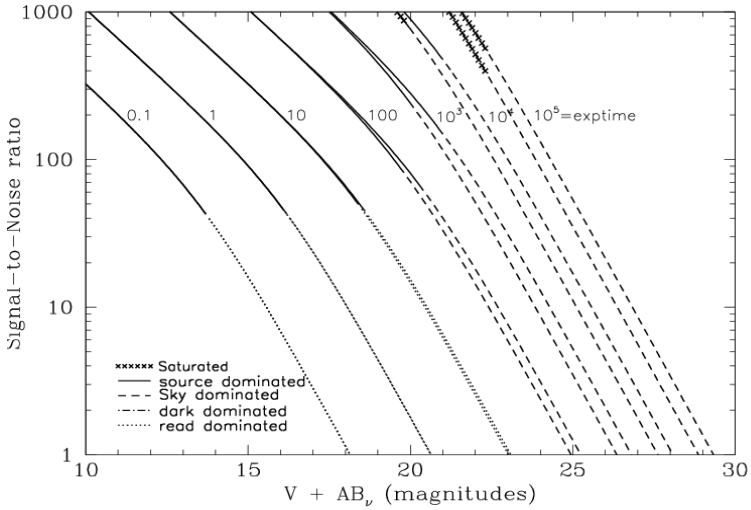

Figure 10.75: Extended source S/N vs. V+ABν for the HRC/F625W filter. Top curves are for low sky and bottom curves are for average sky for a 1 arcsec^2 area.

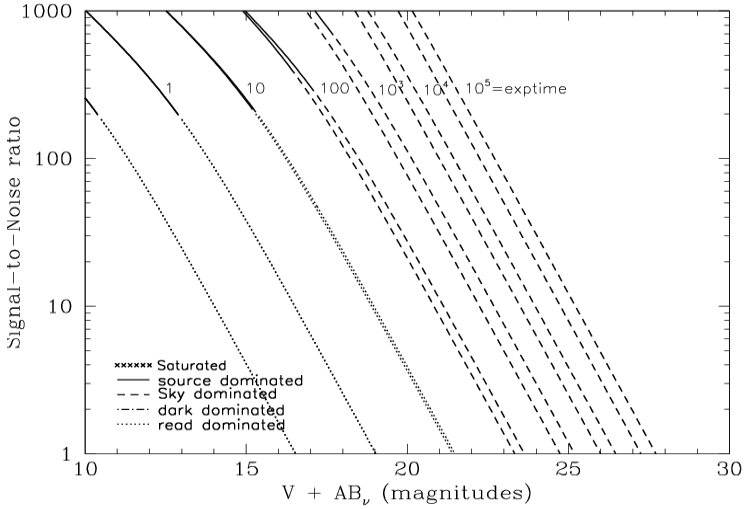

HRC/F658N

Description

Hα filter.

Figure 10.76: Integrated system throughput for HRC/F658N.

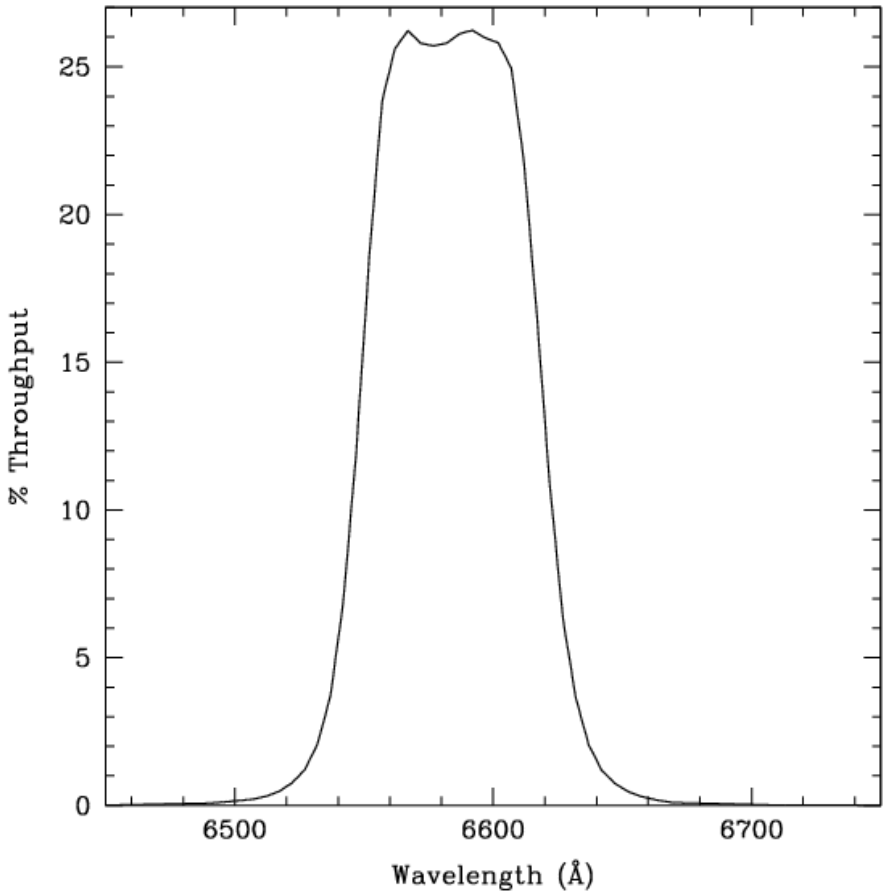

Figure 10.77: Point source S/N vs. V+ABν for the HRC/F658N filter. Top curves are for low sky; bottom curves are for average sky.

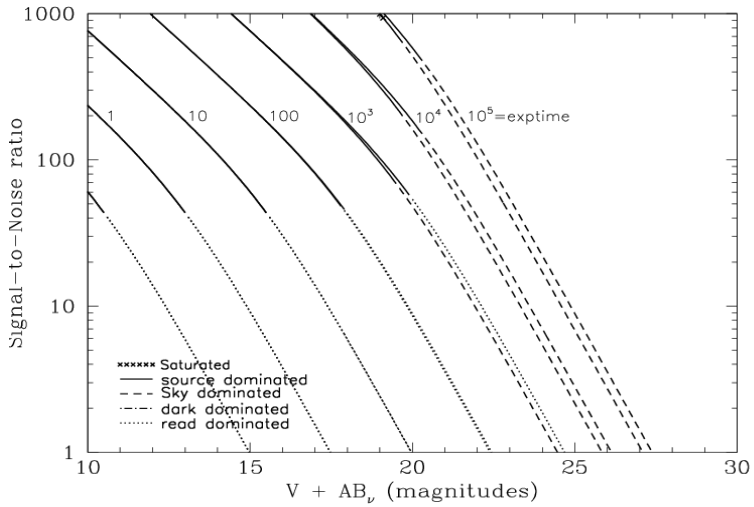

Figure 10.78: Extended source S/N vs. V+ABν for the HRC/F658N filter. Top curves are for low sky and bottom curves are for average sky for a 1 arcsec^2 area.

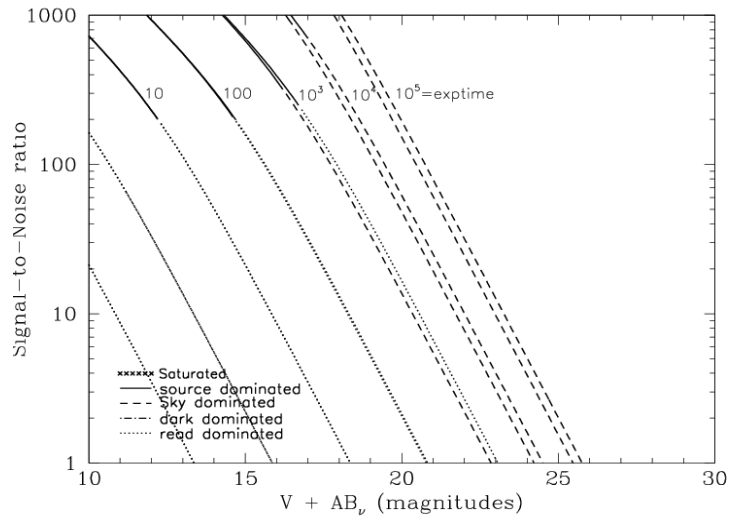

HRC/F660N

Description

NII filter.

Figure 10.79: Integrated system throughput for HRC/F660N.

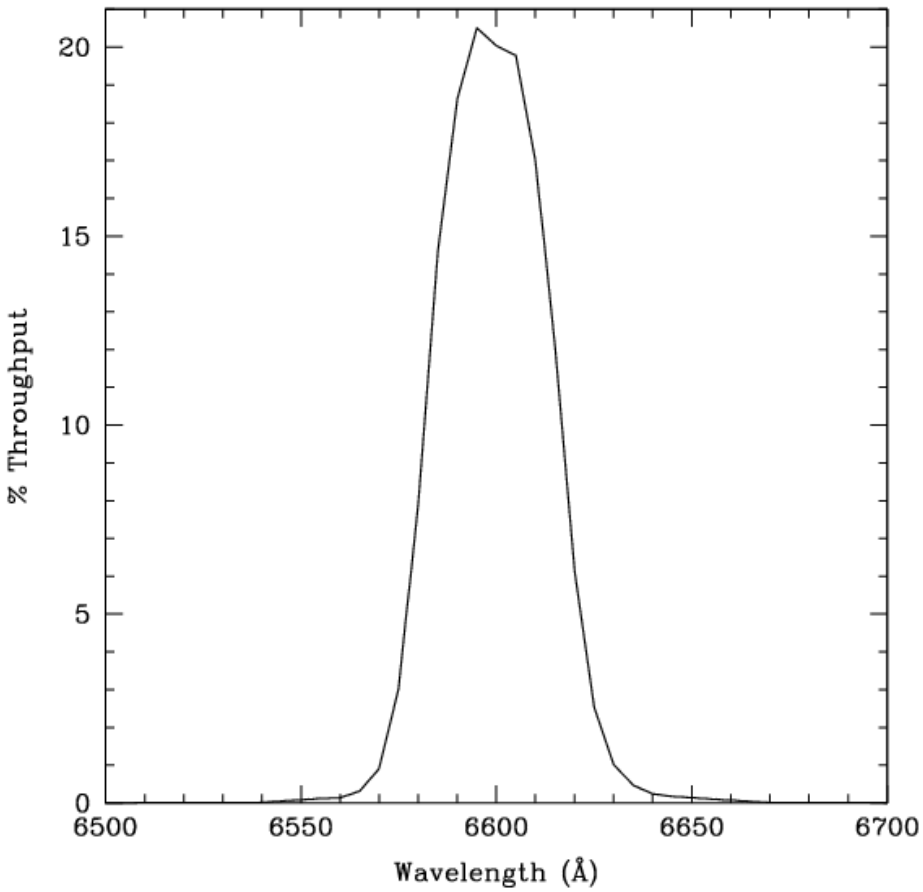

Figure 10.80: Point source S/N vs. V+ABν for the HRC/F660N filter. Top curves are for low sky; bottom curves are for average sky.

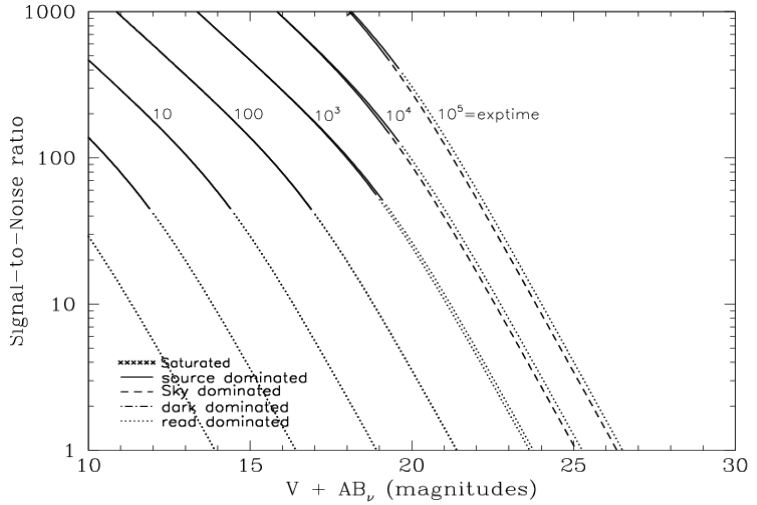

Figure 10.81: Extended source S/N vs. V+ABν for the HRC/F660N filter. Top curves are for low sky and bottom curves are for average sky for a 1 arcsec^2 area.

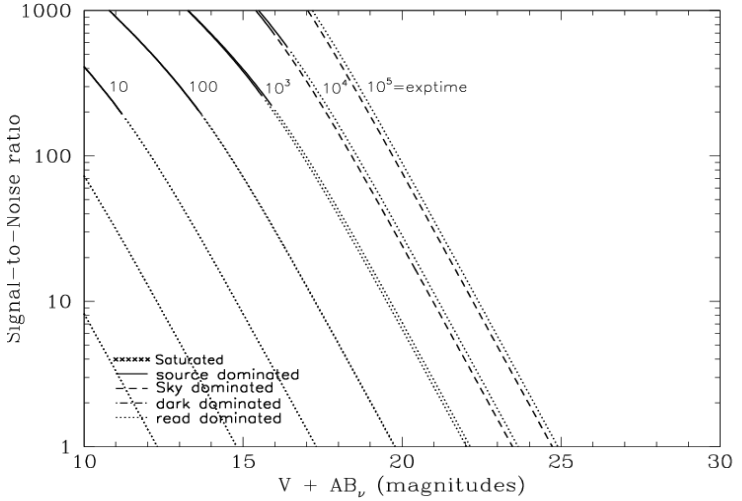

HRC/F775W

Description

Sloan Digital Sky Survey i filter.

Figure 10.82: Integrated system throughput for HRC/F775W.

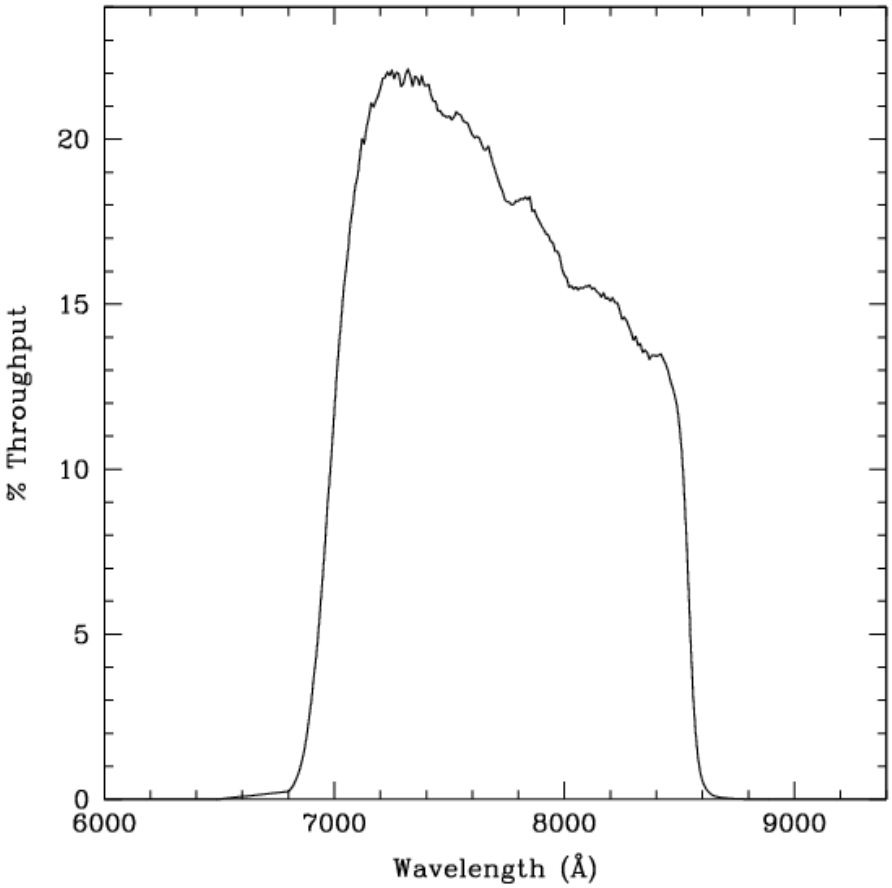

Figure 10.83: Point source S/N vs. V+ABν for the HRC/F775W filter. Top curves are for low sky; bottom curves are for average sky.

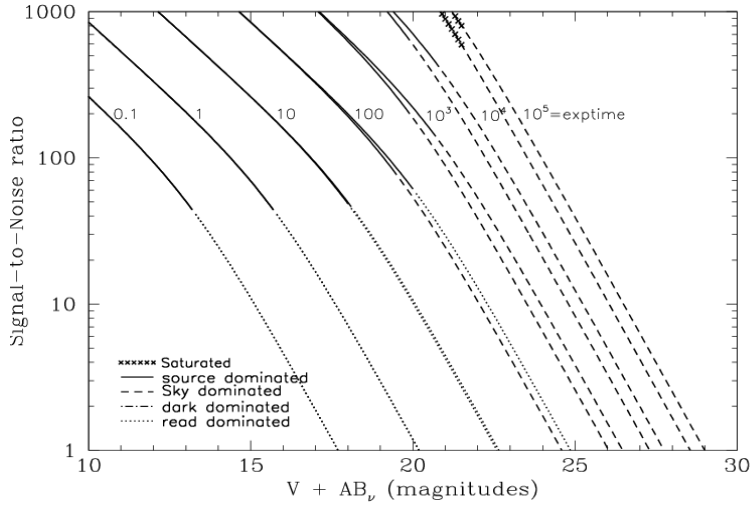

Figure 10.84: Extended source S/N vs. V+ABν for the HRC/F775W filter. Top curves are for low sky and bottom curves are for average sky for a 1 arcsec^2 area.

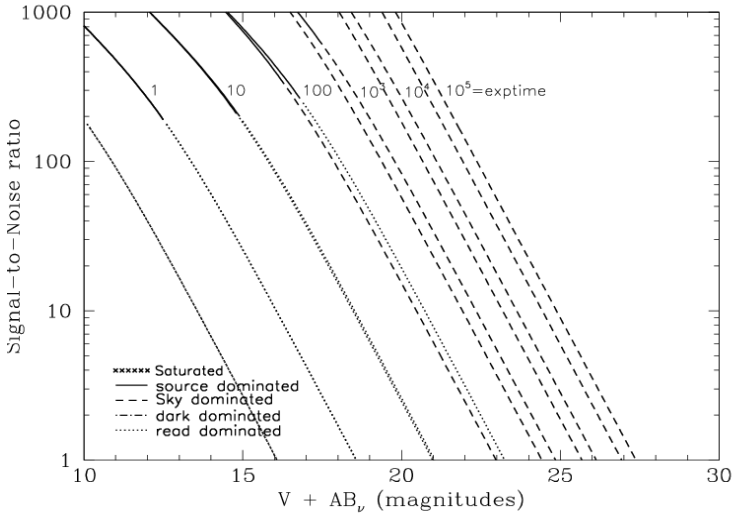

HRC/F814W

Description

Broad I filter.

Figure 10.85: Integrated system throughput for HRC/F814W.

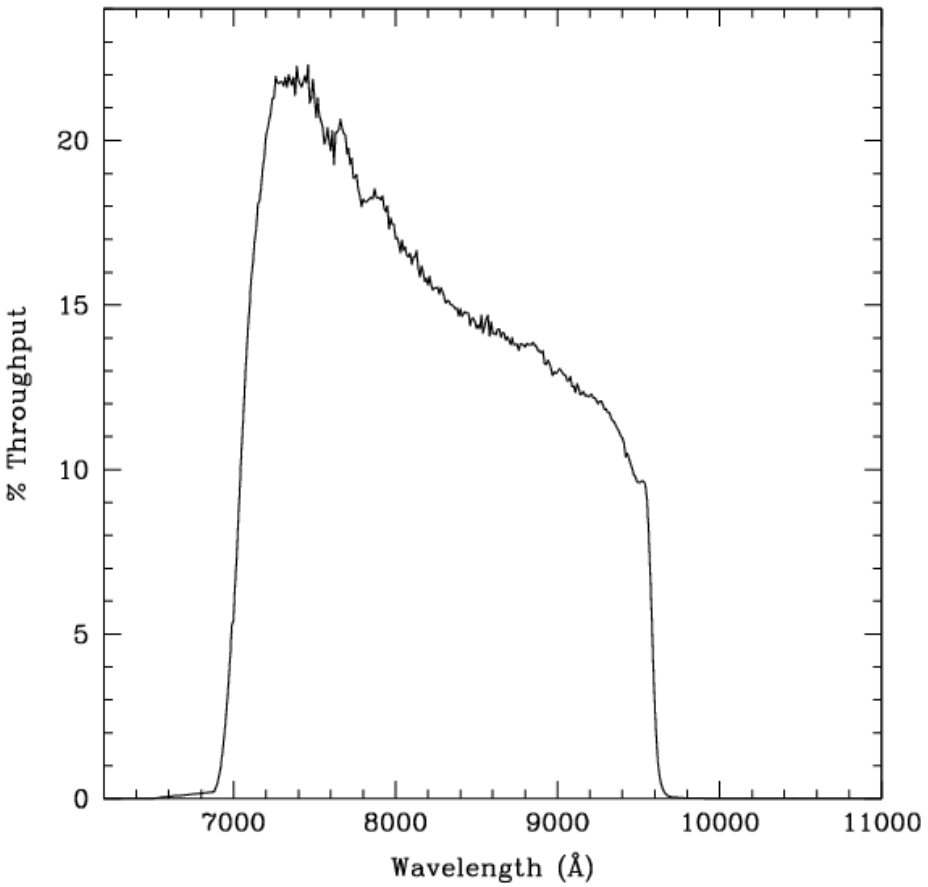

Figure 10.86: Point source S/N vs. V+ABν for the HRC/F814W filter. Top curves are for low sky; bottom curves are for average sky.

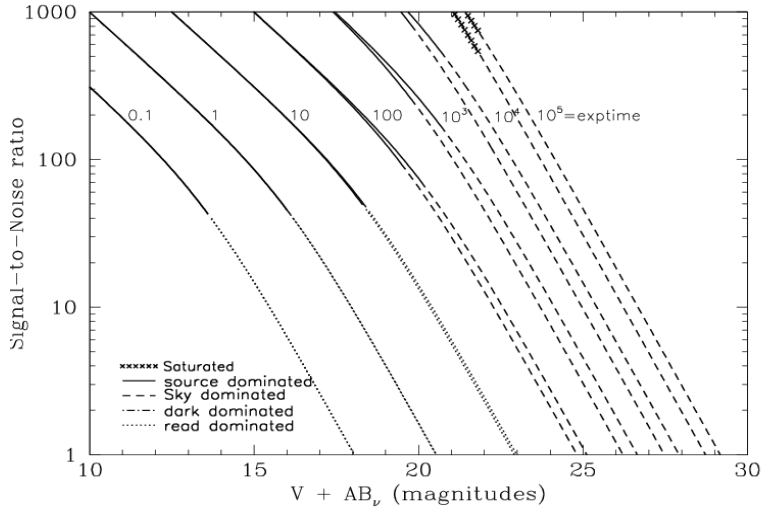

Figure 10.87: Extended source S/N vs. V+ABν for the HRC/F814W filter. Top curves are for low sky and bottom curves are for average sky for a 1 arcsec^2 area.

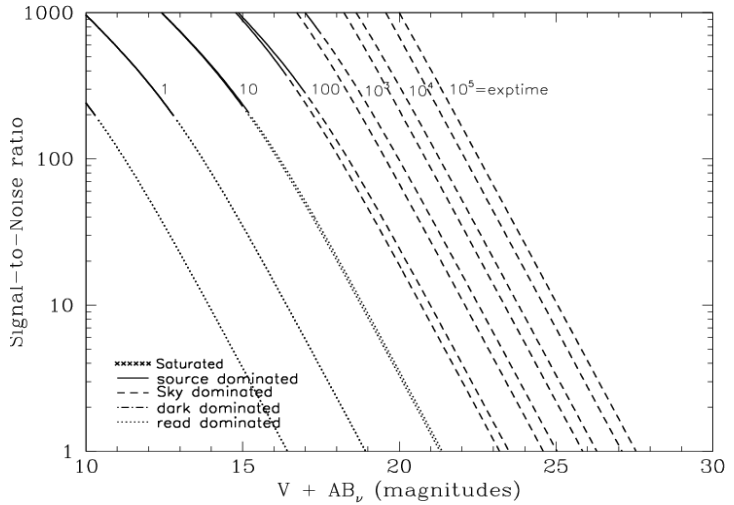

HRC/F850LP

Description

Sloan Digital Sky Survey z filter.

Figure 10.88: Integrated system throughput for HRC/F850LP.

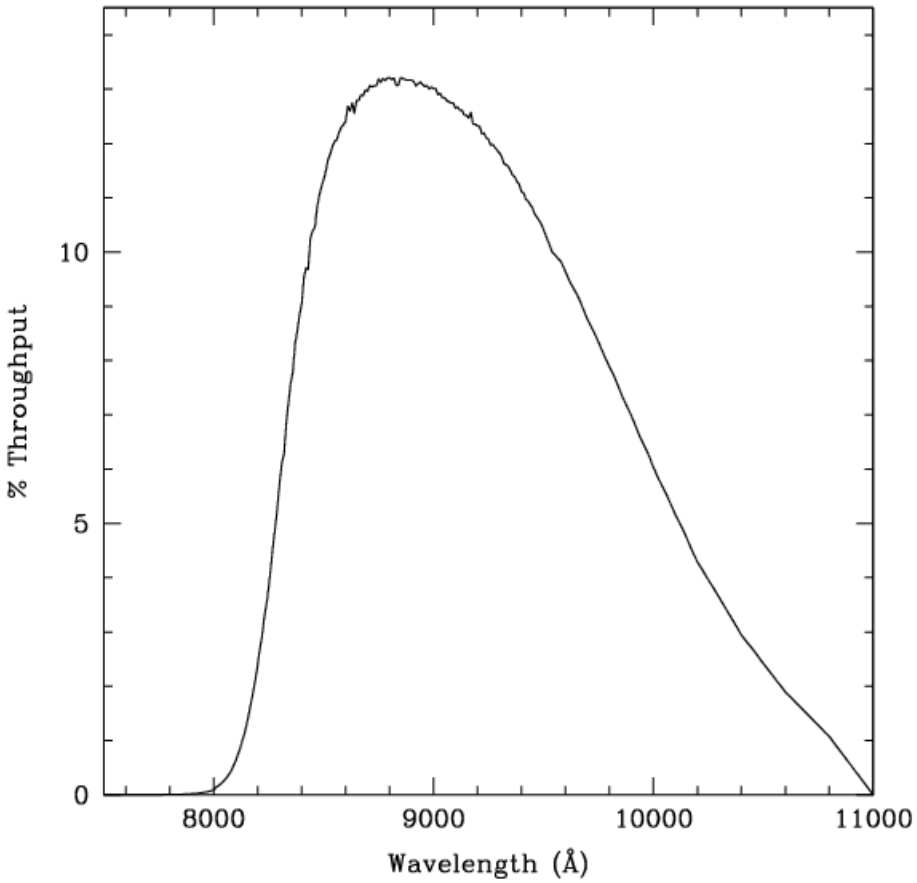

Figure 10.89: Point source S/N vs. V+ABν for the HRC/F850LP filter. Top curves are for low sky; bottom curves are for average sky.

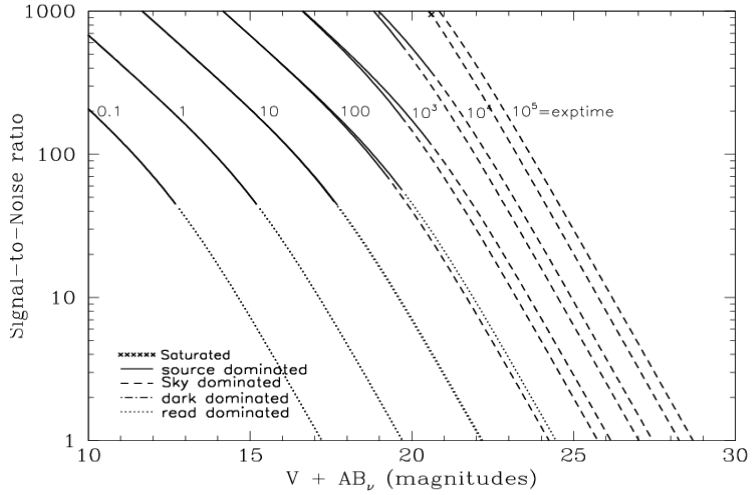

Figure 10.90: Extended source S/N vs. V+ABν for the HRC/F850LP filter. Top curves are for low sky and bottom curves are for average sky for a 1 arcsec^2 area.

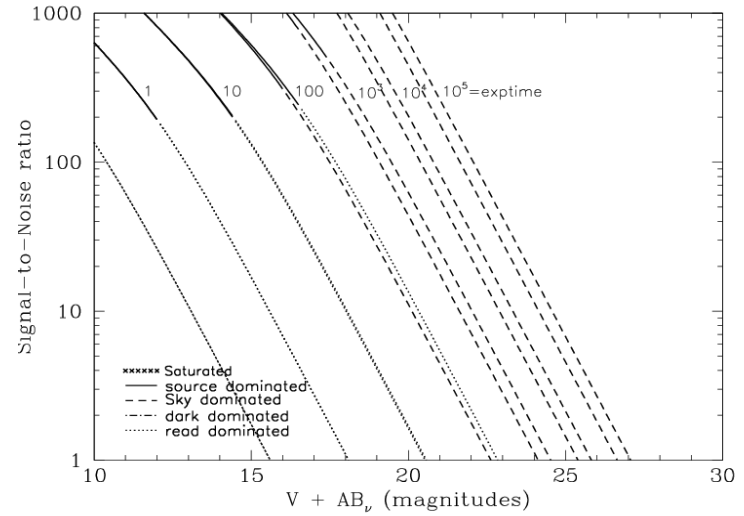

HRC/F892N

Description

Methane filter.

Figure 10.91: Integrated system throughput for HRC/F892N.

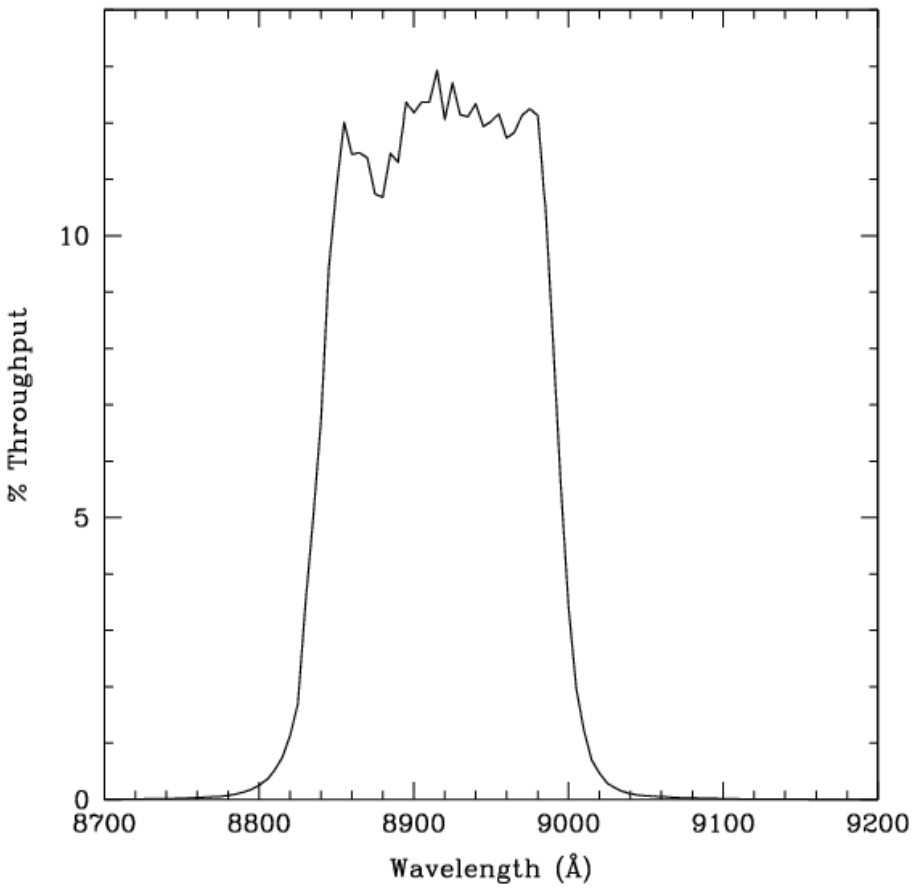

Figure 10.92: Point source S/N vs. V+ABν for the HRC/F892N filter. Top curves are for low sky; bottom curves are for average sky.

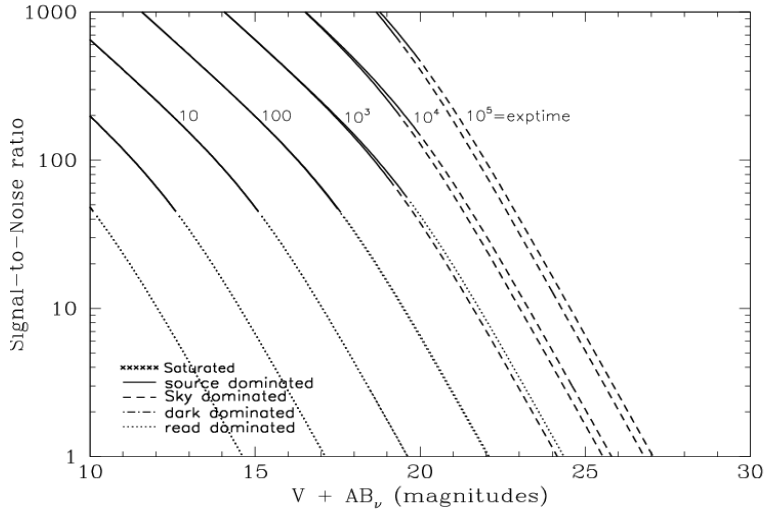

Figure 10.93: Extended source S/N vs. V+ABν for the HRC/F892N filter. Top curves are for low sky and bottom curves are for average sky for a 1 arcsec^2 area.

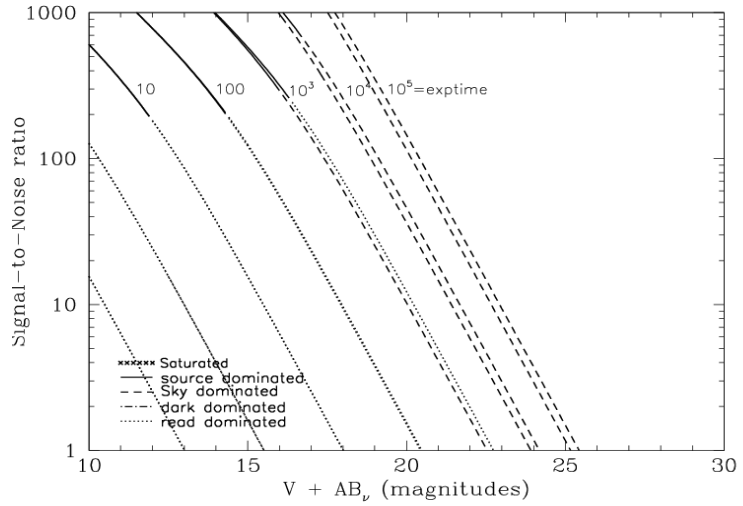

HRC/G800L

Description

Grism.

Figure 10.94: Integrated system throughput for HRC/G800L.

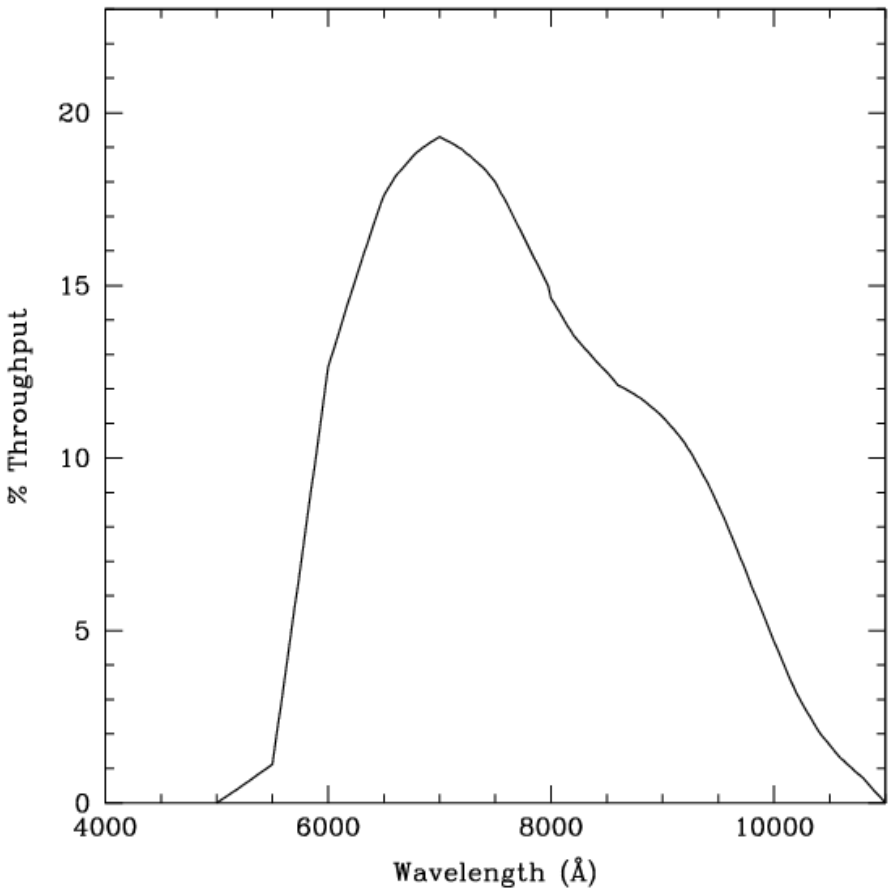

Figure 10.95: Point source S/N vs. V+ABν for the HRC/G800L filter. Top curves are for low sky; bottom curves are for average sky.

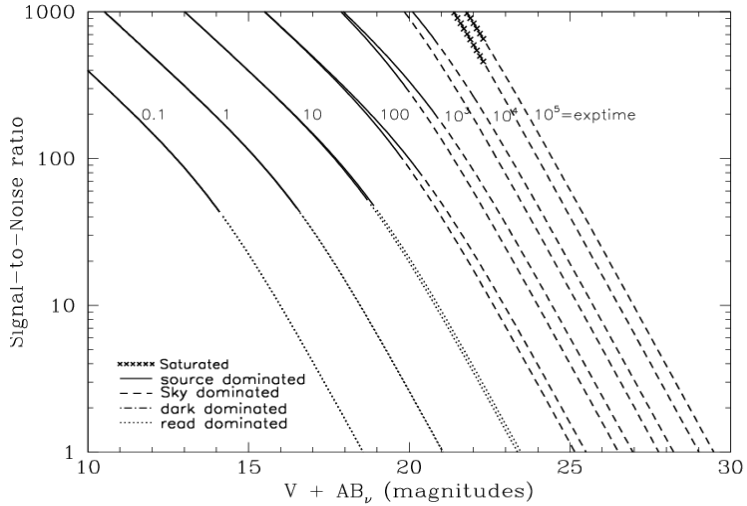

Figure 10.96: Extended source S/N vs. V+ABν for the HRC/G800L filter. Top curves are for low sky and bottom curves are for average sky for a 1 arcsec^2 area.

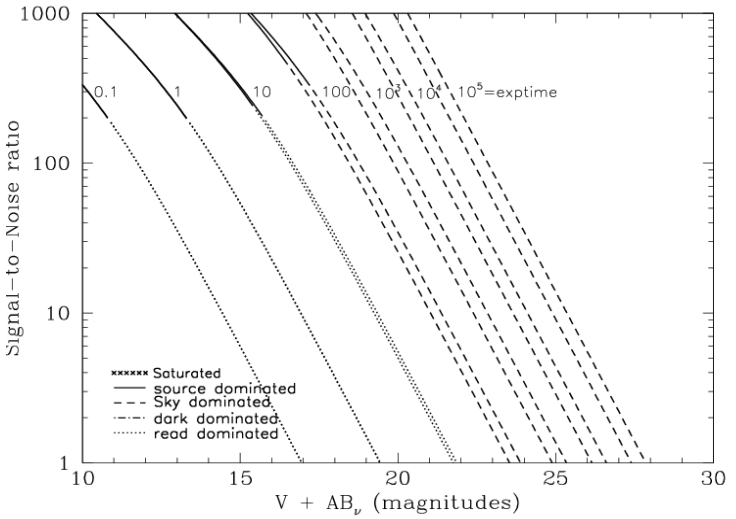

HRC/PR200L

Description

HRC Prism.

Figure 10.97: Integrated system throughput for HRC/PR200L.

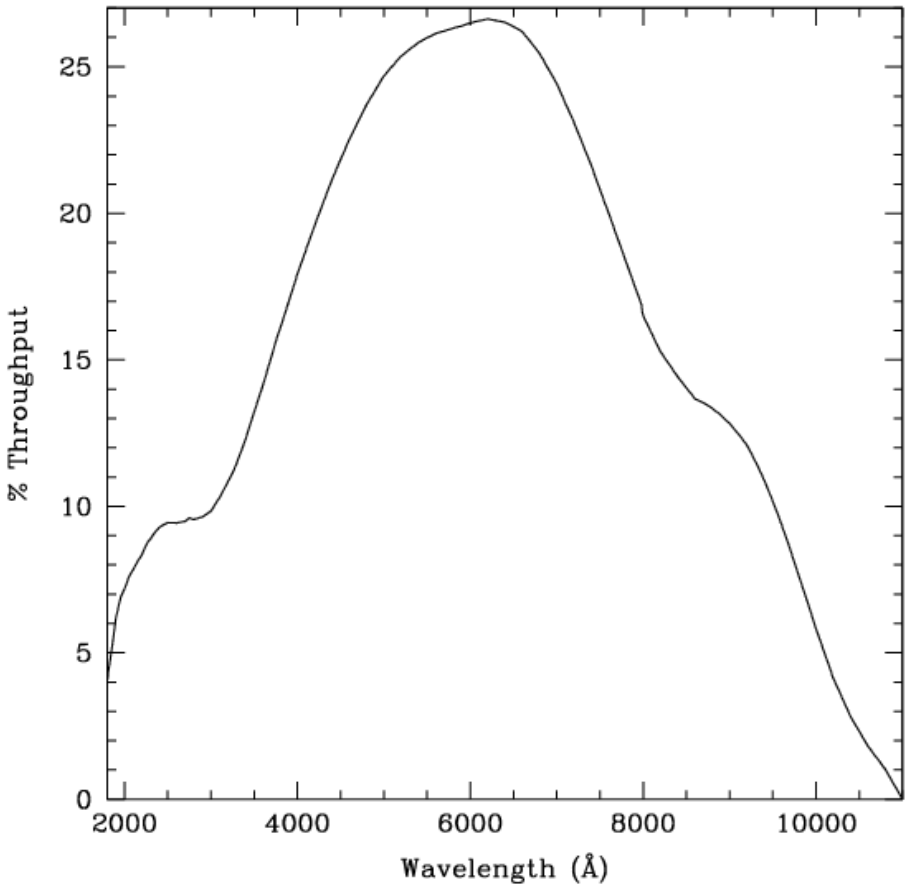

Figure 10.98: Point source S/N vs. V+ABν for the HRC/PR200L filter. Top curves are for low sky; bottom curves are for average sky.

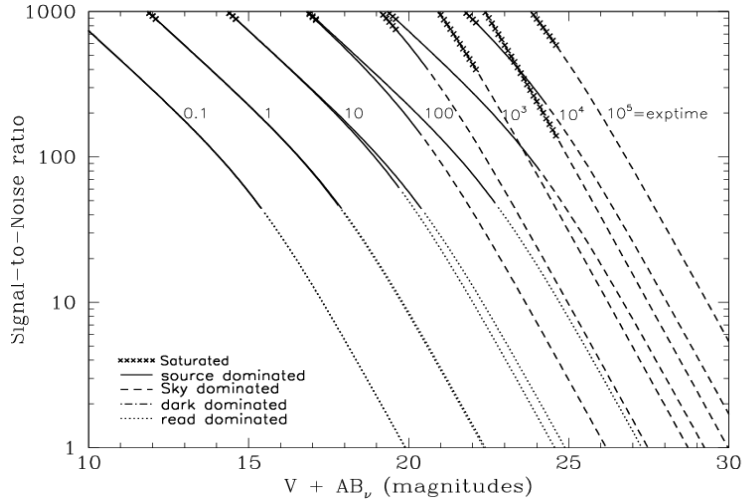

Figure 10.99: Extended source S/N vs. V+ABν for the HRC/PR200L filter. Top curves are for low sky and bottom curves are for average sky for a 1 arcsec^2 area.

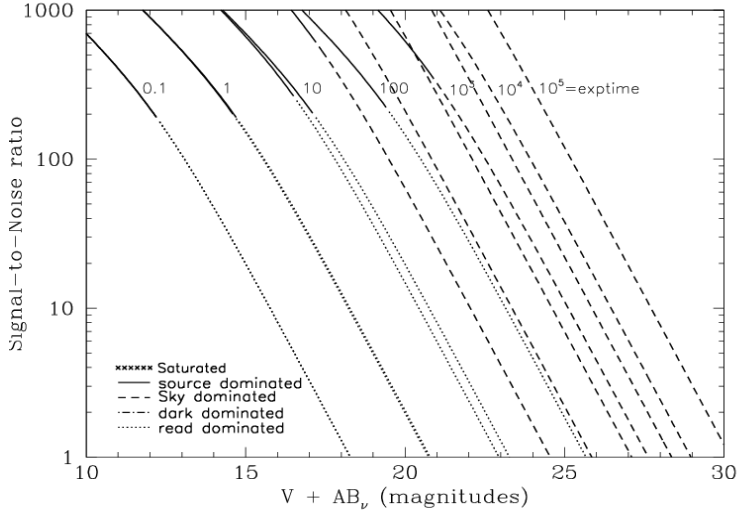

HRC/CLEAR

Description

HRC Clear Filter.

Figure 10.100: Integrated system throughput for HRC/Clear

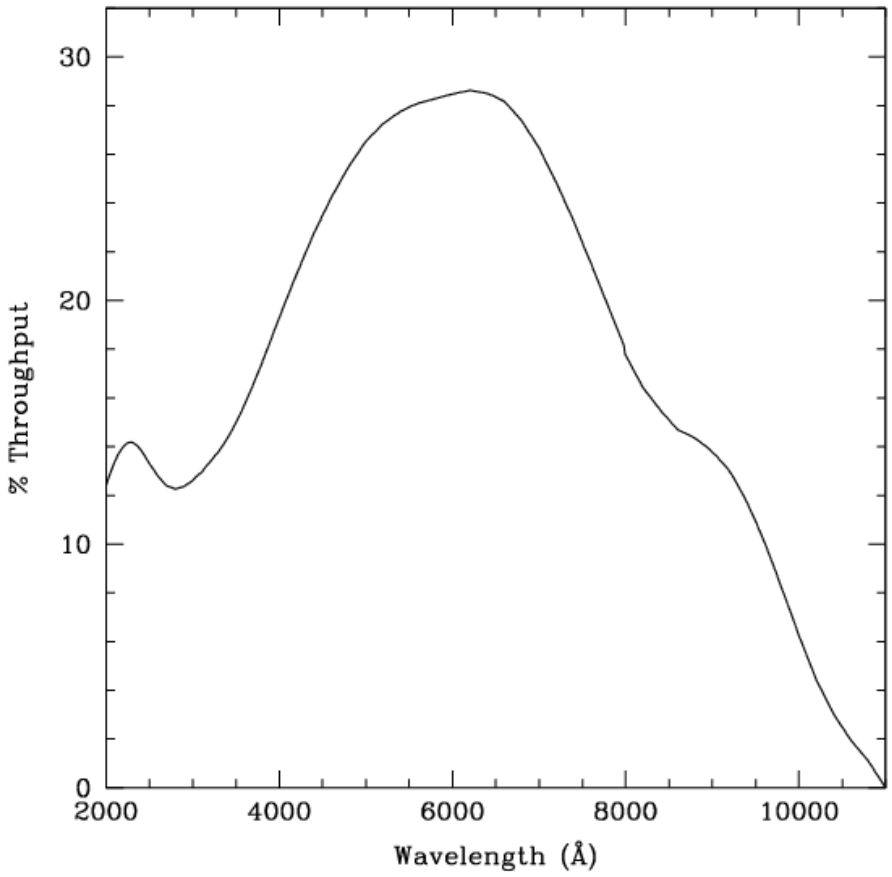

Figure 10.101: Point source S/N vs. V+ABν for the HRC/Clear filter. Top curves are for low sky; bottom curves are for average sky.

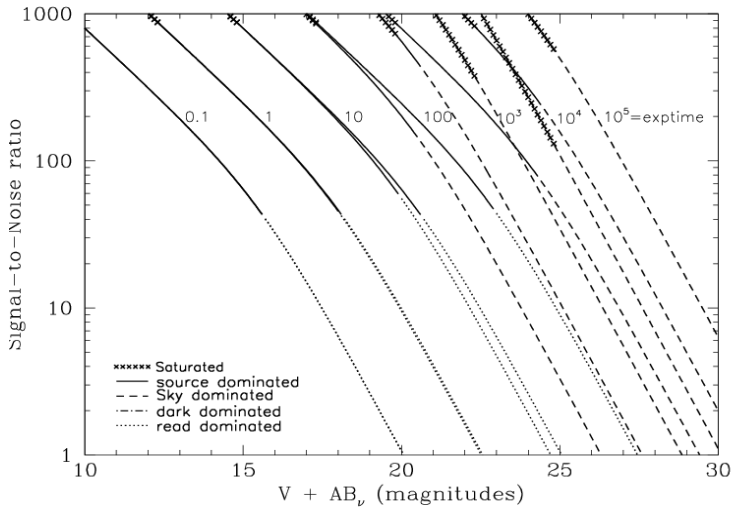

Figure 10.102: Extended source S/N vs. V+ABν for the HRC/Clear filter. Top curves are for low sky and bottom curves are for average sky for a 1 arcsec^2 area.

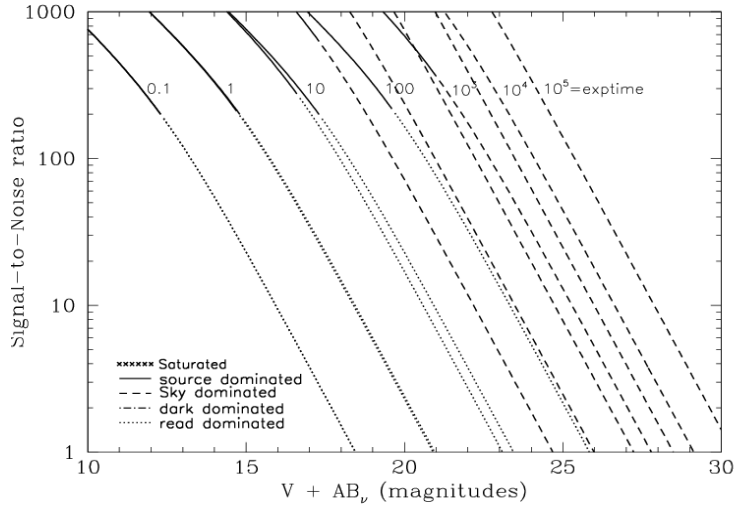

SBC/F115LP

Description

MgF_2 filter.

Figure 10.103: Integrated system throughput for SBC/F115LP.

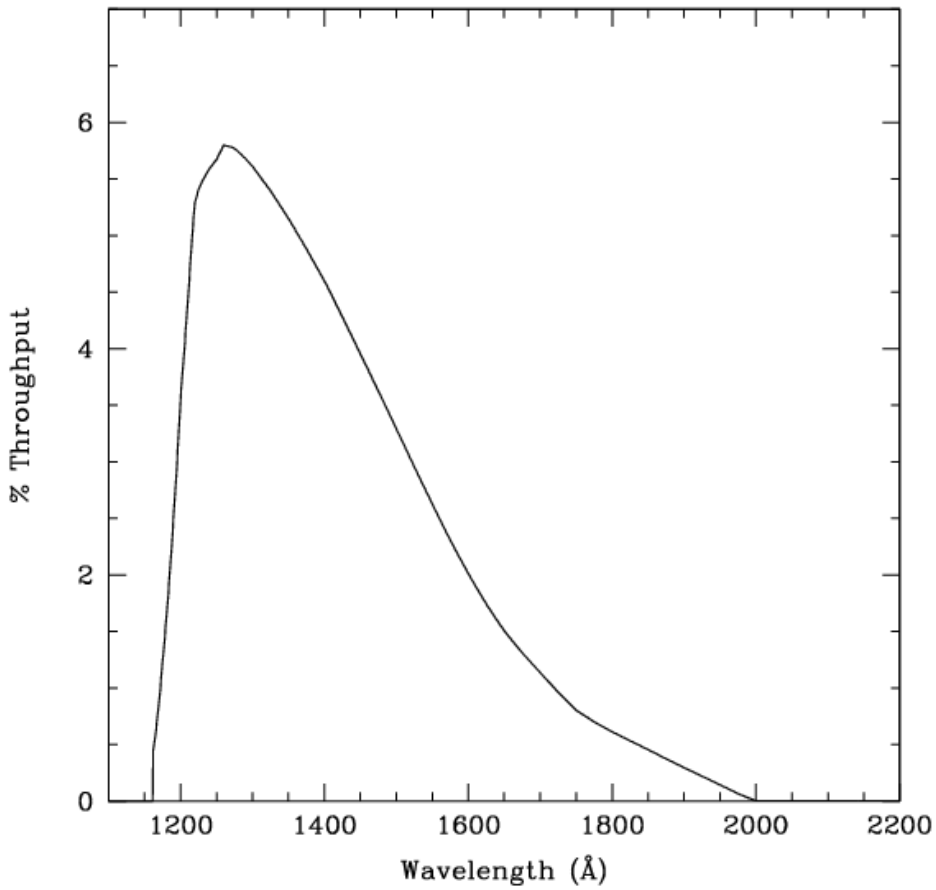

Figure 10.104: Point source S/N vs. V+ABν for the SBC/F115LP filter.Top curves are for low sky; bottom curves are for average sky.

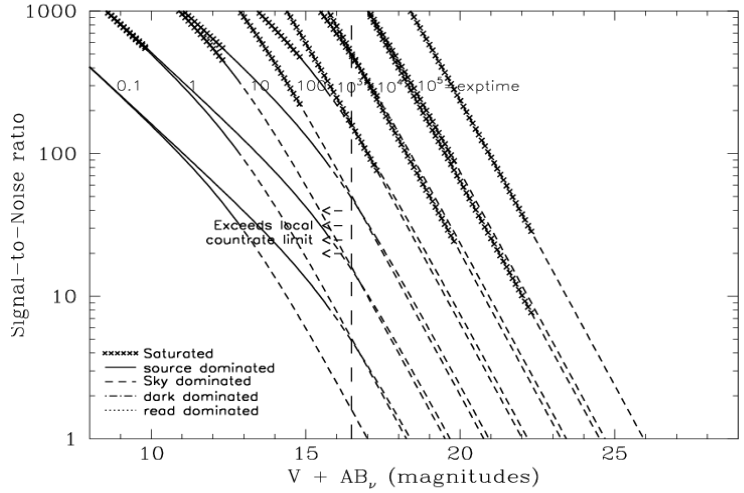

Figure 10.105: Extended source S/N vs. V+ABν for the SBC/F115LP filter. Top curves are for low sky and bottom curves are for average sky for a 1 arcsec^2 area.

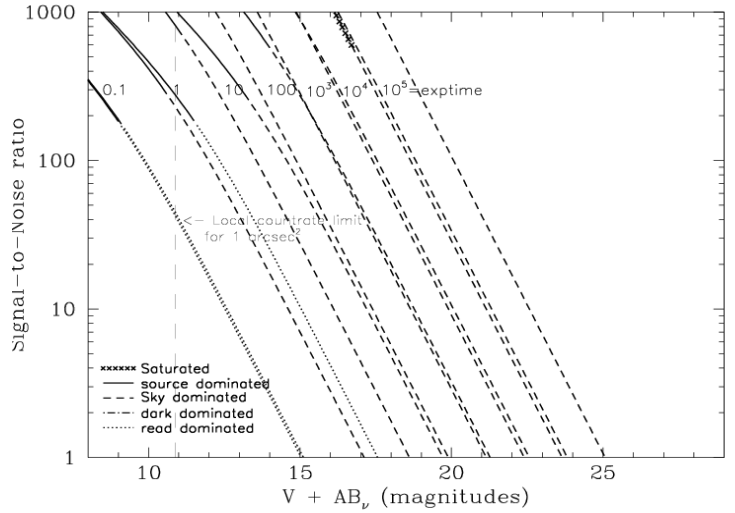

SBC/F122M

Description

Lyman α filter.

Figure 10.106: Integrated system throughput for SBC/F122M.

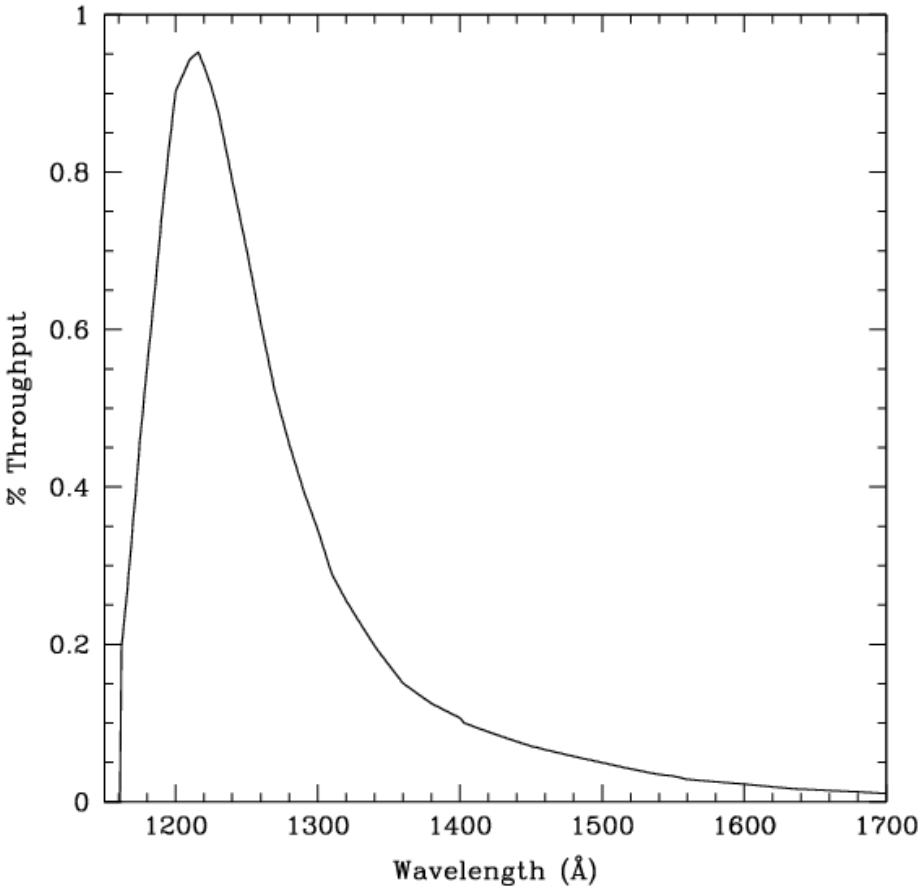

Figure 10.107: Point source S/N vs. V+ABν for the SBC/F122M filter.Top curves are for low sky; bottom curves are for average sky.

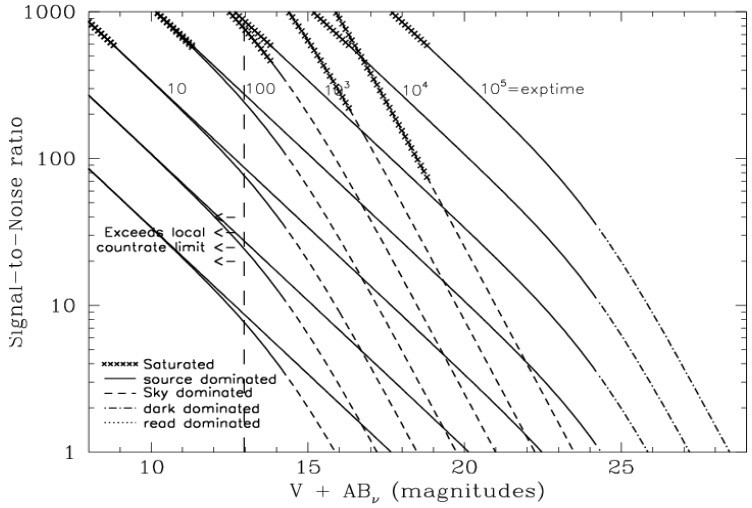

Figure 10.108: Extended source S/N vs. V+ABν for the SBC/F122M filter. Top curves are for low sky and bottom curves are for average sky for a 1 arcsec^2 area.

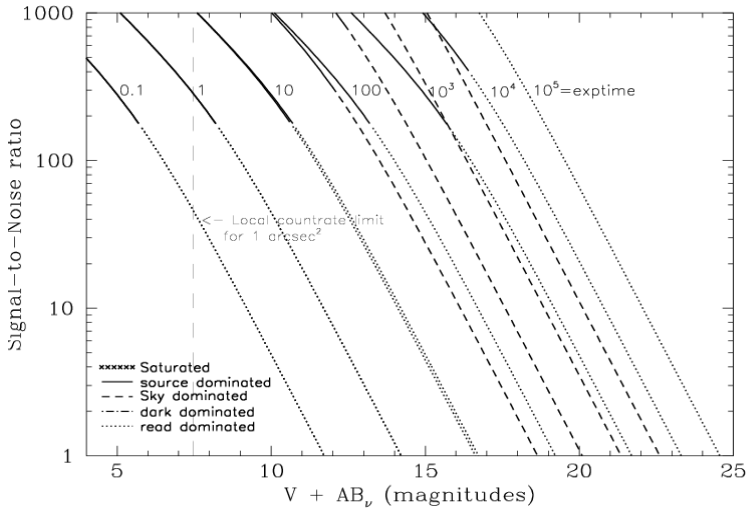

SBC/F125LP

Description

CaF_2 filter.

Figure 10.109: Integrated system throughput for SBC/F125LP.

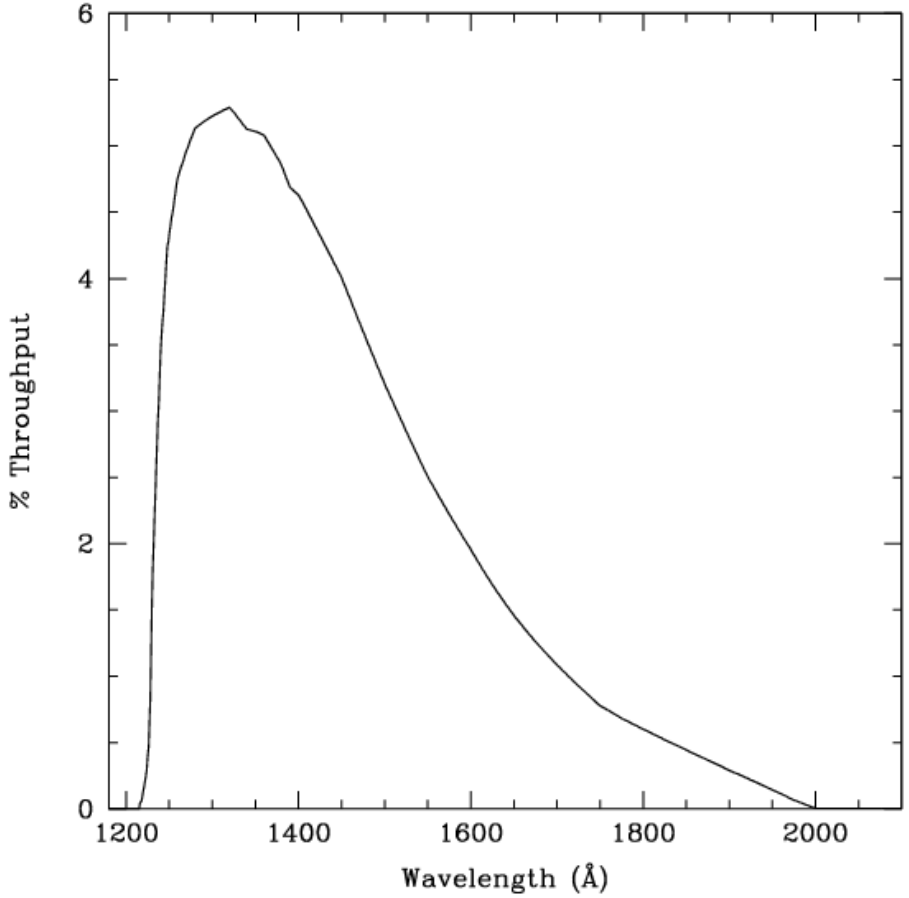

Figure 10.110: Point source S/N vs. V+ABν for the SBC/F125LP filter. Top curves are for low sky; bottom curves are for average sky.

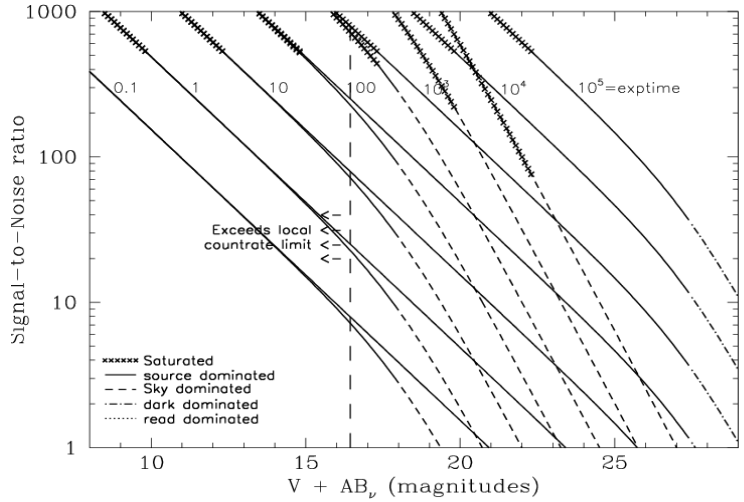

Figure 10.111: Extended source S/N vs. V+ABν for the SBC/F125LP filter. Top curves are for low sky and bottom curves are for average sky for a 1 arcsec^2 area.

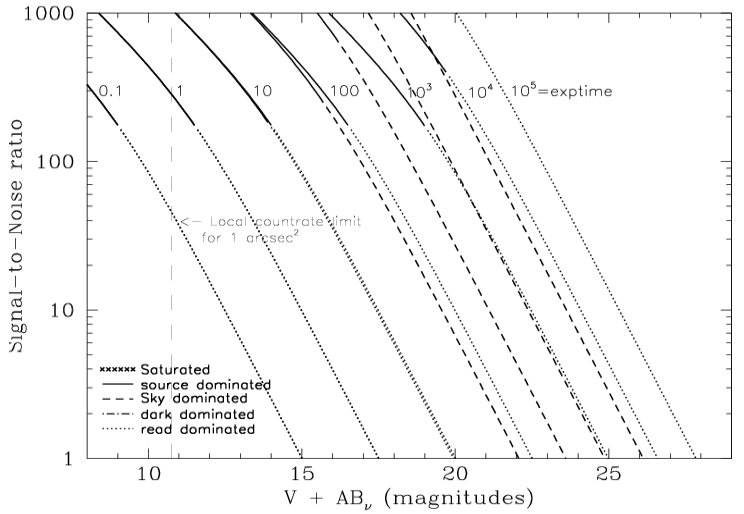

SBC/F140LP

Description

BaF_2 filter.

Figure 10.112: Integrated system throughput for SBC/F140LP.

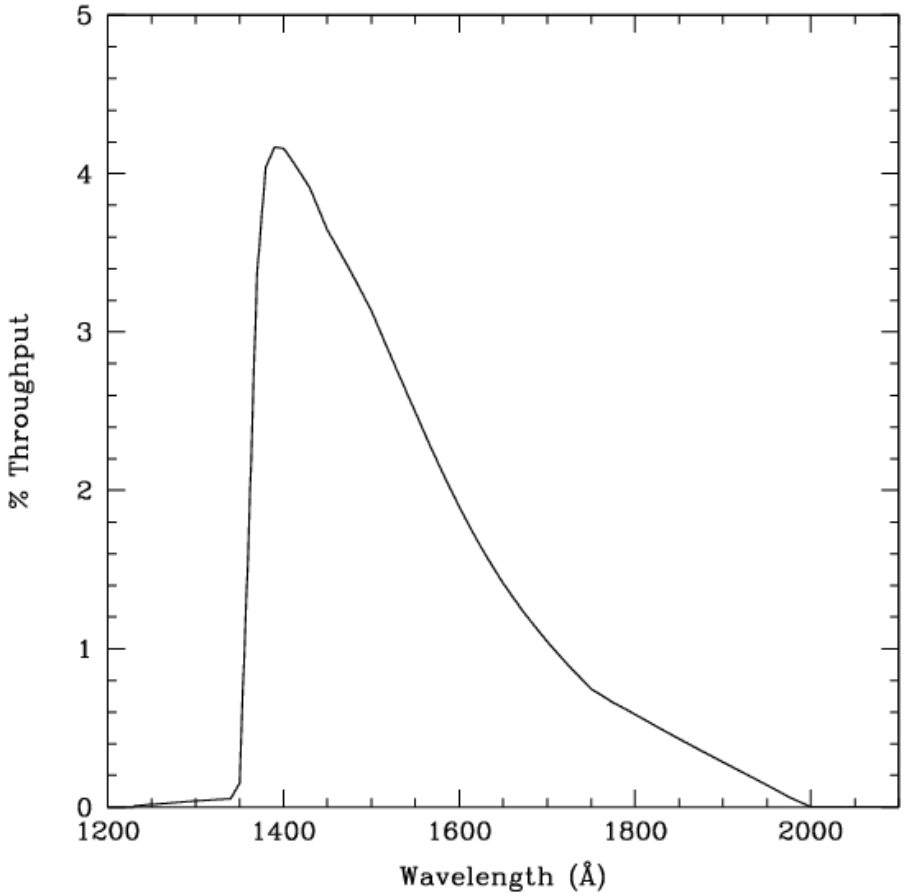

Figure 10.113: Point source S/N vs. V+ABν for the SBC/F140LP filter. Top curves are for low sky; bottom curves are for average sky.

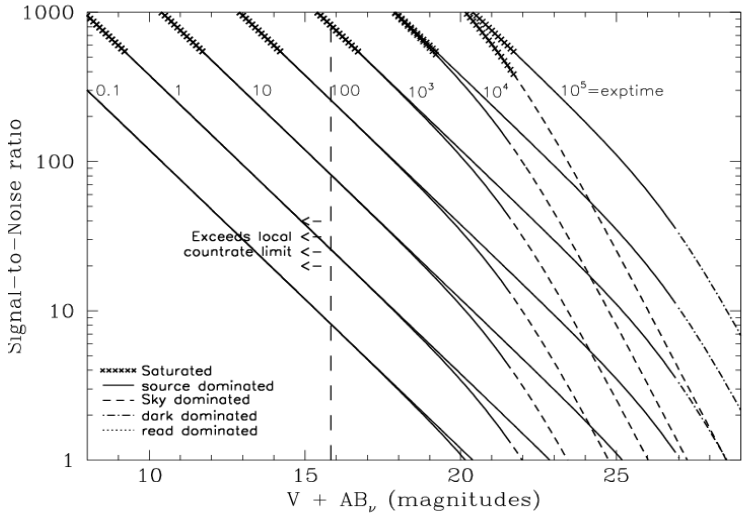

Figure 10.114: Extended source S/N vs. V+ABν for the SBC/F140LP filter. Top curves are for low sky and bottom curves are for average sky for a 1 arcsec^2 area.

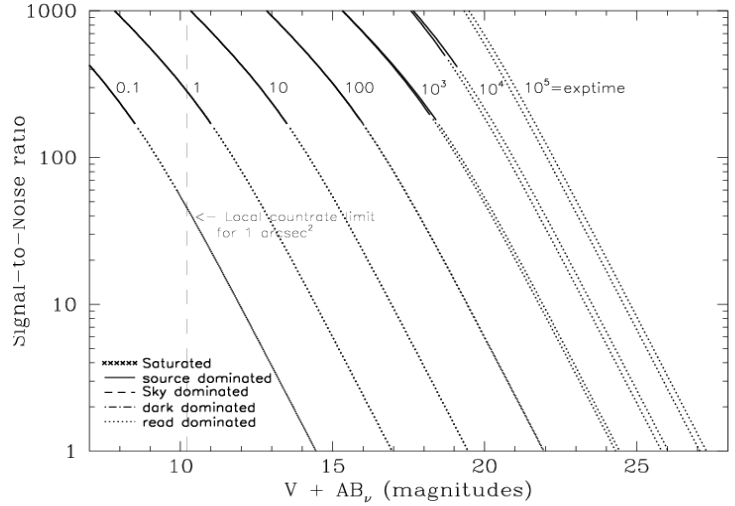

SBC/F150LP

Description

Crystal Quartz filter.

Figure 10.115: Integrated system throughput for SBC/F165LP.

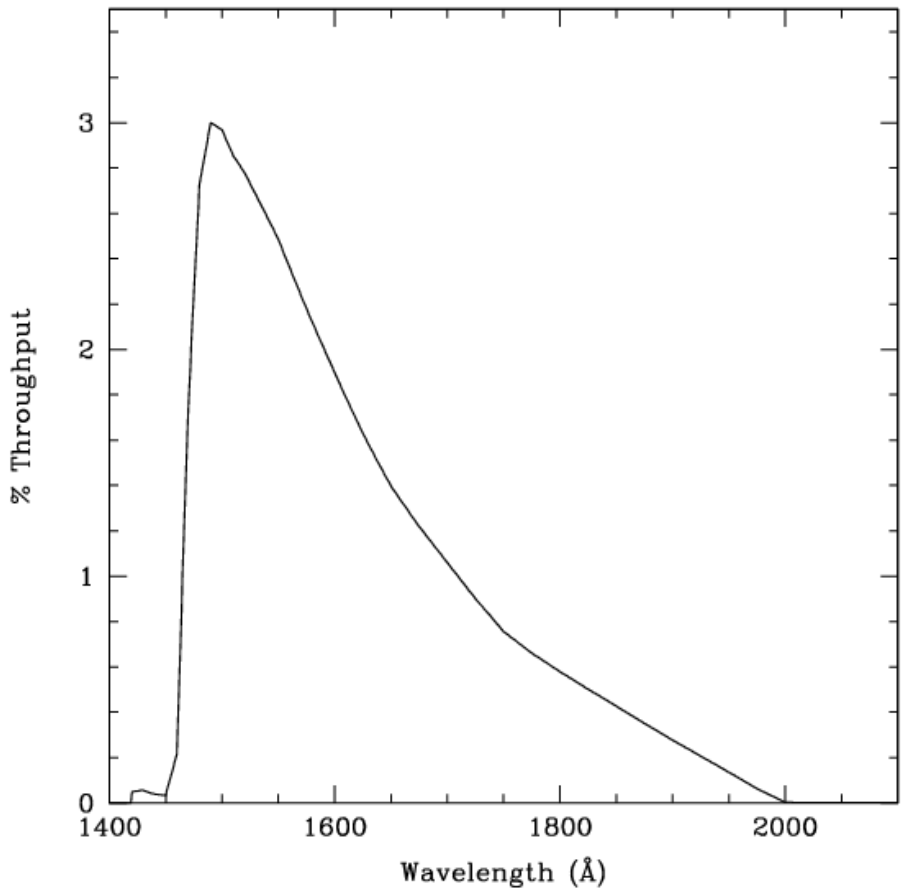

Figure 10.116: Point source S/N vs. V+ABν for the SBC/F150LP filter. Top curves are for low sky; bottom curves are for average sky.

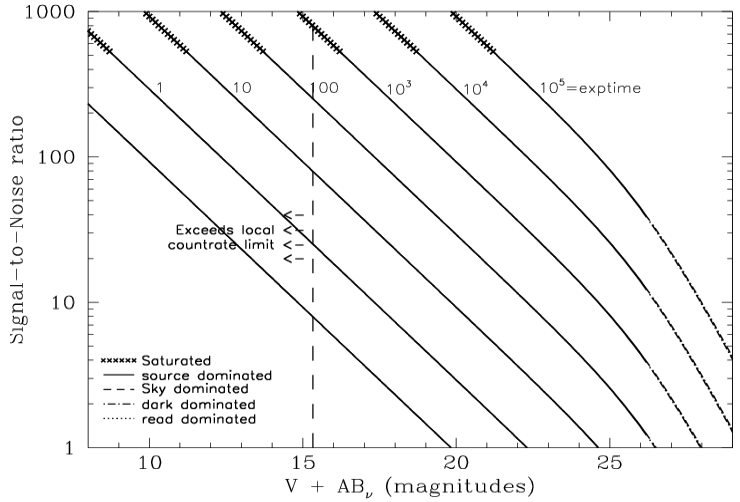

Figure 10.117: Extended source S/N vs. V+ABν for the SBC/F150LP filter. Top curves are for low sky and bottom curves are for average sky for a 1 arcsec^2 area.

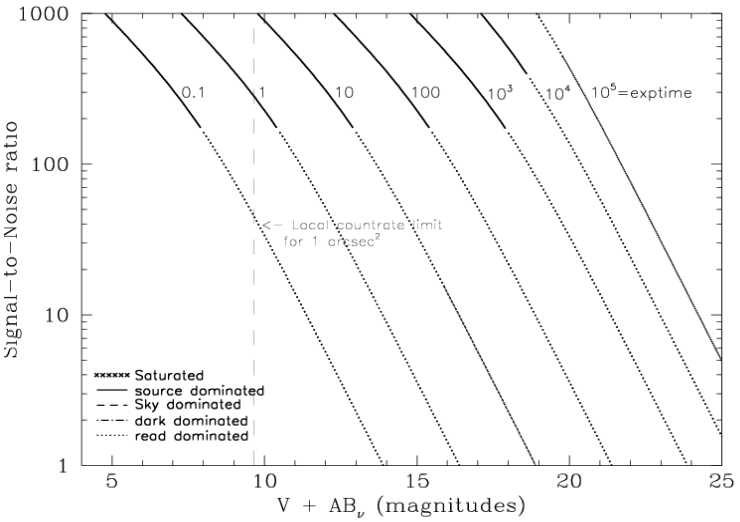

SBC/F165LP

Description

Dynasil filter.

Figure 10.118: Integrated system throughput for SBC/F165LP.

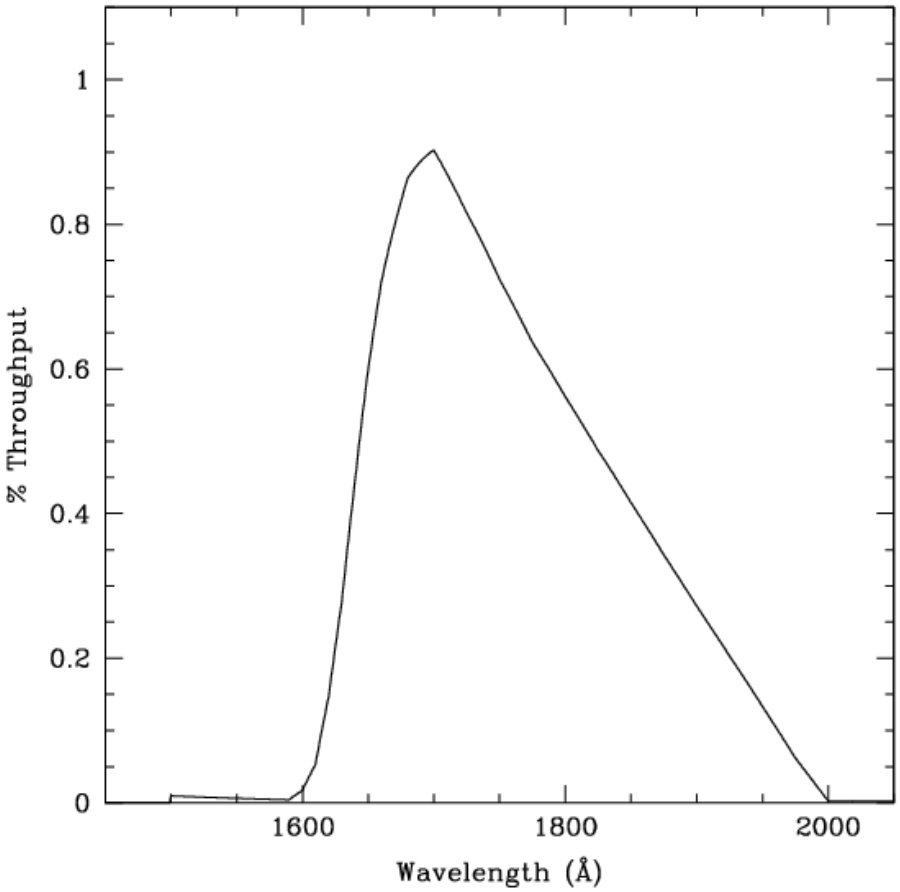

Figure 10.119: Point source S/N vs. V+ABν for the SBC/F165LP filter.Top curves are for low sky; bottom curves are for average sky.

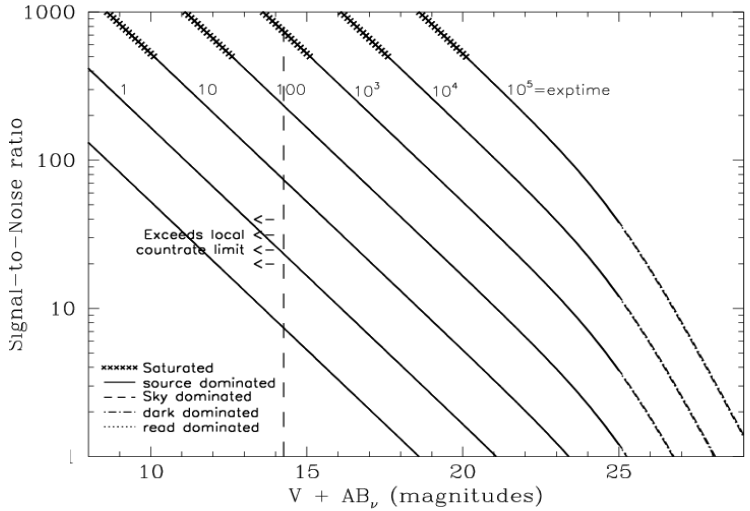

Figure 10.120: Extended source S/N vs. V+ABν for the SBC/F165LP filter. Top curves are for low sky and bottom curves are for average sky for a 1 arcsec^2 area.

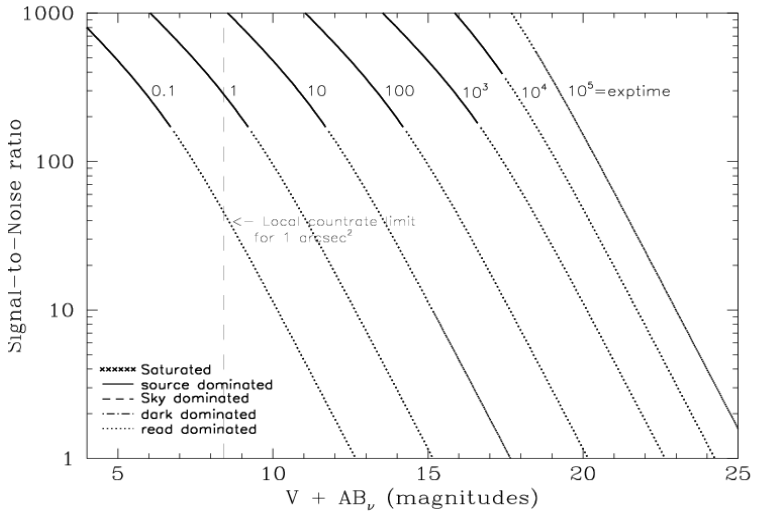

SBC/PR110L

Description

LiF_2 Prism.

Figure 10.121: Integrated system throughput for SBC/PR110LP.

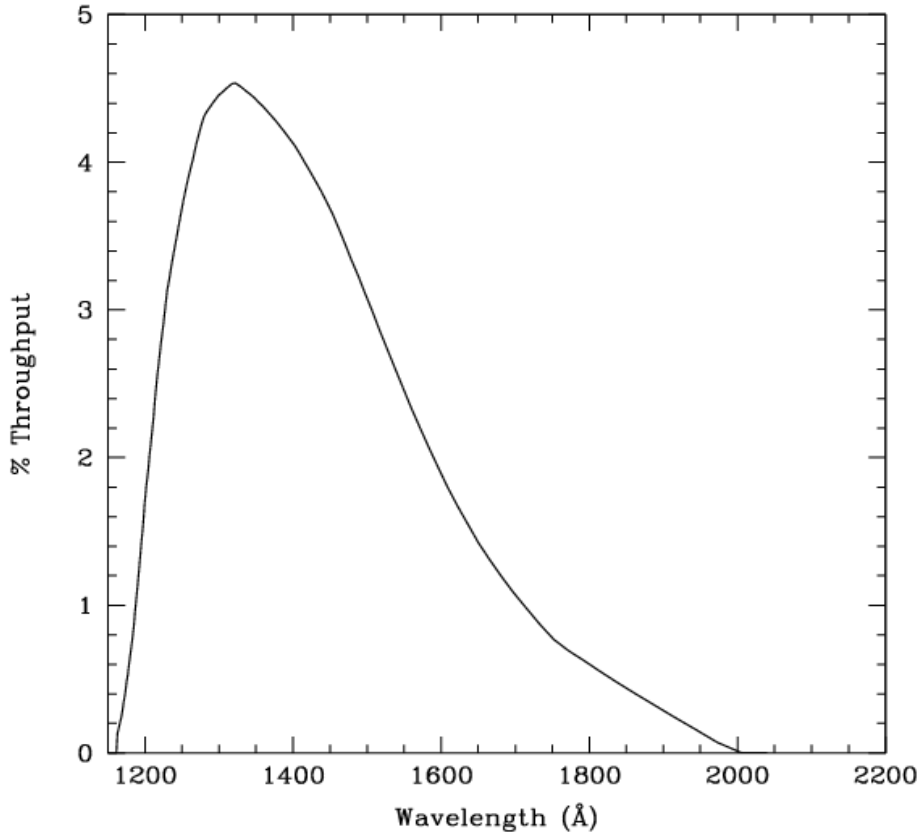

Figure 10.122: Point source S/N vs. V+ABν for the SBC/PR110LP filter. Top curves are for low sky; bottom curves are for average sky.

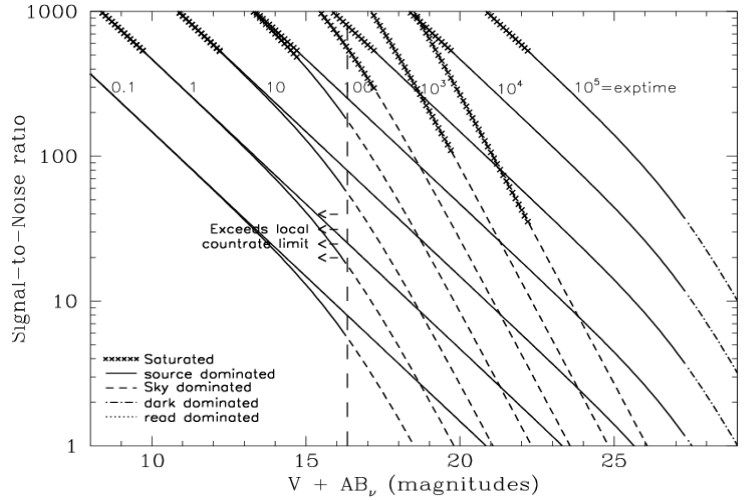

Figure 10.123: Extended source S/N vs. V+ABν for the SBC/PR110LP filter. Top curves are for low sky and bottom curves are for average sky for a 1 arcsec^2 area.

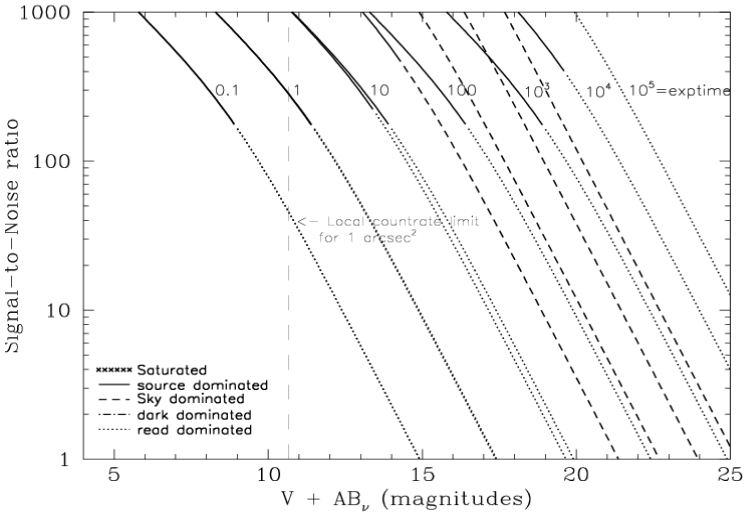

SBC/PR130L

Description

CaF_2 Prism.

Figure 10.124: Integrated system throughput for SBC/PR130LP.

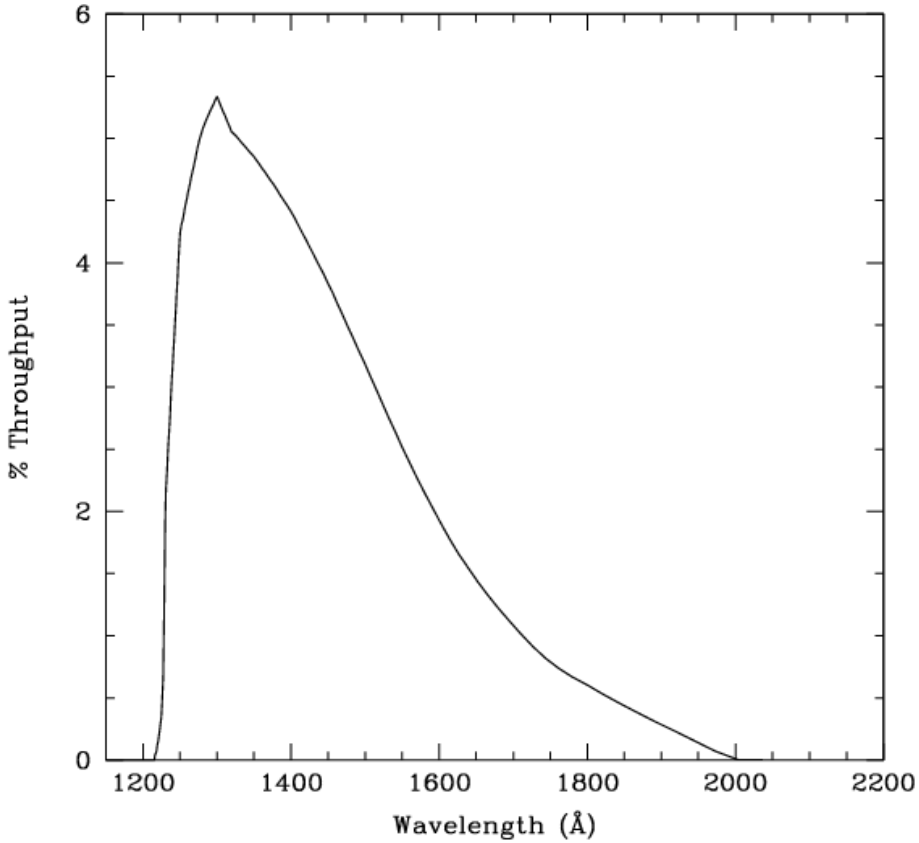

Figure 10.125: Point source S/N vs. V+ABν for the SBC/PR130LP filter. Top curves are for low sky; bottom curves are for average sky.

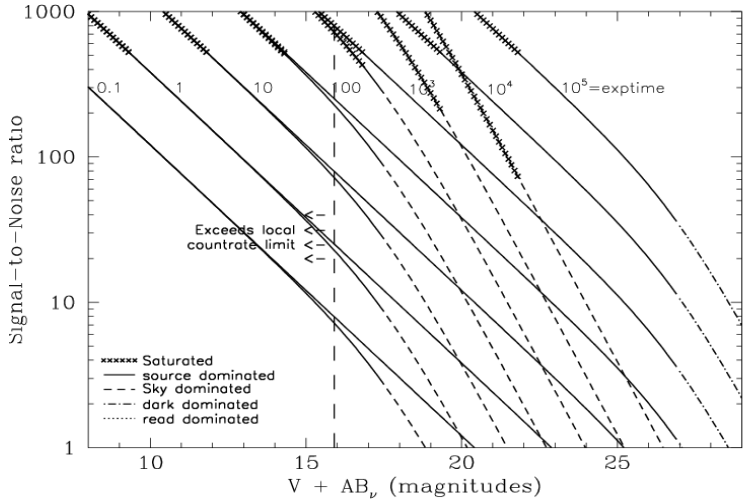

Figure 10.126: Extended source S/N vs. V+ABν for the SBC/PR130LP filter. Top curves are for low sky and bottom curves are for average sky for a 1 arcsec^2 area.

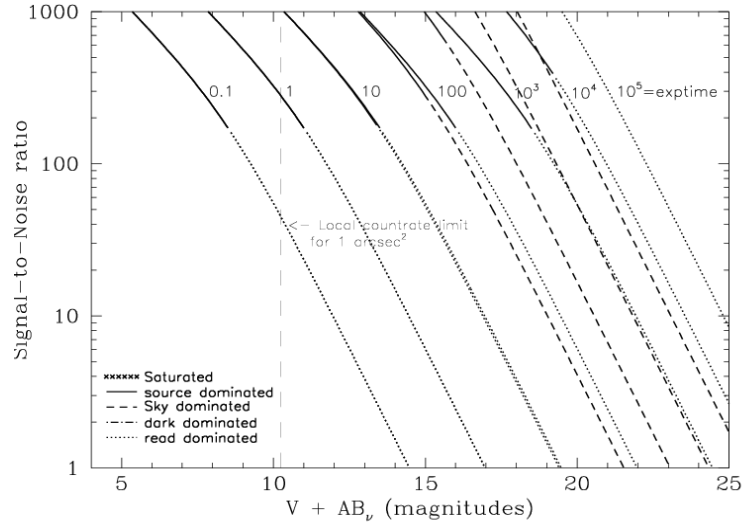

Table 10.1: Color corrections AB_V to go from Johnson V magnitude to AB magnitude for the WFC.

Spectrum	F435W	F475W	F502N	F550M	F555W	F606W	F625W	F658N	F660N	F775W	F814W	F850LP	F892N	G800L	CLEAR
AvgSky	0.62	0.33	0.21	-0.04	0.05	-0.10	-0.22	-0.24	-0.27	-0.40	-0.42	-0.47	-0.47	-0.35	-0.05
LowSky	0.52	0.26	0.14	-0.03	0.03	-0.07	-0.15	-0.18	-0.20	-0.26	-0.27	-0.30	-0.31	-0.23	0.00
O5 V	-0.44	-0.28	-0.15	0.05	-0.04	0.12	0.27	0.38	0.39	0.67	0.75	1.00	0.98	0.55	0.04
B0 V	-0.43	-0.28	-0.17	0.06	-0.04	0.12	0.29	0.40	0.39	0.64	0.71	0.94	0.92	0.54	0.04
A0 V	-0.07	-0.08	-0.07	0.02	0.00	0.08	0.15	0.33	0.29	0.35	0.39	0.48	0.48	0.29	0.14
A5 V	0.04	-0.01	-0.03	0.00	0.00	0.06	0.10	0.22	0.16	0.23	0.25	0.31	0.30	0.19	0.13
F2 V	0.26	0.12	0.05	-0.01	0.02	0.00	-0.03	0.00	-0.03	-0.05	-0.05	-0.04	-0.05	-0.04	0.06
G2 V	0.54	0.28	0.14	-0.03	0.04	-0.07	-0.16	-0.16	-0.17	-0.30	-0.31	-0.34	-0.34	-0.26	0.00
K0 V	0.77	0.40	0.19	-0.06	0.05	-0.12	-0.25	-0.31	-0.31	-0.42	-0.44	-0.47	-0.49	-0.37	-0.04
M0 V	1.41	0.80	0.67	-0.14	0.11	-0.33	-0.59	-0.84	-0.84	-1.21	-1.31	-1.55	-1.52	-1.09	-0.53
M6 V	1.72	0.89	0.71	-0.18	0.12	-0.40	-0.66	-1.17	-1.15	-2.11	-2.34	-2.80	-2.74	-1.96	-1.27
O7 I	-0.40	-0.25	-0.13	0.04	-0.03	0.11	0.25	0.35	0.35	0.63	0.70	0.94	0.92	0.52	0.05
B0 I	-0.34	-0.21	-0.11	0.03	-0.03	0.10	0.22	0.31	0.31	0.52	0.58	0.77	0.75	0.43	0.05
F0 III	0.19	0.07	0.00	0.00	0.01	0.01	0.01	0.06	0.03	0.06	0.06	0.07	0.05	0.04	0.10
G0 III	0.63	0.32	0.15	-0.03	0.04	-0.09	-0.19	-0.24	-0.25	-0.36	-0.38	-0.43	-0.45	-0.31	-0.02
K2 III	1.13	0.57	0.33	-0.07	0.07	-0.19	-0.37	-0.48	-0.48	-0.68	-0.72	-0.83	-0.89	-0.60	-0.17
M0 III	1.56	0.80	0.56	-0.12	0.11	-0.33	-0.58	-0.74	-0.75	-1.24	-1.35	-1.59	-1.62	-1.12	-0.55
M6 III	1.65	0.92	1.19	-0.12	0.18	-0.64	-0.95	-1.20	-1.15	-2.91	-3.24	-3.89	-3.74	-2.83	-2.10
Elliptical	0.95	0.51	0.34	-0.07	0.07	-0.19	-0.36	-0.48	-0.48	-0.81	-0.92	-1.07	-1.18	-0.72	-0.27
Sa	0.80	0.45	0.30	-0.06	0.07	-0.18	-0.36	-0.54	-0.51	-0.75	-0.84	-0.94	-1.05	-0.66	-0.24
Sb	0.81	0.44	0.27	-0.06	0.06	-0.18	-0.34	-0.50	-0.48	-0.75	-0.85	-0.97	-1.09	-0.66	-0.24
Sc	0.08	0.00	-0.71	0.07	-0.03	-0.17	-0.26	-1.76	-0.84	0.40	0.77	1.67	1.26	0.20	0.08
Starburst E(B-V) 0.51-0.60	0.41	0.24	-0.02	0.00	0.04	-0.22	-0.39	-1.38	-0.87	-0.59	-0.67	-0.75	-0.80	-0.56	-0.23
Starburst E(B-V)<0.1	0.23	0.05	-0.96	0.09	-0.03	-0.10	-0.14	-1.16	-0.35	-0.15	-0.19	-0.18	-0.23	-0.16	-0.03
Sun	0.58	0.30	0.17	-0.03	0.04	-0.07	-0.17	-0.17	-0.20	-0.26	-0.27	-0.27	-0.28	-0.23	0.01
Vega	-0.12	-0.11	-0.07	0.02	0.00	0.08	0.16	0.35	0.32	0.39	0.43	0.56	0.49	0.32	0.14

Table 10.2: Color corrections AB_V to go from Johnson V magnitude to AB magnitude for the HRC.

Spectrum	F220W	F250W	F330W	F344N	F435W	F475W	F502N	F550M	F555W	F606W	F625W	F658N	F660N	F775W	F814W	F850LP	F892N	G800L	PR200L	Clear
AvgSky	3.56	2.58	2.01	1.89	0.63	0.32	0.21	-0.04	0.05	-0.09	-0.22	-0.24	-0.27	-0.39	-0.42	-0.47	-0.47	-0.35	0.21	0.29
LowSky	5.31	3.37	1.84	1.72	0.65	0.33	0.22	-0.04	0.05	-0.11	-0.24	-0.27	-0.30	-0.45	-0.48	-0.55	-0.30	-0.39	0.18	0.26
O5 V	-1.53	-1.24	-0.86	-0.81	-0.44	-0.26	-0.15	0.04	-0.04	0.11	0.27	0.38	0.39	0.66	0.76	1.02	0.98	0.55	-0.45	-0.57
B0 V	-1.16	-0.98	-0.72	-0.69	-0.44	-0.27	-0.17	0.06	-0.04	0.11	0.28	0.40	0.39	0.63	0.72	0.96	0.92	0.54	-0.31	-0.41
A0 V	1.75	1.54	1.19	1.16	-0.06	-0.08	-0.07	0.02	0.00	0.07	0.15	0.33	0.29	0.35	0.39	0.48	0.48	0.29	0.33	0.39
A5 V	2.60	2.15	1.41	1.35	0.05	-0.01	-0.03	0.00	0.00	0.05	0.10	0.22	0.16	0.23	0.25	0.31	0.29	0.19	0.36	0.43
F2 V	3.49	2.52	1.45	1.35	0.27	0.11	0.05	-0.01	0.02	0.00	-0.03	0.00	-0.03	-0.05	-0.05	-0.04	-0.05	-0.04	0.31	0.38
G2 V	5.66	3.29	1.63	1.63	0.55	0.26	0.14	-0.03	0.04	-0.06	-0.15	-0.16	-0.17	-0.30	-0.31	-0.34	-0.34	-0.26	0.25	0.33
K0 V	6.82	4.47	2.39	2.26	0.78	0.38	0.19	-0.06	0.05	-0.11	-0.24	-0.31	-0.31	-0.42	-0.44	-0.47	-0.49	-0.37	0.23	0.31
M0 V	7.73	5.93	3.90	3.76	1.40	0.76	0.67	-0.14	0.12	-0.31	-0.58	-0.84	-0.84	-1.20	-1.32	-1.57	-1.52	-1.09	-0.24	-0.15
M6 V	7.30	6.31	4.31	4.23	1.71	0.84	0.71	-0.18	0.13	-0.37	-0.65	-1.17	-1.15	-2.09	-2.37	-2.83	-2.75	-1.98	-0.99	-0.90
O7 I	-0.33	-0.55	-0.60	-0.56	-0.40	-0.24	-0.13	0.04	-0.03	0.10	0.25	0.35	0.35	0.62	0.71	0.96	0.92	0.51	-0.11	-0.14
B0 I	-0.72	-0.69	-0.55	-0.54	-0.34	-0.20	-0.11	0.03	-0.03	0.09	0.22	0.31	0.31	0.51	0.59	0.78	0.75	0.43	-0.15	-0.21
F0 III	3.69	2.75	1.58	1.47	0.20	0.06	0.00	0.00	0.01	0.01	0.01	0.06	0.03	0.06	0.06	0.07	0.05	0.04	0.34	0.42
G0 III	6.58	4.21	2.24	2.13	0.63	0.31	0.15	-0.03	0.04	-0.08	-0.19	-0.24	-0.25	-0.36	-0.38	-0.43	-0.45	-0.31	0.24	0.32
K2 III	8.43	6.56	3.78	3.56	1.13	0.54	0.33	-0.07	0.07	-0.17	-0.36	-0.48	-0.48	-0.67	-0.73	-0.84	-0.89	-0.60	0.11	0.19
M0 III	7.71	7.02	5.14	5.01	1.55	0.76	0.56	-0.11	0.12	-0.31	-0.57	-0.74	-0.75	-1.23	-1.36	-1.61	-1.62	-1.12	-0.25	-0.17
M6 III	6.27	6.17	4.45	4.28	1.67	0.89	1.19	-0.12	0.18	-0.60	-0.93	-1.20	-1.15	-2.88	-3.29	-3.93	-3.74	-2.87	-1.83	-1.75
Elliptical	5.20	4.63	2.82	2.63	0.95	0.48	0.34	-0.07	0.07	-0.17	-0.36	-0.48	-0.48	-0.80	-0.93	-1.08	-1.18	-0.72	0.01	0.09
Sa	4.35	3.53	2.38	2.34	0.80	0.43	0.30	-0.06	0.07	-0.17	-0.35	-0.54	-0.51	-0.75	-0.85	-0.94	-1.05	-0.66	0.03	0.11
Sb	3.73	3.10	2.11	2.16	0.81	0.42	0.27	-0.06	0.07	-0.17	-0.34	-0.50	-0.48	-0.74	-0.86	-0.98	-1.09	-0.66	0.02	0.10
Sc	2.09	1.15	0.15	-0.07	0.07	-0.01	-0.70	0.07	-0.03	-0.17	-0.25	-1.76	-0.85	0.34	0.77	12.85	9.95	0.19	0.22	0.285
Starburst E(B-V) 0.51-0.60	1.82	1.63	1.13	1.14	0.41	0.23	-0.02	0.00	0.04	-0.21	-0.38	-1.38	-0.87	-0.59	-0.68	-0.76	-0.80	-0.57	0.00	0.05
Starburst E(B-V)<0.1	0.98	0.95	0.81	0.80	0.22	0.04	-0.96	0.09	-0.03	-0.10	-0.14	-1.16	-0.35	-0.15	-0.20	-0.18	-0.23	-0.16	0.11	0.16
Sun	5.67	3.55	1.83	1.72	0.58	0.28	0.17	-0.03	0.04	-0.06	-0.16	-0.17	-0.20	-0.26	-0.27	-0.27	-0.28	-0.23	0.27	0.36
Vega	1.65	1.48	1.18	1.14	-0.10	-0.10	-0.07	0.02	0.00	0.08	0.16	0.35	0.32	0.38	0.44	0.56	0.49	0.32	0.33	0.39

Table 10.3: Color corrections AB_V to go from Johnson V magnitude to AB magnitude for the SBC.

Spectrum	F115LP	F122M	F125LP	F140LP	F150LP	F165LP	PR110L	PR130L
AvgSky	12.00	14.41	11.83	11.23	10.60	9.25	11.81	11.81
LowSky	-1.78	-2.95	2.73	6.80	10.34	9.00	-1.27	2.69
O5 V	-2.07	-2.18	-2.04	-1.96	-1.91	-1.82	-2.05	-2.04
B0 V	-1.64	-1.53	-1.69	-1.67	-1.63	-1.54	-1.66	-1.69
A0 V	2.65	3.88	2.47	2.09	1.91	1.82	2.51	2.46
A5 V	5.41	7.44	5.24	4.65	4.05	3.14	5.23	5.22
F2 V	7.91	10.17	7.74	7.14	6.51	5.18	7.72	7.71
G2 V	13.82	16.35	13.65	13.05	12.42	11.07	13.63	13.63
K0 V	10.07	10.43	10.00	9.79	9.61	9.31	10.01	9.99
M0 V	11.58	11.94	11.50	11.29	11.11	10.81	11.51	11.49
M6 V	12.06	12.42	11.98	11.77	11.59	11.29	11.99	11.97
O7 I	-0.57	-0.42	-0.61	-0.68	-0.70	-0.71	-0.59	-0.61
B0 I	-0.80	-0.61	-0.87	-0.83	-0.78	-0.75	-0.82	-0.86
F0 III	7.81	10.09	7.63	7.04	6.41	5.07	7.62	7.61
G0 III	9.80	10.16	9.72	9.52	9.34	9.03	9.74	9.72
K2 III	13.32	13.68	13.24	13.04	12.86	12.55	13.26	13.24
M0 III	11.07	11.42	10.99	10.78	10.60	10.30	11.00	10.98
M6 III	10.37	10.73	10.29	10.09	9.91	9.61	10.31	10.29
Elliptical	6.24	6.71	6.11	6.08	5.98	5.90	6.18	6.10
Sa	5.66	6.23	5.52	5.42	5.27	5.06	5.59	5.52
Sb	4.63	5.18	4.49	4.38	4.27	4.24	4.56	4.49
Sc	2.87	3.52	2.71	2.60	2.45	2.32	2.78	2.71
Starburst E(B-V) 0.51-0.60	2.68	3.31	2.52	2.44	2.35	2.13	2.60	2.52
Starburst E(B-V)<0.1	1.33	1.88	1.18	1.13	1.09	1.06	1.25	1.18
Sun	12.00	11.78	12.29	11.79	11.21	10.02	12.02	12.28
Vega	2.74	3.95	2.56	2.20	2.04	1.91	2.61	2.56

10.3 Geometrical Distortion in the ACS

The ACS detectors exhibit more distortion than previous *HST* instruments. The principal reason for this is that the optics have been designed with a minimum number of components, consistent with correcting for the spherical aberration induced by the OTA, without introducing coma. The result is a high throughput, but with focal surfaces far from normal to the principal rays. The WFC detector is tilted at 22° giving an elongation of 8% while the HRC and SBC have a 25° tilt leading to an elongation of 12%. In each case, the scales in arcseconds per pixel are smaller along the radial direction of the OTA (Optical Telescope Assembly) field of view than along the tangential direction.

The orientations of the ACS detector edges are approximately in line with the V2 and V3 coordinate axes of the telescope. Consequently, the eigenaxes of the scale transformation are along the diagonals for WFC, and the apertures and pixels appear non-rectangular in the sky projection. For the HRC and SBC the situation is even more irregular because the aperture diagonals do not lie along a radius of the *HST* field of view. Figure 7.9 shows the ACS apertures in the telescope's V2V3 reference frame. For a telescope roll angle of zero this would correspond to an on-sky view with the V3 axis aligned with North and the V2 with East.

There is not only a strong geometric distortion of ACS detectors but a significant variation of the scale across each detector. For the WFC the scale is changing in amount of 10% from corner to corner. For the HRC and SBC this variation is only about 1% as they cover much smaller fields of view. The area on the sky covered by a WFC pixel varies by about 18% from corner to corner, corrections for which must be made in photometry of extended objects. This variation of scale creates a problematic effect in combining ACS images by the fact that an integral pixel shift near the center of the detector will translate into a non-integral displacement for pixels near the edges. An accurate geometric distortion model and some computational complexity are therefore required to align the images before they are combined.

Accurate geometric distortion corrections for the WFC and HRC detectors by Anderson & King, Calibration Workshop 2002, ACS ISR 2004-15, ACS ISR 2006-01 were derived from observations of the globular cluster 47 Tuc, with multiple pointings and orientations, and through the F475W filter. The geometric distortion models for each of the WFC chips and the HRC detector are expressed in a 4th order polynomial and filter dependent look-up tables. The solution for both cameras is accurate to 0.01 pixels. The coefficients of the 4th order polynomial in the filter dependent look-up tables as well as correction images are installed in the ACS on-the-fly re-calibration (OTFR) pipeline and could be used independently in IRAF task CALACS.

Additionally, an area of the open cluster NGC188, for which accurate astrometry is available, was used to establish the exact location and orientation of the aperture in telescope coordinates. At the same time, the scale factors were confirmed.

For the SBC, the geometric distortion was derived using the observation of globular cluster NGC6681 taken through F125LP. The alignment was established by observing the same globular cluster with the HRC and SBC consecutively to establish the relative locations. The SBC position was derived from the HRC position.

10.3.1 WFC

The rhombus shape of the WFC is evident in Figure 7.9. The angle between the X and Y axes is 84.9° for WFC1 and 86.1° for WFC2. The geometric distortion map for WFC1 and WFC2 is illustrated in Figure 10.127. A vector diagram shows the contribution of the non-linear part of a quadratic fit only. The size of the residuals are scaled by a factor of 5 relative to the sky coordinates and could reach the residuals at about 4.1 arcseconds or 82 ACS/WFC pixels. At the center of chip WFC1 the scale in the X direction is 0.0493 arcseconds per pixel, and 0.0486 arcseconds per pixel in the Y direction. In the case of WFC2, the scale is 0.0498 arcseconds per pixel and 0.0503 arcseconds per pixel in X and Y direction respectively. Between the corner of WFC nearest to the V1 axis and the diagonally opposite corner, the scale increases by 10%. Because of that, WFC1 forms a slightly distorted rectangle 201 by 100 arcseconds in size, while WFC2 is 203 by 103 arcseconds. There is a 2.5 arcsecond gap between the two chips.

The skew of the distortion of the WFC has been shown to change slowly over time (ACS ISR 2007-08). The best estimate of the time-dependence of this skew term has been incorporated into the geometric distortion coefficients used by ***MultiDrizzle*** and the new package ***AstroDrizzle***. This solution is well-tested in pre-SM4 data, and for this time period typical relative position errors across the entire FOV of the ACS WFC are of order 0.05 pixels though errors up to 0.1 pixels have been observed. It was discovered that whatever is causing the time dependent drift in the geometric solution skew term ceased when ACS was switched off during failure. The time dependent terms have been monitored post-SM4 and seem to follow the pre-SM4 slope when the ACS dead time is accounted for. Revisions to the solution have been made to accommodate the ACS dead time.

Geometric distortion affects not only the astrometry but the photometry as well, since it induces an apparent variation in surface brightness across the field of view. In order to preserve the photometric accuracy, an additional correction to the photometry is required, by multiplying the ACS/WFC flat-fielded images by the pixel area map. The effective area of each pixel is shown in Figure 10.128 as a contour plot. The range of area is from 0.89 to 1.08 times the central value.

Figure 10.127: The geometric distortion map for the ACS/WFC, which shows only the non-linear component to the solution.

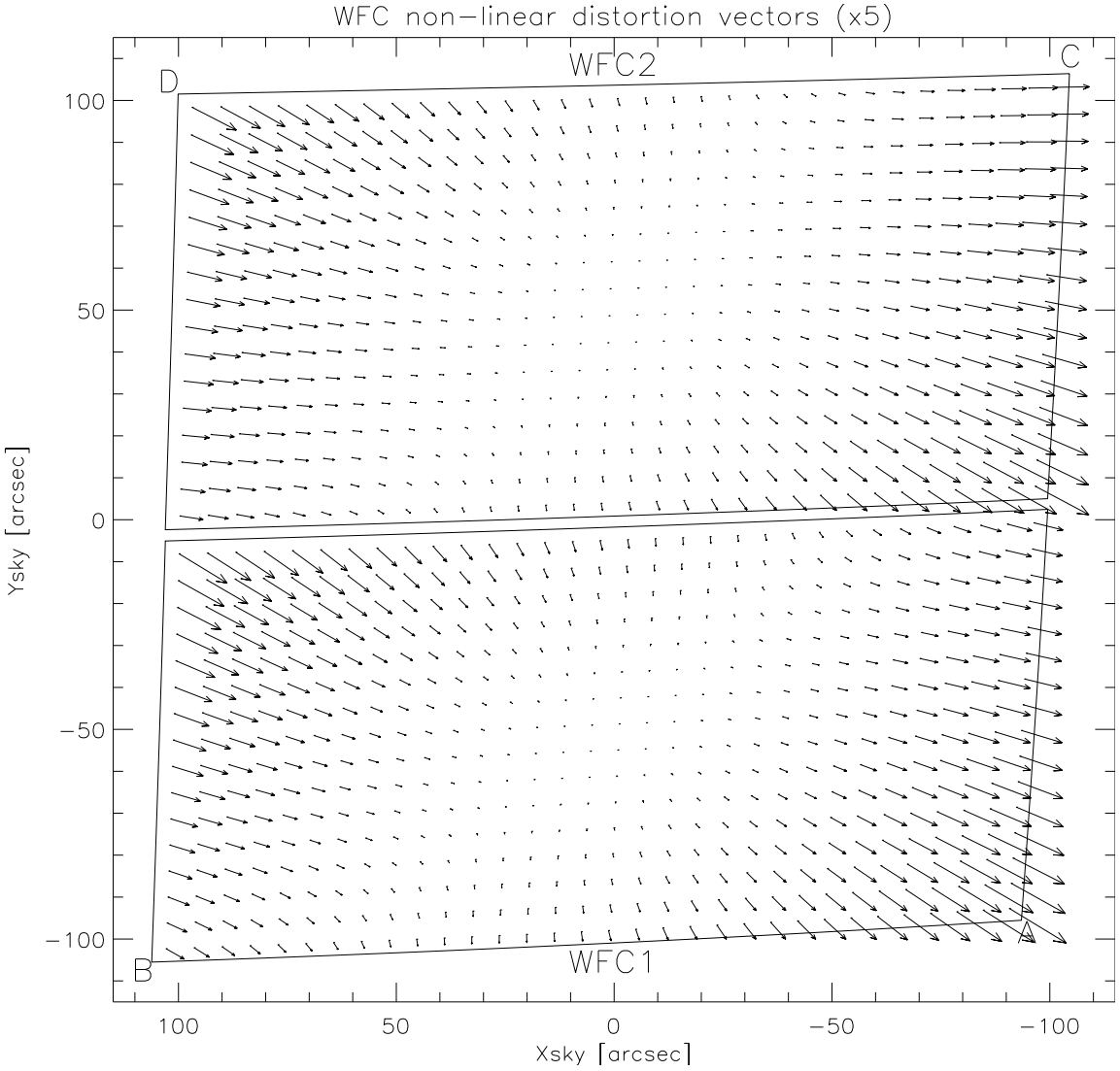

Note that this figure is rotated 180° with respect to the pipeline calibration products, where WFC2 is the lower half of the detector.

Figure 10.128: The map of the effective pixel areas of the ACS/WFC chips.

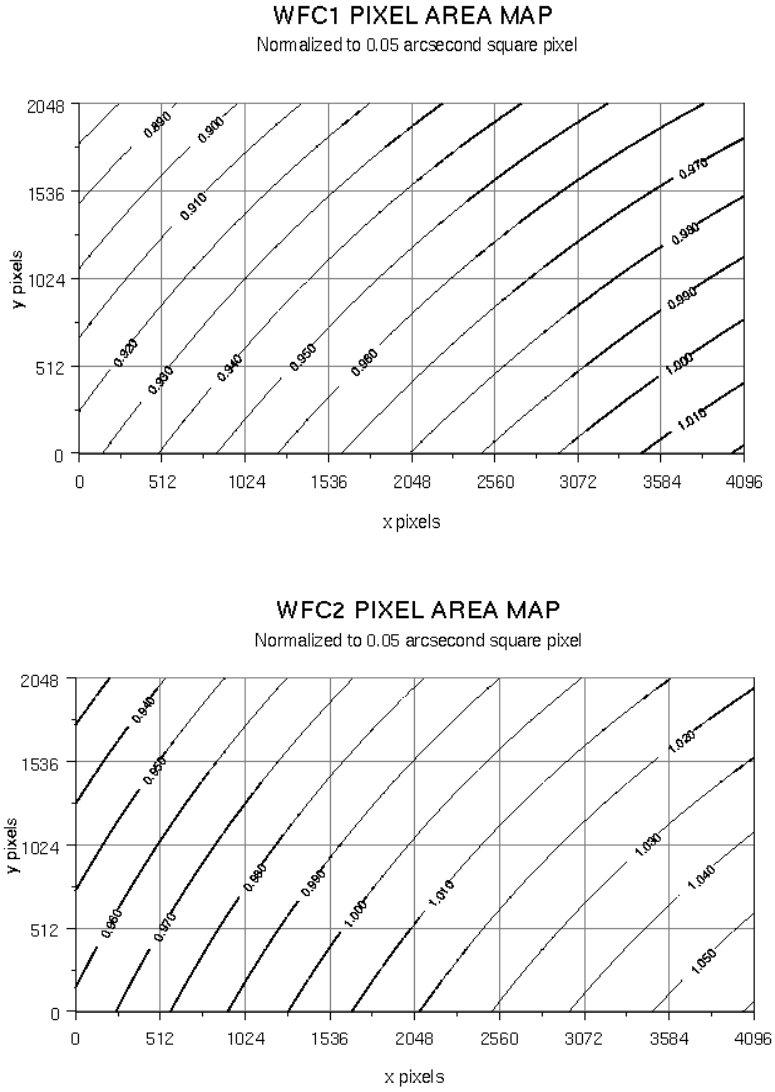

10.3.2 HRC

HRC has been unavailable since January 2007.

The High Resolution Channel has its edges aligned approximately along the V2 and V3 axes. In this case, the center of the aperture lies on a line passing through the V2-V3 origin and making an angle of 22° with the V3 axis. The diagonal of the aperture does not correspond to a radius of the *HST* field of view. So the distortion has no particular symmetry with respect to the detector axes. The focal plane of HRC is also 25° away from the plane normal to the light path, and because of this the scales along the axes differ by 14%. The full field of view of the HRC is less than

30 arcseconds, therefore the scale variation over the field is much less than for the WFC and it is about 1%. At the center, the X and Y scales are 0.0284 and 0.0248 arcseconds/pixel respectively. The average scales across the middle of the detector are 0.02842 and 0.02485 arcseconds/pixel making the X and Y widths 29.1 and 25.4 arcseconds. The slightly non-square projected aperture shape is evident in Figure 7.8. The angle between the X and Y axes on the sky is 84.2°. The geometric distortion map for HRC is given in Figure 10.129, where the residuals from the non-linearity are scaled by a factor of 10 relative to the sky coordinates and could reach the residuals at about 0.14 arcseconds, or 4.9 ACS/HRC pixels.

The same as for the WFC, geometric distortion affects not only the astrometry but the photometry as well, and a correction for the pixel area is required to restore the proper total counts of the target. The effective area of each pixel is shown in Figure 10.130 as a contour plot. The maximum deviation from the central value is about 3%. Because the pixel area map is normalized to square pixels 0.025 arcsecond on a side, rather than an area equal to that of the central HRC pixel, the pixel area map ranges from about 1.1 to 1.15.

Figure 10.129: The geometric distortion map for the HRC.

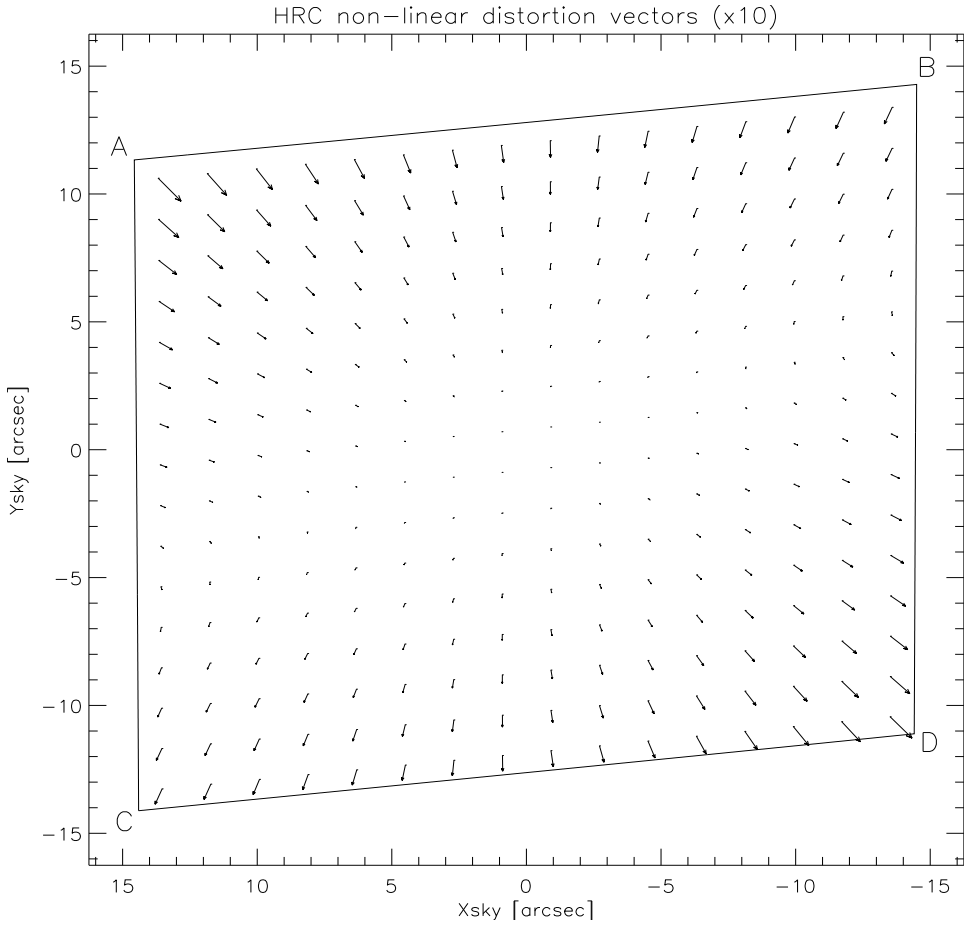

Figure 10.130: The map of the effective pixel areas of the HRC.

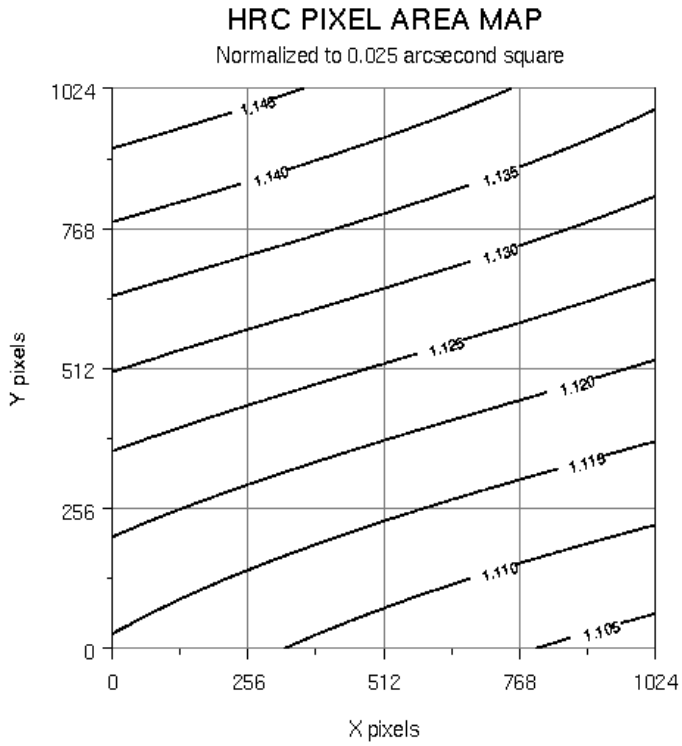

10.3.3 SBC

The Solar Blind Channel contains the MAMA detector. It is centered close to the HRC position in the V2V3 plane and has a slightly larger field of view, about 35 by 31 arcseconds. The scales and distortions have now been measured directly. The maximum distortion displacement is about 2 pixels or 0.06 arcseconds. Figure 10.131 shows the distortion map for the SBC detector.

The HRC and SBC both have much smaller areas than the WFC. For the SBC, the X direction scale is 0.0338 arcseconds/pixel and the Y direction scale is 0.0301 arcseconds/pixel. Similar to the HRC, the SBC exhibits a 13% difference between X and Y scales with a variation across the aperture of a little over 2%. As with the other cameras, geometric distortion affects photometry by a variation in pixel size across the SBC.

The map of the effective pixel areas of the SBC is shown in Figure 10.132. Because the pixel area map is normalized to square pixels 0.025 arcseconds on a side, rather than an area equal to that of the central SBC pixel, the pixel area map ranges from about 1.58 to 1.65. (Meurer et al. 2002).The maximum deviation from the central value is just over 2%.

Figure 10.131: The geometric distortion map for the ACS/SBC

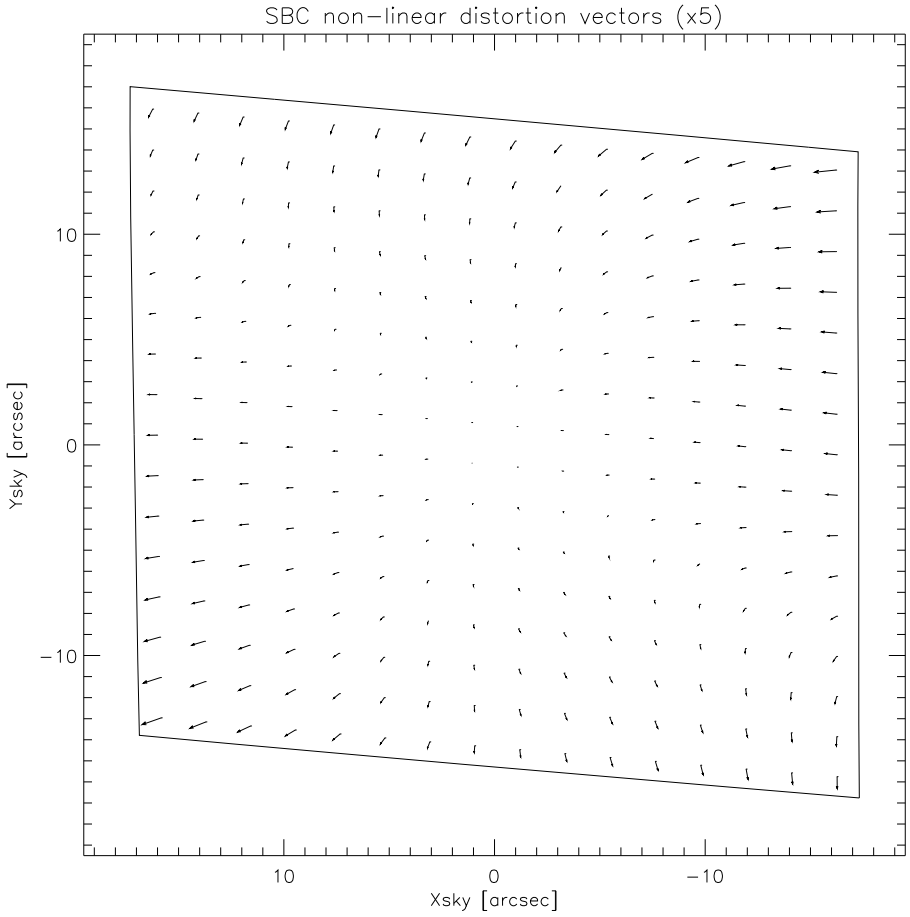

Figure 10.132: The map of the effective pixel areas of the ACS/SBC. The areas are normalized to 0.025 arcsecond square pixels.

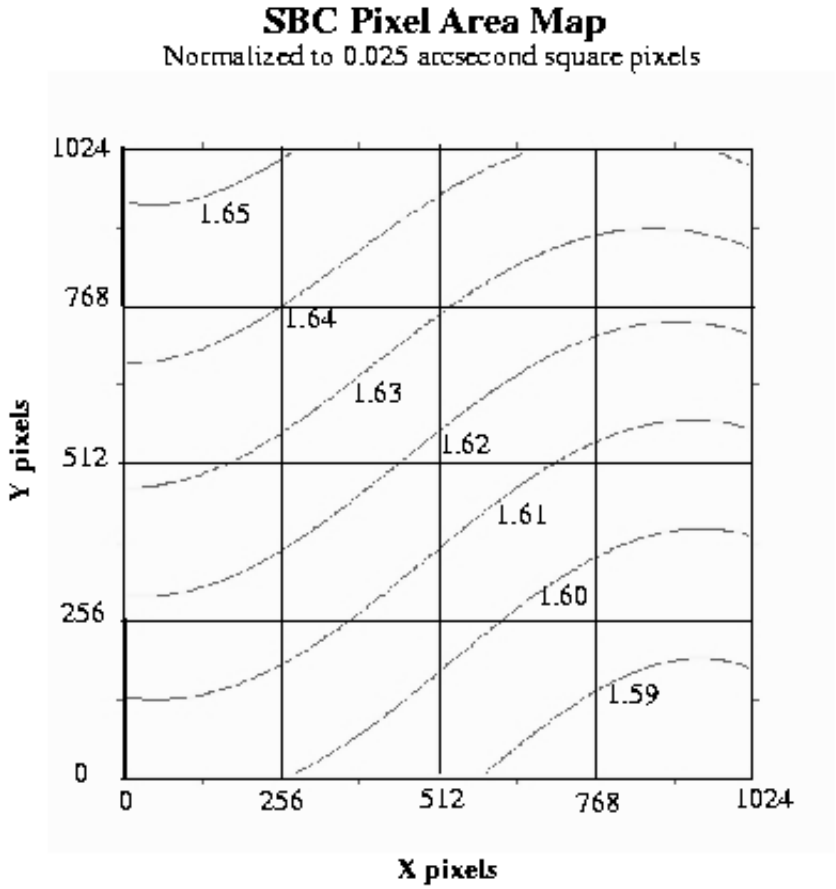

Glossary

The following terms and acronyms are used in this Handbook.

2MASS: Two Micron All Sky Survey.

ABMAG: $-2.5 \log (F_\nu) - 48.60$ where F_ν is the flux from the source in erg cm^{-2} sec^{-1} Hz^{-1}

AB$_\nu$: Correction to ABMAG to account for the fact that the source spectrum is not constant in F_ν ($ABMAG=V+AB_\nu$)

ACS: Advanced Camera for Surveys

ACS-R: Repaired ACS from SM4

ADC: Analog to digital converter

Aladin: Interactive sky atlas (http://aladin.u-strasbg.fr)

APT: Astronomer's Proposal Tool

ASIC: Application-Specific Integrated Circuit in CEB-R

aXe: Spectroscopic Data Extraction Software

BOP: Bright Object Protection

BOT: Bright Object Tools for SBC proposing

calacs: ACS calibration pipeline software

CCD: Charge Coupled Device. Solid-state, light detecting device

CDS: Correlated Double Sampling mode in CEB-R (dual-slope integration or clamp-and-sample)

CEB: CCD Electronics Box

CEB-R: New CCD Electronics Box installed during SM4

CMD: Color Magnitude Diagram

CP: Call for Proposals

CR: Cosmic ray

CR-SPLIT: Division of a CCD exposure into shorter exposures to be used for cosmic ray rejection

CS: Contact Scientist for a *HST* proposal

CTE: Charge transfer efficiency

CVZ: Continuous viewing zone

DN: Data number

DSI: Dual-Slope Integrator

DSS: Digital Sky Survey

ETC: Exposure Time Calculator. ETCs are Web-based tools which can be accessed through the ACS Web pages.

ERO: Early release observations

FGS: Fine Guidance Sensors

FOS: Faint Object Spectrograph

FOV: Field of view

FTP: File Transfer Protocol. Basic tool used to retrieve files from a remote system. Ask your system manager for information about using FTP.

FUV: Far ultraviolet (~912 to 2000 Å)

FWHM: Full width at half maximum

GALEX: Galaxy Evolution Explorer

GHRS: Goddard High-Resolution Spectrograph

GO: General Observer

GSC: Guide Star Catalog

GSC2: Guide Star Catalog II

GTO: Guaranteed Time Observer

Help Desk: Facility for getting help on *HST* related topics via e-mail. help@stsci.edu.

HRC: High Resolution Channel

HST: Hubble Space Telescope

IDT: Investigation Definition Team

IR: Infrared

IRAF: Image Reduction and Analysis System. The environment in which STSDAS operates.

ISR: Instrument Science Report

IUE: International Ultraviolet Explorer Satellite

K: Degree Kelvin

L-flats: Low Frequency Variations Flats

LMC: Large Magellanic Cloud

LVPS-R: replacement Low Voltage Power Supply

MAMA: Multi-Anode Microchannel Array

MAST: STScI Multi-mission Archive

MCP: Microchannel Plate

MPP: Multi Pinned Phased, a CCD mode that reduces dark current rate

NICMOS: Near-Infrared Camera and Multi-Object Spectrograph

NIR: Near infrared

NUV: Near ultraviolet (~2000 to 4000 Å)

OTA: Optical Telescope Assembly

OTFR: On-the-fly re-calibration pipeline that has the ability to select the most up-to-date reference files for science images at the time of request.

PASP: Publications of the Astronomical Society of the Pacific

PC: Program Coordinator

Phase I proposal: A proposal for observing time on *HST*

Phase II program: An approved *HST* program; includes precise detail of how program is to be executed

PI: Principal investigator

P-flats: pixel-to-pixel high-frequency flats

POS TARG: POSition TARGet is used to move the sky in the FOV of the camera

PRF: Pixel Response Function

PSF: Point-spread function.

PyRAF: version of IRAF implemented in the Python language

QE: Quantum Efficiency

QEH: Quantum Efficiency Hysteresis

Quadrant: Section of detector that is read-out by an amplifier. For WFC, there are 4 amplifiers, two for each detector, so each amplifier reads one 2048 x 2048 pixel quadrant.

RA: Right Ascension

RAS: *HST* simulator used in ground tests to accurately simulate the full field OTA illumination, and is used to calibrate *HST* instruments. Also know as RAS/HOMS, the Refractive Aberrated Simulator/Hubble Opto-Mechanical Simulator.

reference file: data file containing ACS parameters or calibration information which is used by the calibration pipeline

rms: Root mean square

RQE: Responsive Quantum Efficiency

SAA: South Atlantic anomaly

SBC: Solar-Blind Channel

SDSS: Sloan Digital Sky Survey

SIDECAR: System Image, Digitizing, Enhancing, Controlling, And Retrieving

SITe: Scientific Image Technologies; company that designed the ACS CCDs

SLIM: Slitless Spectroscopy Simulator

SM4: Servicing Mission 4 to *HST* in May 2009

SMOV: Servicing Mission Observatory Verification

S/N: signal-to-noise ratio

SNAPSHOT: Short exposures taken during unused blocks of telescope time.

SSDR: Solid state data recorders

ST-ECF: Space Telescope European Coordinating Facility

STAN: Space Telescope Analysis Newsletter

STIS: Space Telescope Imaging Spectrograph

STScI: Space Telescope Science Institute

STSDAS: Space Telescope Science Data Analysis System. The complete suite of IRAF data analysis and calibration routines used to process *HST* data.

synphot[1]***:*** STSDAS synthetic photometry (IRAF) software package

TAC: Telescope Allocation Committee

TECs: Thermal Electric Coolers

Tiny Tim: PSF simulation software developed by John Krist & Richard Hook

TIR: Technical Instrument Report

URL: Uniform resource locator. Address for WWW.

UV: Ultraviolet

UVIS: Ultraviolet and Visual (CCD channel of WFC3)

WFC: Wide-Field Channel

WFC3: Wide Field Camera 3, new instrument installed during SM4

WFPC2: Wide Field Planetary Camera-2. Replacement for WF/PC installed during first servicing mission of December 1993.

WWW: World Wide Web. Hypertext-oriented method for finding and retrieving information over the Internet.

1. Synphot will soon be replaced by the pysynphot package, a significantly improved re-implementation of Synphot written in Python. Please visit the pysynphot Web page at http://stsdas.stsci.edu/pysynphot.

Index

T

W

Z